

# Development of characterization methods for thin film solar photovoltaics using time-resolved and hyperspectral luminescence imaging

Gilbert El Hajje

▶ **To cite this version:**

Gilbert El Hajje. Development of characterization methods for thin film solar photovoltaics using time-resolved and hyperspectral luminescence imaging. Materials Science [cond-mat.mtrl-sci]. Université Pierre et Marie Curie - Paris VI, 2016. English. NNT : 2016PA066604 . tel-01666039

**HAL Id: tel-01666039**

**https://theses.hal.science/tel-01666039**

Submitted on 18 Dec 2017

**HAL** is a multi-disciplinary open access archive for the deposit and dissemination of scientific research documents, whether they are published or not. The documents may come from teaching and research institutions in France or abroad, or from public or private research centers.

L'archive ouverte pluridisciplinaire **HAL**, est destinée au dépôt et à la diffusion de documents scientifiques de niveau recherche, publiés ou non, émanant des établissements d'enseignement et de recherche français ou étrangers, des laboratoires publics ou privés.

# UNIVERSITÉ DE PIERRE ET MARIE CURIE

*ÉCOLE DOCTORALE : ED 397 – Physique et Chimie des Matériaux*

# THÈSE présentée par :

**Gilbert EL-HAJJE**

Soutenue le : **16 Décembre 2016**

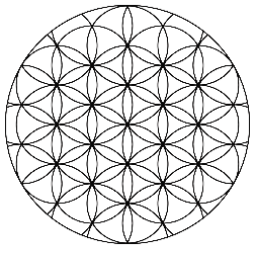
Pour obtenir le grade de : **Docteur de l'université de Pierre et Marie Curie**

Discipline/ Spécialité : Physique des Matériaux

# Développement de nouvelles méthodes de caractérisation optoélectroniques des cellules solaires photovoltaïques par imagerie de luminescence

- Devant le jury composé de:

| | |
|---|---|
| **Dr GUILLEMOLES Jean-François** | **Directeur de thèse** |
| **Dr LOMBEZ Laurent** | **Encadrant de thèse** |
| **Mr ORY Daniel** | **Encadrant de thèse** |
| **Dr. KLEIDER Jean-Paul** | **Rapporteur** |
| **Dr. BALOCCHI Andrea** | **Rapporteur** |
| **Dr. ROCA i CABARROCAS Pere** | **Examinateur** |
| **Dr. UNOLD Thomas** | **Examinateur** |
| **Dr. FRAGOLA Alexandra** | **Examinateur** |
| **Dr. PAUL Nicolas** | **Examinateur** |



***في ذكرى رحيل المرحومة جدتي روز، المرحومة جدتي هيلين، المرحوم جدي جورج والمرحوم جدي توفيق.***

***لهم أعطي الراحة الأبدية يا يسوع.***

***أمين.***

# Development of characterization methods for thin film solar photovoltaics using time-resolved and hyperspectral luminescence imaging

**Gilbert El-Hajje**

02/01/2014 – 16/12/2016

# ACKNOWLEDGMENTS

*Après trois ans de thèse au sein de l'IRDEP, il est sans doute vrai qu'une thèse est une formation par la recherche et pour la recherche. On se lance dans des études doctorales très souvent poussé par notre ambition, par notre passion envers la recherche, et surtout, par notre volonté de vouloir réaliser des découvertes et être pionnier dans son domaine. A un certain point qui succède le point de démarrage de la thèse, on se rend compte rapidement, qu'avoir une bonne performance de chercheur scientifique n'est tout simplement pas suffisant. On s'aperçoit que très souvent, ce qui compte le plus, est l'aspect « humain » des choses, et le support moral qu'on a la chance de recevoir de la part de notre entourage. Ceux qui nous suivent et encadrent de plus près sont dans un premier plan les personnes de notre famille et les personnes appartenant à notre cercle de vie privée mais incontestablement aussi, les personnes qui se sont engagées à être encadrantes de notre travail doctoral. Ces-dernières, ce sont les personnes qui choisissent de superviser nos travaux, les diriger, faire en sorte à ce qu'on avance sur chaque aspect à la fois personnel et scientifique.*

*Dans mon cas, j'ai eu la chance d'avoir à mes côtés, tous les jours, deux encadrants exceptionnels : Laurent Lombez et Daniel Ory. Commençons par Dr. Lombez, AKA « Le Médecin des Cellules Solaires ». Il s'agit d'un personnage scientifique qui malgré son jeune âge, est déjà reconnu à l'international pour ses remarquables travaux de recherches sur le photovoltaïque. Je le remercie infiniment pour être toujours à l'écoute, toujours disponible. Son riche expérience fait de lui la personne vers laquelle je me dirige dans les situations les plus dures (i.e. les soumissions et les taches de dernière-minute, les problèmes techniques insurmontables et pleins d'autres « worst case scenario »). Ses conseils toujours pertinents et sa capacité à proposer des solutions innovantes ont été un moyen indispensable à ma réussite. Passons à la deuxième personne de mon « duo d'encadrants », AKA « Le Monsieur Ory ». Son expérience très riche et vaste dans le milieu professionnel avant de se lancer dans la R&D, a été aussi un premier atout pour solutionner la majorité de mes problèmes techniques (optomécaniques plus précisément). Je le remercie en premier lieu pour être une personne toujours à l'écoute de mes problèmes (parfois non intéressants), pour sa patience, son suivi régulier et surtout pour le temps qui m'a réservé. Je n'oublierai jamais nos fameuses séances de « brainstorming » très*

*fructueuses, génératrices de PI. En plus de sa passion pour la mécanique, je suis fier de lui faire découvrir une nouvelle passion, qui est aujourd'hui la sienne, « Le MaaMoul Libanais » !*

*Un pilier indispensable pour mes travaux de thèse, fut mon directeur de thèse, Dr. Jean-François Guillemoles. Je souhaite avant tout le remercier pour avoir accepté de diriger ma thèse. Je le remercie surtout pour ses interventions, ses commentaires, ses conseils et ses avis toujours aussi pertinents. Son rôle d'expert dans la recherche scientifique fut surtout essentiel en matière de progression et d'évolution. Il m'a appris certaines éthiques et moyens de communication dans le milieu scientifique qui est assez compétitif, rendant ma progression plus efficace et fluide. Je lui serai toujours reconnaissant.*

*Dans un cadre plus global, je tiens à exprimer ma gratitude envers l'ensemble du personnel de l'IRDEP. Une pensée particulière va à l'équipe remarquablement masculine du bâtiment F : Laurent, Daniel, Jean, Pierre, François, Trung, Enrique, et la liste est certainement non exhaustive. La « super » bonne ambiance créée par cette équipe m'a offert un environnement de travail exceptionnellement agréable. Je compte sur vous pour maintenir le niveau «assez particulier » des blagues et des histoires (les gens du F comprendront ;)) . Finalement, je tiens aussi à remercier toutes les personnes du bâtiment K, votre accueil a toujours été chaleureux et amicale. Un grand merci aussi aux différents doctorants pour les beaux moments passés ensemble à l'IRDEP ou même pendant les conférences : François, Sébastien, « Solénge », Charlène, Fabien, Julien et encore une fois la liste est non exhaustive !*

*Finalement, et pour bien conclure cette section, j'offre ces travaux de thèse à mes parents qui, grâce à eux, je suis à ce stade d'études et de réussite aujourd'hui. J'offre ces travaux aussi à mes frères Georges et Magid, ma famille entière, ma femme Salma, mes amis Rémie (Ramroum), Mario, Guy, Rami, Imad et beaucoup d'autres. Leur présence dans ma vie a été une source de réconfort et d'inspiration dans les moments les plus dures. Je vous remercie pour tout.*

*Mes sincères salutations*

*Gilbert El-Hajje*

# Contents

**Index of Symbols** ..... **1**

**Introducing the *PhD* project** ..... **5**

**The General Context of Photovoltaic Energy** ..... **7**

**Chapter I. Theoretical background on CIGS PV devices and their luminescence properties** ..... **10**

1.1 Chalcogenide Cu(In,Ga)$Se_2$ thin-film technology ..... 10

1.1.1 Introduction on CIGS PV technology & Cell configuration ..... 11

1.1.1.1 Back Contact ..... 12

1.1.1.2 CIGS Absorber Layer – Deposition Methods ..... 12

1.1.1.3 CdS Buffer Layers ..... 13

1.1.1.4 Front Contact ..... 13

1.1.2 The particular case of micro-CIGS solar cells used in our experiments ..... 16

1.2 Physics of PV device luminescence ..... 17

1.2.1 Recombination Mechanisms ..... 18

1.2.2 Time-Resolved Photoluminescence (TRPL) ..... 23

1.2.3 Generated carrier dynamics under the influence of electric fields ..... 25

1.2.4 Spectrally Resolved Photoluminescence ..... 26

1.2.5 Spectrally-Resolved Electroluminescence & LED-PV Reciprocity Relations ..... 28

1.2.6 Reciprocity between Photoluminescence and Electroluminescence of solar cells ..... 31

1.2.7 Information derived from the luminescence intensity, its spectral and spatial variations ..... 31

1.3 TRPL studies on CIGS solar cells: The literature contradiction dilemma ..... 32

1.3.1 Theoretical aspect: Physics of charge carrier dynamics in Cu(In,Ga)$Se_2$ PV devices ..... 32

1.3.2 Photo-excitation-dependent TRPL decay analysis on CIGS ..... 33

1.3.3 Voltage-bias-dependent TRPL decay analysis ..... 35

1.3.4 Photo-excitation energy-dependent TRPL decay analysis ..... 37

**Chapter II. Optoelectronic Characterization of PV Devices** ..... **38**

2.1 Standard Solar Cells Characterization Techniques ..... 38

2.1.1 J-V Characteristics ..... 38

2.1.2 External Quantum Efficiency ..... 40

2.1.3 Capacitance-based Techniques ..... 42

2.2 Advanced Luminescence-Based Characterization Techniques ..... 43

2.2.1 Hyperspectral Imager ..... 44

2.2.2 Scanning Confocal Microscope (SCM) ..... 45

2.2.3 Comparison between the HI and the SCM ..... 47

2.2.4 Time-Resolved Fluorescence Lifetime Imaging (TRFLIM) ..... 48

2.2.4.1 Overview of technologies and Operating principles of TRFLIM ..... 48
2.2.4.2 Design and development of a setup dedicated to TRFLIM ..... 50
2.2.4.3 Spatial and Temporal resolutions of the detection system ..... 52
2.2.4.4 Characteristics of the excitation system ..... 58
2.2.4.5 Concluding the construction of the complete TRFLIM setup with a proof of concept ..... 60

**Chapter III. Quantitative local access to optoelectronic properties of Cu(In,Ga)$Se_2$ PV devices using Time-Resolved Luminescence ..... 62**

3.1 General introduction and objectives ..... 62
3.2 Development of a unified understanding of charge carrier dynamics in Cu(In,Ga)$Se_2$ PV devices ..... 62
3.2.1 Introduction ..... 62
3.2.2 Physical model based on carrier recombination centers and shallow defects acting as carrier traps 63
3.2.3 Photo-excitation intensity-dependent and electrical carrier-injection dependent time-resolved luminescence experiments ..... 65
3.2.4 Investigating the potential influence of the built-in electric field ..... 69
3.2.5 Identifying the characteristics of probed carrier recombination ..... 72
3.2.6 Brief summary and conclusion ..... 76
3.3 Optical alternative for the study of metastabilities in Cu(In,Ga)$Se_2$ PV devices ..... 77
3.3.1 Metastabilities-induced distortions of Current-Voltage characteristics ..... 77
3.3.2 Optical evidence of the effect of metastabilities activation on minority carrier dynamics ..... 79
3.3.2.1 Introduction & Methodology ..... 79
3.3.2.2 Basic Characterization ..... 80
3.3.2.3 Qualitative optical observation of a blue photon recovery effect ..... 82
3.3.2.4 Hysteresis cycle of the “DCD” parameter ..... 84
3.3.2.5 Hysteresis cycle of the carrier trapping lifetime ..... 86
3.3.2.6 Brief Conclusion ..... 87
3.4 Contactless quantification of trapping defects density in Cu(In,Ga)$Se_2$ PV devices ..... 88
3.4.1 Development of a physical model for the reconstruction of the time-resolved luminescence decays88
3.4.2 Application to the photo-excitation intensity-dependent time-resolved luminescence decays ..... 92
3.4.3 Application current injection-dependent time-resolved luminescence decays ..... 93
3.4.4 Discussion on the application to the photo-excitation intensity-dependent and current injection-dependent time-resolved luminescence decays ..... 94
3.4.5 The effect of the trapping defects density on global photovoltaic performance ..... 94
3.4.6 An attempt at a quantitative optical spectroscopy of trapping defects ..... 97
3.4.7 Discussing the choice, the limitations and relevance of the physical model ..... 101

**Chapter IV. Quantitative luminescence-based imaging of optoelectronic properties of thin film PV devices102**

4.1 Introduction ..... 102
4.2 Spatially-resolved, spectrally-resolved and time-resolved luminescence of Cu(In,Ga)$Se_2$ PV devices ..... 103
4.2.1 Quantitative electrical mapping of the variations of PV performance indicators following metastabilities activation ..... 103

4.2.2 Quantitative optical mapping of trapping defects-induced variations in PV performance indicators107

4.2.2.1 Mapping the effect of light-soaking on the quasi-Fermi levels splitting deduced from electroluminescence imaging ..... 107

4.2.2.2 Micrometric mapping of charge carrier lifetimes and trapping activity ..... 110

4.2.2.3 Optical micrometric mapping of the absolute trapping defects density ..... 114

4.2.2.4 Mapping the micrometric losses in quasi-Fermi levels splitting ..... 115

4.2.2.5 Investigating the effect the photo-excitation energy ..... 118

4.3 Time-Resolved Fluorescence Lifetime Imaging (TRFLIM) of Solar Cells ..... 121

4.3.1 GaAs solar cell – An experimental study ..... 121

4.3.2 GaAs solar cell – A numerical study & material properties extraction ..... 126

**Conclusion ..... 131**

**Bibliography ..... 134**

**List of peer-reviewed publications & proceedings ..... 143**

**Appendix A ..... 144**

**Résumé ..... 147**

**Summary ..... 148**

# Index of Symbols

| Symbol | Unit | Description |
|---|---|---|
| $a$ | $cm^{-1}$ | Absorptivity |
| $A$ | % | Absorption probability |
| AM1.5 | | Air Mass 1.5 |
| $B_{rad}$ | $cm^3s^{-1}$ | Radiative recombination coefficient |
| $c$ | $ms^{-1}$ | Light velocity |
| $C$ | F | Capacitance |
| $C_n$, $C_p$ | $cm^6s^{-1}$ | Auger recombination coefficient for electron and hole |
| CBD | | Chemical bath deposition |
| DCD | | Dominant Carrier Dynamics parameter |
| $D_n$, $D_p$ | $cm^2s^{-1}$ | Diffusion coefficient of electron and hole |
| $E$ | $Vcm^{-1}$<br>eV | Electric field<br>Photon energy |
| EL | | Electroluminescence |
| $E_a$ | eV | Activation energy |
| $E_{c,}$, $E_{v,}$ | eV | Conduction and valence band edge of semiconductor |
| $E_f$ | eV | Fermi level |
| $E_{fn}$, $E_{\mathrm{fp}}$ | eV | Quasi-Fermi level of electrons and holes |
| $E_g$ | eV | Energy bandgap of semiconductor |
| $e_n$ | $s^{-1}$ | Electron emission rate |
| $E_t$ | eV | Trap energy level |
| $EQE$ | % | External quantum efficiency |
| $f$ | | Occupancy of defect states |
| $f_c$ | % | Collection function (probability to collect a photogenerated carrier) |
| $FF$ | % | Fill factor |
| FWHM | | Full Width at Half Maximum |
| $G$ | $cm^{-3}s^{-1}$ | Generation rate |
| GW | s | Gate width |

| | | |
|---|---|---|
| $h, \hbar = h/2\pi$ | eV.s | Planck's constant, and Planck's reduced constant |
| HI | | Hyperspectral Imager |
| $I$ | A | Current |
| $I_{TRPL}$ | Hits.s$^{-1}$ | Time-resolved photoluminescence decay intensity |
| $I_{TRL}$ | Hits.s$^{-1}$ | Time-resolved luminescence decay intensity |
| $I_{TRPL}^{tot}$ | Hits.s$^{-1}$ | Integrated time-resolved photoluminescence decay intensity |
| IQE | % | Internal Quantum Efficiency |
| $J$ | A.cm$^{-2}$ | Current density |
| $J_{inj}$ | cm$^{-2}$.s$^{-1}$ | Density of injected current flux |
| $J_{sc}$ | A.cm$^{-2}$ | Short-circuit current density |
| $J_{ph}$ | A.cm$^{-2}$ | Photocurrent density |
| $J_0$ | A.cm$^{-2}$ | Saturation current density |
| $J_o^{rad}$ | A.cm$^{-2}$ | Radiative short-circuit current density |
| $J_{01}$ | A.cm$^{-2}$ | Saturation current density for the dark current of ideality A=1 |
| $J_{02}$ | A.cm$^{-2}$ | Saturation current density for the dark current of ideality A=2 |
| $k$ | | Boltzmann constant |
| $N_{A,i}$, $N_{D,i}$ | cm$^{-3}$ | Acceptor and donor density in the semiconductor |
| N.A. | | Numerical Aperture |
| $N_t$ | cm$^{-3}$ | Electron trap density |
| $N_1$ | cm$^{-3}$ | Carrier population occupying the valence band |
| $N_2$ | cm$^{-3}$ | Carrier population occupying the accessible density of trap states |
| $N_3$ | cm$^{-3}$ | Carrier population occupying the conduction band |
| PL | | Photoluminescence |
| PSF | m | Point Spread Function |
| $P_{max}$ | W | Maximum power generated by a solar cell |
| $q$ | C | Elementary charge |
| $R_{rad}$ | s$^{-1}$ | Radiative recombination rate |
| $R_s$ | ohm or ohm.cm² | Series resistance |
| $R_{sh}$ | ohm or ohm.cm² | Shunt resistance |
| $R_{SRH}$ | s$^{-1}$ | Shockley-Read-Hall recombination rate |
| $S_n$, $S_p$ | cm.s$^{-1}$ | Recombination velocity of electron and holes |
| SCM | | Scanning Confocal Microscope |
| SCR | | Space Charge Region |

| | | |
|---|---|---|
| SR | $A.W^{-1}$ | Spectral Response |
| T | K | Temperature |
| TFRLIM | | Time-resolved fluorescence lifetime imaging |
| TRL | | Time-resolved luminescence |
| TRPL | | Time-resolved photoluminescence |
| V | V | Voltage |
| $V_{oc}$ | V | Open-circuit voltage |
| $V_{oc}^{rad}$ | V | Radiative open-circuit voltage |
| $V_{bi}$ | V | Built-in voltage |
| $W$ | cm | Width of the space charge region in the absorber |
| $W_{\mathrm{Rec}}^{occ}$ | | Occurrence weight of direct carrier recombination events |
| $W_{Traps}^{occ}$ | | Occurrence weight of carrier trapping events |
| $Y_{PL}$ | $cm^{-2}.sr^{-1}.eV^{-1}.s^{-1}$ | Photoluminescence yield |
| $\alpha$ | $cm^{-1}$ | Absorption coefficient of the semiconductor |
| $\Delta\mu$ | eV | Quasi-Fermi levels splitting |
| $\Delta\mu_{eff}$ | eV | Effective quasi-Fermi levels splitting |
| $\overline{\Delta\mu}$ | eV | Central, statistical Quasi-Fermi levels splitting value |
| $\varepsilon$ | $Fm^{-1}$ | Dielectric function |
| $\sigma_n, \sigma_p$ | $cm^2$ | Capture cross-section for electrons and holes |
| $\nu_n^{th}, \nu_p^{th}$ | $cm.s^{-1}$ | Thermal velocity of electron and hole |
| $\phi$ | $cm^{-2}.sr^{-1}.eV^{-1}.s^{-1}$ | Luminescence flux |
| $\phi_{bb}$ | $cm^{-2}.sr^{-1}.eV^{-1}.s^{-1}$ | Spectral photon density of a black body |
| $\lambda$ | cm | Wavelength |
| $\eta$ | % | Solar cell efficiency |
| $\eta_{PL}$ | % | Photoluminescence efficiency |
| $\rho$ | ohm.cm | Resistivity |
| $\Gamma$ | m | Penetration depth |
| $\psi_D$ | $cm^{-3}$ | Density of trap states |
| $\mu_n, \mu_p$ | $cm^2.V^{-1}s^{-1}$ | Electron and hole mobility in semiconductor |
| $\tau_b$ | s | Bulk minority carrier lifetime |
| $\tau_{cap}$ | s | Carrier capture lifetime |
| $\tau_{em}$ | s | Carrier emission lifetime |
| $\tau_n, \tau_p$ | s | Carrier lifetime |
| $\tau_{rad}$ | s | Radiative recombination lifetime |

| | | |
|---|---|---|
| $\tau_{\mathrm{Rec}}$ | s | Recombination centers-related carrier lifetime |
| $\tau_{tot}$ | s | Total carrier lifetime |
| $\tau_{Traps}$ | s | Carrier trapping lifetime |
| $\tau_{rec}^{v}$ | s | Vertically averaged profile of carrier recombination lifetime |

# Introducing the *PhD* project

From the evolution of the solar power conversion efficiencies of photovoltaic solar cell technologies, we can learn that the second generation thin-film solar photovoltaics are progressively catching up with monocrystalline-based silicon solar cells. There is no doubt that the latter are occupying the vast majority of today's market shares both in terms of production and installation. However, with CIGS-based thin film PV recently surpassing the record efficiency of multicrystalline silicon, it is safe to expect that second generation thin film PV could indeed start to occupy an increasingly important market share in the PV industry. Such increase in efficiency will eventually induce an increase in the production of the thin film PV panels. However, CIGS-based PV is known to suffer from instabilities issues due its material composition and metastabilities, even at the PV panel scale. Therefore, the future industries dedicated to its production, would be in need of special in-line characterization methods to closely monitor and examine this material that is much more complex than the typical monocrystalline silicon.

CIGS-based PV is at the heart of my PhD project. My aim is to develop new and innovative, luminescence-based characterization methods that have industrial applications. The reason, for which we chose the luminescence of PV devices as a tool, is because it can be optically generated and detected, without the need to physically contact the PV device, which is the case for photoluminescence. This contactless nature of this technique boosts is potential for industrial applications. Throughout my PhD I started by developing different methodologies and revisited the temporal aspect of the photoluminescence of CIGS solar cells. With these methodologies, I translated this aspect into key photovoltaic parameters and properties of the solar PV device. Then, by combining the spectral and temporal aspect of their luminescence, I developed a tool for a contactless evaluation of PV performance losses in the different areas of a thin film PV device. All of the developed methods were applied at both the local and global scale of the CIGS solar cell, using the scanning confocal microscope and the hyperspectral imager setups. Luminescence imaging the spatial aspect to all of my findings and helped us assess the spatial behavior of its PV performance and parameters.

The final part of my PhD was dedicated to the design, the development and the exploit of a new optical characterization setup at IRDEP. The latter is built to perform time-resolved fluorescence lifetime imaging. This technique has so far been used in the fields of biology, organic chemistry and in medicine. My goal was to build a setup that can be used for the characterization of the different PV

technologies. I will present the different building steps of the setup, the evaluations of its characteristics and finally present a panel of proofs of concept on PV devices, and some applications.

I would finally like to add that in addition to all of the above, I worked in parallel on a collaboration with a team from the University of Valencia. The aim of this collaboration was to quantify the spatial inhomogeneities of the properties of perovskite-based solar cells by mapping their luminescence. I summarize in *Appendix A* the main findings of this collaboration.

# The General Context of Photovoltaic Energy

After decades of industrialized growth mainly sustained by fossil energies, tremendous quantities of greenhouse gases have been emitted in the atmosphere. Those gases, mainly methane and carbon dioxide accumulate in the atmosphere and contribute to the warming of our planet, thus confronting our society to the challenge of drastically reducing their emission. According to the International Panel on Climate Change (IPCC) Fourth Assessment Report [1], the carbon dioxide concentration has risen from 280 ppm in the pre-industrial era – late eighteenth century - to approximately 380 ppm nowadays. Keeping the rate of greenhouse gas emissions at its present level would eventually lead to a global carbon dioxide concentration of about 450 to 650 ppm by 2100. Depending on the considered energetic scenario, we would be lead to a mean global temperature increase of 1.1 to 6.4 degrees, thus causing drastic climatic changes [1]. We must thus act as soon as possible in order to reduce both our energy consumption and our dependence towards carbon-intensive solutions, among which fossil fuels. The sector of energy production contributes for about 25.9% to our carbon dioxide emissions. Within the energy sector, electricity production represents about 30% of these emissions. It is thus necessary to look for alternative ways of producing electricity. Solar energy is the most abundant form of energy on Earth. The incident energy that reaches our planet is about 2.1012 GWh over the course of a whole year, which is the equivalent of 11,000 times the yearly global energy consumption. We can see that there is an incomparable potential to be used, and the photovoltaic technology is one way to take advantage of this potential. Even in a country with a very average illumination level, such as France, the entire electricity demand can be met by covering 1% of the surface of the country with a system that has a conversion efficiency as low as 10%. Such a surface represents only one sixth of the constructed area in the country.

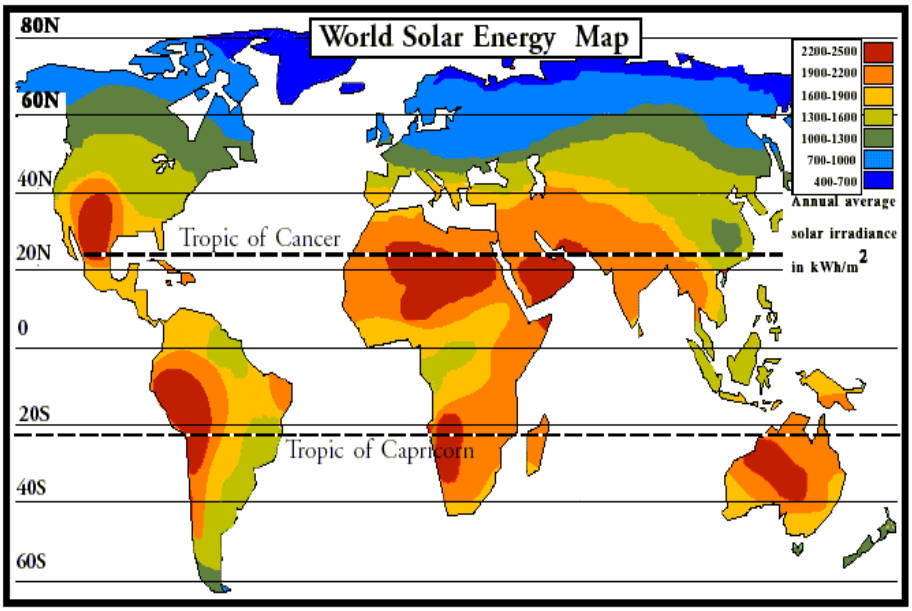



**Figure 1: Annual average solar irradiance**

Photovoltaic technologies remain the most commonly used solar energy collecting technologies today and will continue to see rapid and steady growth. Each of these photovoltaic technologies have its own advantage and drawbacks and it is not certain which one will dominate the market in the following decades; however it is certain is that the photovoltaic technologies will help countries develop a clean and renewable future.

Finally, Fig. 2 below illustrates the evolution throughout the years of the solar power conversion laboratory efficiencies of the major solar PV technologies:

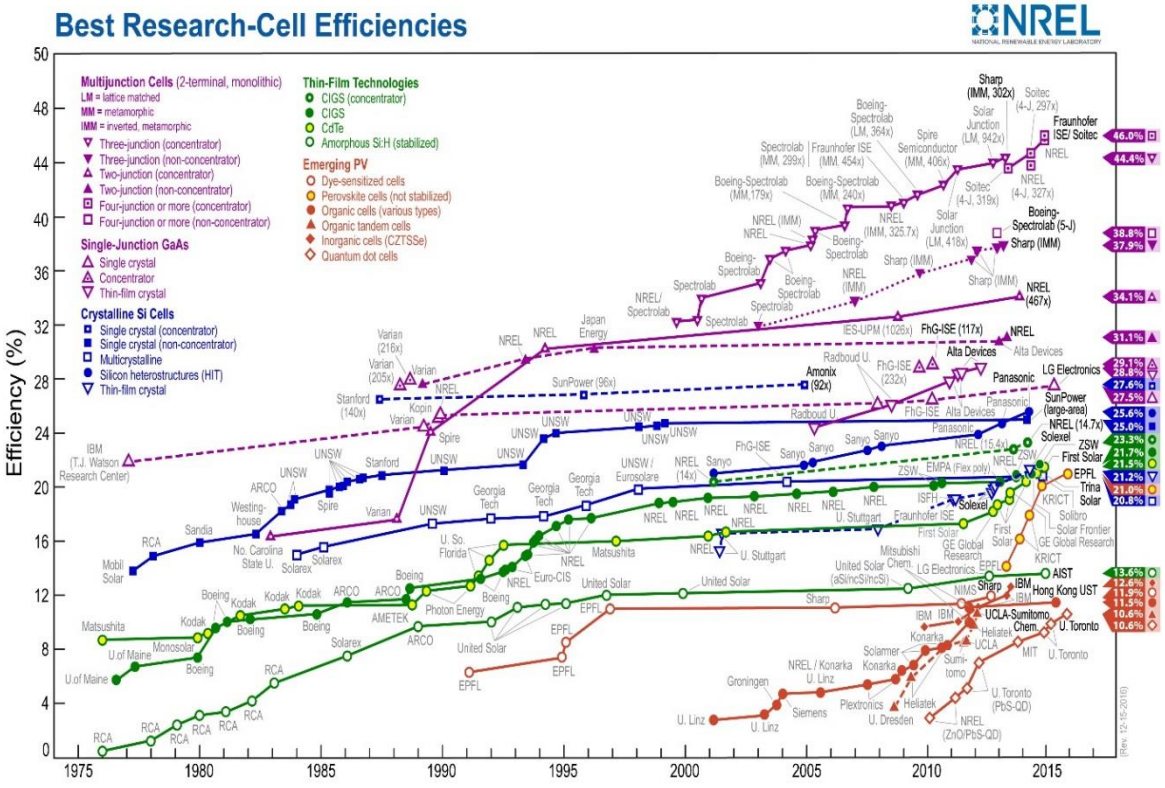



**Figure 2: Evolution of record solar cell efficiencies for different technologies until year 2016**

# Chapter I. Theoretical background on CIGS PV devices and their luminescence properties

Photovoltaics (PV) is a method of generating electrical power by a direct conversion of solar radiation into current electricity using semiconductors with an overall conversion efficiency that ranges from 20% to 35% depending on the considered technology. Photovoltaic solar panels are the most commonly used solar technology to generate electricity energy. They can act as small decentralized power stations when simply placed on the top of a roof. The electricity produced by household possessing photovoltaic panels is usually sold to the network at a higher price than the market price, thus allowing the investor to get his money back. In countries such as Germany or France, the existence of a feed-in tariff has largely contributed to the development and popularity of this technology [2]. Centralized production in photovoltaic farms is also a solution but can be problematic when competing with other uses of land. There are several kinds of solar PV technologies that are currently available. However, each of them is based on quite different concepts and science and each has its unique advantages. Analysis and comparison between different technologies can help adopt the most efficient and beneficial technology given a specific set of conditions.

## 1.1 Chalcogenide Cu(In,Ga)$Se_2$ thin-film technology

Thin films are made by depositing thin layers of photosensitive materials in the micrometer (μm) range on a low-cost backing, such as glass, stainless steel or polymers. The first generation of thin film solar cell produced was a-Si. To reach higher efficiencies, thin amorphous and microcrystalline silicon cells have been combined with thin hybrid silicon cells. With II-VI semiconductor compounds, other thin film technologies have been developed, including cadmium telluride (CdTe) and copper-indium-gallium-diselenide(CIGS).The main advantages of thin films are their relatively low consumption of raw materials, high automation and production efficiency, ease of building integration and improved appearance, good performance at high ambient temperature, and reduced sensitivity to overheating. The current drawbacks are lower efficiency and the industry's limited experience with lifetime performances. For utility production, thin film technologies will require more land than crystalline silicon technologies in order to reach the same capacity due to their lower efficiency. So, land availability and cost must be taken into consideration when thin film technology is considered. However, thin film technologies are growing rapidly. In recent years, thin film production units have increased from pilot scale to 50 MW lines, with some manufacturing units in the gigawatt (GW) range. As a result, thin films technologies are expected to increase their market share significantly by 2020.

Now several companies, such as Solar Frontier [5], TSMC-Solar [6], and MiaSolé [7], have begun operating facilities with over 100MW/yr production capacity.

### 1.1.1 Introduction on CIGS PV technology & Cell configuration

For some time, the chalcopyrite semiconductor $CuInSe_2$ and its alloy with Ga and/or S [$Cu(In,Ga)Se_2$ or $Cu(In,Ga)(Se,S)_2$], commonly referred as CIGS, have been leading thin-film material candidates for incorporation in high-efficiency photovoltaic devices. $CuInSe_2$-based solar cells have shown long-term stability and the highest conversion efficiencies among all thin-film solar cells, recently reaching 22.3% on a glass substrate [9]. A variety of methods have been developed to prepare CIGS thin film. Efficiency of solar cells depends upon the various deposition methods as they control optoelectronic properties of the layers and interfaces. CIGS thin film grown on glass or flexible (metal foil, polyimide) substrates require p-type absorber layers of optimum optoelectronic properties and n-type wide band gap partner layers to form the p-n junction. The current record for a CIGS solar cell grown on a flexible substrate is at 20.3% [10]. Transparent conducting oxide and specific metal layers are used for front and back contacts of CIGS solar cells.

Cell preparation starts with the deposition of back contact, usually Mo, on glass, followed by the p-type CIGS absorber, CdS or other weakly n-type buffer layer, undoped ZnO, n-type transparent conductor (usually doped ZnO: Al), metal grid, and antireflection coating. It requires an additional encapsulation layer and/or glass to protect the cell surface. The structure of a CIGS solar cell (seen in Figure 1.1 taken from ref [31]) is quite complex because it contains several compounds as stacked films that may react with each other. Fortunately, all detrimental interface reactions are either thermodynamically or kinetically inhibit at ambient temperature [12].

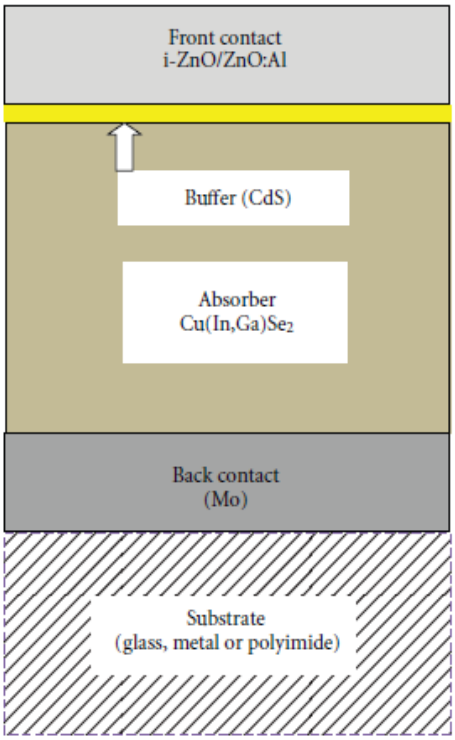



**Figure 1.1: Schematic cross-section of a chalcopyrite-based thin-film solar cell.**

#### 1.1.1.1 Back Contact

Molybdenum (Mo) is the most common metal used as a back contact for CIGS solar cells. Several metals, Pt, Au, Ag, Cu, and Mo, have been investigated for using as an electrical contact of CIS- and CIGS-based solar cells [13– 15]. Mo emerged as the dominant choice for back contact due to its relative stability at the processing temperature, resistance to alloying with Cu and In, and its low contact resistance to CIGS. The typical value of resistivity of Mo is nearly $5 \times 10^{-5}$ Ω cm or less. The preferred contact resistivity value is ≤0.3Ω cm. Results have been reported in several papers [13, 16, 17] concerning the influence of the mechanical and electrical properties of the Mo films on the performance of the photovoltaic devices. Molybdenum is typically deposited by e-gun evaporation [17, 18] or sputtering [19–21] on soda-lime glass which ideally provides an inexpensive, inert, and mechanical durable substrate at temperatures below 500–600◦C.

#### 1.1.1.2 CIGS Absorber Layer – Deposition Methods

I–III–$VI_2$ semiconductors, such as CIS or CIGS are often simply referred to as chalcopyrites because of their crystal structure. These materials are easily prepared in a wide range of compositions and the corresponding phase diagrams are well investigated [22–24]. For the preparation of solar cells, only slightly Cu-deficient compositions of p-type conductivity are suited [25, 26]. A wide variety of thin-film deposition methods has been used to deposit Cu(In,Ga)Se2 thin films. To determine the most promising

technique for the commercial manufacture of modules, the overriding criteria are that the deposition can be completed at low cost while maintaining high deposition or processing rate with high yield and reproducibility. Compositional uniformity over large areas is critical for high yield. Device considerations dictate that the $Cu(In,Ga)Se_2$ layer should be at least 1 μm thick and that the relative compositions of the constituents are kept within the bounds determined by the phase diagram. The most promising deposition methods for the commercial manufacture of modules can be divided into two general approaches that have both been used to demonstrate high device efficiencies and in pilot scale manufacturing. The first approach is vacuum coevaporation in which all the constituents, Cu, In, Ga, and Se, can be simultaneously delivered to a substrate heated at 400◦C to 600◦C and the $Cu(In,Ga)Se_2$ film is formed in a single growth process. The second approach is a two-step process that separates the delivery of the metals from the reaction to form device-quality films. Typically the Cu, Ga, and In are deposited using low-cost and low-temperature methods that facilitate uniform composition. Then, the films are annealed in a Se atmosphere, also at 400◦C to 600◦C. The reaction and anneal step often takes longer time than formation of films by coevaporation due to diffusion kinetics, but is compatible with batch processing.

#### 1.1.1.3 CdS Buffer Layers

Semiconductor compounds with n-type conductivity and band gaps between 2.0 and 3.6 eV have been applied as buffer for CIGS solar cells. However, CdS remains the most widely investigated buffer layer, as it has continuously yielded high-efficiency cells. CdS for high-efficiency CIGS cells is generally grown by a chemical bath deposition (CBD), which is a low-cost, large-area process. However, incompatibility with in-line vacuum-based production methods is a matter of concern. Physical vapor deposition- (PVD-) grown CdS layers yield lower efficiency cells, as thin layers grown by PVD do not show uniform coverage of CIGS and are ineffective in chemically engineering the interface properties. The role of the CdS buffer layer is twofold: it affects both the electrical properties of the junction and protects the junction against chemical reactions and mechanical damage. From the electric point of view the CdS layer builds a sufficiently wide depletion layer that minimizes tunneling and establishes a higher contact potential that allows higher open circuit voltage value [27, 28]. The buffer layer also plays a very important role as a “mechanical buffer” because it protects the junction electrically and mechanically against the damage that may otherwise be caused by the oxide deposition (especially by sputtering).Moreover, in large-area devices the electric quality of the CIGS film is not necessarily the same over the entire area, and recombination may be enhanced at grain boundaries or by local shunts. Together with the undoped ZnO layer, CdS enables self-limitation of electric losses by preventing defective parts of the CIGS film from dominating the open circuit voltage of the entire device[29].

#### 1.1.1.4 Front Contact

There are two main requirements for the electric front contact of a CIGS solar cell device: sufficient transparency in order to let enough light through to the underlying parts of the device, and sufficient conductivity to be able to transport the photo-generated current to the external circuit without too much resistance losses. Transparent conducting metal oxides (TCO) are used almost exclusively as the top contacts. Narrow lined metal grids (Ni–Al) are usually deposited on top of the TCO in order to reduce the series resistance. The quality of the front contact is thus a function of the sheet resistance, absorption and reflection of the TCO as well as the spacing of the metal grids [30]. Nowadays CIGS solar cells employ either tin doped $In_2O_3$ or, more frequently, RF-sputtered Al-doped ZnO.

Once the full $Cu(In,Ga)Se_2$ solar PV device deposition is made, the obtained result regarding the total stack is illustrated in Figure 1.2 taken from ref [11].

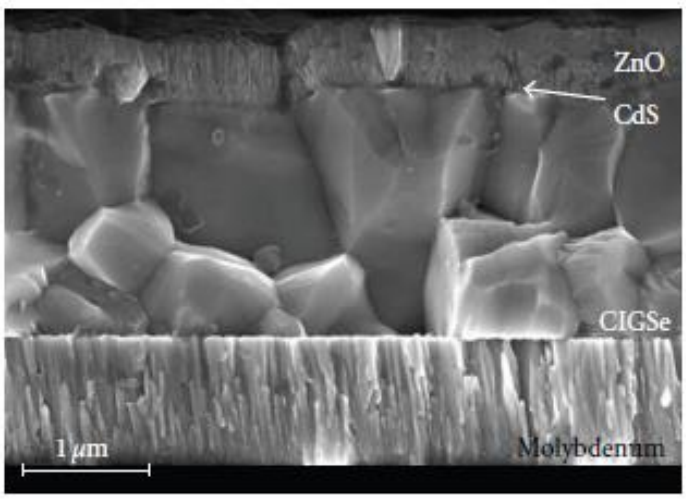



**Figure 1.2: Scanning electron micrograph of the cross-section of a typical chalcopyrite solar cell with $Cu(In,Ga)Se_2$ (CIGSe) absorber**

The corresponding energy band diagram of the total CIGS PV device can be seen in Figure 1.3.:

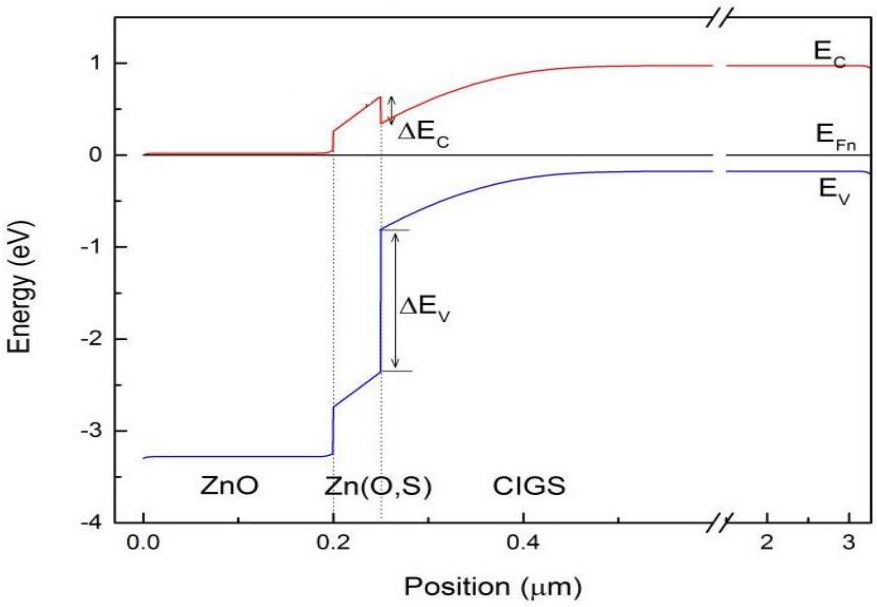



**Figure 1.3: Energy band diagram of a full CIGS PV device**

It is well known that CIGS has a large deviation from stoechiometry attributed to antisite defects, vacancies and defect clusters in the material. Zhang [37] has calculated the transition energy for a large number of defects in CIS, and the results are summarized in Figure 1.4. Knowledge of the defect energies as well as their densities is an important input to develop meaningful device models. DLTS is a standard diagnostic technique for determining the trap properties such as trap energy level, capture cross section, and trap concentration.

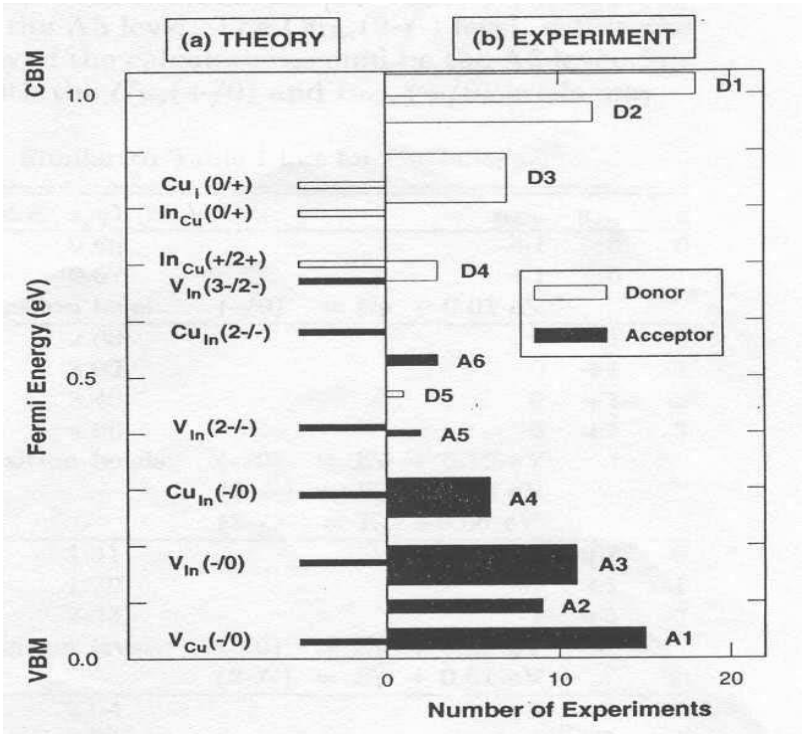



**Figure 1.4: Defect Transition Energy Diagram of $\alpha$ - $CuInSe_2$ [37]**

### 1.1.2 The particular case of micro-CIGS solar cells used in our experiments

In usual studies on the inhomogeneities of the CIGS cells at the micrometer scale, standard laboratory samples are investigated. Compared to the area effectively probed, these cells are much larger (usually more than 0.1 $cm^2$). Such areas may cause measurement artifacts. More precisely, when performing optoelectrical measurements one can suffer from sheet resistance effects under a high excitation flux when doing photoluminescence measurements. Thus, we will study in this thesis circular CIGS microcells, as presented in Figure 1.5. To underline the advantages of such a device, we introduce the general concept of the microcell.

The microcells are designed for use under concentrated sunlight. The main purpose of their development is to save material. Moreover, taking advantage of the light concentration, these cells demonstrated a 4% absolute efficiency increase when compared to corresponding large area cells [106, 107]. This increase results from the simultaneous logarithmic increase of the open-circuit voltage.

Different aspects usually limit the concentrated photovoltaic technology (CPV). Firstly, strong current densities are reached (several $A/cm^2$), resulting in resistive limitation of the front layer. Secondly the temperature may increase to result in a global efficiency loss. Due to their small scale, the microcells efficiently overcome these difficulties [107].

To elaborate on these cells, different fabrication techniques are explored. As a proof of concept, they were originally made of usual large cells that were artificially reduced. Their elaboration was made by Myriam Paire during her thesis at IRDEP [152].

This kind of cell is under study in this thesis. Previous characterization work on this type of solar cells has been done by Amaury Delamarre [153] during his PhD work. In particular, he performed hyperspectral luminescence imaging experiments on these devices to extract their properties such as the local dark saturation currents, the EQE, the quasi-Fermi levels splitting, the sheet resistance and current transport efficiency.

Our investigated samples are glass/Mo/CIGS/CdS/ZnO circular microcells with diameters varying between 20 µm and 30 µm. The 2µm thick CIGS absorber prepared using a three-stage co-evaporation method, possesses an optical bandgap energy Eg=1.1730 eV and the following composition ratios:

$$\frac{Ga}{Ga+In}=0.26 \quad \& \quad \frac{Cu}{Ga+In}=0.78 .$$

It is also to be noted that the CIGS absorber possess a V-shaped [Ga/ (Ga+In)] composition gradient.

The CdS layer is deposited by Chemical Bath Deposition (CBD) technique. The bath is composed of cadmium acetate ($Cd(CH_3CO_2)_2$), thiourea ($SC(NH_2)_2$) and ammonia ($NH_3$) in aqueous solution. The deposition is done at 65°C under constant agitation during approximately 5 minutes. The samples are then rinsed in distilled water and any parasitic particle is removed by ultrasound. The thickness of the CdS layer is around 50 nm.

Finally the TCO layers were deposited by sputtering and consist of a 50 nm layer of i-ZnO and a 350 nm layer of ZnO-Al.

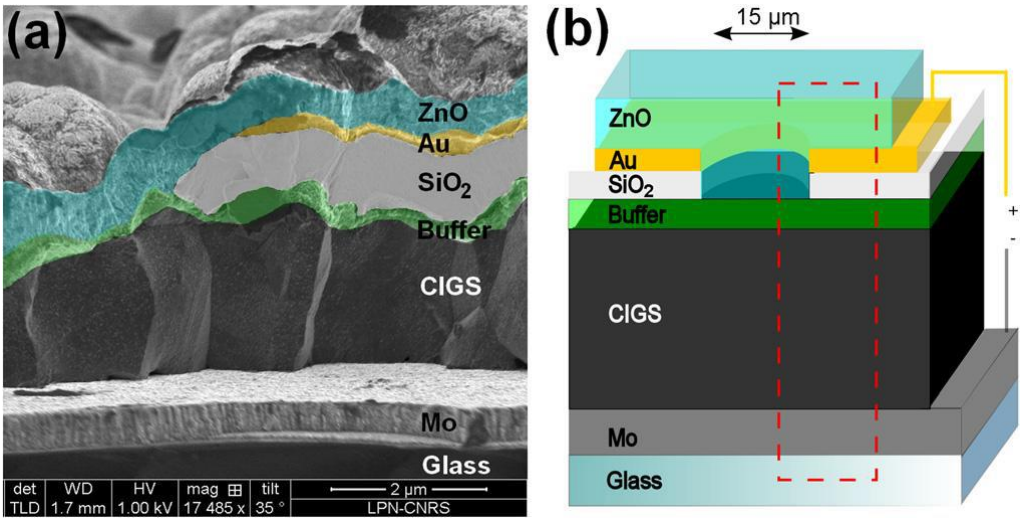



**Figure 1.5: (a) SEM image and (b) scheme of a microcell structure. Figure from ref [106]**

To obtain microcells, a 400 *nm* thick insulating $SiO_2$ layer as well as a 20 *nm*/300 *nm* Ti/Au bilayer are deposited above the CdS layer. Holes obtained by photolithography in the $SiO_2$ delimit the microcell. The ZnO layers are obtained by sputtering. The contact is therefore done at the perimeter of the cell by the Au layer. An SEM image of the resulting structure is shown in Fig.1.5(a). From a characterization point of view, such a structure is convenient as small areas are easily investigated by various setups. Moreover, we do not suffer from the top layer sheet resistance, so that electric measurement at the perimeter of the cell is directly comparable to the luminescence measurement. Such observations are usually made impossible by the large area cells. The CIGS luminescence being usually weak, strong excitation are needed (such as 10000 suns equivalent illumination), so that the efficient temperature management is also an advantage.

## 1.2 Physics of PV device luminescence

Luminescence is "cold light", light from other sources of energy, which can take place at normal and lower temperatures.

In the process of luminescence, when radiation is incident on a material some of its energy is absorbed and re-emitted as a light of a longer wavelength (Stokes law). In the process of luminescence, wavelength of light emitted is a characteristic of a luminescent substance and not of the incident radiation. The emission of light takes place at characteristics time after absorption of the radiation. The luminescence emission is seen to be spontaneous, thus it is seen to be taking place simultaneously with absorption of radiation.

The light emitted could be visible light, ultra-violet, or infrared light.

This cold emission, i.e. luminescence, involves two steps: (1) The excitation of electronic system of a solid material to higher energy state, and (2) subsequent emission of photons.

In the case of an external voltage applied as the excitation source, we speak of electroluminescence (EL), and in case, an incident light source is used, we speak of the photoluminescence (PL). Solar photovoltaic cells for example can reciprocally function as LEDs or current generators.

Therefore, the source of PL and EL radiation is the transition of electrons from higher occupied electronic states into lower unoccupied states where it recombines with a hole, under the emission of a photon. Comparing to other investigation techniques, PL methods offer several advantages in the field of PV, it is non-destructive, non-invasive, and can actually be performed at each fabrication step of our solar cells. We must note that there are other types of luminescence such as: Cathodoluminescence, thermoluminescence, etc…

In the first part of the chapter, we will be describing the classical mechanisms behind the physics of the luminescence of PV devices. That includes the radiative recombination process that matters the most of which is unavoidable.

In the second part, we will discuss the temporal aspect of photoluminescence and explaining the charge carrier dynamics and what one can expect to observe and deduce while performing time-resolved photoluminescence experiments.

In the third part, we switch from the description of the temporal to the spectral characteristics of the photoluminescence. In particular, we will be including the absorptivity of solar PV devices and end up by presenting and explaining the Generalized Planck's law for luminescence emission that relates the intensity of the latter to the optical properties of the PV device.

In the final part of this chapter we will focus on the reciprocity relations between the functioning of a system in LED & and PV mode. This will include the description of the spectral characteristics of solar PV electroluminescence.

### 1.2.1 Recombination Mechanisms

In a nondegenerate semiconductor, the equilibrium density of electron-hole pairs is constant at a given temperature. The law of mass action [67] arises from thermodynamics and relates the product of electrons and holes to the intrinsic density, which is specific to a material. The law of mass action is written as:

$$n^0 p^0 = n_i^{\,2}(T) \tag{1.1}$$

Here $n^0$ is the free-electron density, $p^0$ is the free-hole density at equilibrium, and $n_i$ (T) is the intrinsic density at the absolute temperature T in degrees Kelvin. $n_i$ is related to the effective conduction-band $N_c$ and valence-band $N_v$ densities of states by the relationship:

$$n_i^2(T) = N_c N_v \exp\left(-E_g / kT\right) \tag{1.2}$$

Excess carriers can be electrically or optically injected into the semiconductor, creating a nonequilibrium concentration:

$$np > n_i^2(T) \tag{1.3}$$

Assuming that each quasi-Fermi level $E_{Fn}$ & $E_{Fp}$ is flat from the injecting contact through the majority carrier regions and throughout the space-charge region or SCR, only in the minority carrier regions, the quasi Fermi levels shall be allowed to vary. In the complete SCR the splitting of the quasi-Fermi levels equals the applied voltage bias and it holds:

$$np = n_i^2 \exp\left\{\frac{E_{Fn} - E_{Fp}}{kT}\right\} = n_i^2 \exp\left\{\frac{qV}{kT}\right\} \tag{1.4}$$

If one aims at deriving a general routine for the determination of the diode quality factors for different recombination mechanisms, equation (1.4) can be generalized as:

$$(np)^{1/A} == n_i^{2/A} \exp\left\{\frac{qV}{AkT}\right\} \quad \text{, with } A \text{ the diode quality factor.} \tag{1.5}$$

In equation (1.5), we distinguish between three different cases of carrier recombination mechanisms that will be detailed later on:

If A=1, then the regime corresponds to radiative electron-hole pair recombination. If A=2, then an electron or a hole is involved in a defect-related recombination. Finally, if A=3, three particles are involved in an Auger-type recombination mechanism.

Thermodynamics drives the system toward the equilibrium described by Eq. (1.2). In the absence of further injection, equilibrium is restored via various recombination mechanisms that will be discussed in this chapter. In an intrinsic material or under high-injection conditions, n ~p, and the recombination process is called bimolecular decay. Bimolecular recombination rates will be derived in this section. If the medium is extrinsically doped with donors or acceptors, the minority-carriers are holes or electrons, respectively. For the case of CIGS, a p-doped material forms the absorber of the PV device and the minority carriers are therefore electrons. We have:

$$p^0 = N_A \text{ ,} \qquad n^0 = \frac{n_i^2}{N_A} \qquad \text{=> p-doped CIGS} \tag{1.6}$$

Here, $p^0$ is the free hole-density that is derived from the law of mass motion. If both donors and acceptors are present, compensation occurs and:

$$p_0 = N_D - N_A \tag{1.7}$$

Now, let's assume that at t =0 the system is brought out of equilibrium , *Δn, Δp* excess electron, hole pairs per unit volume are produced by an injection pulse where:

$$\begin{cases} \Delta n(x,t) = n(x,t) - n_0 \\ \Delta p(x,t) = p(x,t) - p_0 \end{cases} \tag{1.8}$$

Here n(x,t) and p(x,t) are the non-equilibrium electron and hole concentrations, respectively.

It is to be noted that $n_0$ and $p_0$ can be position-dependent at the vicinity of the interfaces.

The solution for Δn(x, t) is found by solving the time-dependent continuity equation [68]. For field-free or quasi-neutral regions of the semiconductor, the continuity equation reduces to the time-dependent diffusion equation. The diffusion equation is a partial differential equation relating the net diffusion of minority carriers into a volume and the net recombination of the carriers within the volume. After the generation of electron-hole pairs, the diffusion equation for Δn(r, t) is given by:

$$\frac{\partial \Delta n(r,t)}{\partial t} = D\nabla \Delta n(r,t) - \frac{\Delta n(r,t)}{\tau} \tag{1.9}$$

Here, τ is the recombination lifetime, which may also be a function of other parameters including Δn. Also, D is the minority electron diffusivity. For a general solution of this equation, one first assumes that the time and spatial variables can be separated. The electron concentration (Δn) can be written as:

$$\Delta n(r,t) = f(t)g(r) \tag{1.10}$$

Substituting Eq. (1.10) into the diffusion Eq. (1.9), it can be shown that:

$$\frac{1}{f(t)}\frac{df(t)}{dt} + \frac{1}{\tau} = D\frac{\nabla^2 g(r)}{g(r)} = C \tag{1.11}$$

The left-hand side of Eq. (1.11) is a function of time only, and the right-hand side is a function of spatial variables only. Thus, each side of the equation must equal a constant that is designated by the value C. One can write an ordinary differential equation as a function of time for the left-hand side. Here, we will examine solutions of the time-dependent components of Δn(t) assuming that C = 0:

$$\frac{d\Delta n}{dt} = -\frac{\Delta n}{\tau} \tag{1.12}$$

Equation (1.12) forms the basis for all of the upcoming theoretical and experimental sections. Such equation is extremely important. Based on it, we have a fist proof of the mathematical nature of the temporal evolution of the excess minority carrier density following a pulsed excitation. We can directly see that the time-decay of this density follows an exponential mathematical law. The decay time is called the minority carrier recombination lifetime "τ".

In terms of minority carrier dynamics, the emitted luminescence intensity originates from radiative recombination between the generated electron-hole pairs. At this stage, we assign to these carriers a first definition of **radiative recombination** lifetime $\tau_{rad}$. The intensity of the time-resolved luminescence signal strictly depends on the rate at which occur these radiative events. This rate is called the radiative recombination rate $R_{rad}$ and depends on the excitation level. As Δn increases so does the number of radiative events and consequently the TRPL decay intensity increases. The rate can hence be expressed as:

$$R_{rad} = \frac{d\Delta n}{dt} = -\frac{\Delta n}{\tau_{rad}} \tag{1.13}$$

For a p-doped and direct bandgap semiconductor such as a CIGS PV device, the radiative recombination coefficient is written as:

$$B_{rad} = \frac{1}{p_0 \tau_{rad}} \tag{1.14}$$

This will provide an expression for $R_{rad}$ as a function of $B_{rad}$:

$$R_{rad} = B_{rad} p_0 \Delta n \tag{1.15}$$

In high injection level scenario, to the bimolecular type of radiative recombinations, an **Auger recombination** is added, with $C_{p,n}$ the Auger recombination coefficient. The recombination stops being only bimolecular but becomes a mix of bi-molecular and three-carrier type of recombinations.

Similar to radiative recombination, Auger recombination also is an intrinsic recombination process which cannot be avoided and which is active in chalcogenide devices. The net recombination rate for Auger recombination is given by:

$$R_{Auger} = C_p (p^2 n - {p_0}^2 n_0) + C_n (n^2 p - {n_0}^2 p_0) \tag{1.16}$$

For a p-type absorber (such as a CIGS absorber) with $p \approx p_0 \approx N_A$ which is exposed to small carrier injection or medium excitation, the Auger excitation probability of an electron is very small due to the small number of electrons being minority carriers. Then, the Auger-limited lifetime is determined by hole excitation and it is expressed as:

$$R_{Auger} = C_p N_A^2 \Delta n \tag{1.17}$$

In a real PV device we find undesirable densities of localized states that originate from either impurities or mechanical defects such as dislocations. In addition, major sites of minority-carrier recombination are surfaces or interfaces that contain bonding defects. The energy levels of surface defects often lie in the forbidden gap, producing surface or interface states. The physics of the recombination at deep level defects is discussed later on.

We can hence deduce that other types of routes exist for carrier recombination in a semiconductor. The nature of these additional routes will strictly depend on the nature of these localized states and their characteristics such as their energy level within the forbidden gap, their chemical nature, their charge, capture cross section and many others.

The **non-radiative recombination** of electron-hole pairs at defect levels in the bandgap was first discussed by Shockley and Read [69] and by Hall [70]. Later work by Sah et al. [71] added to the understanding of the role of such defects. This common mechanism in minority-carrier kinetics is frequently called the Shockley-Read-Hall (SRH) recombination mechanism. The physics involves minority-carrier capture at defects that have quantum levels in the bandgap of the semiconductor. The SRH recombination rate is derived in most semiconductor textbooks [68, 72] and is shown to be:

$$R_{SRH} = \frac{\sigma_p \sigma_n v_{th} N_t \left[ pn - n_i^2 \right]}{\sigma_n \left[ n + n_i \exp\left( \frac{E_t - E_i}{kT} \right) \right] + \sigma_p \left[ p + n_i \exp\left( \frac{E_i - E_t}{kT} \right) \right]} \tag{1.18}$$

and has units of $cm^{-3}s^{-1}$. Here, $N_t$ is the volume density of deep levels; $\sigma_p$ and $\sigma_n$ are the hole and electron capture cross-sections, respectively; and $E_t$, is the energy level of the trap. The electron and hole concentrations are *n* and *p*, respectively, and $v_{th}$ is the thermal velocity that is considered identical for the electrons and holes. A logarithmic plot of $R_{SRH}$ versus $E_t - E_i$ shows a plateau at $E_t = Ei$. The maximum non-radiative recombination rate occurs at defects levels that lie at or near midgap. When the defect energy level is near either band, thermal emission to the band quenches the recombination process. For the case, when $E_t$ lies near $E_c$ the denominator term $n_i \exp\left( \frac{E_t - E_i}{kT} \right)$ becomes very large.

This term describes the emission of trapped electrons to the conduction band. Because of electron emission, the electron occupancy is small and the recombination rate is decreased.

### 1.2.2 Time-Resolved Photoluminescence (TRPL)

Based on all what we have discussed so far, we learned that three different routes can be taken by carriers after generation: Radiative bimolecular recombination, Auger recombination , non-radiative deep SRH recombination and carrier trapping by shallow electron or hole trap levels lying at the vicinity of the conduction and valence band. In figure 1.6 below we show a schematic illustration of these events:

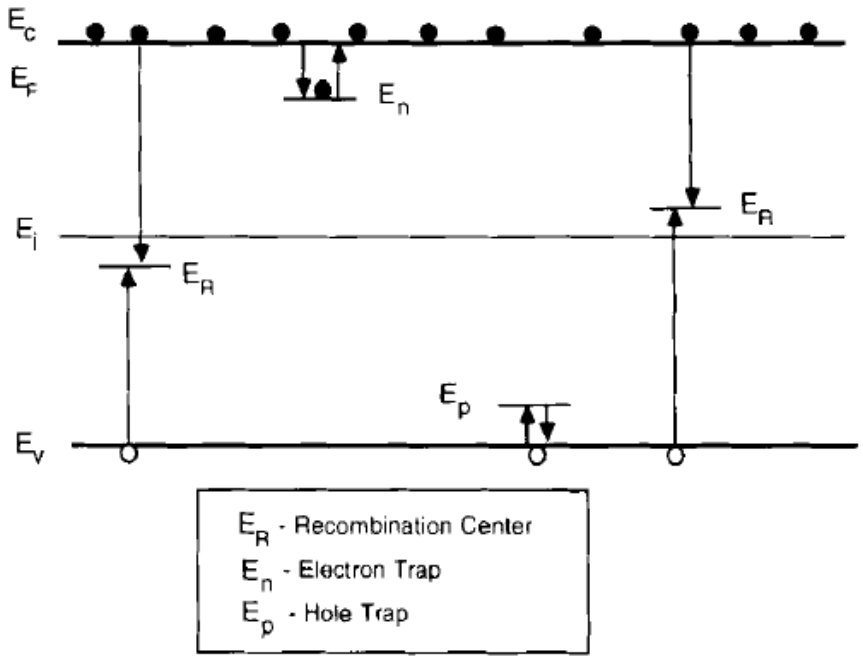



**Figure 1.6: Schematic diagram of impurity-related energy levels within the forbidden gap of a semiconductor. Levels are labeled as to whether the defect is likely to be a trap or a recombination center according to the Shockley-Read-Hall model. (taken from Ref [65])**

Figure 1.6 shows the forbidden gap of a semiconductor that has several types of impurity levels. Those near the midgap position are labeled recombination centers. Also shown are levels that are designated as electron traps and hole traps. These lie near the conduction band and the valence band, respectively. The defect level described by Eq. (1.18) may be either a trap or a recombination center, depending on $E_t$. The defect level is a trap when the absolute value $|E_i - Et|$ is large ($\sim E_g/2$) and the energy level $E_t$, lies near either band. A captured hole or electron is thermally emitted back to the valence band or to the conduction band, respectively. In either type of trap, an emission term in the denominator of Eq. (1.18) dominates, and $R_{SRH}$ decreases many orders of magnitude relative to $E_t$, being midgap. The demarcation between trapping and recombination centers is described in detail elsewhere [73]. If the energy level $E_t$, lies near midgap $E_i$ , $R_{SRH}$ becomes very large, and recombination is the most probable event. Thus, midgap centers ($E_t - E_i$) are very effective recombination sites.

When more than one defect type is present, the total, low-injection lifetime is described by a single minority-carrier lifetime τ, where:

$$\frac{1}{\tau} = \frac{1}{\tau_{rad}} + \sum_i \frac{1}{\tau_i} \tag{1.19}$$

Here, $\tau_i$ is the non-radiative/trapping lifetime for each specific type of defect. Equation (1.19) results from the notion that recombination probabilities are additives. The defects here are assumed to be uniformly distributed in the volume of the semiconductor. They may be localized at specific locations in the material. In particular, recombination levels are usually generated at surfaces and interfaces because of the high concentration of impurities and bonding defects. These defects are the origin of the parameter called the surface or interface recombination velocity. In addition, under this low-injection condition, the Auger recombination rate is negligible.

From an experimental point of view, we remind that the TRPL signal is the result of the different recombination or trapping events. By decay dynamics we refer to its mathematical behavior. We have seen from the previous equations that it naturally obeys an exponential decaying law, only if τ is constant. However, does the presence of multiple types of lifetimes involve different decaying velocities? In other terms, can the TRPL decay present a mono, double or even triple exponential decay?

Experimentally, as SRH events become more frequent, a weaker TRPL intensity is obtained. Unfortunately, this means that SRH events do not influence the dynamics of the decay but only its intensity and hence cannot be directly extracted. One can therefore conclude that two different samples with the same PV material under the same excitation conditions, can be compared based on the overall TRPL intensity. Such comparison can eventually provide relative information on their relative density of SRH states and their material quality.

For trapping events however, things become more interesting. Trapping does not lead to a loss of carriers but rather a delay factor of the radiative recombinations. Such characteristic is expected to have its direct signature on the TRPL decay as one could expect to observe two different decay lifetimes characterized by two states of carrier dynamics. The first state being related to direct radiative recombination events, and the second related to carrier trapping events. From a kinetics point of view, the delaying effect of traps would then be translated in a slower decay of the luminescence signal.

Based on the previously combined knowledge of carrier dynamics, the temporal evolution of the luminescence intensity $I_{TRPL}(t)$ can be mathematically expressed as:

$$I_{TRPL}(t) = B_{rad} p_0 \Delta n(t) + C_p {p_0}^2 \Delta n(t) \tag{1.20}$$

Firstly, Equation (1.20) tells us that the luminescence intensity depends on the initial doping level of the CIGS solar cell and the excitation level of the PV device. For a given CIGS device, $p_0$ is defined during the device fabrication process. Δn however, can be varied experimentally by tuning the excitation level. Three cases can be defined: Case of low-moderate injection level according to which $\Delta n_0 << p_0$, the case of moderate injection level for which $\Delta n \geq p_0$ and the case of high injection level for which for which $\Delta n >> p_0$. In the low and moderate injection level scenario, it is the bimolecular type of recombination that predominates. According to the literature [131], chalcogenide thin films exhibit radiative lifetime values $\tau_{rad}$ in the range of $10^{-6}\,s$.

Up to a certain extent, at very high injection levels, it is possible that recombinations become purely Auger-type of recombination. Very few or no pure experimental data exist for the Auger coefficients of chalcogenide materials. In order to estimate the relative importance of Auger recombination for chalcogenide absorbers in thin film solar cells, we follow the argument of Bube [157] who gives a lower limit for the Auger coefficient of $C_p = 10^{-28} cm^{-6} s^{-1}$.In addition, the lifetime of minority carriers in the Auger limit is given by: $\tau_{Aug} = (C_p N_A^2)^{-1}$. We learn from this expression, that the Auger recombination is the limiting process in the case of high doping concentrations. Hence, based on the Bube approximation for $C_p$, the Auger limited lifetimes for the doping densities of $N_A = 10^{15}, 10^{16}, 10^{17}, 10^{18} cm^{-3}$ are $\tau_{Aug} = 10^{-2}, 10^{-4}, 10^{-6}, 10^{-8}\, s$, respectively. We conclude that the Auger limited recombination would become critical for doping densities in the order of $10^{18} cm^{-3}$.

In the upcoming experimental sections of the thesis we will present a methodology that leads to accurate extraction of lifetime and material information from a TRPL decay.

### 1.2.3 Generated carrier dynamics under the influence of electric fields

In this section we will study one additional parameter that is believed to have an influence on the generated charge carriers. That parameter is the electric field that is created once the junction is formed within the photovoltaic material. We will also precise under which experimental conditions it is relevant to consider the effect of charge separation on the probed carrier dynamics.

R.K. Ahrenkiel[74] and A.J. Nozik [75] conducted through simulation work, the first rigorous studies of the effects of electric fields on the time-resolved photoluminescence spectra in III-V semiconductors. The need for this analysis originated from the fact that under experimental conditions where drift is important enough to have a clear influence on the recombination channels of charge carriers. The importance of the drift depends on the width of the space-charge region $W_{SCR}$ and the intensity of the electric field. The experimental conditions such as the value of the applied voltage-bias and the photo-excitation level will determine the "screening" degree of the electric field.

Their analysis is based on the solution of the one-dimensional, semiconductor transport equations using the drift-diffusion approximation:

$$\begin{cases} \dfrac{\partial n(x,t)}{\partial t} = g(x,t) + D_n \dfrac{\partial^2 n(x,t)}{\partial x^2} + \mu_n \dfrac{\partial}{\partial x}\left[E(x,t)n(x,t)\right] - R_n \\ \dfrac{\partial p(x,t)}{\partial t} = g(x,t) + D_p \dfrac{\partial^2 p(x,t)}{\partial x^2} - \mu_p \dfrac{\partial}{\partial x}\left[E(x,t)p(x,t)\right] - R_p \\ \dfrac{\partial E(x,t)}{\partial x} = \dfrac{q}{\varepsilon}\left[p(x,t) - n(x,t) + N_d(x) - N_a(x)\right] \end{cases} \quad (1.21)$$

Where n(x,t) and p(x,t) are the bulk densities of electrons and holes, $D_n$ and $D_p$ are the diffusion coefficients for electrons and holes, $\mu_n$ and $\mu_p$ are their motilities, q is the electron charge, ε is the bulk dielectric constant, and $N_d$ and $N_a$ are the densities of donor and acceptor ions, respectively.

Based on the set of equations (1.21), the TRPL decay $I_{TRPL}(t)$ can also be calculated as:

$$I_{TRPL}(t) = \int_0^d \left[n(x,t)p(x,t)\right]\exp(-\alpha x)dx \quad (1.22)$$

Where α is absorption coefficient at the PL wavelength, and d is the active layer thickness.

Two injection scenarios are considered to study the effect of the electric field on TRPL decay. It shows that under high photo-injection conditions where the minority carrier photogeneration is 10 times the majority carrier concentration, the SCR is canceled-out/screened by the photogenerated carriers in less than 0.2 *ps*. Under intermediate and low injection levels where the minority carrier photogeneration is smaller than the majority carrier concentration, the PL is quenched in the first few picoseconds due to electron hole separation. We can hence deduce that in case where the electric field is not screened by the injection level, its effect must be taken into account for semiconductors having PL decay lifetimes in the order of a few picoseconds.

### 1.2.4 Spectrally Resolved Photoluminescence

Any system of temperature *T* emits light following the Planck's law of radiation. This body can be brought out of equilibrium, as for example a semiconductor under a laser pump. As a result of excess carrier concentration, spontaneous radiative recombination of electron hole pairs occurs. This effect strongly increases the emission of photons with energy higher than the bandgap.

The recombination of a hole at an energy $E_1$ and an electron at an energy $E_2$ results in an emission of a photon at an energy $E_3 = E_2 - E_1$. The following recombination rate is obtained [159]:

$$R_{sp}(E_3) = \left|M^2\right| g(E_1, E_2)(1 - f(E_1)) f(E_2) \frac{c_0}{n_{refr}} D_\gamma(E_3) \tag{1.23}$$

$\left|M^2\right|$ is a matrix element coupling the initial and final states, $f(E)$ the occupation probability of the electrons, $c_0$ the speed of light in vacuum, $n_{refr}$ the material refractive index and $D_\gamma$ the photon density of states. $g(E_1, E_2)$ is a combined density of states, reflecting the density of states at $E_1$ & $E_2$, but also the conservation of momentum [159]. The first quantities are also related to the absorption coefficient $\alpha(E_3)$ so that at equilibrium, the emission is:

$$R_{0,sp}(E_3) = \alpha(E) \frac{{n_{refr}}^2}{4\pi^3 \hbar^3 c_0^2} E^2 \frac{1}{\exp\left(\frac{E}{kT}\right) - 1} \tag{1.24}$$

This comprises all the transitions emitting a photon at an energy E regardless of the initial states of the electron hole pair. However the energy levels at $E_1$ and $E_2$ may belong to distinct bands, whose occupations are described by distinct quasi-Fermi levels $E_{Fn}$ & $E_{Fp}$ in equation (1.23). Noting $\Delta\mu = E_{Fn} - E_{Fp}$, the emission in case of excess carrier concentrations is given by [41]:

$$R_{sp}(E) = \alpha(E) \frac{{n_{refr}}^2}{4\pi^3 \hbar^3 c_0^2} E^2 \frac{1}{\exp\left(\frac{E - \Delta\mu}{kT}\right) - 1} \tag{1.25}$$

This expression is a generalization of Planck's and Kirchhoff's emission laws, for a body comprising two distinct carrier populations. It enlightens that the photon emission comprises the information of the quasi-Fermi level splitting. As outlined in the previous section, this is a highly important quantity in the solar cell mechanisms.

$R_{sp}$ is a rate of recombinations in a volume element, resulting in a photon emission in a solid angle unit. It must be considered that $\alpha(E)$ & $\Delta\mu$ in equation (1.25) depend on the position *r* in the volume of the cell. The physically accessible quantity is the emission at a surface position *r'*. It results from an integral of the emission rate, taking into account reabsorption and reflections.

In case $\Delta\mu$ is not position-dependent, we write the emission flux Φ:

$$\Phi(E, r', \theta) = A(E, r', \theta) \frac{\cos(\theta)}{4\pi^3 \hbar^3 c_0^2} E^2 \frac{1}{\exp\left(\frac{E - \Delta\mu_{eff}}{kT}\right) - 1} \tag{1.26}$$

$A(E, r', \theta)$ is the probability of absorption of a photon of energy *E*, at the surface position $r'$ and the angle $\theta$.

The quasi-Fermi level splitting is noted here $\Delta\mu_{eff}$ , since it was assumed to be constant in the material, which is not necessarily true. This assumption will be used frequently in justified cases in the following sections.

The $\cos(\theta)$ factor express that the emission follows the Lamberts law, which is valid for most absorbing materials.

We see from these considerations that a semiconductor with a non-zero $\Delta\mu$ will emit a significant luminescence signal. Therefore we need excitation methods to introduce excess carrier concentration. The latter can be of an optical nature and in this case the emitted signal will be the photoluminescence of solar PV devices. Its intensity will obey the generalized Planck's law given by equation (1.26).

### 1.2.5 Spectrally-Resolved Electroluminescence & LED-PV Reciprocity Relations

If we describe the operation of a solar cell and a light emitting diode (LED), one can deduce that both systems function in a reciprocal way such as the first system's topology of functioning depends on the inverse phenomenon of the other. In a general way, a solar cell's physical action is transforming radiation energy into electricity while an LED transforms electrical energy into light. Theoretically, based on the principle of detailed balance[42], we consider that at thermodynamic equilibrium if one photon injected causes the creation of one electron-hole pair (photovoltaic operation), such an event must be compensated by the opposite phenomenon stating that one electron-hole pair injected should lead to the creation of one photon (electroluminescence). Based on the complementary behavior of these two systems, one might believe that a perfect solar cell would also be a perfect LED, however in reality this is not the case.

If we take for example today's leading high-efficiency silicon solar cells that have already approached the SQ-limit, therefore, in a practical way we can consider such solar cells to be almost perfect. If we are ever to produce LEDs based on the same designs of the previous solar cells we might find that the result isn't as "perfect" as we expected. For example, a highly sophisticated record holder silicon solar cell, once in LED mode, results in an external quantum efficiency $EQE_{LED}$ of approximately 1% only. On the opposite side, organic semiconductor-based LEDs prove to have quite a respected $EQE_{LED}$ of 15% [43] comparing to solar cells made from organic materials that have very low power conversion efficiencies. Therefore, it is safe to conclude that at the practical level, quality requirements for solar cells and LEDs diverge in a considerable way.

*U.Rau* expressed in his paper [42] a reciprocity theorem that relates the carrier collection properties of a solar cell to its spectral electroluminescence (EL) emission. His reciprocity theory approaches the Shockley-Queisser identity [44] of an LED and a solar cell in the limit of infinite charge carrier mobility $\mu_p$ and an infinite nonradiative lifetime $\tau_{nr}$ where we can only consider that radiative recombinations are totally dominant over non-radiative recombinations.

This theory starts by considering the fact that in thermal equilibrium, each point $r_s$ belonging to the surface of our solar cell is initially irradiated from each element of the spherical angle of the ambient with a spectral flux density corresponding to a blackbody radiation with refractive index n=1:

$$\phi_{eq}(E\gamma,\theta) = A(E\gamma)\phi_{bb}(E\gamma)\cos(\theta) \tag{1.27}$$

Since we are dealing with solar cells, a fraction of the absorbed photons will generate free electron-hole pairs along the optical path, while the other portion of the incident radiation will be re-emitted from the cell surface. The resulting charger carriers will have a probability $F_c(r_S,\theta,\varphi,E_\gamma)$ of being collected by the junction of the cell. Therefore, the probability that one photon impinging on the solar cell contributes one elementary charge q to the short-circuit current is given by $Q(r_S,\theta,\varphi,E\gamma)=a.F_c$, the quantum efficiency, where *a* is the absorptance of the cell.

Finally, under solar irradiation, an excess flux density $\phi_{sun}$ impinges on the solar cell, leading to a short-circuit current is given by:

$$J_{sc} = q \int_{\Omega_{Sun}} \int_{E_\gamma} \int_{S_c} Q\left(r_S,\theta,\varphi,E\gamma\right)\phi_{sun}\left(\theta,\varphi,E\gamma\right)d\Omega dE\gamma dS \tag{1.28}$$

The integrals actually extend over the angle of incidence$\Omega_{Sun}$, the energy range Eγ of the solar irradiation and the surface are $S_c$ of the solar cell, respectively. We remind that we are in a state of thermal equilibrium: therefore, the solar cell is exposed only to the blackbody radiation from the ambient.

At such state the device cannot distinguish between photons from the sun and those from the ambient: all equilibrium radiation leads to charge carriers that are collected by the junction. We have therefore to account for an "equilibrium" short circuit current resulting from the ambient blackbody flux integrated over the full spherical angle $\Omega_c=2\pi$.

$$J_{sc,0} = q \int_{\Omega_c} \int_{E_\gamma} \int_{S_c} Q\left(r_S,\theta,\varphi,E\gamma\right)\phi_{eq}(\theta,E\gamma)d\Omega dE\gamma dS \tag{1.29}$$

However, in thermal equilibrium, no net current is flowing through the device, therefore *Rau* postulates that the short-circuit current $J_{SC,0}$ is counterbalanced by an equilibrium injection current $J_{em,0}= J_{sc,0}$.This leads to the following equilibrium relation:

$$\delta J_{sc,0} = \delta J_{em,0} = qQ\left(rS, \theta, \varphi, E\gamma\right)\phi_{eq}(\theta, E\gamma) \tag{1.30}$$

This relation reflects a first illustration of reciprocity between what we inject in a solar and what actually emerges from it in a state of thermal equilibrium. It holds for any component $\delta J_{sc,0}$ of $J_{sc,0}$ that is generated from any angular component of the ambient blackbody radiation at any surface element of the solar cell.

Furthermore, a measurement of the quantity $Q\left(rS, \theta, \varphi, E\gamma\right)$ under normal incidence and averaged over the cell surface, would eventually lead to the calculation of the photovoltaic external quantum efficiency EQE.

Next, the theory postulates that, under an applied voltage V, the injected current component $\delta J_{em}$leading to the radiative emission of photons, follows actually an exponential law as a function of V. As we are in an equilibrium state, this current component corresponds to the previously discussed $\delta J_{em,0}$ that is, as a result of the equilibrium state, counterbalanced by $\delta J_{SC,0}$.

Therefore, based on the Shockley's diode law, we can express the excess photon flux density $\phi_{EL}$ as follows:

$$\phi_{EL} = \frac{\delta J_{em,0}}{q}\exp\left(\frac{qV}{KT}\right) - \frac{\delta J_{SC,0}}{q} = \frac{\delta J_{em,0}}{q}\left(\exp\left(\frac{qV}{KT}\right) - 1\right) \tag{1.31}$$

At this step we notice that combining equations (1.29) and (1.30) reveals an important property of the detailed balance between photon emission and photon collection in solar cells where the ability of a solar cell to emit photons is directly linked to the optical generation and carrier collection due to the blackbody radiation:

$$\phi_{EL}\left(rS, \theta, \varphi, E\gamma\right) = Q\left(rS, \theta, \varphi, E\gamma\right)\phi_{eq}(\theta, E\gamma)\left(\exp\left(\frac{qV}{KT}\right) - 1\right) \tag{1.32}$$

Eventually, if we proceed by integrating over the solar cell entire surface and taking into account all of the possible angular emission from each point of this surface, this will lead to total excess photon flux:

$$\phi_{EL}(\mathrm{E}\gamma) = \int_{\Omega_c}\int_{S_c} Q\left(\mathrm{rS},\theta,\varphi,\mathrm{E}\gamma\right)\phi_{eq}(\theta,\mathrm{E}\gamma)d\Omega dS \times \left(\exp\left(\frac{qV}{KT}\right)-1\right) \quad (1.33)$$

From equation (1.33) we can clearly deduce the utility of reciprocity relations where once the device is operated as an LED via the application of a voltage, we are capable of predicting the EQE of our device based on the knowledge of the spectral and angular emittance. Thus the total EL photon flux that we can easily detect experimentally by means of a hyperspectral imager setup that will be discussed later on.

### 1.2.6 Reciprocity between Photoluminescence and Electroluminescence of solar cells

So far we have detailed the spectral characteristics of the photoluminescence and electroluminescence. However, the latter and the former are fundamentally related. From an experimental point of view it is completely possible to combine both PL & EL. This can be done by acquiring a luminescence signal under a light excitation and applied voltage bias, or under an applied voltage and an optical bias. This type of experiment will be done in the scope of the present thesis. *Uwe Rau* worked precisely on an approach that combines these different bias conditions [160]. His work extends the previous reciprocity relations for the more general case of combined EL and PL emission. The study shows that under the same conditions that are sufficient for the original reciprocity relations, the combined emission noted $\Delta\phi^{em}(E)$ depends on the photon energy *E* and is given by the superposition of a PL signal under short-circuit conditions $\Delta\phi^{(sc)}$ caused by the photo-excitation $\Delta\phi^{in}(E')$ and an EL signal driven by the junction voltage $V_j$ according to:

$$\Delta\phi^{em}(E) = \Delta\phi^{(sc)}(E) + Q_e(E)\phi_{bb}(E)\left[\exp\left(\frac{qV_j}{kT}\right)-1\right] \quad (1.34)$$

where $\phi_{bb}(E)$ denotes the spectral photon flux density of a black body, and $kT/q$ is the thermal voltage. The short-circuit PL $\Delta\phi^{(sc)}(E) = Q_{PL}(E,E')\Delta\phi^{in}(E')$ is proportional to the excitation photon flux with the PL quantum efficiency $Q_{PL}$ as a proportionality constant. The proof of equation (1.34) embraces a general reciprocity relation connecting arbitrary electrical and optical input channels of light-emitting diodes, solar cells, or *npn* transistors.

### 1.2.7 Information derived from the luminescence intensity, its spectral and spatial variations

We have seen that the generalized Planck's law and the reciprocity relations can indeed inform us about the characteristics of the solar cells. From equation (1.26) we have learned that the photoluminescence intensity and the corresponding spectrum depend on three parameters: The quasi-Fermi levels splitting profile Δμ(r), the absorptivity A(E,r) and the temperature T. Based on these observations, numerous contributions show how characteristics of devices are determined.

In particular, from equation (1.4), Δμ was determined. In PL and EL, it was shown to equal the voltage applied to the junction [45-54]. Therefore, PL is an access route to $V_{oc}$. In some materials, the Δμ depth profile is found to fluctuate. These depth variations are highly interesting when we trace them back to their origin. For example, important transport properties were found to be at the origin of these fluctuations such as the carrier diffusion length and the surface recombination velocities [55]. Therefore, analyzing the PL signal leads us to the value of Δμ from which we finally extract the material transport properties.
Now, once we determine the Δμ, we can see from equation (1.4) that other key parameters can therefore be accessed such as the material absorption [56] and the charge carrier temperature [57].

Finally, to all of the above we can add the spatial dimension and consequently establish mappings of the latter key parameters. This will allow us to assess and quantify their spatial inhomogeneity. This type of investigation is essential for highly inhomogeneous photovoltaic materials that behave and perform differently throughout their depth or surface. For example, maps of the saturation currents[58,59] and the diffusion lengths [60] were achieved on silicon solar cells. Given its contactless nature, PL has also been demonstrated as an efficient tool for quality control of production lines [61-63]. Maps of Δμ have been recently demonstrated on CIGS solar cells[64].

## 1.3 TRPL studies on CIGS solar cells: The literature contradiction dilemma

So far, we have detailed the theoretical aspects of the spectral and temporal dependencies of the luminescence of PV devices. In the scope of the present thesis, the major experimental focus took place on the temporal aspect of the luminescence. The majority of our discussions in this thesis will focus on the time-resolved techniques. The idea is to analyze the evolution of the luminescence intensity as a function of time. The luminescence "decay" contains crucial information regarding the PV material such as the quantification of its carrier dynamics, the trap density it contains and many more key information.

### 1.3.1 Theoretical aspect: Physics of charge carrier dynamics in Cu(In,Ga)$Se_2$ PV devices

Time-resolved measurements of the photoluminescence decay upon a pulsed excitation allow studying the recombination kinetics in photovoltaic absorber materials. Hence the PL decay time can be an indicator or a measurement tool for the electronic quality of a given semiconductor. TRPL can thus constitute an attractive technique for the qualitative or quantitative inspection of photovoltaic absorber materials.

The theory sketched in this section provides the basic concepts of TRPL measurements of photovoltaic devices and their absorber materials. The physical concepts to interpret TRPL results have been first described in detail by R.Ahrenkiel [66].

The properties of minority carriers are basic to understanding the physics of the III-V and compound semiconductors such as $Cu(In,Ga)Se_2$-based thin film solar cells. In order to design minority-carrier devices, accurate and reliable measurements of minority-carrier parameters are required. The performance of minority-carrier devices depends on these parameters. The efficiency of photovoltaic devices depends strongly on the minority-carrier lifetime, diffusion length and mobility within the semiconducting components. One can also include light-emitting diodes (LEDs) in the category of minority-carrier devices. For example, the efficiencies of both lasers and LEDs are intimately tied to the ratio of nonradiative recombination rates to the radiative rates.

The lifetime can vary by many orders of magnitude in a semiconductor, depending on the purity and growth technique.

The primary emphasis of this chapter is the development of mathematical tools for analyzing time-resolved photoluminescence data. These tools will be developed and will discuss the primary recombination mechanisms that are important in CIGS minority-carrier physics.

Ever since its theoretical and experimental development, the TRPL technique has been extensively applied by the scientific PV community for the study of most of solar cell PV technologies. Studies can be classified as qualitative or quantitative. On the one hand, GaAs structures were at the center of the studies of R.K. Ahrenkiel that managed to access through TRPL to multiple material properties such as the carrier diffusion length, their mobility, the material surface recombination lifetime [74,78]. On the other hand, studies on chalcogenide thin films related the minority carrier lifetime deduced from TRPL measurements to the overall PV efficiency of the device [76][77], as well as the standard PV performance indicators such as the open-circuit voltage $V_{oc}$[78,79]. Other studies, by adding the spatial dimension to their TRPL measurements evaluated the spatial homogeneity of the carrier lifetime in their materials [78,80,81].. Continuing on the quantitative side of TRPL analysis, a study by C.R. Haughn et al. [82] demonstrated how to extract the trap state densities in GaAs heterostructures using intensity-dependent time-resolved photoluminescence. The interesting aspect of their work resides in its ability to correlate the values of trap states densities to the growth rate of the material.

### 1.3.2 Photo-excitation-dependent TRPL decay analysis on CIGS

One of the early TRPL works CIGS solar cell concentrated on the study of structure of this device and the effect of each layer on the TRPL lifetime, and thus, the PV properties and performance of the device.

On the one hand, a work by Shirakata et al. started by the looking at the difference in the TRPL decays between a CIGS thin film and a complete CIGS solar cell [83]. What they deduce is that the PL lifetime of the cell is longer than that of the thin films and they explain that it is consistent with the enhancement with the PL intensity and the elimination of defect related PL as a result of the solar cell formation.

On a more quantitative side, a study by G..H.Bauer et al. [154] performed absolute PL measurements on CIGS films and complete CIGS devices. The authors then compared both measurements by extracting the difference in the quasi-Fermi levels splitting in a CIGS film and the whole CIGS device.

Another two studies made by Shirakata et al. [84,85] focused this time on observing the behavior of the TRPL decay lifetimes while varying the excitation conditions such as the photo-excitation power and frequency. They state that the PL decay time increases with the repetition frequency and the excitation power and admit at the same time that the physical meaning of the PL decay times is not clear.

On the other hand, a work by W.K. Metzger et al. [86] had the same purposes but the approach in this case was quite different. Their study aimed at observing the long PL decay lifetimes in high efficiency CIGS solar cells. The study performed TRPL at the different stages of the fabrication process of the complete CIGS device. The longest mono-exponential decay time of 250 nanoseconds was measured on the CIGS film directly after its deposition. Once it was air-exposed the PL decay time decreases significantly. The study also shows that the deposition of the CdS does not alter the PL decay lifetime.

Finally, by increasing the excitation level the authors show that the mono-exponential decay decreases progressively. The main conclusion here is that TRPL measurements are extremely sensitive to the experimental conditions and directly correlated to the quality and structure of a PV device surface.

By examining what we have summarized so far, we can notice a first contradiction between the two studies: All of Shirakata's studies analyzed and interpreted the TRPL decays by considering them the result of a sum of two exponential decays composed of one "fast" and one "slow" component:

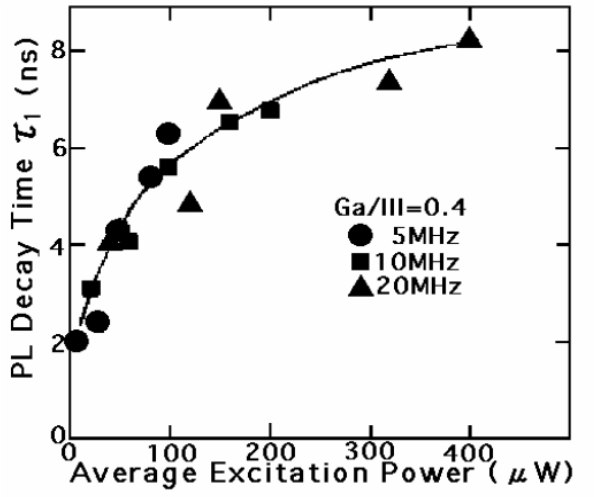
$$I_{TRPL}(t) = C_1 \exp\left(-\frac{t}{\tau_1}\right) + C_2 \exp\left(-\frac{t}{\tau_2}\right) \tag{1.35}$$

Where $C_1$ and $C_2$ are coefficients, and $\tau_1$ & $\tau_2$ are decay times that correspond to the initial and final sections of the decay curves, respectively. Plenty of other works followed through and reported values for $\tau_1$ on CIGS films and solar cells measured under very different injection conditions have ranged from several hundred picoseconds to several nanoseconds[86-95]. Values for the weak long-tail component $\tau_2$ have ranged from several hundreds of picoseconds to tens of nanoseconds.[86,87,93-95].

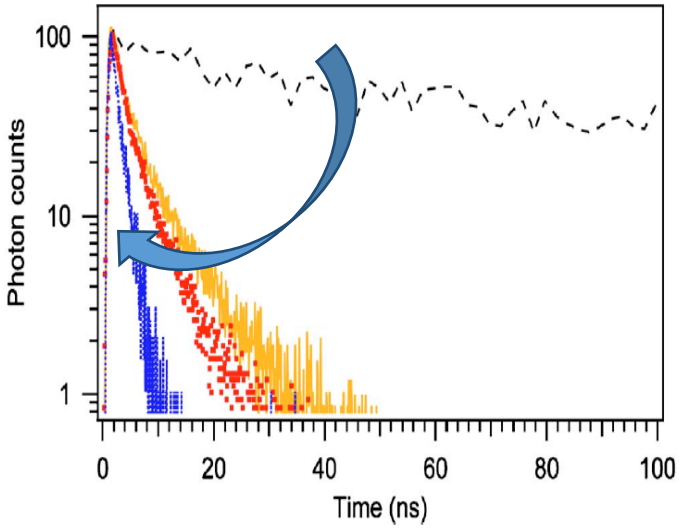
The authors ([86]) extracted material properties and correlated the value of $\tau_1$ & $\tau_2$ decay times to key PV performance indicators and efficiency. Unfortunately, the absence of a physical definition of these lifetimes leaves some uncertainty on the analysis and the information that it produces regarding the CIGS solar cell.

While the work of ref [86] didn't go into the details of the physical nature of this double exponential decay, their decay were simply mono-exponential and remained mono-exponential regardless of the excitation power. Given their high device efficiency this provided us with a first link to the possible

nature of their monoexponential decay and hence the nature of the carrier lifetime that is reflects. The analysis of ref[86] is robust as its analysis is device-oriented and contradicts the findings of the latter works according to Figures 1.7.a and 1.7.b below:




(a)




(b)

**Figure 1.7.a : Evolution of the PL decay time of a CIGS solar cell as a function of the excitation power according to Ref [84]**

**Figure 1.7.b : Evolution of the PL decay time of a CIGS solar cell as a function of the excitation power according to Ref [86]**

According to the first plot, the extracted decay lifetime increases as function of the excitation power, whereas in the second study, the latter clearly decreases as the excitation power is increased.

The figures above are a clear example of how different understandings of the physics of carrier dynamics behind the TRPL decay can lead to opposite interpretations.

### 1.3.3 Voltage-bias-dependent TRPL decay analysis

A recent study by Maiberg et al. [96] characterized CIGS solar cells using voltage-bias dependent time-resolved photoluminescence. The authors claim to have determined the solar cell minority carrier mobility by fitting their TRPL decays under the applied voltage bias. The model on which the authors rely considers a large set of material properties that take into account drift, diffusion and bimolecular recombination. Figure 1.8 presents the experimental decays and the corresponding fitting results of the TRPL decays as a function of an increasing applied voltage:

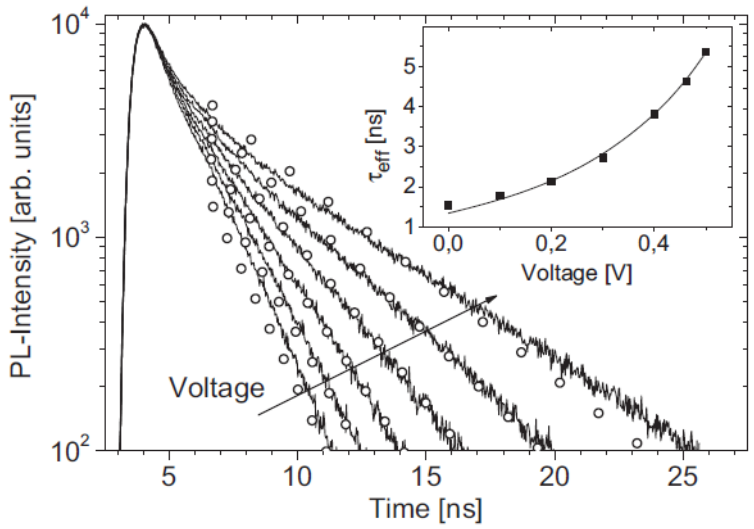



**Figure 1.8: Evolution of the PL decay time of a CIGS solar cell as a function of an applied voltage bias according to Ref [84]**

We can start by observing that the authors TRPL decays correspond to double-exponential decays where an initial fast decay component is followed by a slower one. However, based on their fitting data, it seems as if their model may benefit from a more accurate replication of the investigated CIGS carrier dynamics under a pulsed excitation and an applied voltage bias. We learn in this case that it is important that the model used for fitting should take into account both components of the double-exponential decays. In the present case, the short component isn't taken into account. Only the longer is fitted and the authors show that their effective lifetime increases under an increasing applied voltage.

A previously cited work [75] performed the same type of experiments and obtained the following results:

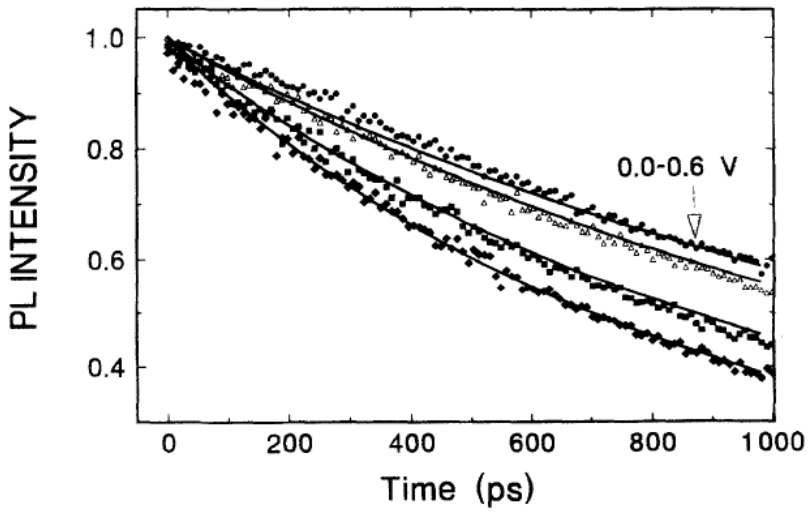


**Figure 1.9: Evolution of the PL decay time of a CIGS solar cell as a function of an applied voltage bias according to Ref [75]**

Here, the authors attempt to model and fit both parts of the decays. They also observe the TRPL decay becomes shorter as the voltage is increased. The authors explain this phenomenon as follows: As the applied voltage is increased, the effective recombination velocity also increases. The latter being proportional to the inverse value of the PL decay lifetime, this probably explains what we observe in Figure 1.9.

### 1.3.4 Photo-excitation energy-dependent TRPL decay analysis

There is one experimental parameter that can still be varied and induce changes in the obtained TRPL decays. That parameter is the photo-excitation energy. We know for example that for CIGS solar cells, the bulk, interface and surface properties of its different photoactive layers are extremely important to control and access. Being able to optically access them is even more important for device characterization. By varying the excitation wavelength of the pulsed laser source, we may be originally convinced that we are actually varying the depth of the region that we are probing within the device. This might lead us to think that by using the excitation energy-dependent TRPL measurements we distinctly probe the very bulk of the CIGS absorber, its interface with the buffer layer or its surface[98]. The reality of things is that the main limitation here is the absorption depth of the laser itself. For example, if we consider a 630 *nm* excitation, the absorption depth is equal to approximately 200 *nm* for CdTe [99], 100 *nm* for CIGS[100] and 50 nm [101] for CZTSe absorbers. Therefore, immediately after a laser excitation a PL signal will be emitted only from the surface/interface regions of the absorber and investigation of the bulk might be possible. Further, in samples with large surface recombination velocities, TRPL decays will be dominated by surface/interface recombination and determination of the bulk carrier lifetime might not be possible.[102] . A recent work by Kuciauskas et al. surpassed this limitation by performing a subbandgap two-photon excitation that lead to two-photon excitation TRPL decays. This technique allowed the authors to directly probe the properties of the bulk of a CdS/CdTe thin film. They deduce a bulk minority carrier lifetime of 66 *ns* and estimated their material radiative bulk lifetime at 950 *ns* [103].

In the context of this thesis, we will perform excitation energy-dependent TRPL analysis but for another purpose that will allow us to optically characterize and quantify a signature trait of CIGS PV devices.

# Chapter II. Optoelectronic Characterization of PV Devices

## 2.1 Standard Solar Cells Characterization Techniques

### 2.1.1 J-V Characteristics

Based on the continuity equation, Shockley [155,156] derived an equation for the dark current-voltage characteristics of an ideal diode which is given by:

$$j_{diode}(V) = j_0\left[\exp\left(\frac{eV}{kT}\right)-1\right] \text{ with } j_0 = e\left(p_{n^0}\frac{D_h}{L_h} + n_{p^0}\frac{D_e}{L_e}\right) \quad (2.1)$$

where $j_0$ is the saturation current density and V the applied voltage. $n_{p0}$ stands for the equilibrium electron density on the p-side, $p_{n0}$ for the equilibrium hole density on the n-side, $L_{e,h}$ the electron and hole diffusion length respectively. $D_{e,h}$ stand for the electron and hole diffusion coefficients respectively.

The simplifying assumptions necessary for the derivation of this equation are abrupt depletion layers, the Boltzmann approximation for charge carrier densities, low injection conditions and no generation or recombination within the depletion layer:

The diode equation of a real diode can be expressed in the form [10]:

$$j_{diode}(V) = j_0\left[\exp\left(\frac{eV}{nkT}\right)-1\right] \text{ with } j_0 = j_{00}\left[\exp\left(-\frac{E_a}{nkT}\right)\right] \quad (2.2)$$

Where *n* is the diode ideality factor, $E_a$ is the activation energy of the saturation current density and $j_{00}$ is a reference current density, which is weakly temperature- dependent.

If the solar cell is illuminated, a photocurrent $j_{photo}(V)$ is generated and the equation for the J-V characteristics is given by:

$$j_{light}(V) = j_0\left[\exp\left(\frac{eV}{nkT}\right)-1\right] - j_{photo}(V) \quad (2.3)$$

where $j_{photo}(V) = f_c(V)J_{sc}$ and $f_c(V)$ is the voltage-dependent collection function.

In the ideal case, the superposition principle holds meaning that the dark IV curve is only shifted by the value of a voltage dependent of the photocurrent. In real solar cells, the diode current does not

necessarily have to be the same in the dark as under illumination. In a CIGS solar cell, a crossing of the dark and illuminated IV is frequently observed (crossover). Many other types of IV curve distortions exist and will be optically investigated and discussed later in the upcoming sections of this thesis.

Furthermore, the commonly called two diode model is nowadays widely accepted as a realistic model for a diode characterized by two different saturation currents. $j_{01}$ & $j_{02}$ are respectively called the first and second saturation currents. The dark characteristic is usually dominated by the second diode current (defect recombination) at low voltages and by the first diode current (thermal recombination) at higher voltage [161].

In addition to recombination currents, resistances phenomena can be present in the device, causing a deterioration of the fill factor (see definition below). Series resistance effects can be due to resistance in the absorber, buffer or window layer. They can also be due to imperfect contact with the connection grid, in which case they will be called contact resistance.

Equation (2.3) becomes:

$$j_{light}(V) = j_{01}\left[\exp\left(\frac{e(V+R_S I)}{kT}\right)\right] + j_{02}\left[\exp\left(\frac{e(V+R_S I)}{2kT}\right)\right] + \frac{(V+R_S I)}{R_{sh}} - j_{photo}(V) \qquad (2.4)$$

Light and dark current – voltage (J-V) measurements (see Figure 2.1) are fundamental to the identification of key PV performance parameters such as the open-circuit voltage $V_{oc}$, the short-circuit current $J_{sc}$, the fill factor FF and ultimately the power conversion efficiency η of the PV device. From light J-V measurements one can also assess the series and shunt resistances from which suffer the PV device by fitting the J(V) curve in both generation and injection operation modes of the solar cell. Fitting the dark current-voltage measurements gives also access to the saturation currents that provide an evaluation of the quality of the CIGS absorber and its interface with the CdS buffer layer.

As shown in Figure 2.1 where Jsc and Voc are noted, the deep grey area is the maximum power output $P_{MP}$; the ratio of $P_{MP}$ to the product of $J_{SC}$ and $V_{OC}$ is the fill factor FF, the cell efficiency $\eta$ is the ratio of $P_{MP}$ and the incident light power $P_{in}$.

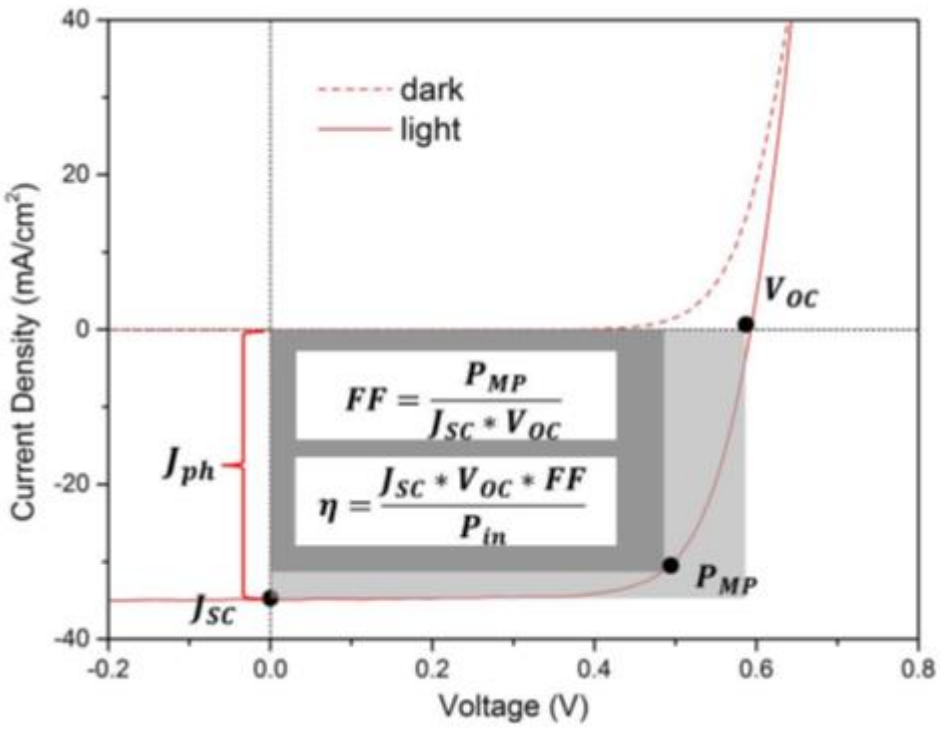



**Figure 2.1: Example of measured dark and light J-V curves on a CIGS cell and the corresponding parameters**

For our experiments, we will use a Keithley programmable voltage source to apply voltage to a solar cell, typically from -0.2 V to 0.9 V for CIGS solar cells. The standard J-V measurement is done at room temperature (+25 ℃) with two illumination conditions, dark and 100 mW/cm$^2$ A.M.1.5 illumination. The standard illumination is achieved with an AAA grade Newport solar simulator.

### 2.1.2 External Quantum Efficiency

A J-V measurement yields information on the absolute value of the short-circuit current density $J_{SC}$ produced in a solar cell. However, the simple measurement does not yield information on the origin of the loss mechanisms that are responsible for the fact that not every photon in the solar spectrum contributes to $J_{SC}$. In an ideal solar cell, corresponding to the Shockley-Queisser limit, every photon with a suitable energy E higher that the bandgap energy $E_g$ leads to one electron-hole pair that is collected at the terminals of the solar cell. In real solar cells, this is not the case and we are interested in knowing the reasons for the losses. An appropriate method to literally shed light onto this problem is the spectrally resolved measurement of the short-circuit current, that is $J_{SC}(E)$ likewise $J_{SC}(\lambda)$, depending on whether the result is plotted versus photon energy or versus wavelength. The external quantum efficiency EQE is defined as the number of electrons collected per photon incident on the solar cell according to:

$$EQE(E) = \frac{1}{e}\frac{dJ_{sc}(E)}{d\phi(E)} \tag{2.5}$$

Where $d\phi(E)$ is the incident photon flux in units of [ϕ] = $cm^{-2}s^{-1}$ in the photon energy interval *dE* that leads to the short-circuit current density $dJ_{SC}$.

A second, frequently used quantity is the spectral response *SR* defined as the current produced per unit optical power incident on the solar cell. Consequently, the spectral response has the unit [*SR*]=A/W and related to the quantum efficiency via:

$$SR = \frac{1}{E}\frac{dJ_{sc}(E)}{d\phi(E)} = \frac{eEQE}{E} \tag{2.6}$$

In the ideal Shockley-Queisser case, we would have *EQE(E)*=1 for $E \geq E_g$ and *EQE(E)*=0, otherwise. In real solar cells, we have *EQE(E)*< 1 even for $E \geq E_g$, resulting either from optical or recombination losses. The optical losses can be further broken down to losses due to reflection and due to parasitic absorption within the device. The reflection losses can be assessed by an additional measurement using a spectrometer, equipped with an integrating sphere determining the reflectance *R*, thus allowing us to quantify this loss mechanism separately. For an opaque solar cell we know that all photons that are not reflected are absorbed in the device, that is, the absorptance *A* is given by *A* = 1 – *R*.

The experimental setup for recording the EQE can be seen in Figure 2.2:

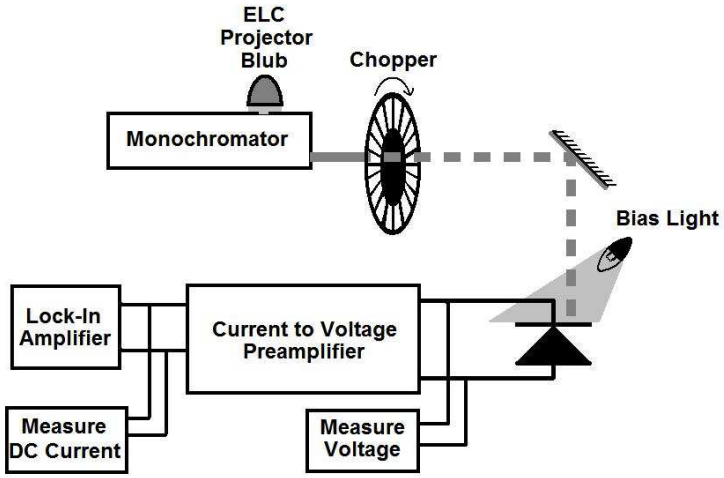



**Figure 2.2: Schematic diagram for EQE measurements**

An example for an EQE measurement on a CIGS cell is displayed in Figure 2.3 taken from ref [33]. The latter illustrates six different types of losses in external quantum efficiency due to optical effects. The upper plain line is the efficiency after losses due to shading from collection grid (1), surface reflection from air/window/emitter/absorber interfaces (2), absorption from the window layer (3), absorption in the emitter layer (4), and incomplete absorption near the bandgap (5). The lower plain line is the external quantum efficiency measured at 0V, thus accounting for incomplete collection of photogenerated carrier (6). In addition, we see the absorption edge, from which the bandgap energy can be estimated.

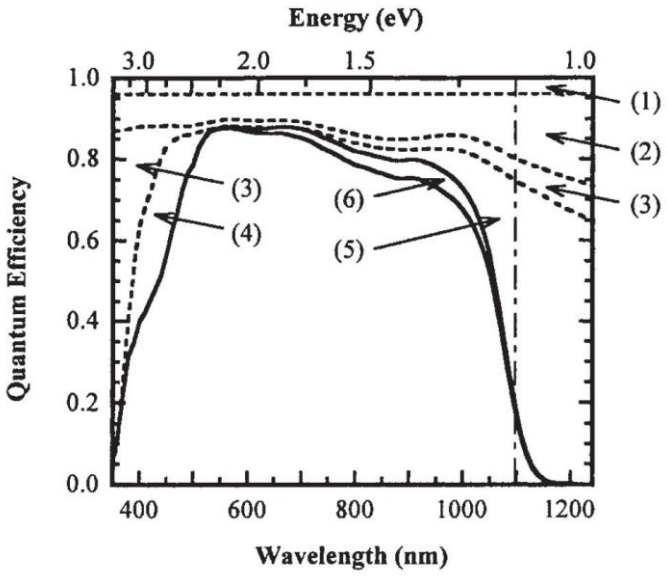



**Figure 2.3: Example of a CIGS solar cell external quantum efficiency and identification of the different optical losses**

### 2.1.3 Capacitance-based Techniques

Capacitance measurements are used to determine the carrier concentration in the absorber layer. In general, for a one-sided junction, capacitance measurements give the carrier concentration on the less-heavily doped side of the junction. In the specific case of p-doped thin-film solar cells, the hole concentration in the absorber is determined. In a p-n junction, the depletion width (W) is given by

$$W = \sqrt{\frac{2\varepsilon}{eN_A}(V_{bi} - V)} \tag{2.7}$$

where ε is the permittivity in the absorber, $N_A$ is the carrier acceptor concentration in the absorber, V is the applied voltage and $V_{bi}$ is the built-in voltage. If the device is modeled as a parallel-plate capacitor, the capacitance per unit area is given by:

$$C = \frac{\varepsilon}{D} \tag{2.8}$$

where D is the separation between the charges on the capacitor plates. Substituting *W* for *D* gives:

$$C = \sqrt{\frac{q\varepsilon N_A}{2(V_{bi} - V)}} \tag{2.9}$$

Plotting $\frac{1}{C^2}$ vs. *V*, should yield a straight line with a slope of $\frac{2}{e\varepsilon N_A}$ and a voltage axis intercept at V=$V_{bi}$ if carrier density is independent of distance into the absorber. Therefore, a direct access to the absorber carrier concentration is obtained.

## 2.2 Advanced Luminescence-Based Characterization Techniques

For the luminescence acquisition, various systems and setups are available. In the context of the present thesis, we will be focusing on the intensity, the spectral, the temporal and the spatial aspects of the luminescence. For the study of the intensity, the spectral and spatial properties of the luminescence we will be using the Hyperspectral Imager (HI). For the study of the intensity, the spatial and the temporal properties of the luminescence signal we will be using the conventional scanning confocal microscope (SCM) setup. In the third part of this section, we will be detailing the Time-Resolved Fluorescence Lifetime Imaging (TRFLIM), a new characterization technique regarding photovoltaics that we develop at IRDEP.

To summarize, we establish in Diagram 2.1 a ”luminescence-based characterization tree” where we included all of the developed luminescence-based characterization methods in this thesis and the type of information it provides on the PV device.

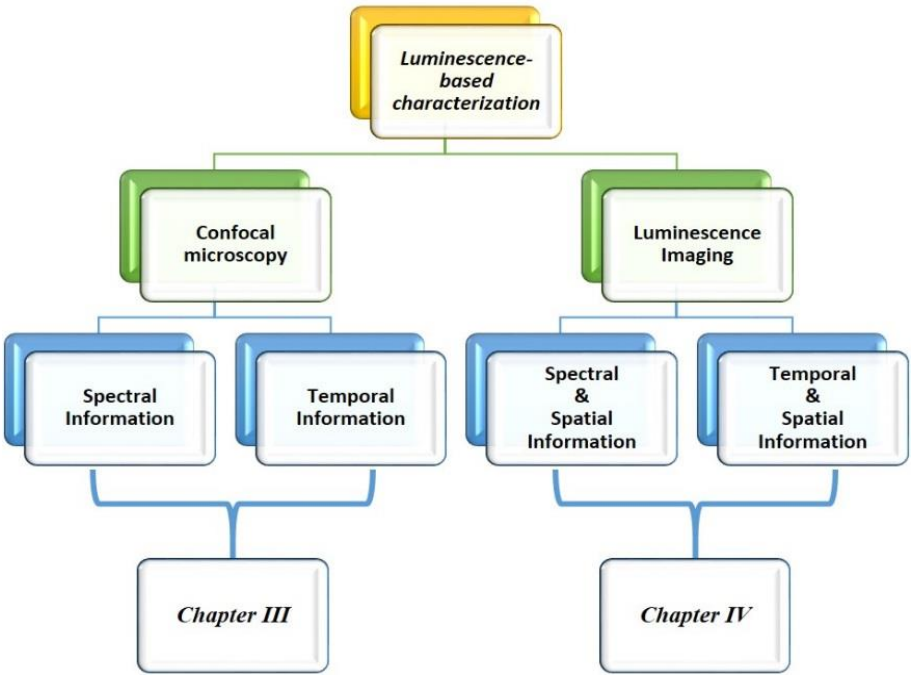



**Diagram 2.1: Tree of luminescence-based characterization methods of PV devices.**

The present manuscript is divided into two major categories of luminescence-based characterization. In particular, chapter III is dedicated to temporal and spatial confocal-based luminescence studies and chapter IV is dedicated in addition to luminescence imaging.

### 2.2.1 Hyperspectral Imager

The basic principle of the HI is to record images of the luminescence at several detection wavelengths. This system is developed by Photon etc., with whom a partnership was built for the photovoltaic applications, coupling the HI with a microscope. It relies on volume Bragg gratings. A schematic of the whole setup is displayed in Fig. 2.4. The sample is illuminated by a laser source through a microscope objective. The luminescence is collected by the same objective and reflected by a mirror towards the detection system. The hyperspectral image is formed by the volume Bragg gratings and recorded by a camera (CCD or InGaAs, depending on the wavelength range)). Besides the light excitation, simultaneous electrical measurements are possible. For the detection part of the system, two configurations are used, for spectral regions from 700 nm to 1000 nm and 900 nm to 1400 nm. In both cases the spectral resolution is 2 nm.
A 2 µm spatial resolution for the luminescence images is achieved with this setup. The luminescence output data are stored in the form of three dimensional cubes where two axes represent an (x, y) space and the third axis (z axis) represents the wavelength.

Initially we set off by a calibration of the setup in order to deal with spatial uniformity, spectral correction, and translate the arbitrary intensity units into absolute units of *Photons/m/m$^2$/s*.

These relative calibrations are obtained with a halogen lamp of known spectrum, coupled into an integrating sphere with a spatially homogeneous output.

We manage to image the output of the sphere to calibrate the setup transmission for each spatial position. We perform the absolute calibration of the intensity at one wavelength.

To do so, we start by imaging a fiber with a certain numerical aperture NA by coupling with a laser. The NA of the fiber has to be smaller than the NA of the previously used objective in order to collect all of the photon flux out of the fiber.

As we can measure the output power, we are then able to accomplish the absolute calibration at the wavelength of the laser used.

Finally we extrapolate to the entire spectral range thanks to the first relative calibration.

The fully detailed calibration process can be found in the thesis of Amaury Delamarre [153].

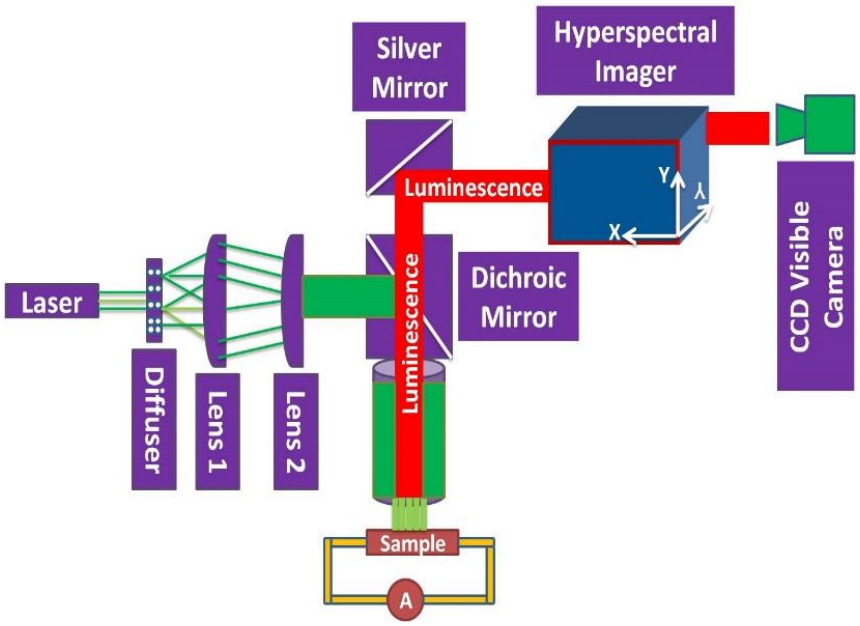



**Figure 2.4: Illustration of the Hyperspectral Imager setup**

### 2.2.2 Scanning Confocal Microscope (SCM)

Whenever luminescence measurements with high spatial resolutions are of interest, a microscope setup must be used. A photoluminescence setup utilizing a confocal microscope is shown in Fig.2.5. In such a configuration, the excitation source is focused onto the sample surface through a microscope lens. The luminescence light is then collected through the same lens, separated from the exciting light beam by means of a beam splitter, and focused onto a fiber connected to the detecting system.

-Ideally, this system exhibits diffraction-limited resolution of approximately: $0.6\lambda/NA$. The sample is mounted on an x-y positioning table, which allows a two dimensional scan of the emitted luminescence radiation.

-As the excitation area in a micro-PL is in the range of 1 $\mu m^2$, very high excitation intensities can be achieved, which may lead to local heating and high-injection effects. This has to be kept in mind when analyzing the data. Efforts should be made to keep the excitation level as low as possible. An excitation level in the order of a few hundreds of Suns can be acceptable for CIGS solar cells [152].

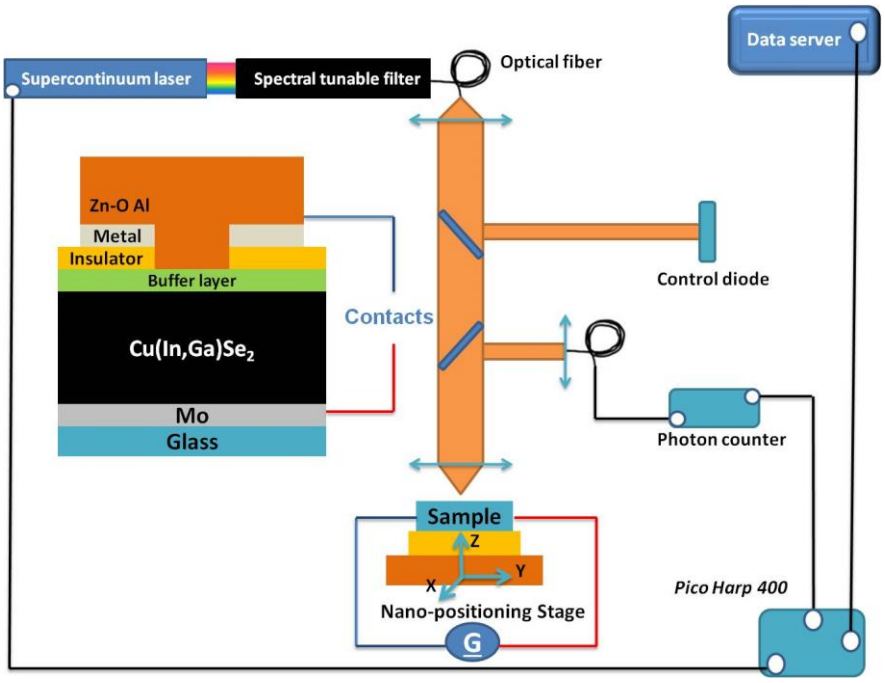



**Figure 2.5: Illustration of the Scanning Confocal Microscope setup**

Our setup dedicated to the spatially-resolved and time-resolved photoluminescence (TRPL) experiments is built as follows:

- The excitation source is a pulsed *Fianium Supercontinuum* laser whose wavelength is selected using a *Photon Etc Laser Line Tunable Filter*. The laser is coupled into a single-mode optical fiber connected to a homemade microscope. The laser pulse duration is 6 *ps* and the repetition rate was set to 20 *MHz*. The sample is then excited using a Nikon objective with a numerical aperture N.A=0.8 and a working distance of 1.2 *mm*. The pulsed excitation wavelength can be selected from a spectral range stretching from 450 *nm* to 1600 *nm*.
- The detection of the photoluminescence decay dynamics is made using the time-correlated single-photon counting technique (TCSPC). In this technique, the laser pulse is split into two beams with a beam splitter. The first beam triggers a time-amplitude converter (TAC) to start ramping up a voltage. The second beam excites PL from the sample. Some of the PL is passed through a long pass filter onto a single photon counting detector from *Aurea* (SPCD). The first emitted photon to be detected by the SPCD sends a stop signal to the TAC, and the TAC voltage is read and stored by a pulse height analyzer. The SPCD is coupled to an opto-electrical converter of the decay (*PicoHarp 400*), finally yielding the histogram of the incoming hits as a function of time, the time being equal to the laser's repetition rate. Based on our configuration, the histogram resolution is equal to 64 picoseconds. Every event recorded, will represent a specific number of hits per unit of time. Finally, the total number of recorded points will represent the overall TRPL decay. We record TRPL decays with a time resolution close to 200 ps.

Now, for the TRPL spatial studies, a Physik Instrumente piezoelectric stage on which the sample is mounted, allowed mapping of the TRPL decays. For this thesis, the scan of our 30 $\mu m$ microcell was done with incremental X and Y steps of 300 *nm*. Which means that every 300 *nm* a TRPL decay is recorded. This resulted in a total of 10201 recorded decays that reconstructed the time-resolved photoluminescence emission of the whole micro CIGS solar cell.

Also, using a KEITHLEY 2400 source meter, small amount of currents can be injected in order to study time-resolved luminescence signal at voltages higher than the open-circuit voltage.

It is to be noted that a wide variety of experimental configurations can accomplish this. Most experiments excite the sample with a pulsed laser source, and detect the PL with a photodiode, streak camera, or single-photon counting. The system response time, wavelength range, sensitivity, operational difficulty, vary widely for each configuration [65].

### 2.2.3 Comparison between the HI and the SCM

Besides our calibration method, the HI setup presents several differences when compared with confocal microscope setup. Setups using hyperspectral imagers acquire directly spectrally resolved images. The acquisition time is therefore strongly reduced by 2 to 3 orders of magnitude. For example, a 150 × 150 $\mu m^2$ cartography would take numerous hours with a confocal setup, but about 10 min with a hyperspectral imager in some cases.

The depth probed in a confocal system is given by $\frac{2n\lambda}{NA^2}$, so in the range of a few microns for *n* (refractive index) around 3 [11]. In the HI system, one of the limitations regarding the depth probed, is linked to the material absorption coefficient. Therefore, for rough samples, this could be an advantage over confocal microscope, where intensity fluctuations are recorded if the depth probed is comparable to the roughness.

In a PL experiment, the main difference arises from the laser excitation, which is focused at one point in confocal system while it is spatially homogeneous for the HI setup. In the first case, carrier transport towards the non-illuminated part occurs. The emitted signal is therefore lowered, requiring excitation powers typically higher than 1000 suns. The information extracted is also influenced by the surroundings.
Here's a table that summarizes the differences between these two solar PV luminescence acquisition setups:

| Criteria | HI | Confocal Microscope |
|---|---|---|
| Acquisition time | Fast, direct acquisition | Acquisition time 2 even 3 orders of magnitude longer |
| Emitted luminescence flux | Absolute units: Photons/m.m².s (Absolute calibration) | Arbitrary units (relative calibration) Absolute calibration possible but technically challenging |
| Laser excitation | Homogeneous | Local, Gaussian excitation profile |
| Spatial resolution | 1-2 µm | High , down to 500 nm |
| Adaptability to rough samples | Yes | No |
| Excitation power | ≈ 1 Sun | ≥1000 Suns |
| Carrier Diffusion Artefacts | ABSENT | PRESENT |

**Table 2.1: Comparison between the HI and the confocal microscope setups**

### 2.2.4 Time-Resolved Fluorescence Lifetime Imaging (TRFLIM)

#### 2.2.4.1 Overview of technologies and Operating principles of TRFLIM

Typical methods to realize FLIM include time-gated FLIM, time correlated single photon counting (TCSPC), and Frequency-Domain FLIM.

As the needs for high frame frequency and high resolution microscopy increase, the option of using frequency modulation FLIM becomes less dominant compared with that of temporal FLIM including time-gated FLIM and TCSPC. On the one hand, and as described in chapter II. TCPSC-FLIM cannot provide as high frame frequency as time-gated FLIM. On the other hand, cameras dedicated to modulation acquisition offer a time resolution of about 3ns which is not suitable for our samples whom typical decay constants are about 0.5 to 1 *ns*. Therefore, our choice was to build a setup based on time-gated FLIM.

Time-gated FLIM acquires different images at different delays after the laser pulsed excitation, as depicted in Figure 2.6.

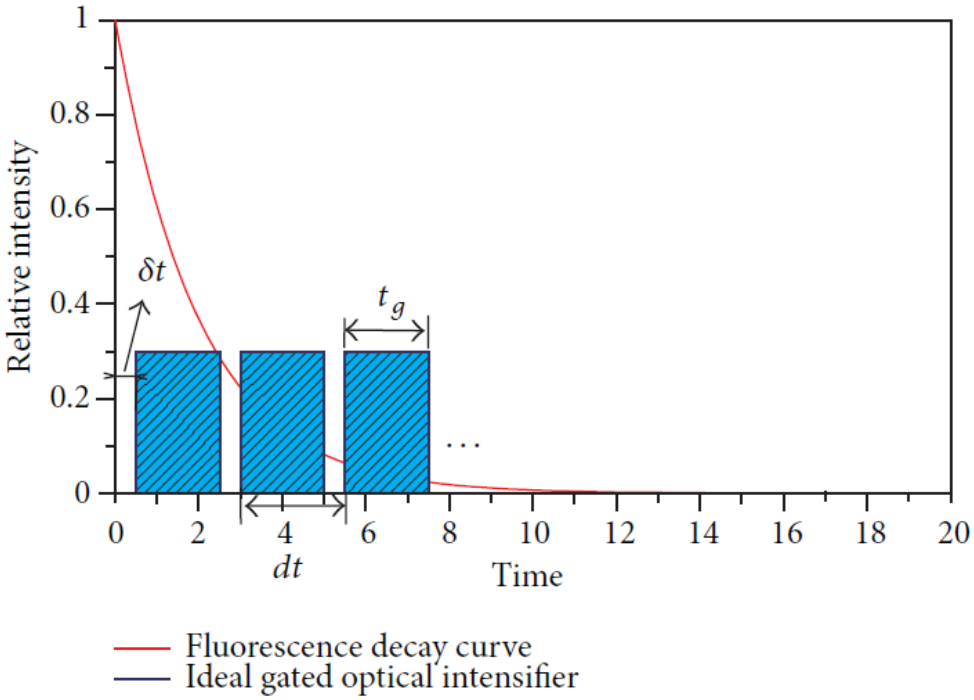



**Figure 2.6: Time-gated FLIM principle**

Due to different types of time-gated FLIM systems, we show in Figure 2.7 a simple abstract model that explains how the system works. The sample is excited by a short pulse laser. Fluorescence images are recorded by an ICCD (intensified Charge-Coupled Device) camera. Control devices realize synchronization of laser and ICCD, and thus gates open at different delay according to laser. Lifetime image will be computed using processed intensity images. We must precise that in our case, an em-ICCD (electron-multiplied ICCD) camera is used with enhanced quantum efficiency in the near-infrared region up to 1100 nm.

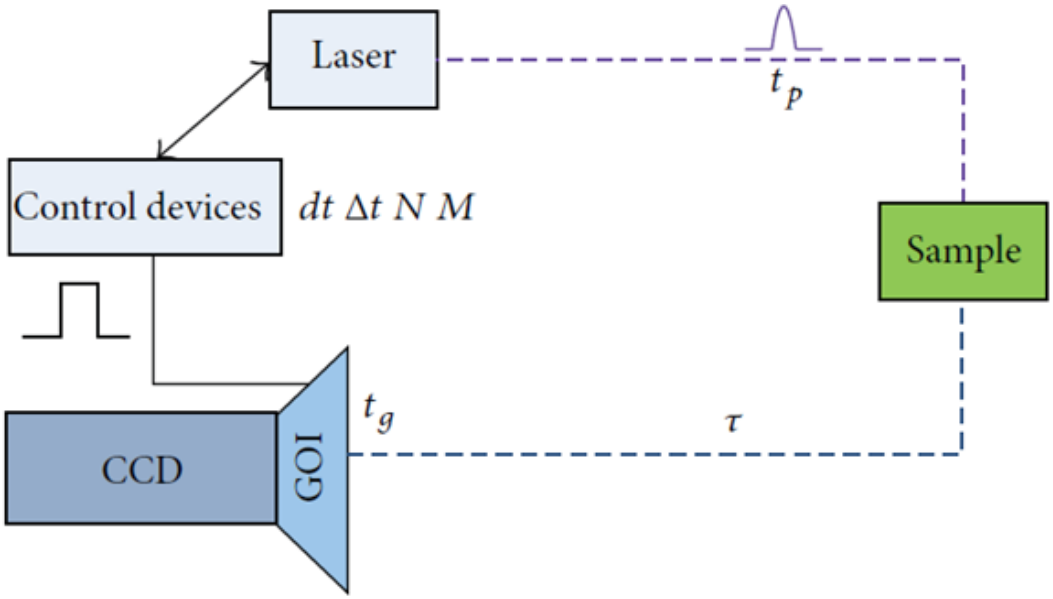


**Figure 2.7: Simplified time-gate FLIM system and temporal parameters.tp shows laser pulse, τ stands for sample lifetime, and tg means gate width of gated optical intensifier or GOI. N, dt, Δt, M and δt represent number of gates opened in one excitation, gate interval of N gates, delay step of different excitations, number of excitations, and the interval between laser excitation and opening of the first gate, respectively.**

To acquire different intensity images at different delays in order to compute lifetime image, it is crucial to control the em-ICCD and laser synchronously. FLIM system can be built up by inner trigger control [143], external trigger control [144], or optical delay control [145] according to different types of em-ICCD and laser utilized. For our case, our em-ICCD camera will be externally triggered by the output electrical pulses of our laser.

More versatile than TCSPC technique, the TRFLIM setup offers the possibility to analyze the sample with homogeneous or focused illumination. Now, for the present case of the TRFLIM techniques, we also expect to obtain three dimensional data hypercubes. However, our third dimension here is the time-dependence of the luminescence signal. In Figure 2.8 we illustrate the hypercube that a TRFRLIM experiment is expected to yield:

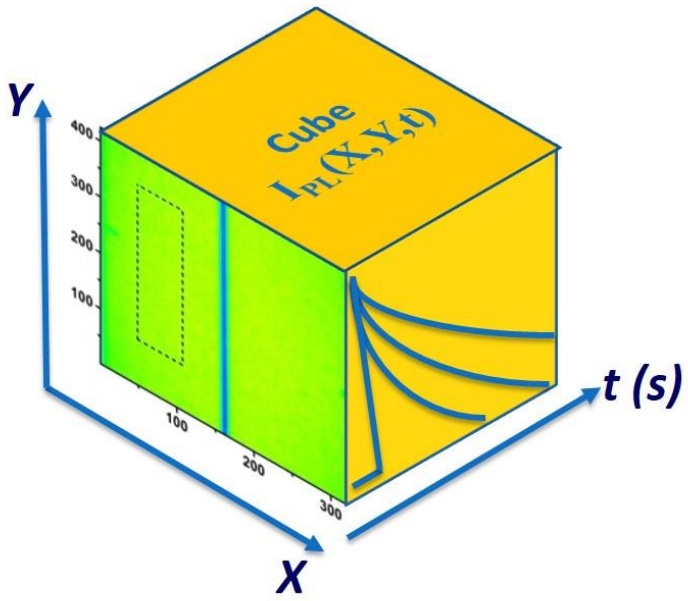



**Figure 2.8: Illustration of a TRFLIM hypercube**

### 2.2.4.2 Design and development of a setup dedicated to TRFLIM

After laying out the theoretical basis of the TRFLIM technique, we can now move on to the execution phase where will design, develop and apply our new opto-mechanical and opto-electronic setup. Our strategy was to breakdown the project into key sub-projects. After finishing each sub-project, we will qualify it, and optimize it until we reach our performance goals.

- Step 1: we focused on the design and development of the detection system of the TRFLIM setup. The detection system will have two main functions. The first being the image formation

while providing a micrometric spatial resolution and making use of the majority of the CCD sensor area. This will be done through the calculation and installation of an imaging lens system. The second is ensuring the time-gating process that will allow to time-resolve the acquired luminescence images. This function will be filled by an em-ICCD (electron multiplied – ICCD) time-gated camera from Princeton Instruments. The temporal resolution that we are aiming at is in the sub-nanosecond region given that the luminescence lifetime of most thin film PV technologies such as CIGS is in the order of few tens of nanoseconds.

- Step 2: Then, we move on to excitation system that will provide the homogeneous or focused pulsed illumination for the studied PV devices. We started by assembling a speckle-filtering optical system. We then proceed by constructing a removable optical system to create a homogeneous excitation.
- Step 3: Development of algorithms and data analysis routines in order to process the TRFLIM hypercubes and extract the properties of the investigated PV device.

The structure of our TRFLIM setup is illustrated in Figure 2.9:

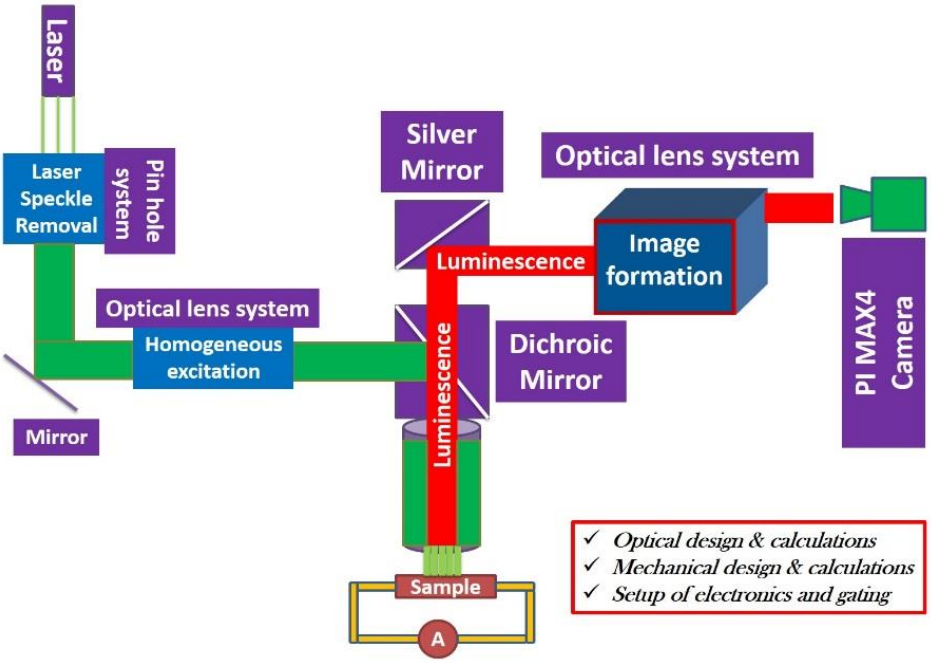



**Figure 2.9: Illustration of the whole TRFRLIM setup that will be constructed**

We start with a pulsed laser that is collimated and has a Gaussian intensity profile. The latter then goes into our assembled Pinhole system that will remove the high spatial frequency speckle from the laser beam. It is then directed to the homogenization optical system which will transform the incident Gaussian laser beam into a homogeneous laser excitation. After reflection on a dichroic mirror with the adapted cut-off wavelength, the reflected laser beam will excite the sample through a microscope objective with a specific working distance, numerical aperture, magnification factor and focal length. At

this stage, the luminescence emitted from the sample is transmitted by the dichroic mirror that will also filter any reflected laser light. The reflected luminescence goes into our designed and assembled optical lens system that will create the luminescence image onto the em-ICCD time-gated camera sensor.

#### 2.2.4.3 Spatial and Temporal resolutions of the detection system

- ***Spatial Resolution***

Before designing and assembling our detection system, we had to clearly define our expected applications of TRFRLIM setup. The requirements of the applications will eventually define the characteristics of our detection system and our optical calculations.

As previously mentioned, we are aiming at micrometric spatial resolutions. In other words, we are aiming at a net imaging of PV devices, such as the micro CIGS solar cells that we studied in the previous sections of the manuscript.

The clarity of the images and therefore our optical system's spatial resolution will be quantified by calculating the contrast of the detected images and the Point Spread Function (PSF).

While we clearly resolve PV devices, we also want to project them in order to make use of the majority of the em-ICCD chip.

We therefore have double variables to optimize while keeping a micrometric resolution of the recorded images.

The em-ICCD chip an area of 13 *mm* x 13 *mm*. We consider an object that is 100 $\mu m$ in size. Our goal is to project it onto a 10 *mm* x 10 *mm* area of the CCD chip. In this case, our magnification factor $\gamma$=100. We know that a part of this magnification is provided by our microscope objective of a focal length $f_1$. The total magnification of the whole optical system including the microscope objective will be the ratio between the equivalent focal length of the lens system that we want to design $f_{ls}$ and the focal length of our microscope objective:

$$\gamma = \frac{f_{ls}}{f_1} \tag{2.10}$$

In our case, $f_1$ is equal to 2 *mm*. Which means that in order to meet our $\gamma$=100 goal, $f_{ls}$ should be equal to 200 *mm*. At first impression, one would be tempted to directly choose a single lens that will have a focal length of 200 *mm*. This choice does indeed meet our $\gamma$=100 goal but highly damages our spatial resolution goal that should be micrometric. Such choice would lead a quite large PSF because the latter at the diffraction limit is given by:

$$PSF = \frac{\lambda}{2\sin\theta_c} \tag{2.11}$$

where $\lambda$ is excitation wavelength and $\theta_c$ is the collection angle according to which the image is formed. If a 200 *mm* lens is used, $\theta_c$ becomes very weak in the order of 3.57 *deg* which leads to an ideal PSF of 36 $\mu m$ and hence an unacceptable spatial resolution is expected because experimentally the PSF will be much larger than the ideal one.

Therefore, the solution that we propose is the following: Instead of using a single 200 *mm* focal length, we use two different lenses with an equivalent focal length of 200 *mm*.

Based on such configurations, our optical calculations should take into account the following: The focal length of the first lens $f_i$, the focal length of the second lens $f_j$, the space between the lenses $e$, the ratio between the focal lengths $R$, and finally the distance at which the image will be formed $EF_i$, which is the physical distance between the first lens of the system and the point of image formation of the whole lens system. All of these quantities should lead to a final optical detection lens system combined with a microscope objective.

All of the previous optical parameters are linked through the following equation:

$$EF_i = e + \left( R\left(1 - \frac{e}{f_i}\right)\right) \tag{2.12}$$

We ran multiple simulations and numerical calculations and it yielded the following characteristics for our system: $\begin{cases} f_i = 85mm \\ f_j = -100mm \\ e = 28mm \\ EF_i = 160mm \end{cases}$

Such lens system has an equivalent focal length of $f_{ls} = 200mm$.

Once coupled with the microscope objective, our whole image formation optical system should have the following properties: $\gamma = 100 \;\&\; PSF = 8.25\mu m$

With such properties our designed image formation system satisfies both our magnification requirements and our spatial resolution requirements. A PSF=8.25 µm means that a distinguishable information can fit into a single pixel and that no overlap occurs with a neighboring pixel information.

Now it was time to put our designed detection system to the test. We start by assembling and installing the calculated lens system, coupled to our microscope objective. The second step consists of measuring the spatial resolution of our detection system.

Our approach consists of using a white lamp that will homogeneously illuminate a 1951 USAF resolution test chart. It is a pattern that consists of groups of three bars with dimensions ranging from

500 µm (Element 1 of Group 0) down to 2.1 µm (Element 6 of Group 7). The largest bar the imager cannot discern is the limitation of its resolving power. The common format consists of six groups in three layers of patterns. The largest groups, forming the first layer, are located on the outer sides. The smaller layers repeat the same pattern but are progressively smaller toward the center. Each group consists of six elements, numbered from 1 to 6. Within the same layer, the odd-numbered groups appear continuously from 1 through 6 from the upper right corner. The first element of the even-numbered groups is at the lower right of the layer, with the remaining 2 through 6, at the left. The higher the group order, the smaller the line pairs.

Because our goal is a micrometric resolution, we aim at imaging the smallest group dimension of the USAF target which is the sixth element of the order 7 group that has line pairs distanced by *2.19 µm*. See Figure 2.10 below:

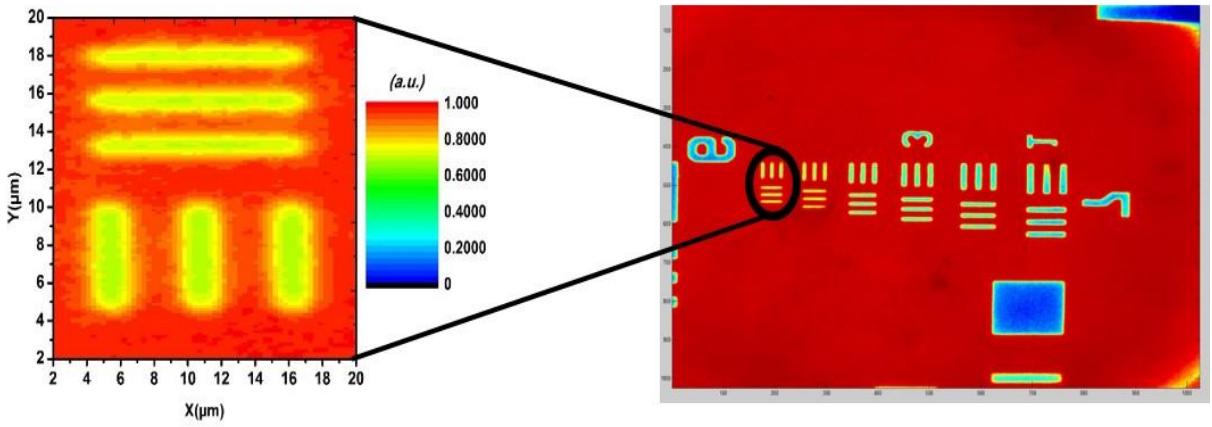



**Figure 2.10: Experimental imaging of the smallest order 7 group of the USAF test target**

The picture obtained is by definition the convolution of the Transfer Functions of the target, the microscope objective, the assembled lens system and the PIMAX4 camera.

We draw both their corresponding horizontal and vertical intensity profiles, as seen in Figure 2.11:

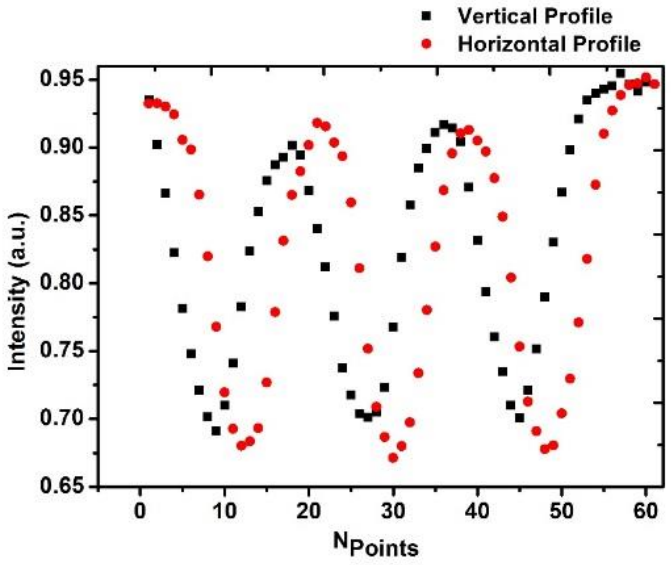



**Figure 2.11: Horizontal and vertical intensity profiles of the sixth element of the order 7 group**

We can see from these profiles that the lines are well resolved as no overlapping is observed for both horizontal and vertical intensity profiles. In order to quantify the spatial resolution, we can calculate the contrast based on these intensity profiles using:

$$C = \frac{I_{\max} - I_{\min}}{I_{\max} + I_{\min}} \tag{2.13}$$

We obtain a contrast value of $C = 0.18$. This means that, given that the minimum line pairs distance is 2.19 µm, our total detection system spatial resolution is smaller than 2.19 µm given that the corresponding contrast is greater than zero. So far we are sure that we can clearly distinct objects separated by at least 2.19 µm.

In order to find out the exact value of our detection system's spatial resolution, we perform PSF measurements. The experience consists of imaging a collimated laser beam with a Gaussian intensity profile and measure the pixel surface that it occupies. In our case, we find an intensity profile with a FWHM value of 3 pixels=39 $\mu m$, as seen in Figure 2.12 below.

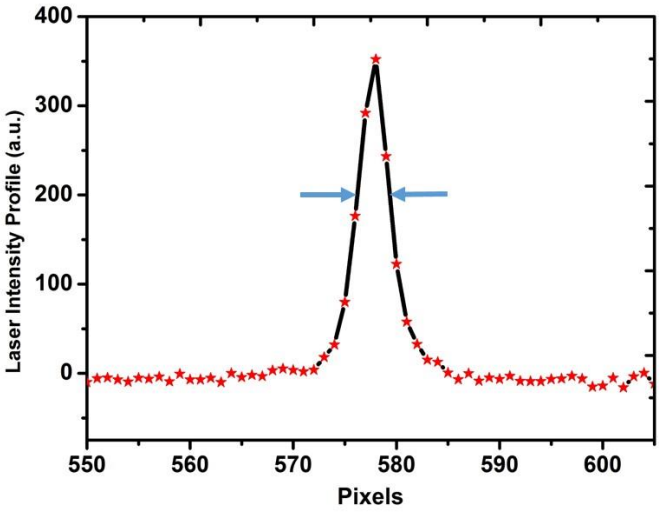



**Figure 2.12: Measurement of the intensity profile of a collimated laser beam**

Finally, when combining this PSF value with the total magnification of our assembled imaging and detection system, we find that the overall spatial resolution of our system is equal to 0.8 $\mu m$.

- ***Temporal Resolution***

After the measurement of our system spatial resolution, comes the measurement of its temporal resolution. The latter is strictly a characteristic of our PIMAX4 camera and its value is independent of our assembled optical system. It is an intensified EMCCD camera (emICCD) that features back-illuminated 1024 x 1024 frame transfer EMCCD fiber optically coupled to a variety of filmless intensifiers. The advantages of intensifiers and the benefits of EMCCD are combined in one camera that delivers single-photon sensitivity and quantitative performance for scientific imaging and spectroscopy research. Our PIMAX4 ensures high linearity, high sensitivity, and ultrafast subnanosecond gating, dual gain control, programmable timing generator.

Based on the specifications of the camera, the minimum achievable temporal resolution is theoretically equal to the minimum gate width. Hence, in the best case scenario, we can hope to obtain 480 *picoseconds* as a temporal resolution. In order to experimentally quantify it, we perform the following experiment.

Using a picosecond width laser pulses, we aim at resolving the intensity profile of the detected laser intensity. The corresponding time-gating configuration of our camera consists of selecting the minimum gate width available which is 480 *ps*. In order to properly perform such measurements, the synchronization between the pulsed laser excitation and the opening of the gates for the detection (see Figure 2.13) is crucial. Therefore, our solution consisted of using the output electronic pulses signal of the laser in order to externally trigger our PIMAX4. In this case the excitation and the detection are

simultaneously triggered with the same electronic signal. The trigger consisted of 730 *ns* wide pulses with a peak voltage amplitude of $V_p$ = 1.7 V et and a repetition rate of 1 *MHz*.

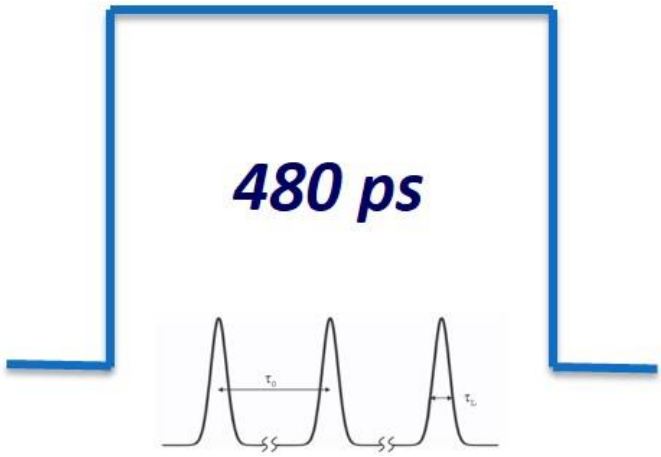



**Figure 2.13: Illustrating the synchronization between the excitation pulses and the gate opening**

After a successful synchronization of the both excitation and detection, we were able to acquire time-resolved images of the laser reflection before, during and after its detection during a 480 *ps* gate opening. The time-resolved profile of the laser intensity can be seen in Figure 2.14 below:

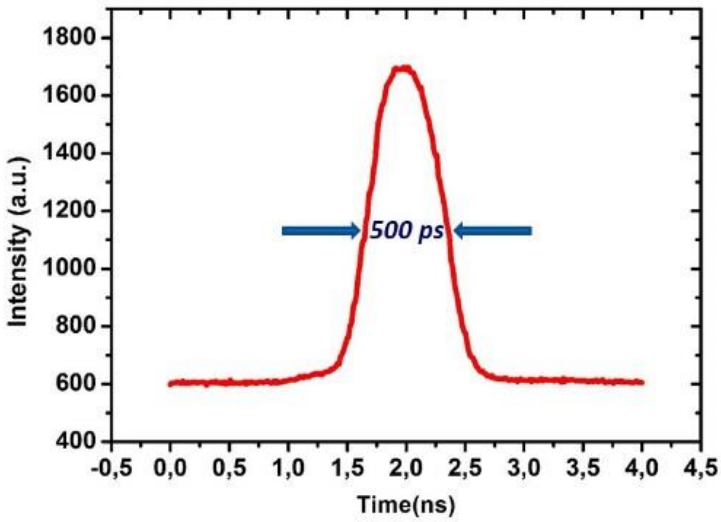



**Figure 2.14: Temporal profile of the time-gated laser reflection**

Ideally, one would expect to obtain temporal laser profile that exactly replicates the time-gate of the *PIMAX4* which a square-shaped profile with a temporal width of 480 *ps*.

In our case, we obtained a rather Gaussian intensity profile that has a FWHM value of 500 *ps*. We can hence conclude that we came quite close to the ideal case and that the 500 *ps* temporal resolution of our detection system is satisfying.

To conclude, this section was dedicated to an experimental evaluation of key parameters of our designed TRFLIM detection setup. We successfully reached highly acceptable resolutions of our system that are quite close to its theoretical limitations. We achieved a spatial resolution of 0.8 $\mu m$ and a temporal resolution of 500 *ps.*

#### 2.2.4.4 Characteristics of the excitation system

Now that the assembly and testing of the TRFLIM detection system is done, we move on to work on its excitation system. The latter consisted of green pulsed laser from Talisker, the *Talisker Ultra 532_DS_0412_4* from *Coherent*. This is a high power pulsed laser originally designed for industrial applications such as metal carving and steel cutting. In the table below, we gathered some of its main specifications:

| ***Talisker Ultra 532_DS_0412_4*** | |
|---|---|
| **Wavelength** | **532 *nm*** |
| **Mean Output Power** | **15 *W*** |
| **Repetition Rate** | **From 200 *kHz* up to 1 *MHz* (1 pulse /µs )** |
| **Pulse Width** | **15 *ps*** |
| **Beam Diameter** | **2.2±0.4 *mm*** |
| **Peak Output Power** | **0.94 *MW*** |
| **Surface Output Energy** | **395 $\mu J/pulse/cm^2$** |

**Table 2.1: Specifications of the *Talisker Ultra 532_DS_0412_4***

Given the very high power of our excitation system, security was our first concern. Therefore, we started by laying out a plan in order to minimize the risk of exposure to such powerful light source.

In order to assess the risk, we started by calculating a key parameter which is the *Maximum Permissible Exposure* limit or *MPE* for short. The *MPE* differs from one laser source to another based on each laser specifications. For the present case of the *Talisker Ultra 532_DS_0412_4*, we were able to calculate an *EMP* of $2.5x10^{-5}\ J/pulse/m^2$.

We assume that our assembled optical excitation situation will result in a homogeneous 1 *cm* in-diameter pulsed laser beam. This means that once operating at maximum power, our excitation source

will deliver an output energy that is $1.5x10^5$ *EMP*. In other words, the delivered energy will be 5 orders of magnitude larger than the maximum permissible exposure limit for such excitation source.

These numbers reflect a very high level of danger to which the user of the TRFLIM can be exposed. Therefore, the first step towards an enhanced security and protection was to eliminate any physical contact between the user and the laser source. To do so, we started by programming, using an old-school emulator, a computer interface that communicates with the *Talisker* according to a specific set of commands. At this stage the user can safely operate the *Talisker* by controlling its power, repetition rate, diagnose its state etc…

The assembly phase of the excitation system starts with building a speckle filtering optical system (as seen Figure 2.15). Our configuration consisted of two microscope objectives. The first has a 10X magnification factor and a numerical aperture N.A. of 0.1. The second has a magnification factor of 40X and an N.A. =0.65. Both microscope objectives are placed on facing the other. In between we place a 50 µm in-diameter Pinhole. Each of the three optical elements is placed on XYZ mounting stage for a micrometric positioning precision. The 40X objective should be placed at exactly its focal length from the Pinhole so that the incident laser beam is focalized at the center of the Pinhole. Then, the 10X microscope is also placed at exactly its focal length from the center of the Pinhole so it's properly collected the exiting laser light. The final result is a speckle-free collimated laser beam exiting the end of the 10X microscope. The laser beam diameter is now equal to 0.9 *cm* which is the entry diameter of the 10X microscope.

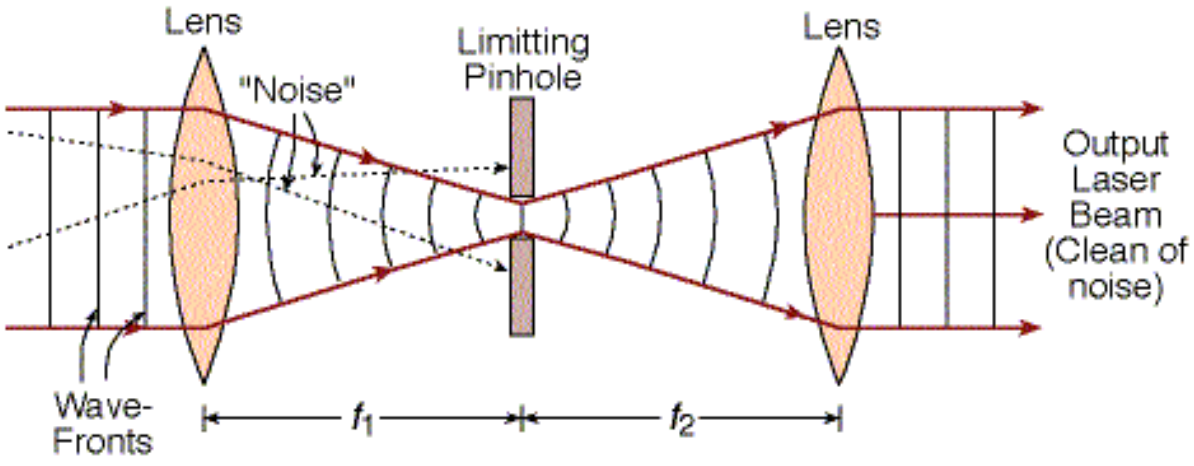



**Figure 2.15: Laser spatial filtering setup and principle**

The choice of the characteristics of the speckle-filtering system was based on the calculations of the optimal Pinhole diameter. Such optimization will maximize the filtering of the spatial noise and at the same time minimize the optical power losses of the output laser beam.

The optimal Pinhole diameter $D_{opt}$ is calculated as follows [158]:

$$D_{opt} = \frac{f\lambda}{a} \tag{2.14}$$

Where *f* is the focal length of the first microscope objective, λ is the laser wavelength and *a* is the radius of the input laser beam. In our case we find $D_{opt} = 48\mu m$. This justifies our choice of 50 µm Pinhole diameter.

Now that the optimal Pinhole diameter is calculated, we can proceed by calculating the potential loss in optical laser power at the exit of the whole Pinhole system. The losses are calculated by establishing the ratio between the output laser power $P_{out}$ and the input laser power $P_{in}$.

The ratio is expressed as [158]:

$$\frac{P_{out}}{P_{in}} = 1 - \exp\left( -\frac{1}{2}\left( \frac{\pi a D_{opt}}{\lambda f} \right)^2 \right) \tag{2.15}$$

In our case, we find $\frac{P_{out}}{P_{in}} = 0.998$, which translates into only 0.2% in output laser power loss.

Finally, in order to also make sure that our present configuration yields an optimal speckle filtering, our system must obey the following condition:

$$\frac{2f\lambda}{D} < 2a \tag{2.16}$$

In our case, $\frac{2f\lambda}{D} = 1.064mm < 2.2mm$. The condition being respected, our configuration does provide an optimal speckle filtering and an optimal laser power transmission.

#### 2.2.4.5 Concluding the construction of the complete TRFLIM setup with a proof of concept

The assembly of the whole TRFLIM setup is done at this stage. We completed the first two major project steps . We have also experimentally quantified the different caracteristics of the global excitation and detection systems. These measurements meet the requirements for the use of this system for PV applications.

Now that the complete TRFLIM setup is installed, we looked for an improvement of the security while operating the complete system. To do so, we developed a *Matlab*-based code that renders our TFRLIM setup operation completely automatic. Adding this automation to the developed interface that remotely controls the *Talisker* enhances the overall operational security. The algorithm behind the developed automation code is executed using a single command and takes into account every single operation step

of a typical TFRLIM experience, i.e. from the moment the acquisition software is launched until the final data analysis and display of the processed TRFLIM cubes.

The very first TFRLIM experiment that followed its different construction phases, was carried out on a perovskite-based solar cell. The aim of this experiment was to record and observe a time-resolved photoluminescence decay using our setup. In particular, our excitation system was still in confocal mode and we therefore acquired time-resolved images of a photoluminescence spot, we then plotted its temporal profile as seen in Figure 2.16 below:

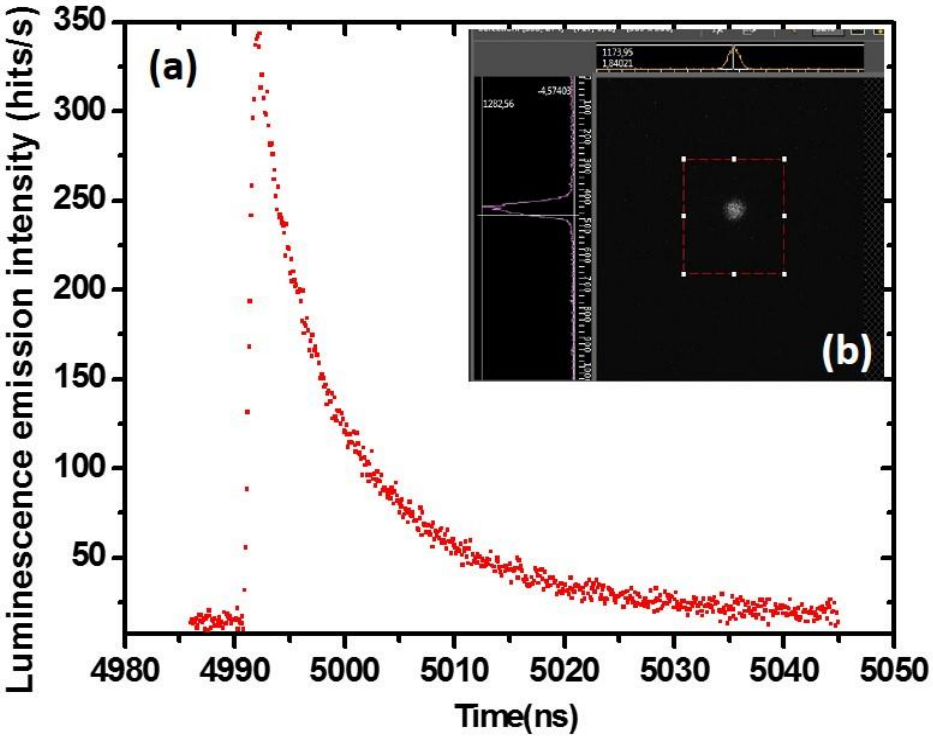



**Figure 2.16: First TRFLIM result on a perovskite-based solar cell**

In the Figure 2.16.b inset we show the PL spot detected by the camera. The camera then time-resolves this PL spot which results in a series of PL images at different time steps. We can also see in the inset the horizontal and the vertical intensity profiles of the PL signal. Finally, we then plot the temporal profile of the PL intensity for each pixel of the image, we find the time-resolved photoluminescence decay as seen in Fig 2.16.a. We can see that the temporal resolution is as good as expected. Now that we mastered the synchronization between the *Talisker* and the *PIMAX4* we obtain a quite sharp rise-time of the *PIMAX4* camera which allowed a clean temporal resolution of the rest of PL decay as see in the plot. A rapid analysis of the obtained decay reveals a carrier recombination lifetime of about 13 *ns*. But again, our goal here was just to demonstrate the capability of our setup to successfully provide time-resolved luminescence images of the solar PV device with a good measurement quality.

# Chapter III. Quantitative local access to optoelectronic properties of $Cu(In,Ga)Se_2$ PV devices using Time-Resolved Luminescence

## 3.1 General introduction and objectives

This third chapter of the thesis is composed of two main parts. In the first part we revisit the temporal aspect of the luminescence of CIGS solar cells. In particular we propose a physical model that helps understand and analyze the carrier dynamics in CIGS. Our challenge was to construct a model that adapts to all changes in the experimental conditions. The second main part of the chapter is dedicated to the development of new applications of the time-resolved photoluminescence technique in CIGS. These applications are inspired by the understanding we developed in the first part. In other terms, we will be presenting optical alternatives for the usual electrical measurements, by looking at the time-resolved photoluminescence decays. Finally, our final goal was to develop a tool that extracts the defects density in CIGS using our optical approach. These densities will then be correlated to key PV performance indicators.

## 3.2 Development of a unified understanding of charge carrier dynamics in $Cu(In,Ga)Se_2$ PV devices

### 3.2.1 Introduction

We have learned so far that while TRPL techniques provide a generous access to PV materials properties, the interpretation of the experimental data varies significantly from one PV technology to the next. This is mainly due to the fact that different PV device configurations and compositions lead to different carrier dynamics. For accurate interpretations of the TRPL signals one should establish a robust theoretical understanding of carrier dynamics and apply it to the interpretation of the TRPL signals. We have also seen in the previous bibliographical sections that TRPL measurements are extremely sensitive to the experimental conditions. For the particular CIGS-based thin film PV devices, we have seen multiple clear case studies where two TRPL independent studies on the same PV material and the same experimental conditions, can lead to completely opposite conclusions and interpretations.

In particular we will propose a definition of each lifetime and each exponential component in equation (1.31). We will then confront our theory with experimental TRPL data.

### 3.2.2 Physical model based on carrier recombination centers and shallow defects acting as carrier traps

In the case of a double exponential decay, two lifetimes governing the decay can be extracted, a short and a longer decay lifetimes $\tau_1$ & $\tau_2$. The short one $\tau_{Rec}$ has been proposed by R.K. Ahrenkiel as the lifetime related to recombination centers and direct recombination mechanisms, i.e. band-to-band recombination and non-radiative SRH recombination [78].

The longer one $\tau_{Traps}$ will be related to the presence of emission traps. The latter have a finite density of accessible states delaying the emission of the PL signal. This is explained by the dependence of the capture and the residence lifetimes on the energy levels $E_T$ and the density $N_T$ of the shallow trap states [104].

An initial proof for this statement originates from the fact that under high injection regimes, the longer decay disappears and the decay becomes mono exponential [78]. The short decay lifetime however, exhibits a weak sensitivity to the photo-injection level.

At the moment of photo injection, the recombination centers govern the photoluminescence emission. During this process, the number of photogenerated carriers is much larger than the number of emission traps. In this case, we observe a mono-exponential decay characterized by a fast decay lifetime [78]. However, as the excess carrier concentration decreases with time, traps start to reduce the effective recombination rate and the latter gives the data the appearance of a longer recombination lifetime than the actual recombination lifetime.

In the context of the model used here (see Figure 3.1 below), which is in accordance with our experiments, it is the short lifetime that is indicative of the recombination lifetime. The longer lifetime, due to trapping, is indicative of carrier mobility losses, as well as the material quality, since it reflects the dominance of defective trap states on the photo-generated minority carrier dynamics.

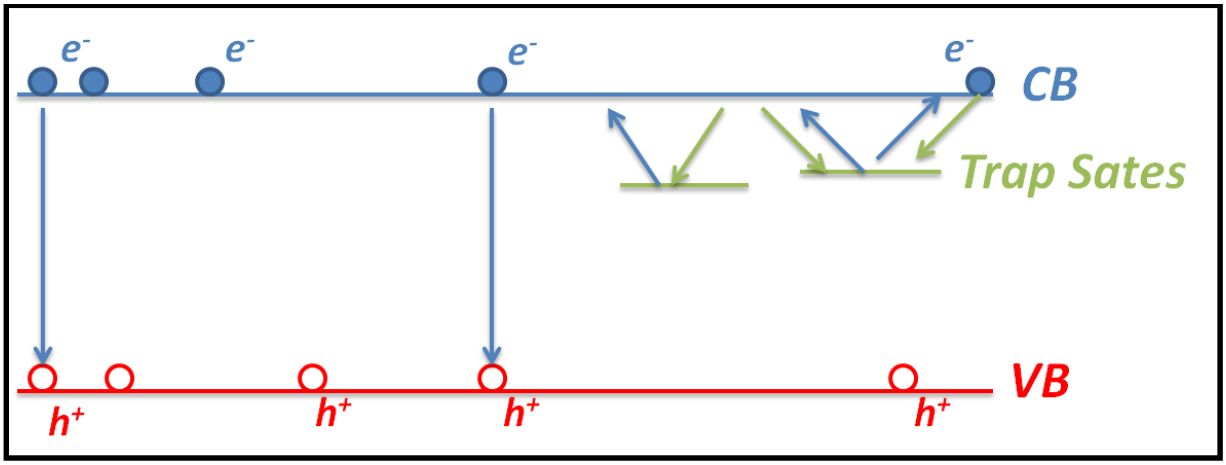



**Figure 3.1: Schematic illustration of the charge carrier dynamics**

Consequently it is inaccurate to ignore the short exponential decay and the study should not only focus on the second longer decay lifetime. The latter shouldn't be considered as the characteristic carrier lifetime. Therefore, one should not confuse the long trap-related lifetime with a long radiative lifetime that indicates a good quality material [105].

At this stage, we propose a detailed version of equation (1.35), we define the occurrence weights of the two types of events: direct recombination events via recombination centers and trap states emission events. The corresponding occurrence weights are noted $W_{R-centers}^{occ}$ & $W_{Traps}^{occ}$ respectively.

The notion of occurrence weights and the attribution of each lifetime to as specific type of event is one of the main novelties introduced by this section of the thesis. Based on them one can start by considering the TRPL decay as a direct reflection of what the carrier are actually experiencing in real-time.

Describing the detected luminescence intensity decay as the sum of two exponential decays governed by $W_{Traps}^{occ}$ and $W_{\mathrm{Re}c}^{occ}$ results in the following expression:

$$I_{TRPL}(t) = W_{\mathrm{Rec}}^{occ} e^{\frac{-t}{\tau_{\mathrm{Re}c}}} + W_{Traps}^{occ} e^{\frac{-t}{\tau_{traps}}} \tag{3.1}$$

By fitting equation (2), we can extract the values of each of the occurrence weights of the two events and finally establish their ratio. It is then possible to quantify the occurrence frequency and influence of each type of events. The dominant regime in carrier dynamics is thus extracted using the following new parameter:

*DCD* being the *Dominant Carrier Dynamics*, $$DCD = \frac{W_{\mathrm{Rec}}^{occ}}{W_{\mathrm{Rec}}^{occ} + W_{Traps}^{occ}} \tag{3.2}$$

*DCD* is a new parameter that we created and introduced. For the time-resolved luminescence techniques, *DCD* is highly important for the following reasons: Based on its mathematical description in equation (3.2), the *DCD* values will fluctuate between 0 and 1. These values are direct indicators of the state of minority carrier dynamics within the CIGS material. For example, a *DCD* value converging towards unity reflects a state of carrier dynamics where direct recombination events completely dominate carrier trapping events. For such state, the activity of shallow trap states is negligible and this represents the best case scenario where the overall carrier dynamics and hence the transport properties of the PV material are free from any negative influence of trapping events.

A worst case scenario for the state of carrier dynamics is characterized by a *DCD* value approaching zero. This means the carrier trapping activity is at its highest and that material's electronic transport

properties are badly damaged. We can hence conclude that *DCD* provides an optical tool for a qualitative evaluation of the material's trapping defects density.

### 3.2.3 Photo-excitation intensity-dependent and electrical carrier-injection dependent time-resolved luminescence experiments

In this study we discuss the effects of the incident excitation power and the effects of the electrical current injection into the solar cell on the bi-exponential TRPL decays observed in CIGS solar cells. Based on the previous physical model, we will show that it is possible to explain all of the observed experimental variations of carrier dynamics.

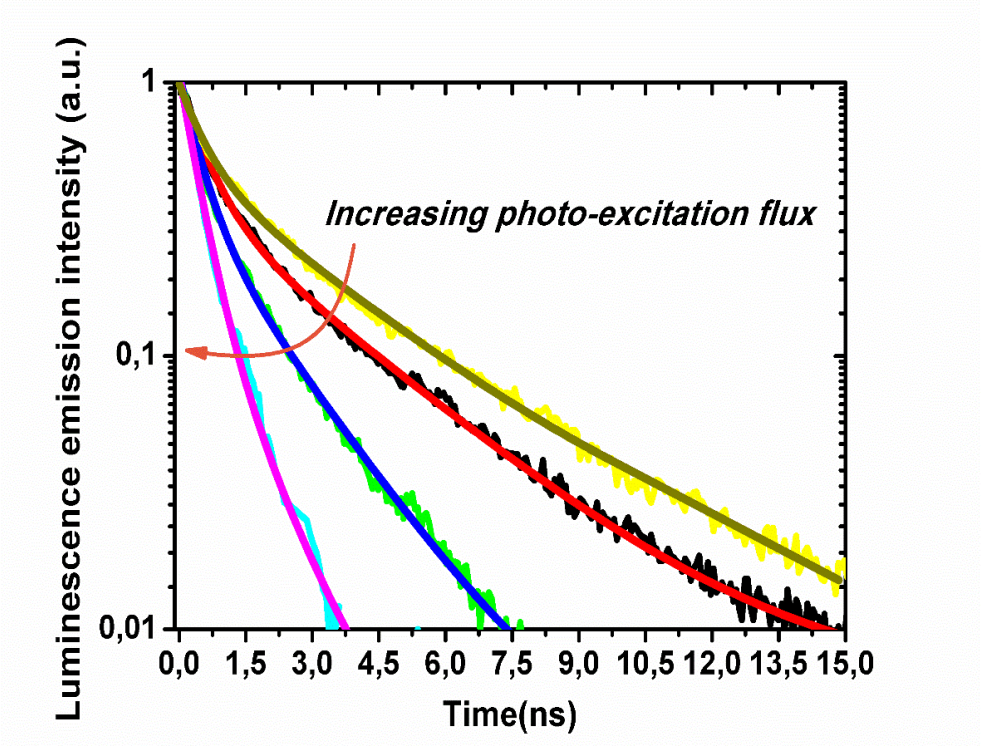
A standard micro CIGS solar cell [106] with a 25 µm diameter is used for this study.

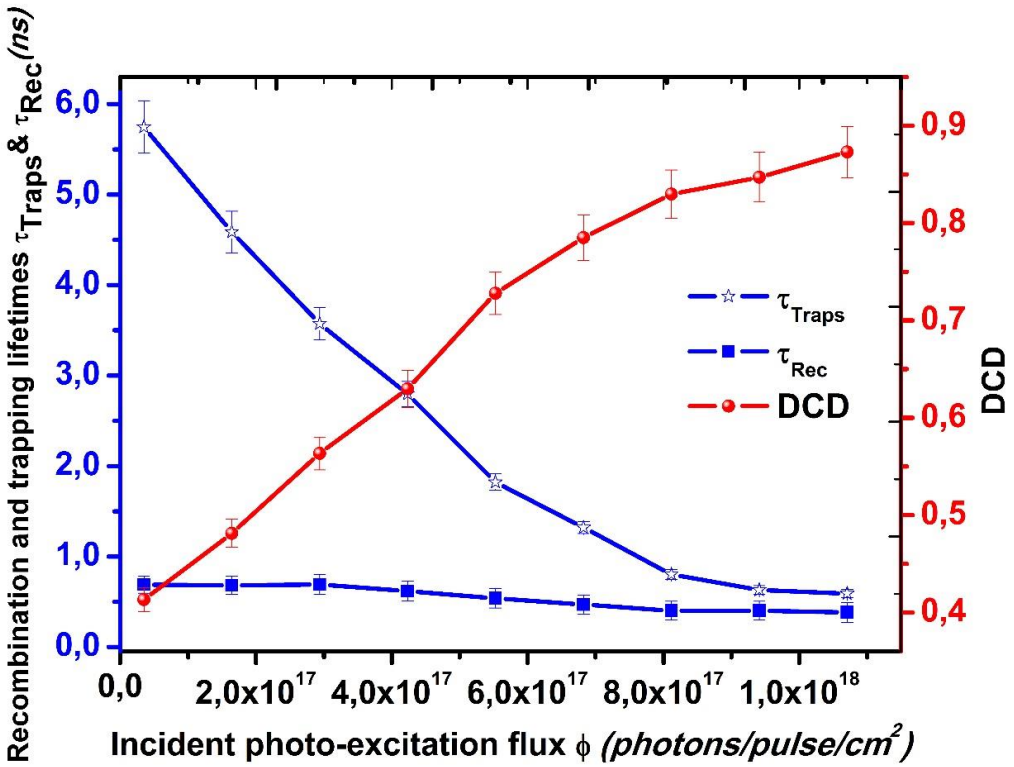
A basic J (V) characterization yielded the following performance parameters: Voc=0.67 V, Jsc=30.4 mA/cm$^2$, FF=68.4 % and $\eta \cong 14\%$.

We start by acquiring a set of time-resolved photoluminescence (TRPL) decays. The luminescence decay, centered at an energy of 1.13 eV, corresponds to band to band transitions in our experiments performed at room temperature (confirmed by measurements of the PL yield as a function of incident power).

For this set, the solar cell is at open-circuit voltage condition, and the incident photo-excitation flux ϕ is varied between 3.5x10$^{16}$ photons/pulse/cm$^2$ and 1.2x10$^{18}$ photons/pulse/cm$^2$. The wavelength is set to 700 nm. The evolution of the carrier dynamics as a function of ϕ is illustrated in Figure 3.2.a:

**a.**






**b.**

**Figure 3.2: a. Evolution of the TRPL decays as a function of the photo-excitation intensity. b. Evolution of recombination lifetime, the trapping lifetime and the *DCD* parameter as a function of the photo-excitation intensity.**

We find a bi-exponential decay that consists of a short decay followed by a longer one. The latter gets shorter as the incident photo-excitation flux is increased.

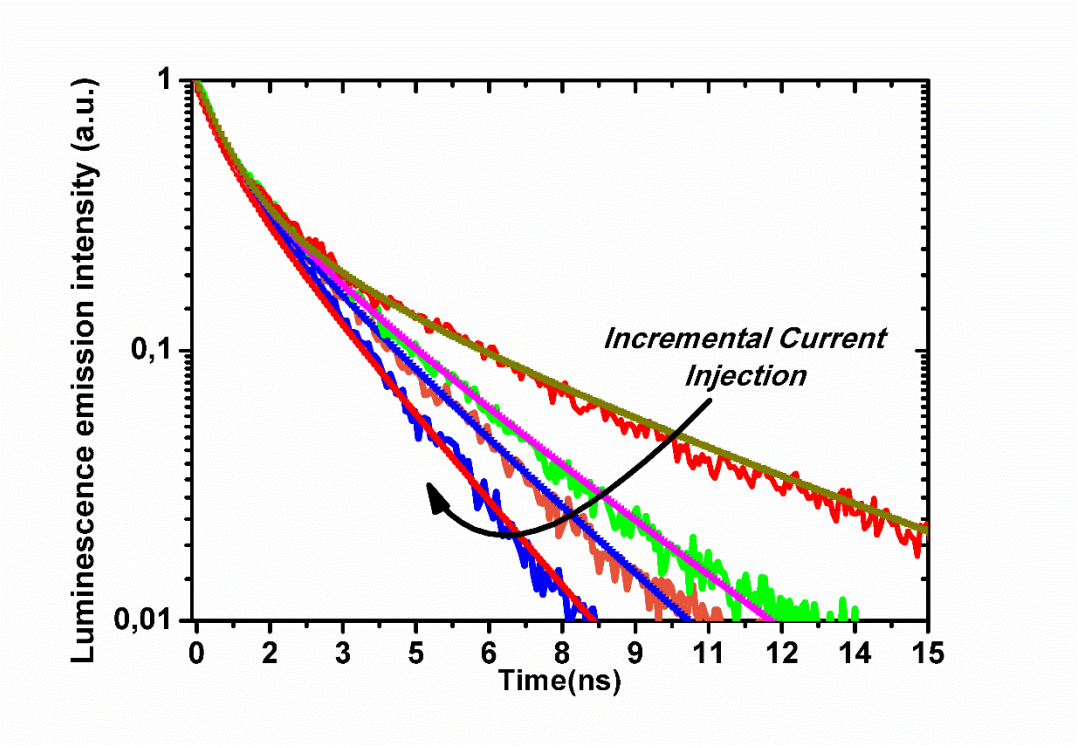
Figure 3.2.b represents the evolution of the two lifetimes and the DCD ratio as a function of the excitation power. While $\tau_{Rec}$ appears to be weakly influenced by the increasing excitation intensity, $\tau_{Traps}$ strongly diminishes from 5.75 ns to approximately 0.6 ns. When the incident photon flux becomes higher than $7x10^{17}$ photons/pulse/cm$^2$ the TRPL decay is considered as almost completely mono-exponential with values of the DCD higher than 0.85. Above this excitation threshold no values are extracted and the DCD ratio converges towards unity. As we have explained previously and will be further discussed here, this effect is explained by a decreasing contribution of the traps states to the carrier dynamics when the light-induced carrier density increases.

Now comes the part where in addition to the pulsed light excitation source, we study the effect of electrically injected carriers on the time-resolved luminescence (TRL) decay time.

A set of experimental TRL decays under incremental values of injected current $J_{inj}$($s^{-1}cm^{-2}$) is acquired. The incident excitation photon flux is maintained constant at $3.5x10^{16}$ Photons/Pulse/cm$^2$. The value of

the injected currents is experimentally measured. Same goes for the total luminescence decay time. In addition to the known micro CIGS solar cell surface, it is then possible to calculate the value of $J_{inj}(s^{-1}cm^{-2})$. For this type of experiments, photoluminescence and electroluminescence occur simultaneously. The methodology for sorting out and analyzing the TRL decays is different than the one used for the TRPL experiments. Here, excess electroluminescence intensity is obtained for each value of $J_{inj}$. Such intensity appears in a form of a constant background that increases as the injected current is increased. Such background should not in any case be confused with the background noise of the experiments.

In Figure 3.3.a. and Figure 3.3.b. respectively, we display the TRL decays and the carrier dynamics as a function of $J_{inj}$.




**a.**

**b.**

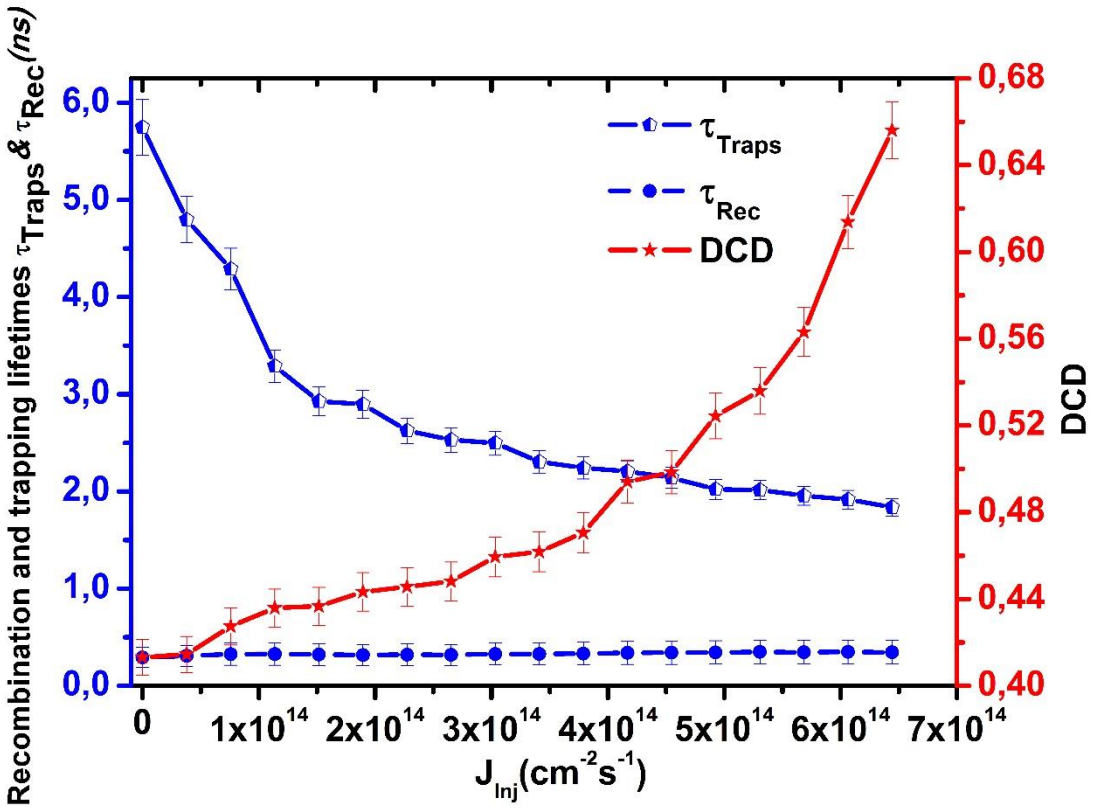



**Figure 3.3: a. Evolution of the TRL decays as a function of the electrical carrier injection. b. Evolution of recombination lifetime, the trapping lifetime and the DCD parameter as a function of electrical carrier injection.**

Figures 3.3.a and 3.3.b reveal a similarity between the tendencies of the carrier dynamics under increasing optical and electrical excitation intensities. Once again, the longer part of the TRL decay gets shorter as $J_{inj}$ is increased, the DCD increases and the faster part of the decay remains almost unchanged.

When the electrical carrier injection increases the TRL decay becomes progressively mono-exponential with values of the DCD rapidly increasing towards unity. This effect is explained by a direct occupation of the accessible density of trap states by the electrically injected carriers. This phenomenon progressively weakens the trapping activity which is illustrated by the value of the trapping lifetime that is 3 times smaller for the last TRL decay compared to the initial one.

However, a fundamental difference exists behind the observed similarity between the two sets of experiments. The difference is mainly based on the variation of two different fundamental quantities. The first being the ratio between the density of photogenerated carrier density and the density of accessible trap states density. The second is the occupation of accessible trap states under electrical current injection. Both however, exhibit the same effect on the system carrier dynamics.

To be more precise, in the TRL(Jinj) experiments, the value of the injected current is increased. It tends to electrically occupy the inactive shallow trap states density present at the absorber surface and its interface with the CdS buffer layer [108]. As the latter density decreases, so does the delay in the luminescence emission induced via carrier trapping. This explains why the TRL decays in Figure 3.3.a are becoming shorter under an increasing value of injected current.

In the TRPL(ϕ) experiments, the value of excitation power is also increased. In this case, the excess photogenerated carrier density becomes progressively dominant over the accessible trap states density. This increasing ratio between the former and the latter densities is at the origin of the observed convergence from a double to a mono-exponential decay.

On the one hand, for both TRPL(ϕ) & TRL(Jinj) experiments , the short carrier lifetime demonstrates a weak sensitivity with respect to both excitation sources (Figures 3.2.b and 3.3.b.). This proves that the short decay lifetime is indeed related to direct recombination events that are not influenced by trapping-induced delays.

One the other hand, we observed an important decrease in the longer decay lifetime under both excitation sources. Firstly, the excitation power amplifies the activity of the recombination centers causing lesser carriers to be involved in trap emission-related events. Secondly, current injection is continuously saturating the accessible states of the traps and therefore significantly attenuating their activity. A mutual consequence of the above is a decrease in the trapping lifetime. This can be observed is Figures 3.2.b and 3.3.b.

When it comes to the evolution of the DCD parameter, the latter quantifies the influence of the shallow trap states on the overall carrier dynamics. The higher the DCD, the lower their influence is. Now, we have seen that both TRPL(ϕ) & TRL(Jinj) experiments lead to a decrease in the influence of the existing shallow trap states, this eventually explains the convergence of the DCD towards unity, for both types of time-resolved experiments.

Finally, whether it is the current injection, the excitation energy or the excitation power that is being increased, the final state regarding the carrier dynamics is the same. The latter is characterized by a total dominance of direct recombination events over the trapping events.

### 3.2.4 Investigating the potential influence of the built-in electric field

In this section, we investigate the effect of the electric field on our previous results. On the one hand we check if the absence or presence of the electric field modifies or has any link with the observed hysteresis phenomenon. On the other hand, we will also track any change in the previously discussed behavior of carrier dynamics under increasing optical or electrical excitation intensity.

Our methodology consists of preparing two CIGS samples. The first sample contains the complete stack of layers. The second sample however, is missing the *ZnO* front contact layer and contains the same absorber and buffer layer as the first sample. Depriving the second sample from its front contact changes the built-in electric field. Given the highly inhomogeneous nature of chalcogenide CIGS devices, the comparison of the two samples does not consist of a numerical comparison of the obtained results, but, as mentioned earlier on, it is the behavior of carrier dynamics that will be compared under exactly the same experimental conditions. Our analysis will hence be qualitative.

We are aware that in the present context, the ideal comparison methodology would be probing the same region of the same sample with and without the front contact. However, given the micrometric excitation spot size, this can be quite challenging. In addition, we remind that in our bibliographical analysis on time-resolved techniques, we discussed the effect of the electric field on time-resolved luminescence decays and concluded that even under very low injection regimes, it only influences the carrier dynamics within the first picoseconds of the luminescence decay. This section is consequently another way of confirming the latter findings.

On the previously mentioned CIGS samples, we perform excitation power-dependent TRPL. For each decay and for each sample, we start by extracting the trapping and recombination lifetimes. These parameters as then plotted as a function of the incident photon flux in the absence and presence of the ZnO front contact layer:

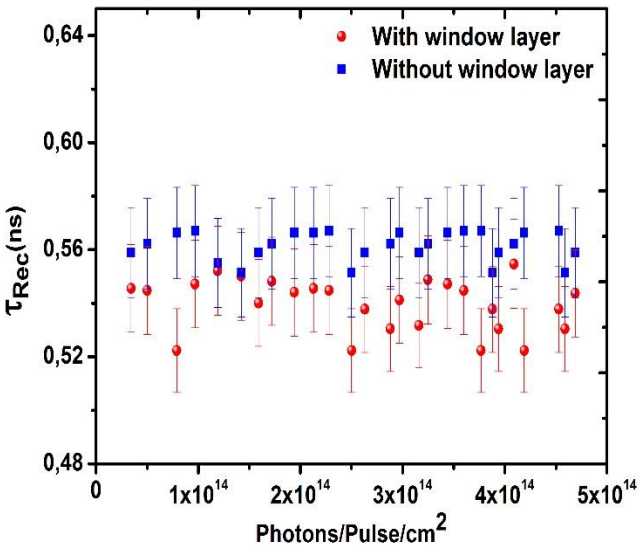



**Figure 3.4.a: Evolution of the recombination lifetime as a function of the incident photo-excitation flux in the presence and the absence of the window layer**

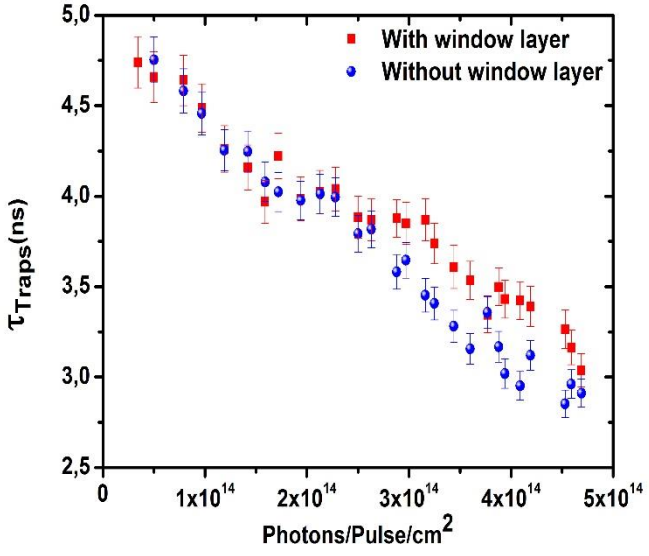



**Figure 3.4.b: Evolution of the trapping lifetime as a function of the incident photo-excitation flux in the presence and the absence of the window layer**

Based on previous bibliographical analysis, the photo-excitation regime used here and in the earlier experiments is considered as moderate. This means that, in case the electric field exists, it is more likely to be completely screened by the photo-generation. This is confirmed by Figure 3.4.a and 3.4.b where the recombination and trapping lifetimes exhibited on the one hand closely comparable values and the other hand, they evolved in the same way whilst the incident photo-excitation flux is increased. Their behavior remain consistent with our previous findings, where the recombination lifetime is constant and the trapping lifetime continues to decrease as the photogeneration-to-accessible traps density ratio continues to increase.

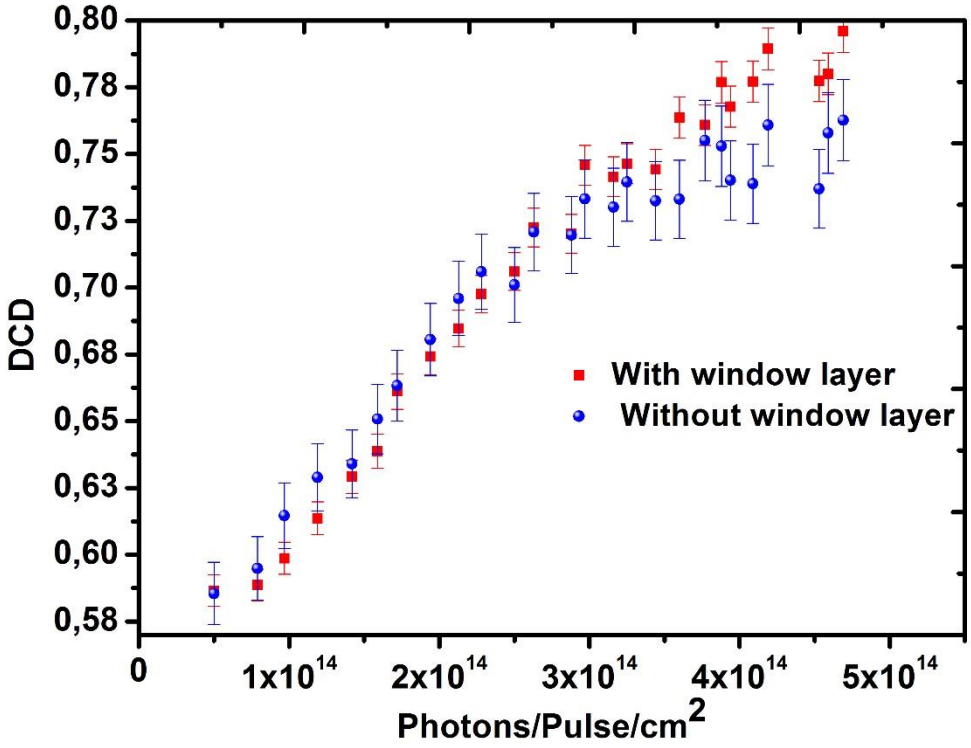



**Figure 3.5: Evolution of the *DCD* parameter as a function of the incident photo-excitation flux in the presence and the absence of the front contact**

As predicted by the two earlier plots, the *DCD* parameter further confirms the absent influence of the electric field on the dynamics of the time-resolved photoluminescence decays. In both cases, we obtain the usual convergence of the DCD toward unity as the incident photo-excitation flux is increased, predicted by the previous mutual decrease of the trapping lifetime.

We can conclude so far that the absence or the presence of the TCO front contact layer/electric field do not have an influence neither on our discussions nor the expected behavior of the probed carrier dynamics.

### 3.2.5 Identifying the characteristics of probed carrier recombination

We have so far attributed the first part of the fast luminescence decay to recombination events and extracted what we considered as minority carrier recombination lifetime and the corresponding occurrence weight of recombination events. In this section we aim to analyze the recombination type of carrier: bimolecular or Auger recombination. We also aim at identifying the radiative recombination events that are behind the time-resolved luminescence intensity. Accessing this information would provide a more complete picture of the knowledge we developed on minority carrier dynamics in CIGS solar devices.

The overall recombination net rate $R_n$ describing the temporal evolution of the excess minority carriers can be expressed as:

$$R_n = An + Bn^2 + Cn^3 \tag{3.3}$$

As expressed by equation (3.3), $R_n$ is composed of three recombination regimes that are: Auger-type recombination involving three particles, bimolecular recombination involving two particles and finally a mono-molecular regime involving a single particle.

Given that the time-resolved luminescence signal is the result of $R_n$, one must evaluate the time-derivative of the time-resolved luminescence signal and plot it as a function of the TRL signal itself, in order to identify the dominating recombination regime.

Therefore, what we will evaluating and plotting in this case is: $\frac{\partial I_{TRL}(t)}{\partial t} = f(I_{TRL}(t))$

Starting with, $I_{TRL} \propto np \propto n^2$ then,

$$\frac{\partial n}{\partial t} = R_n \propto A\sqrt{I_{TRL}} + BI_{TRL} + CI_{TRL}^{\frac{3}{2}}$$

Which yields:

$$\frac{\partial I_{TRL}}{\partial t} \propto 2\frac{\partial n}{\partial t} \propto 2n^2\left(A + Bn + Cn^2\right)$$

$$\Rightarrow \frac{\partial I_{TRL}}{\partial t} \propto 2\sqrt{I_{TRL}}\left(A\sqrt{I_{TRL}} + BI_{TRL} + CI_{TRL}^{\frac{3}{2}}\right)$$

$$Finally \Rightarrow \frac{\partial I_{TRL}}{\partial t} \propto AI_{TRL} + BI_{TRL}^{\frac{3}{2}} + CI_{TRL}^{2}$$

Therefore, if a linear dependence is observed regarding the initial fast decay, than the latter is characterized by a mono-molecular type of recombination.

This dependence is evaluated for the two experimental sets of time-resolved decay under an increasing optical and electrical injection, respectively:

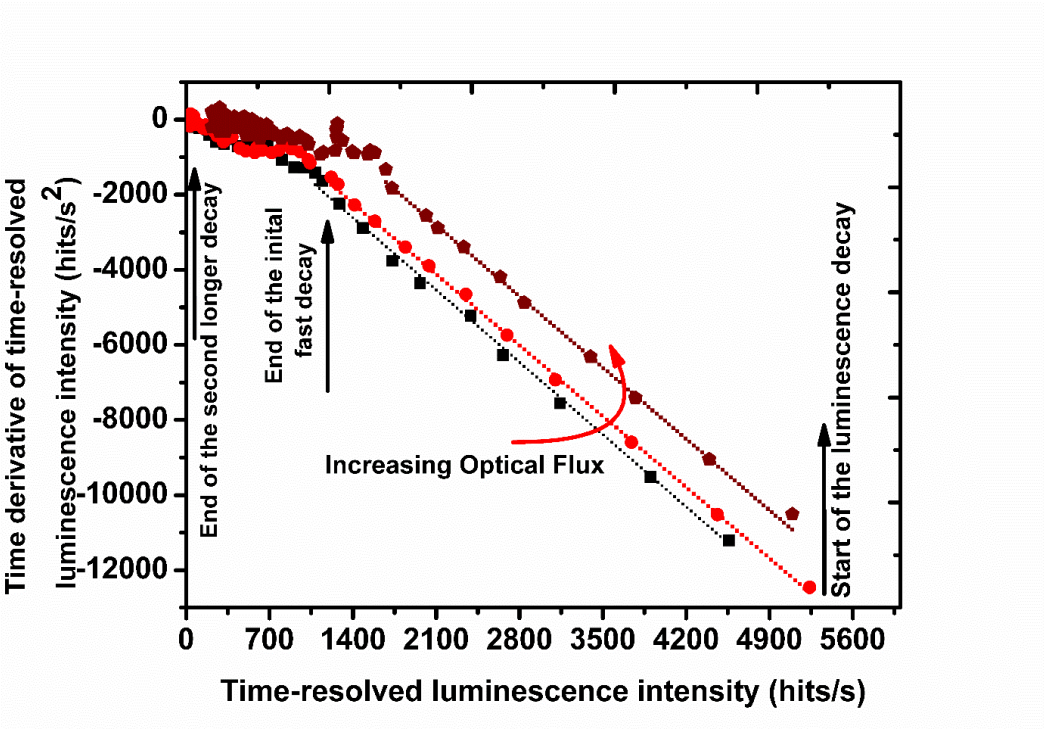



**Figure 3.6: Identifying the carrier recombination type for the photo-excitation dependent time-resolved photoluminescence decays**

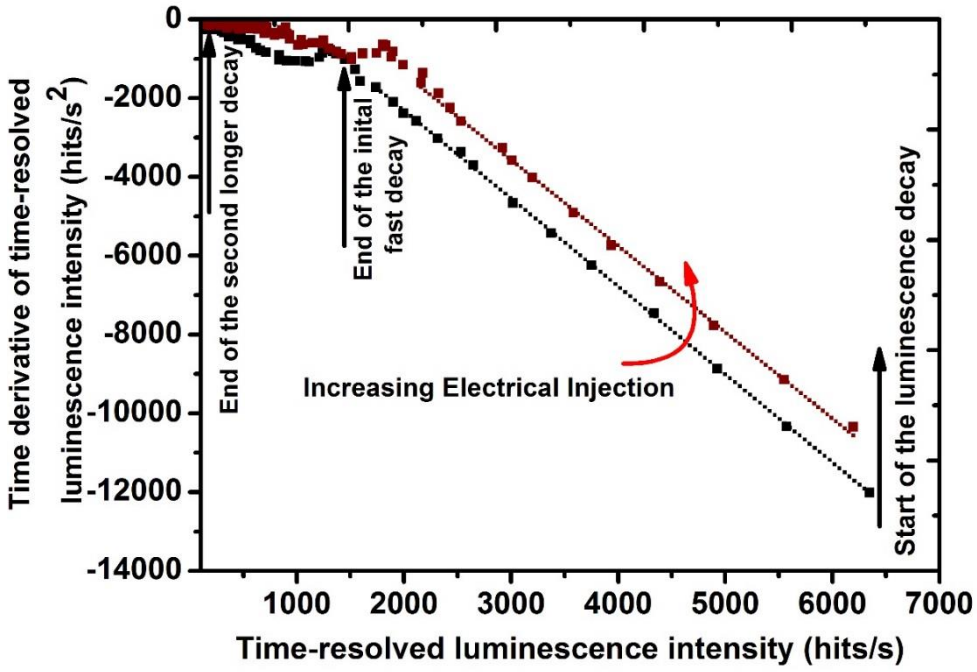



**Figure 3.7: Identifying the carrier recombination type for the current-injection dependent time-resolved luminescence decays**

For both experimental sets, we selected the decays corresponding to the lowest and highest photo and electrical excitations. Once the decays are selected, we focus on the region of the overall luminescence decay corresponding to the initial fast one. Then, a linear fit is applied. We can see from Figure 3.6 and Figure 3.7 that, for the initial fast part of all the decays, $\frac{\partial I_{TRL}(t)}{\partial t} = f(I_{TRL}(t))$ exhibits a clear linear behavior. This means that, for all of the chosen ranges of optical and electrical injection intensities, the short carrier lifetime does indeed corresponds to a mono-molecular-type of recombination that involves a single particle. In addition, we can also see that in both cases, the slopes of the linear tendencies are indeed parallel which confirms once again that in the early nanoseconds of the decay, the recombination lifetime and the decay dynamics are constant. Finally, from a qualitative point of view, one may think that the initial fast part of the decay may seem to represent a small portion of the overall decay in a normal $I_{TRL}(t)$ curve as a function of time (Figures 3.2.a and 3.3.a). However the new representation of $\frac{\partial I_{TRL}(t)}{\partial t} = f(I_{TRL}(t))$ seen in Figures 3.6 and 3.7, shows that large majority of the excess carriers do decay in the early nanoseconds of the overall. This makes the initial fast part of $I_{TRL}(t)$ important and valuable for the analysis of the minority carrier dynamics. Based on this observation; we remind that in the literature the fast decaying part is sometimes neglected [96,105]. Here on the contrary, we show that

it is indeed crucial for the analysis that would be otherwise, based only on only a small portion of the initially generated excess minority carriers.

Now, we move on to identifying the dominant source of radiative recombination that is behind the luminescence intensity. While the latter are highly dominated by non-radiative recombinations in a CIGS material, we find it interesting to also characterize the source of radiative recombination.

The literature [109] shows that in order to able to identify the dominant source of radiative recombination, one can perform two different consecutive studies on the resulting PL spectrums. These two studies consist in initially examining the PL spectral shift, and the intensity peak of the PL spectrums as the excitation power is being varied, and the next study illustrates the evolution of the value of the PL yield as a function of the varying incident excitation power.

First of all, using the range of photo-excitation fluxes used in Figure 3.2.a, we acquired the PL spectra at room temperature. As we tend to increase the excitation power, we directly increase the injection level in a way that the conduction band becomes increasingly populated by a greater pumping rate of photogenerated election all the way from the valence band.

Under such conditions, radiative recombinations occur at a much higher rate and thus the emerging PL flux becomes more and more intense. In our case, we found that peak emission wavelength remains constant at 1095 *nm*. Ref [109] proposes two methods in order to identify the dominant recombination regime and more particularly, the two methods consist in the determination of the two parameters "β" and "*k*" respectively. β is actually the slope of the variation of the position of the peak PL intensity in meV as a function of the excitation power. In case β ≈0 meV/decade that means that the dominant radiative recombination regime behind the resulting PL flux is a "Band-to-Band" recombination regime, else, it is a "DAP" , a *Donor-Acceptor Pair* recombination regime.

Our spectra lead to a value of β ≈0 and we can initially deduce that the dominant source of radiative recombination is a "Band-to-Band" radiative recombination regime.

As for the second method that consists in the calculation of "*k*", Ref [109] shows that, the resulting PL yield $Y_{PL}$ is related to the excitation power through: $Y_{PL}=\phi^k$, where ϕ is the excitation power. It shows also that for the values found of k ranging between $k$=1 and $k$=2, this would mean that the radiative source is "Band-to-Band" recombinations.

In our case, we plotted the obtained PL yield as a function of ϕ and the result is shown in Figure 3.8:

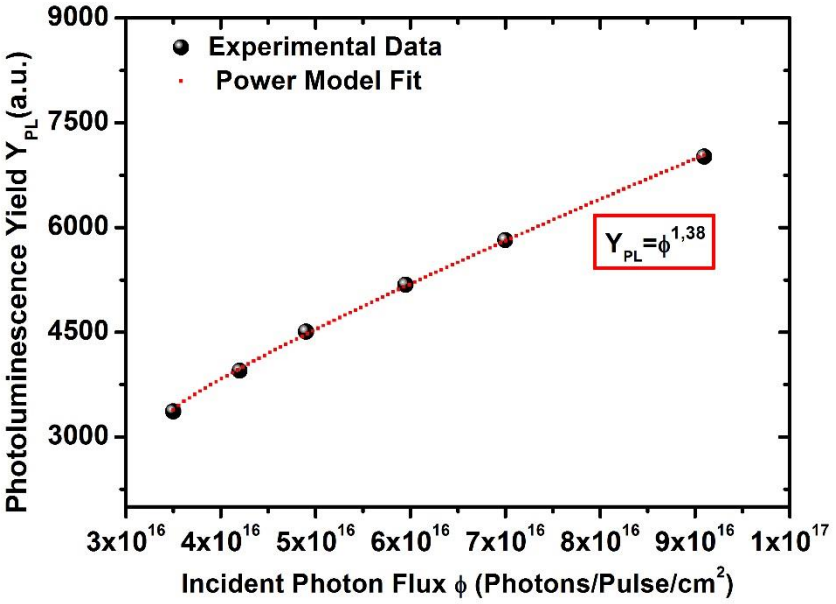



**Figure 3.8: Photoluminescence yield as a function of the incident photo-excitation flux**

We can see that the mathematical power model fit we used yielded a value of $k$ , $k$=1.3819. Such a result confirms furthermore the fact that our dominant source of radiative recombination is characterized by a "Band-to-Band" recombination regime.

The combined values of β and $k$ strongly confirm this conclusion.

### 3.2.6 Brief summary and conclusion

In *Section 3.2* of the current chapter, we demonstrated the importance of a complete, coherent understanding of the characteristics of a TRPL decay. The short decay lifetime is shown to be related to direct, mono-molecular recombination events. Through power dependent PL spectra analysis we prove that band-to-band recombination is the radiative recombination source of the detected luminescence intensity. Whereas the second, longer decay lifetime is attributed to the trapping effect of shallow defect states. We also demonstrated the importance of investigating the evolution of occurrence weights of the events characterized by both decay lifetimes, which led to the definition of a new key parameter, the *DCD*. A methodology is established for the application of the time-resolved luminescence characterization technique either under optical or electrical carrier injection. We show that regardless of the excitation source, the carrier dynamics of a CIGS solar cell exhibit the same behavior. We prove that the similarity arises from a decreasing influence of the material trap states on the overall carrier dynamics. Under electrical carrier injection, it is the progressive occupation of the available trap states that attenuates their effect. Under optical excitation however, it is the photogeneration of carriers that is increased. This consequently amplifies the dominance of excess carriers over the accessible trap states.

## 3.3 Optical alternative for the study of metastabilities in $Cu(In,Ga)Se_2$ PV devices

One of the signature traits of $Cu(In,Ga)Se_2$ solar cells is the fluctuations in its photovoltaic performance, following the activation of metastable defects by applying a voltage and/or light bias [109-112]. The chemical nature of these metastabilities and their effects have been thoroughly investigated by means of electrical characterization such as photo-capacitance, deep level optical spectroscopy, and admittance spectroscopy measurements [113][114] or by using electroluminescence[115].

In the present section, and based on all of the above understanding of carrier dynamics in CIGS PV devices, we develop a contactless optical alternative for the study of these metastabilities.

The methodology is based on the analysis of excitation energy-dependent time-resolved photoluminescence (TRPL) signals. It leads to the observation of a hysteresis phenomenon. The amplitude of this phenomenon was compared between CIGS solar cells with different absorber/buffer layer interface properties. The developed characterization method was compared with classical current-voltage measurements. We prove that this new application of TRPL techniques provides a reliable understanding of the physics of metastable defects in terms of quantifying the shift in minority charge carriers dynamics that it induces.

### 3.3.1 Metastabilities-induced distortions of Current-Voltage characteristics

Distortion to current – voltage curves have been commonly reported in CIS or CIGS solar cells with a variety of buffer layers, such as CBD CdS, ZnS(O,OH), and InS(O,OH) [117, 118, 119].

In general, the J-V distortion in CIGS can be divided into J-V crossover and J-V red kink, as seen in Figure 3.9 taken from Ref[120]. The J-V crossover refers to a failure of dark/light superposition of their current-voltage curves whereas the J-V red kink refers to the distortion of J-V curves under only long-wavelength-photon illumination (>610 nm) at initial forward bias. Researchers [117-119] have investigated the physical mechanism of these J-V distortions on the traditional CdS – CIGS solar cells, and their models suggests that such J-V distortions are due to the conduction band secondary barrier at the buffer layer-absorber interface.

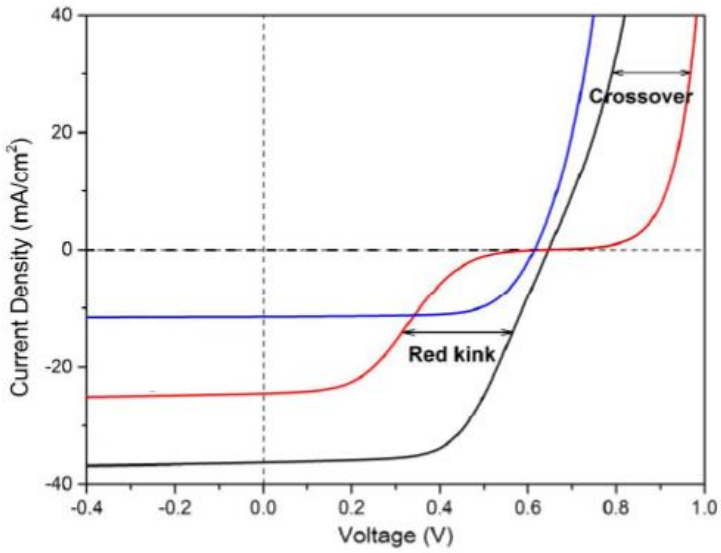



**Figure 3.9: J-V distortion of in a CIGS solar cell [120]**

For the crossover distortion, we can see that to achieve the same amount of current density at forward bias, the dark curve needs to consume more voltage compared to the light curve.

Experimentally, the J-V crossover has been chemically associated with the different recipes in cell fabrication, such as varying oxygen content and indium doping in the buffer. The measurement of doping density of the buffer is a challenging task and it is difficult to immediately tell the accuracy of their results. So the challenge remaining is how to explain and identify the experimental J-V crossover with the unknown change doping densities of Zn(O,S) layers in our cells. That's where studies usually refer to numerical simulations, to correlate these parameters to the observed crossover[122].

Whereas for kinked J-V curve under red-light illumination in CIGS solar cells, we can see that at reverse or small forward voltage bias, the cell has well-behaved current collection proportional to the J-V curve under white-light illumination. At forward bias between 0.2 V to Voc, it shows an impeded current collection, called "red kink", and at forward bias above Voc until 0.8 V the red-light J-V curve overlaps with the dark one.

It has been found that the J-V red kinks varies with different recipes, such as varying oxygen fraction in the sputter beam and substitution of non-In-doped ZnS target with In-doped ZnS target. The device-physics question is how to relate these experimental J-V red kinks to CBO (conduction band offset) and doping density. Numerical simulation allows investigating the J-V red kinks with varying oxygen fraction in the sputter beam and In-doped or not.

In addition the effect of blue photon exposure time has been found to be crucial for the elimination of the J-V red kink. As seen in Figure 3.17, Ref [120] illustrates the initial red light J-V as a function of

white-light exposure time. The red-light curve prior to any white-light exposure was the most distorted. The curves gradually shifted towards the well-behaved light J-V curve with increasing time of white-light exposure. Therefore, this light exposure demonstrates a "healing" effect where the kink diminishes progressively with the exposure time.

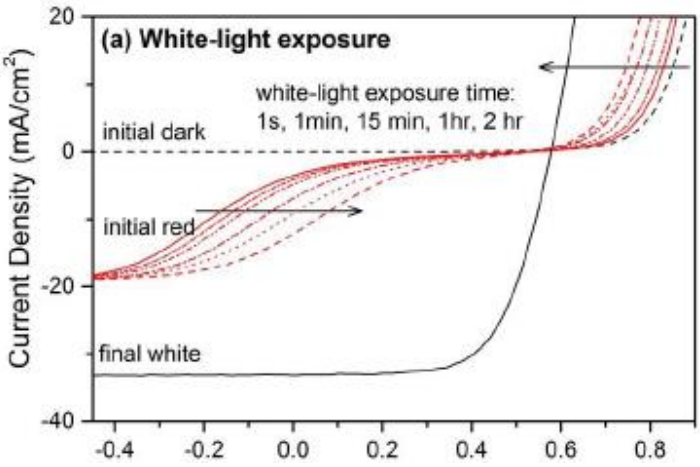



**Figure 3.10: Effect of white light-exposure on J-V distortions [120]**

### 3.3.2 Optical evidence of the effect of metastabilities activation on minority carrier dynamics

#### 3.3.2.1 Introduction & Methodology

We learned from the previous section that by varying the wavelength of the excitation light from red to blue, it is possible to modulate the effect of metastabilities on the electrical performance of CIGS solar cells. In this section of the thesis, we attempt to alter the properties of the CIGS device by optically probing the effect of the interface metastabilities. What we propose is excitation energy-dependent time-resolved photoluminescence experiments where the CIGS sample will be excited by a range of wavelengths including red and blue light. The strategy is to closely monitor any significant change in the behavior of the TRPL decays as the excitation energy is increased. We know that in order to activate the interface metastabilities, an excitation energy between 2 eV and 2.4 eV (gap of the CdS buffer layer) is needed. Particular attention will be paid for the TRPL decay for these high excitation energies.

Two CIGS solar cells were fabricated for this study. Both samples have the same absorber properties, however, one absorber has been preserved under vacuum before deposition of its CdS layer, whereas the second absorber was exposed to air during 48 hours prior to the deposition of the CdS layer. Therefore, the difference between the behaviors of the samples investigated in the present work is expected to originate from the CdS/CIGS interface.

Once activated, using short excitation wavelengths, these defects directly induce important variations in the solar cell performances [121][122].

Basic J(V) characterization under one Sun excitation was carried out using the solar simulator. It enabled a preliminary verification of the degradation that occurred within the second sample absorber surface and CIGS/CdS interface.

Then, two sets of TRPL decays acquisitions were made on each sample:
The first set consists of exciting the sample starting with an 850 *nm* excitation followed by lower excitation wavelength values with a step of 50 *nm* until a 450 *nm* excitation wavelength is reached. The changing time of the different excitation wavelengths is equal to 10 seconds. For each excitation wavelength, a TRPL decay is acquired. This set will be referred to as Set 1.

The second set of TRPL decays acquisitions immediately follows the first set with a reversed order of excitation wavelengths. The sample is therefore initially excited using a 450 *nm* excitation wavelength followed by higher wavelength excitations until an 850 *nm* wavelength excitation is reached. This set will be referred to as Set 2.

The purpose behind this experimental procedure is that using a wide range of excitation wavelengths progressively probes the carrier dynamics within the CIGS absorber surface, as well as the CIGS/CdS interface and a portion of the CdS itself.

In order for the interpretations not to be a function of the incident excitation power but only a function of the localization and the density of the metastabilities, the two sets of experiments were carried out while maintaining a fixed incident photon excitation flux at $1.4\text{x}10^{15}$ *photons/pulse/cm*$^2$.

Now that the problem has been positioned, the work can consequently extend to the study of the behavior of minority carrier dynamics following the activation of metastabilities in CIGS solar cells.

#### 3.3.2.2 Basic Characterization

From the corresponding dark J(V) curves, the dark saturation currents $J_{01}$ and $J_{02}$ were extracted for both samples and compared by fitting the two-diode model equation:

$$J = j_{01}\left[\exp\left(\frac{qV}{kT}\right)-1\right] + j_{02}\left[\exp\left(\frac{qV}{2kT}\right)-1\right] \tag{3.4}$$

In Table 3.1, the photovoltaic parameters of the two samples are presented.

| | **Preserved Sample (Sample 1)** | **Air exposed Sample (Sample 2)** |
|---|---|---|
| **$V_{oc}$** | **0.701 V** | **0.42 V** |
| **$J_{sc}$** | **30 mA/cm$^2$** | **18 mA/cm$^2$** |

| | | |
|---|---|---|
| **FF** | **75.6 %** | **60.4 %** |
| **Efficiency η** | **15.9%** | **4.57 %** |
| **$J_{01}$** | **$4.557x10^{-16}$ A** | **$5.842x10^{-16}$ A** |
| **$J_{02}$** | **$3.468x10^{-10}$ A** | **$1.482x10^{-8}$ A** |
| **Light-Dark J(V) crossover** | **Weak crossover** | **Important crossover** |

**Table 3.1: Comparison of the samples performance parameters**

The performance degradation of the sample whose absorber has been air-exposed can be clearly noticed. It actually affected every major performance parameter leading to a significant drop in the cell power conversion efficiency.

By examining the values of the dark saturation currents $J_{01}$ and $J_{02}$, one can observe that the values of $J_{01}$ are close in both cases. On the contrary, the air-exposed sample exhibited a value of $J_{02}$ two orders of magnitude higher than the preserved sample. $J_{02}$ is typically related to the quality of the absorber surface and the space-charge region (depending on whether the Fermi level is pinned or not), whereas the first saturation current $J_{01}$ is generally linked to the performance and properties of the absorber bulk [123]. This is coherent as the degradation is not expected to be localized in the quasi neutral region.

A further investigation indicates that in the case of the air-exposed sample an important crossover between its dark and light J(V) curves exists , whereas in the case of the sample that has been preserved under vacuum conditions, these curves exhibited a less pronounced crossover, close to superposition. It has already been shown that a crossover between a solar cell dark and light J(V) curves can be linked to a significant defects density located at the absorber/CdS interface [123]. Such observation supports the hypothesis regarding the localization of the degradation at the surface of the air-exposed sample.

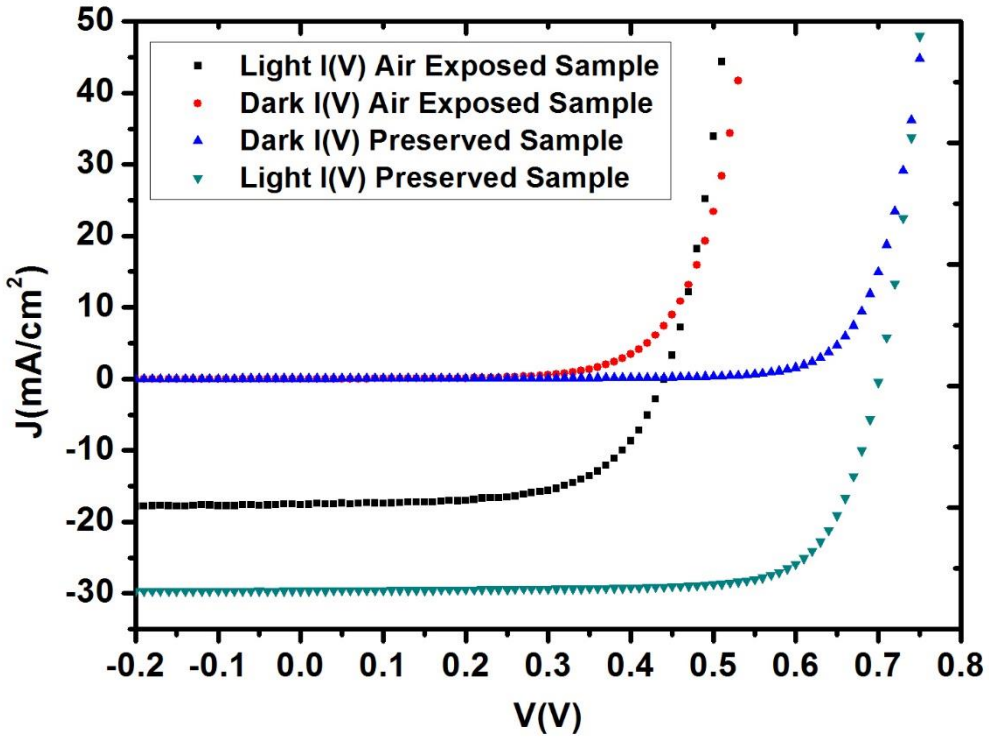



**Figure 3.11: J (V) characterization of the studied samples under dark and illuminated conditions**

### 3.3.2.3 Qualitative optical observation of a blue photon recovery effect

At this stage, a first description of the wavelength-dependence of the TRPL decays can be made. In Figure 3.12 the TRPL decays are presented for 850 *nm* and 450 *nm* excitation wavelengths. A work published by Alonso *et al*. in Ref[124] provided the optical properties of $CuGa_xIn_{1-x}Se_2$ alloys. The corresponding absorption coefficients $\alpha(\lambda)$ were found to be equal to $\alpha(\lambda = 850) = 4.71x10^4\, cm^{-1}$ and $\alpha(\lambda = 450) = 2.37x10^5\, cm^{-1}$. Consequently, the penetration depth $\Gamma(\lambda) = \frac{1}{\alpha(\lambda)}$ approximately varies from $\Gamma(\lambda = 850) = 212\, nm$ to $\Gamma(\lambda = 450) = 42$ *nm*. The resulting penetration depths are significantly smaller than the absorber thickness and are contained within the space charge region.

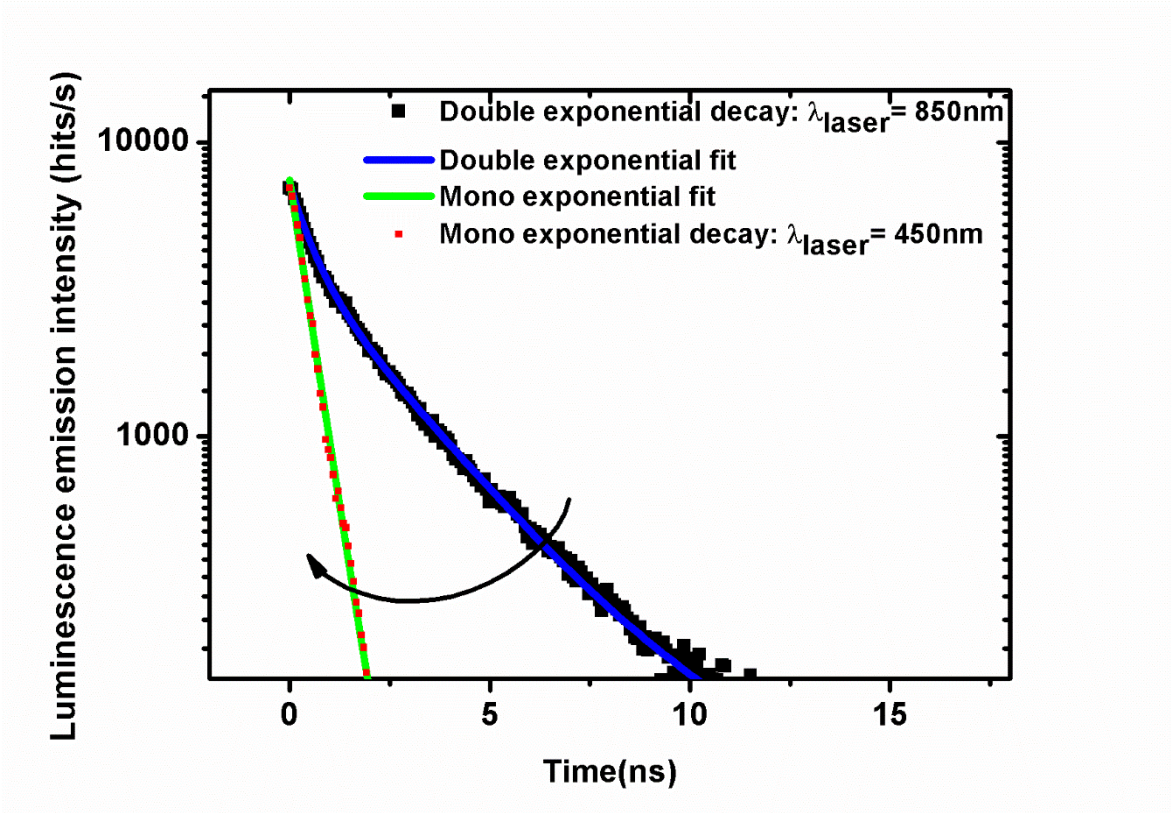



**Figure 3.12: Evolution of the TRPL decay behavior under a decreasing value of excitation wavelength**

The corresponding decays exhibit a transition from a double exponential behavior to a mono exponential behavior when the excitation wavelength is reduced from 850 *nm* to 450 *nm*.

The decays presented in Figure 3.12 are a first indication regarding the effect of the defects activation on the minority carrier dynamics: As the excitation wavelengths get shorter, the activation of interface defects becomes dominant. By the time the 450 *nm* excitation is reached, the probed defects become saturated by optical means of excitation.

Consequently a transition from a double to a mono exponential decay is observed. The short decay persists and the longer decay disappears. The latter no longer influences the minority carrier dynamics.

If we are to establish an analogy to the electrical signature of metastabilities activation on the distortion of J-V curves, we should remind that exposure to high energy photons is known as the blue photon recovery effect. The latter is found to eliminate the distortion of the J-V curves.

In the case of the present thesis, we can see that the use of high energy blue photons, i.e. 450 *nm* wavelength, eliminated the second longer part of the decay. Given that we attributed the latter to interface trapping defects, this confirms that Figure 3.12 is the equivalent of an optical blue photon recovery effect and an alternative for the electrical effect where blue photon exposure eliminates the J-V curve distortion.

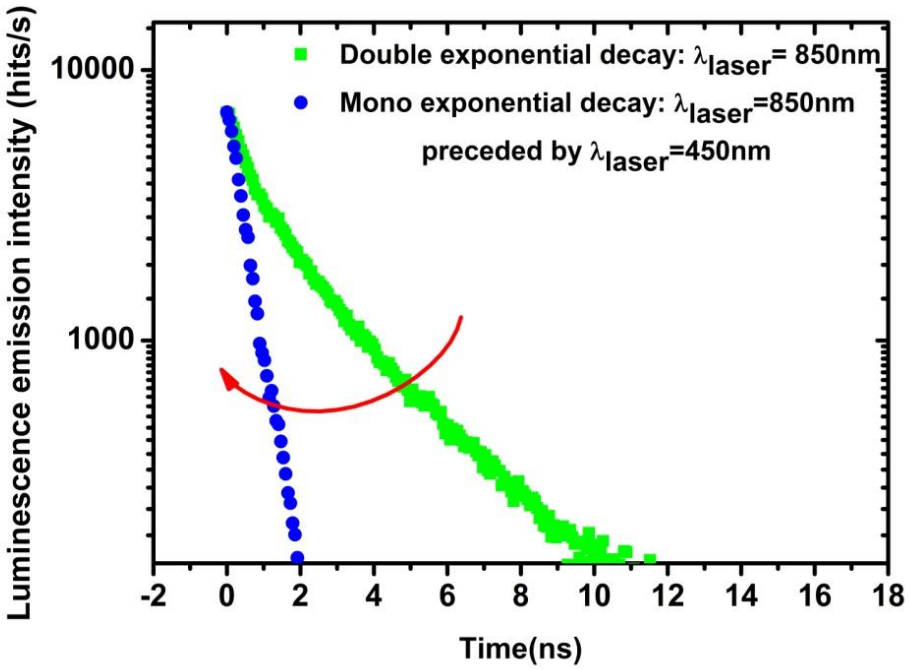



**Figure 3.13: Different dynamics of the TRPL decay under the same excitation wavelength**

In order to prove that these trapping defects are indeed metastable and that our finding are compatible with an optical blue photon recovery effect, we excited the sample using an 850 *nm* wavelength directly after the 450 *nm* that lead to the transition to the mono-exponential decay in Figure 3.12. Interestingly, we can see that even though the same excitation wavelength is used, the 850 *nm* leads to a double exponential decay in Figure 3.12 and a mono exponential decay in Figure 3.13. We can therefore explain this phenomenon by an optical blue photon recovery effect. The blue light eliminated the effect of trapping defects that play the role of absorber/buffer layer interface metastabilities.

#### 3.3.2.4 Hysteresis cycle of the "DCD" parameter

In order to obtain a deeper insight on the observed shift in the minority carrier dynamics, the evolution of the *DCD* parameter is plotted for both samples and for both Set 1 and Set 2, as a function of the excitation energy.

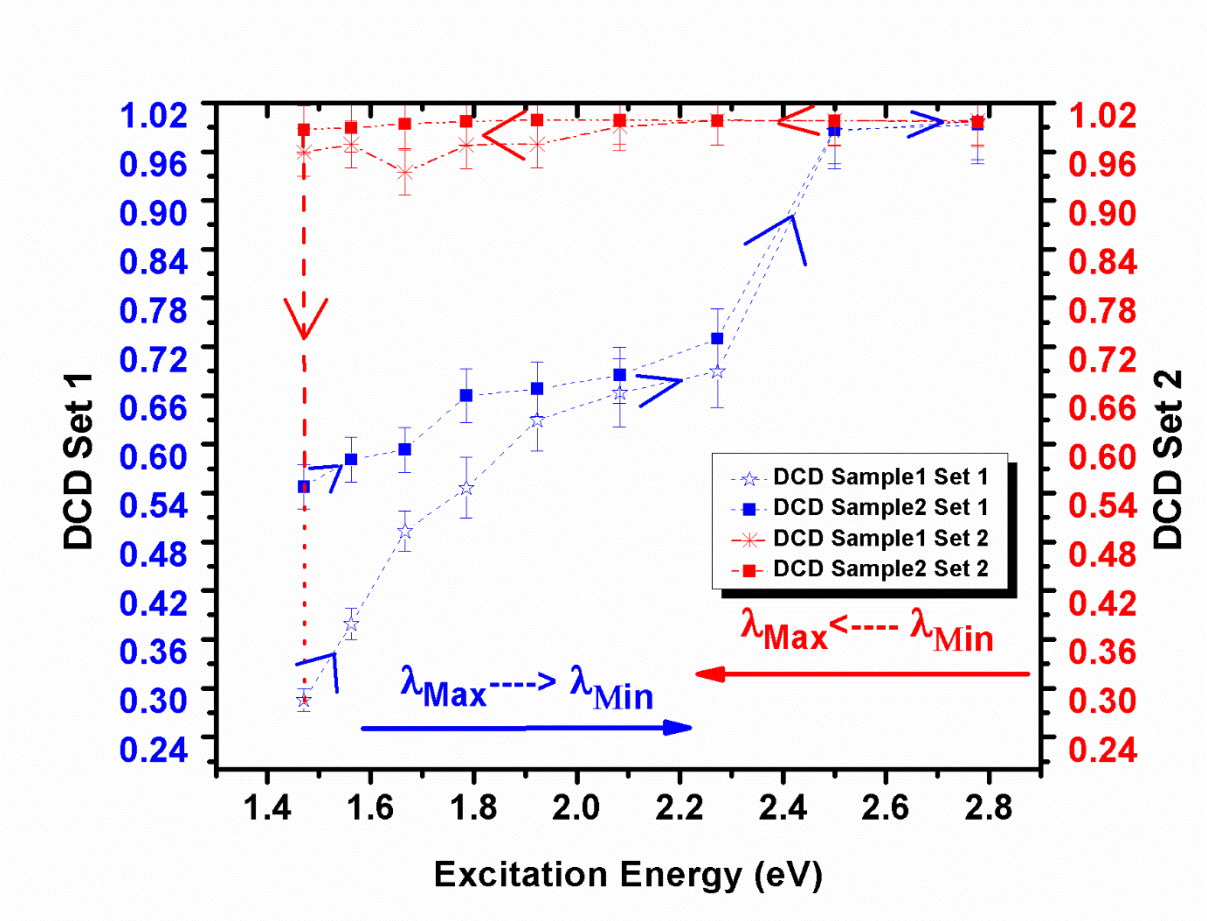



**Figure 3.14: Evolution of the DCD parameter for both of the TRPL acquisition sets**

As the excitation energy is increased, it can be seen that for both samples, the DCD parameter tends to converge towards unity. It can be interpreted as defects becoming activated and increasingly "filled" by optical means. When DCD tends to unity, recombination centers-related events are predominant over the non-radiative trapping events. This corresponds to the measured mono exponential decay.

Another feature regarding the convergence of the DCD parameter is the fact that, for both studied solar cells, a sudden increase of the DCD value is obtained when the excitation energy becomes greater than 2.3 eV. This is related to the bandgap energy of the CdS buffer layer that is equal to 2.4 eV. This eventually reflects the importance of the effect of interface metastabilities on the photogenerated minority carrier dynamics.

The sudden transition of the DCD towards unity at 2.3 eV, is a direct indication of an activation of the underlying buffer layer metastabilities. Such effect has been observed under blue-light illumination using electrical measurements such as admittance spectroscopy and capacitance-voltage profiling [125]. Sub Gap Modulated Photo-Current Spectroscopy [126] has also been used for investigating the metastabilities of alternative buffer layers and its behavior under thermal annealing and light soaking. In comparison with these electrical studies, the main advantage of the presented work is that it offers a contactless optical alternative for the study of these metastabilities. It provides crucial information such

as the quantification of the evolution of minority carrier dynamics following metastable defects activation.

Finally, according to the second experimental set of acquisitions, a complete activation and saturation of the interface defects induced a hysteresis cycle of the DCD parameter in both samples. In fact, it can be noticed that the value of the DCD parameter becomes independent of the excitation energy as the interface and surface defects remain activated (DCD $\geq$ 0.95). The underlying dynamics are still governed by direct recombination events. This is not the case of recombination centers whose signature of the TRPL decay is constant, irrespective of the excitation wavelengths.

#### 3.3.2.5 Hysteresis cycle of the carrier trapping lifetime

As previously mentioned, two minority carrier lifetimes are extracted in the case of a double exponential decay: $\tau_{\mathrm{Rec}}$ & $\tau_{Traps}$. The evolution of the extracted lifetimes is represented for both samples in Figure 3.15:

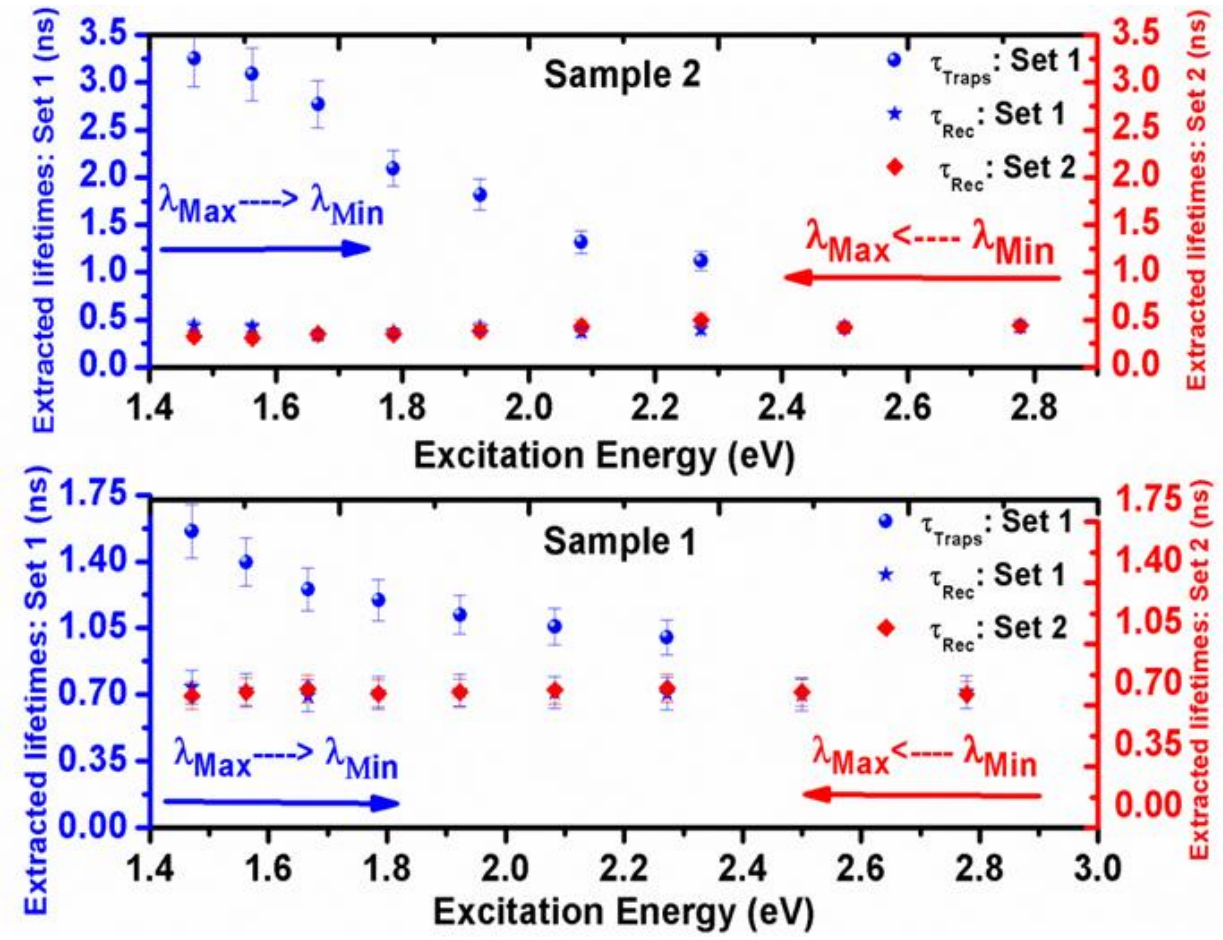



**Figure 3.15: Evolution of the minority carrier lifetime as a function of the excitation energy and for the two experimental sets and for both Sample 1 (up) and Sample 2 (down)**

The corresponding minority carrier recombination lifetime $\tau_{\mathrm{Rec}}$ exhibits a uniform behavior characterized by constant lifetime values. This is evidence that $\tau_{\mathrm{Rec}}$ characterizes direct band-to-band recombination events that are not influenced by the value of the excitation energy as long as the latter is greater than the bandgap energy. It can also be seen that Sample 1 exhibited higher values of $\tau_{\mathrm{Rec}}$ in comparison with Sample 2: $\overline{\left(\frac{\tau_{Rec1}}{\tau_{Rec2}}\right)} = 2.01 \pm 0.13$. This validates the nature of this short decay lifetime and consequently highlights its potential in detecting a better minority carrier dynamics quality, hence, a better material quality.

Furthermore, the analysis of $\tau_{Traps}$ grants access to more information regarding the performance shift under defects activation. As the incident energy becomes comparable to 2.4 $eV$ which represents the energy required to activate the CIGS/CdS interface, a decrease in the value of $\tau_{Traps}$ is observed. Such evolution is mirrored by the decrease in the occurrence weight (DCD ratio) of trap-related emission events. As the excitation energy is increased, interface traps with higher energy levels are being activated, inducing a continuous decrease of its overall occurrence weight and inactive density. Consequently, their induced delay becomes increasingly weaker, which finally explains the observed decrease in $\tau_{Traps}$.

Once the excitation energy of 2.3 $eV$ is surpassed, the weight of events characterized by $\tau_{Traps}$ decreases to the point where the TRPL decay becomes mono exponential. Thus, it is impossible to extract values of $\tau_{Traps}$. This is why for E>2.3 $eV$ no points for $\tau_{Traps}$ exist in Figure 3.15. It is to be reminded that for this particular excitation energy that the sudden shift of the DCD towards unity was obtained.

Across all of the excitation energies, lower values of $\tau_{Traps}$ are obtained for Sample 2 with the preserved absorber compared to the values obtained for Sample 1 with the air-exposed absorber. This is an additional proof regarding the nature of the events characterized by $\tau_{Traps}$, the latter being proportional to the shallow trap states density.

#### 3.3.2.6 Brief Conclusion

We established a methodology in this section that offered a new application of time-resolved photoluminescence techniques. We prove that the latter can be an efficient characterization tool for the understanding of the physics of metastable defects activation and its effect on the minority carrier dynamics of a particular CIGS solar cell. This effect is shown in this study by an underlying hysteresis phenomenon regarding the minority carrier dynamics following the activation of the metastabilities. For instance, this contactless characterization method is used as a comparative technique between different

PV performances by examining the amplitude of the defects activation on the solar cell minority carrier dynamics. This new application also created an optical version of the well-known blue photon recovery effect.

## 3.4 Contactless quantification of trapping defects density in Cu(In,Ga)$Se_2$ PV devices

If we follow the thesis methodology so far, we can see that we started by laying out the fundamentals for an accurate comprehension of the minority carrier dynamics in CIGS PV devices that are revealed by the time-resolved luminescence experiments. The effect of trapping defects has been experimentally elaborated and discussed in the first section of this chapter. This paved the way for us to develop a new application of time-resolved luminescence techniques and demonstrate its capacity to be an optical alternative for the classical electrical studies of metastabilities in CIGS solar cells.

In this part of the thesis, we will take things further, as we will develop and reveal a much more important aspect of time-resolved luminescence of CIGS devices. What we will be aiming at is a further theoretical and experimental development of this characterization method so it can result in a quantitative analysis of the investigated device. More precisely, we will demonstrate in this section, how to quantify the PV device trapping defects density by analyzing its time-resolved luminescence decay, regardless of the experimental conditions. This is achieved by probing time resolved photoluminescence and numerically reconstructing the experimental decays of Figures 3.6.a, 3.7.a & 3.19 that were obtained by either varying the photo-excitation power, the injected current or the photo-excitation energy.

We will ultimately reveal a direct link between the PV performance of the investigated device and its trapping defects density values that is extracted using our developed method. This link will amplify the importance of the work that will be proven to be a reliable and quantitative PV performance indicator.

### 3.4.1 Development of a physical model for the reconstruction of the time-resolved luminescence decays

We start by a establishing a system of differential rate equations that describes the dynamics of the different populations that are behind the experimentally observed time-resolved luminescence decays. All of the parameters used to solve this system are actual experimental data. Then, an optimization procedure is used in order to reconstruct the experimental TRL decay and extract the system trap states density.

The first parameter taken into consideration is the experimental charge carriers' photogeneration. Experimentally, a laser pulse is used in order to induce the photogeneration. Therefore, in order to replicate the experimental excitation conditions of $3.5 \times 10^{16}$ *Photons/Pulse/cm*$^2$ delivered within a 6 ps pulse width, the following function is used:

$$P(t) = \frac{P_0}{\left(\cosh\left(\frac{t}{\tau_p}\right)\right)^2} \quad (3.5)$$

P(t) is the laser pulse temporal profile , $P_0$ is the actual peak power which is equal to 23.5 $mW$, $\tau_p$ is the laser pulse width which is equal to 6 ps.

From the laser pulse temporal profile, we deduce the temporal profile of the incident photon flux $\phi$ using:

$\phi(t) = \frac{\lambda P(t)}{hc}$, with λ the excitation wavelength.

Three different populations of states are defined here: $N_1$, $N_2$ and $N_3$. $N_1$ is the population occupying the valence band, $N_3$ is the population occupying the conduction band and $N_2$ is the population occupying the accessible shallow trap states. The densities of accessible states with the CB and the VB are considered as infinite reservoirs compared to that of the shallow traps which we denote here as $\Psi_D$ and aim to determine its value.

In order to describe the dynamics behind the experimental decays, the system considers three different types of events: Firstly, direct carrier recombination events, such as SRH and band-to-band recombination. The corresponding lifetime $\tau_{Rec}$ is extracted from the initial fast part of the experimental time-resolved photoluminescence decay. The second and third type of events will be related to the existence of the shallow trap states. In particular, traps capture charge carriers and then emit them by means of thermal activation. Consequently, a capture lifetime $\tau_{Cap}$ and an emission lifetime $\tau_{em}$ are defined. Experimentally, the identified long lifetime $\tau_{Traps}$ that has been attributed to the shallow traps, is the result of capture and emission events.

A more complete version of Figure 3.1 is provided by Figure 3.16 below that takes into account all of the key quantities introduced in this section:

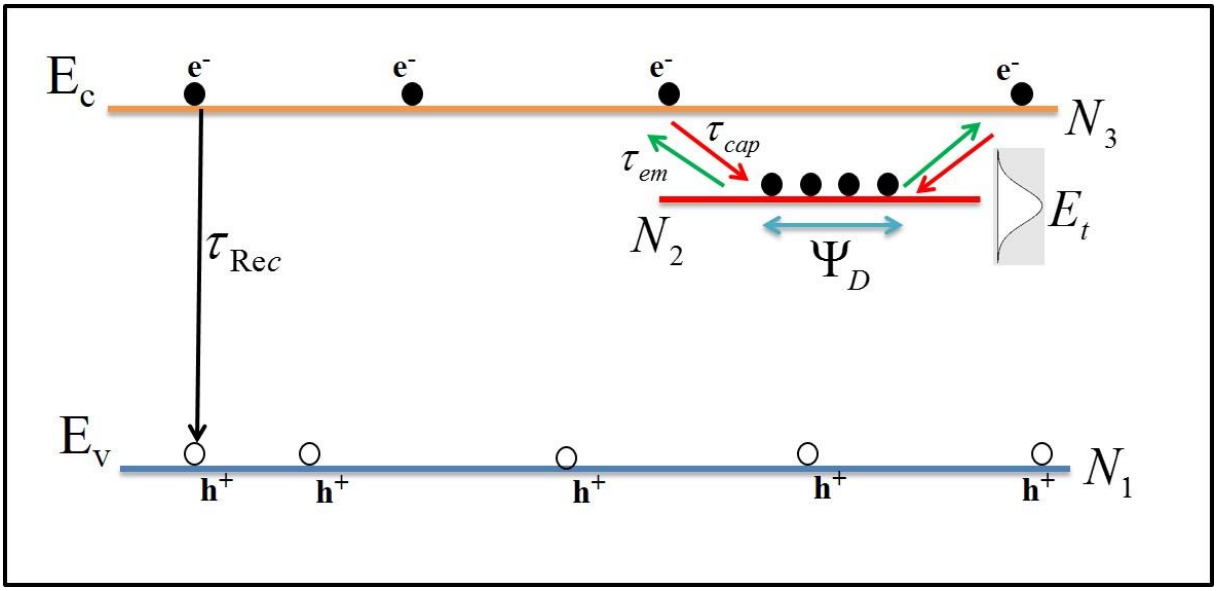



**Figure 3.16: A more complete schematic illustration of the probed charge carrier dynamics**

Now that all of the parameters have been defined, we were able to establish the system of differential rate equations that replicates the experimentally probed carrier dynamics:

$$\begin{cases} \dfrac{dN_1}{dt} = +\dfrac{N_3}{\tau_{\mathrm{Rec}}} \\ \dfrac{dN_2}{dt} = \left(1-\dfrac{N_2}{\Psi_D}\right)\left(\dfrac{N_3}{\tau_{Cap}}\right)-\left(\dfrac{N_2}{\tau_{em}}\right) \\ \dfrac{dN_3}{dt} = \dfrac{N_2}{\tau_{em}}-\left(1-\dfrac{N_2}{\Psi_D}\right)\left(\dfrac{N_3}{\tau_{Cap}}\right)-\left(\dfrac{N_3}{\tau_{\mathrm{Rec}}}\right) \end{cases} \tag{3.6}$$

The generation which takes place during $\tau_p$ is written as:

$$G = \frac{1-R(\lambda=700nm)}{\Gamma(\lambda=700nm)}\int_0^{\tau_p}\phi(t)dt \tag{3.7}$$

R ($\lambda$=700 *nm*) is the reflection coefficient that is found to be close to 20%.

$\Gamma$($\lambda$=700 nm) is the photo-penetration depth which is estimated at 1 µm.

In order for the shallow trap states density to be the only unknown parameter, the capture and the emission lifetimes need to be calculated. The values of these lifetimes are dependent on the properties of the material shallow traps. In other terms, one needs to determine the nature of the shallow trap (donor or acceptor), its energy level $E_t$ and its capture cross section $\sigma_e$.

Theoretical calculations [36] and capacitance spectroscopy measurements [114][115] established a list of the possible carrier traps in a $Cu(In,Ga)Se_2$ absorber. Our choice of the trap level characteristics will be the one that leads to the smallest reconstruction error of the time-resolved luminescence decay.

One particular study [115] showed that at room temperature, the electron trap level that exhibited a dominance in its activity ( in terms of emission and capture rates) over the other trap levels is a donor level $In_{Cu}^{++}$ located 0.34 *eV* below the absorber conduction band. Its capture cross section is equal to $4x10^{-13}$ $cm^2$. Firstly, this particular electron trap among many others fulfills the above selection criteria regarding the minimization of our decay reconstruction error. Secondly, in one of our previous works [108] we showed that the shallow trap states present at the absorber/buffer layer interface govern the TRPL decays obtained on CIGS solar cells. Finally, a study found in [127] also proved the existence of an interface defect present at 0.8 *eV* above the valence band for a bandgap of around 1.15 *eV* which means that is located at the same energy position of the latter electron trap level. In our upcoming discussion we will demonstrate on multiple occasions that this is indeed the type of trap states that exist within the devices we are studying.

In order to take into account any additional uncertainty driven by the choice and calculation of the trap energy level, we'll consider the presence of an energy distribution of this particular trap state. Therefore, in the upcoming calculations, a Gaussian distribution of electron trap states has been chosen with a central value of 0.34 *eV* and a full width at half-maximum (FWHM) value of 100 *meV*. (The outcome variation of our solution is less than 5 % for a FWHM as high as 150 *meV).*

Now that the properties of the trap states are determined, the emission and the capture lifetimes can be calculated as follows:

$$\begin{cases} \dfrac{1}{\tau_{em}} = \sigma_e \nu_{th} N_c \exp\left(-\dfrac{E_t}{kT}\right) \\ \dfrac{1}{\tau_{cap}} = \Psi_D \sigma_e \nu_{th} \end{cases} \tag{3.8}$$

$\upsilon_{th}$ is the thermal velocity, k is Boltzmann's constant and T is the temperature.

The numerical procedure consists of varying $\Psi_D$ over a large array of different values. For each value, the system of rate equations in (3.27) results in a decay $TRL_{Num}$ that is a reconstruction of the experimental one $TRL_{Exp}$. The optimization procedure then selects the value of $\Psi_D$ for which the reconstruction error is minimized. The latter error is calculated over the whole set of decay points $N_p$ and is expressed as:

$$\xi = \frac{\sum_{i=1}^{N_p}\left[\left(\frac{\left|TRL_{Exp}(i) - TRL_{Num}(i)\right|}{TRL_{Exp}(i)}\right)x100\right]}{N_p} \tag{3.9}$$

We obtain values of ξ varying between 2% and 7%. These operations are repeated for all of the experimental decays.

In Figure 3.17.a below, we illustrate how the solution of the system of rate equations results in a reconstruction of the experimental TRPL decay. Figure 3.17.b illustrates how the reconstruction is made using an array of trapping defects density values and how the optimization algorithm choses the value that leads to a minimum of reconstruction error. In the present example, the reconstruction error ξ is equal to 5% and the corresponding $\Psi_D$ is equal to 4.7x10$^{14}$ *traps/cm*$^3$.

**(a)**

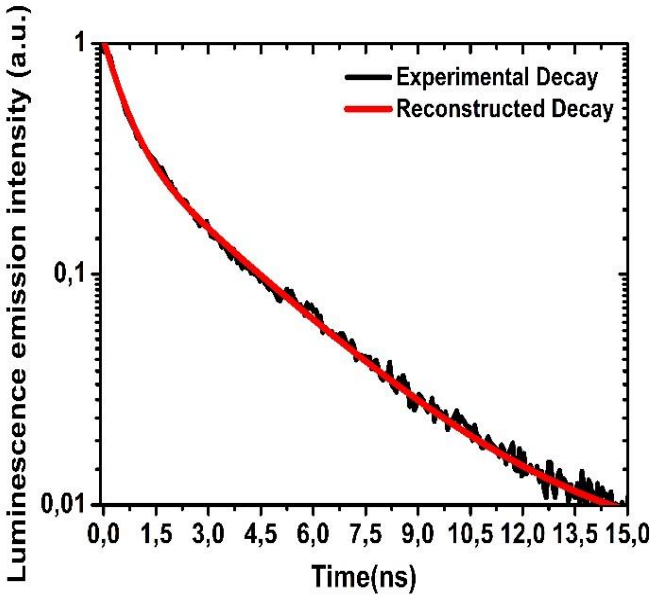



**Figure 3.17.a Example of an experimental TRPL decay reconstruction**

**(b)**

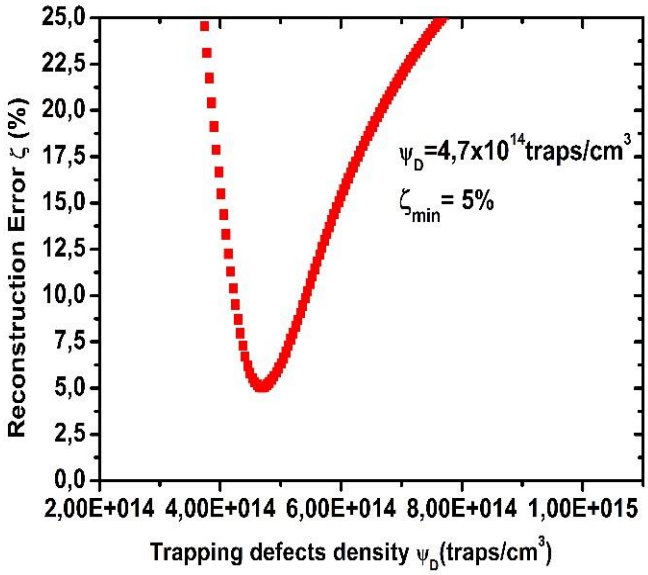



**Figure 3.17.b Illustration of the reconstruction error minimization**

### 3.4.2 Application to the photo-excitation intensity-dependent time-resolved luminescence decays

The data presented in Figure 3.18 illustrates the values of the material's trap states density as a function of an increasing photo-excitation flux.

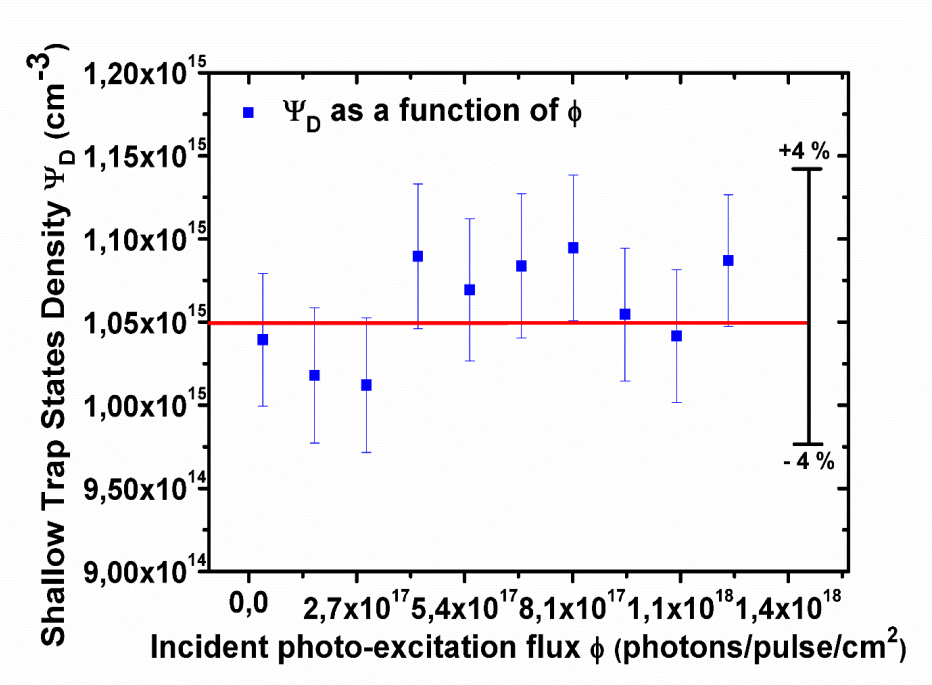



**Figure 3.18: Evolution of the material trap states density as a function of the photo-excitation flux**

The obtained values exhibited weak power dependence and fluctuations ranging from -4 % to +4% with respect to their average value of $1.06x10^{15}$ $cm^{-3}$.

### 3.4.3 Application current injection-dependent time-resolved luminescence decays

**a.**

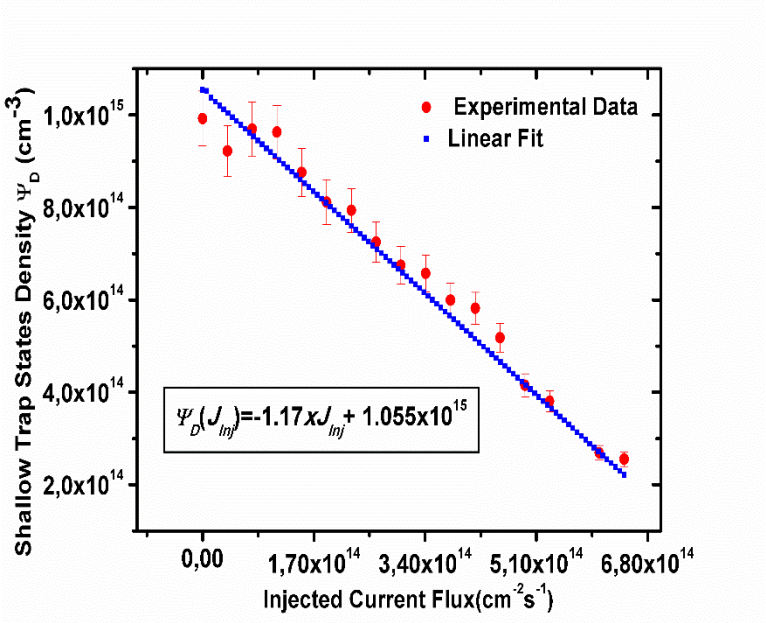



**Figure 3.19.a : Evolution of the material trap states density as a function of injected current under a constant photo-excitation flux**

**b.**

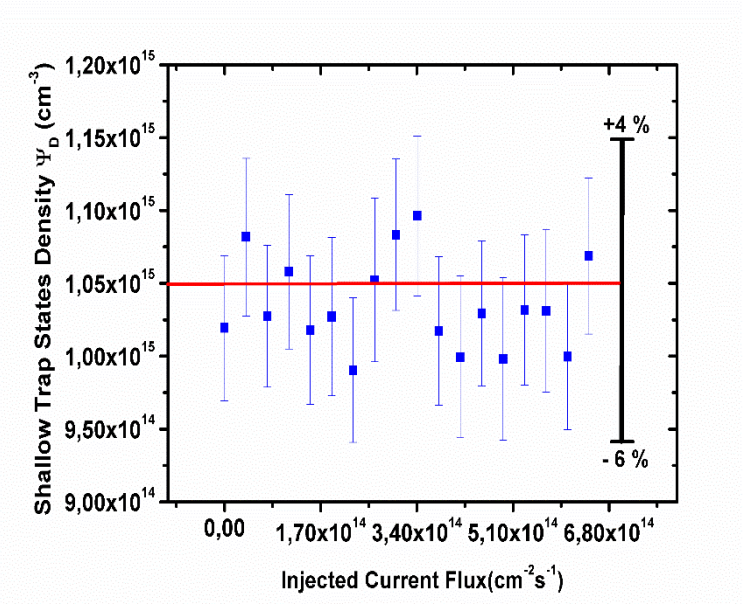



**Figure 3.19.b : Evolution of the material trap states density taking into account the variations of the injected current flux**

According to Figure 3.19.a, the trap states density decreases from $1.05x10^{15}$ *traps.cm*$^{-3}$ down to $2.5x10^{14}$ *traps.cm*$^{-3}$ as the injected current flux is increased from 0 up to $6.45x10^{14}$ *cm*$^{-2}$*.s*$^{-1}$. In addition, $\Psi_D(J_{Inj})$ exhibits a linear behavior. A linear fit is thus applied to the obtained values as seen in Figure 3.19.a.

The electrical generation $G_{elec}$ is then added to the system of the rate equations in order to take into account the effect of electrical carrier injection. It consists of a constant number of carriers electrically injected during the time-resolved experiments. Once again, the correction here consists of updating the number of electrically injected carriers and hence taking into account the excess carrier populations that it induces. Similarly to the case of excitation power dependent TRPL decays, the obtained values of the trap states density exhibited fluctuations ranging from -6% to +4% as seen in Figure 3.19.b.

### 3.4.4 Discussion on the application to the photo-excitation intensity-dependent and current injection-dependent time-resolved luminescence decays

We were so far able to prove (Figures 3.18 & 3.19.b) that our model can indeed provide precise reconstructions of the experimental time-resolved luminescence decays and quantify the material trap states density.

For the TRL($J_{inj}$) experiments, before taking into account the different values of the injected current, we evidenced the existence of a linear relationship between the accessible trap states density and the injected current flux. In addition, by evaluating $\Psi_D(J_{Inj}=0)$ we were able to find the actual value of the trap states density to be equal to *1.05x10*$^{15}$ *cm*$^{-3}$.

From the TRPL($\phi$) & TRL($J_{inj}$) experiments, we proved that our model is self-consistent with respect to a variation of the incident excitation power and the injected current, when the latter are taken into account. This was proved by the constant value of $\Psi_D(\phi)$ that it provides.

From the TRPL($\phi$) experiments, we see that only one contactless measurement of a TRPL decay, is needed for the calculation of the shallow trap states density. Apart from being contactless, this represents an additional advantage of the presented technique.

### 3.4.5 The effect of the trapping defects density on global photovoltaic performance

At this stage we will test if our defect quantification method can be used as a reliable indicator of thin film PV solar cells performance. In other terms we will try to evidence the existence of a link between a trap states density derived from TRPL experiments using our method, and the standard PV performance indicators such as its short-circuit current $J_{sc}$ , open-circuit voltage $V_{oc}$, its fill factor FF and its power conversion efficiency $\eta$.

To do so, standard J(V) characterization will be performed on five CIGS solar cell devices. We proceeded by depositing a metallic grid on top of complete CIGS device. This resulted in a matrix of CIGS solar cells with equivalent surface areas. All five devices therefore have the same structure and type of layers.

Additionally, the CIGS absorber was prepared using the same three-stage co-evaporation process. For each device, all of the performance parameters are extracted (see Table 3.2). For device number 2, we intentionally exposed its absorber surface to air before the deposition of the buffer layer. For the four remaining devices, the absorber surface was preserved under vacuum.

Then, we perform a single acquisition of a TRPL decay on each CIGS device. Using our previously developed method, we finally extract the value of the trap states density within each device.

According to Figure 3.20, the open-circuit voltage of the device decreases from 0.7 *V* to 0.42 *V* as the trapping defects density increases from $2.98 \times 10^{14}$ *traps.cm*$^{-3}$ to $6.6 \times 10^{15}$ *traps.cm*$^{-3}$.

Then, by applying a two-diode-model fit to our obtained J(V) curves, we also extracted the corresponding dark saturation current $J_{01}$ & $J_{02}$. This helped us identify if the trapping defects that we are quantifying are located in the bulk of our absorber ($J_{01}$-dependent) or close to its surface and interface with the CdS buffer layer ($J_{02}$-dependent). According to Figure 3.20, we identify an interestingly clear linear dependence between the $J_{02}$ dark saturation current and the trapping defects density $\Psi_D$. $J_{02}$ increases linearly with $\Psi_D$. No link is identified between $J_{01}$ and $\Psi_D$. The values of the former exhibited very little response to the variations of $\Psi_D$ in comparison with what we have observed for the case of $J_{02}$. This is evidence that $\Psi_D$ is indeed the density of the interface trapping defects within the studied solar cells.

Finally, it is to be noted that device 2 exhibited the highest $J_{02}$ and $\Psi_D$ value amongst all of the investigated devices. This confirms the intentional degradation of the quality of its absorber/buffer layer interface. As for the four remaining devices, the differences between the $\{J_{02}, \Psi_D\}$ values are most likely due to the device fabrication processes that produce a spatially inhomogeneous quality of the absorber/buffer layer interface. This hypothesis is supported by a recent study made by Paul *et al.*[129] showing that using the nano-DLTS technique, a spatially-resolved correlation exists between the electrical traps and the physical structure of the CIGS solar cell.

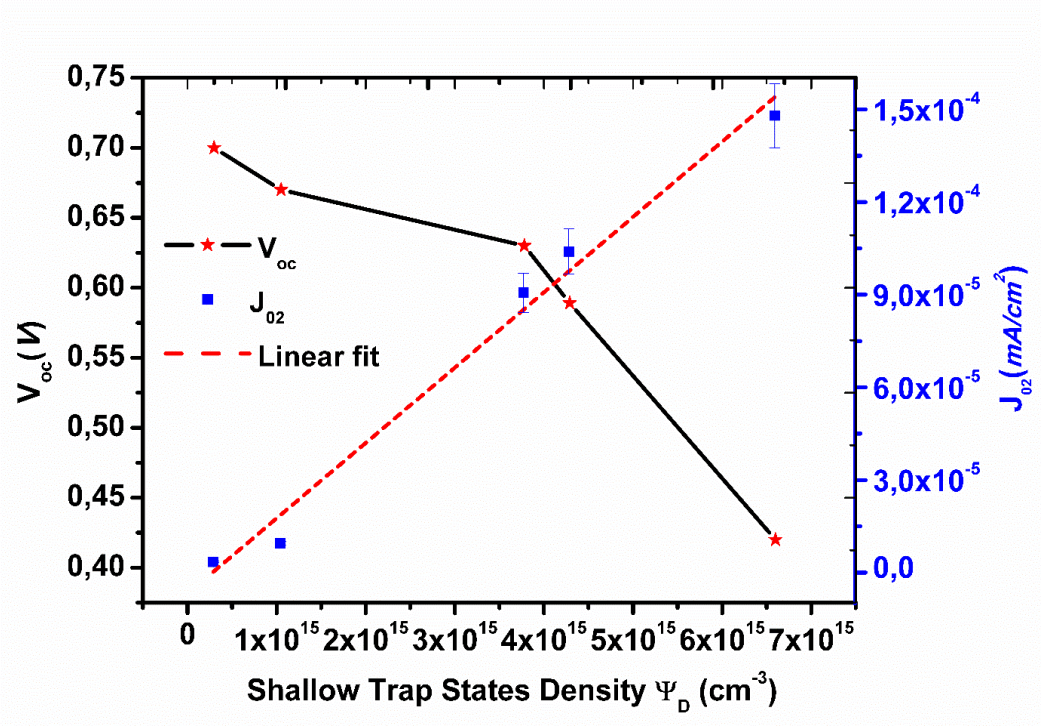



**Figure 3.20: Evolution of $V_{oc}$ and $J_{02}$ as a function of the shallow trap states density**

| | $J_{sc}(mA/cm^2)$ | $V_{oc}(V)$ | FF(%) | η(%) | $J_{01}(mA/cm^2)$ | $J_{02}(mA/cm^2)$ | $\Psi_D(cm^{-3})$ |
|---|---|---|---|---|---|---|---|
| **Device 1** | **30.4** | **0.67** | **68.4** | **14** | **$4.82x10^{-12}$** | **$9.49x10^{-6}$** | **$1.05x10^{15}$** |
| **Device 2** | **18** | **0.42** | **60.4** | **4.57** | **$5.84x10^{-12}$** | **$1.48x10^{-4}$** | **$6.6x10^{15}$** |
| **Device 3** | **30** | **0.7** | **75.6** | **15.9** | **$4.56x10^{-12}$** | **$3.47x10^{-6}$** | **$2.98x10^{14}$** |
| **Device 4** | **35.8** | **0.63** | **69.7** | **15.72** | **$7.35x10^{-12}$** | **$9.07x10^{-5}$** | **$3.78x10^{15}$** |
| **Device 5** | **36.5** | **0.594** | **62.1** | **13.35** | **$7.04x10^{-12}$** | **$1.04x10^{-4}$** | **$4.29x10^{15}$** |

**Table 3.2: List of the different performance indicators of all five CIGS devices**

In the literature, several studies investigated the effect of trapping defects on the overall PV device performance. One study was able to extract the trapping defects density based on the TRPL decays of GaAs heterostructures [82]. The authors of the latter work established a correlation between the trapping defects density values and the material growth rate.

For CIGS-based technologies, some studies intentionally varied the defects density levels in the material by either changing the selenium supply levels [128] or the gallium content [127] .Even when the

gallium content was changed from 0.0 to 0.8, the defect bandwidth and its position relative to the valence band remained constant. The defect density, calculated using DLTS (Deep Level Transient Spectroscopy), is found to approach midgap and act as SRH recombination centers. This study however was not conclusive regarding the effect of trapping defects on PV performance as the increase in the Ga content itself directly increases the $V_{oc}$ as the bandgap energy is increased. The other PV parameters consequently change also, making it difficult to study distinctly the impact of trapping defects.

In Ref [128] however, the study focuses on the effect of one particular type of defects which is the well-known ((In or Ga) $_{Cu}$) defects near the CIGS surface. It is the same type of defects that is at the center of our study. Ref[128] shows that as the Se supply level is decreased, the density and hence the effect of this type of defects becomes more significant in terms of PV performance degradation. It was also shown that the device with the higher Se supply level exhibited the highest $V_{oc}$, regardless of the applied temperature. We can finally deduce from Ref[128] that a decrease in the Se supply level, induces deeper level defects that progressively cause inferior performance of the CIGS device , in particular , lower $V_{oc}$ values.

In addition to the $J_{02}$, Table 3.2 shows that it is the open-circuit voltage that revealed a dependence on the device shallow trap states density amongst all of the standard PV performance parameters. We deduce that the thin film CIGS device that suffers from the highest trap states density is expected to have the lowest open-circuit voltage. On the one hand these results come in good agreement with the study done in Ref[128] where the highest density of ((In or Ga) $_{Cu}$) defects ( ($In_{Cu}^{++}$ in our case) induced the lowest $V_{oc}$. On the other hand, this validates once more, the type and characteristics of the trapping defects that we are studying here.

### 3.4.6 An attempt at a quantitative optical spectroscopy of trapping defects

So far, we have successfully demonstrated how to extract the trapping defects density of a CIGS solar cell based on the mere analysis of its time-resolved luminescence decays. We showed that regardless of the photo-excitation power or the amount of electrically injected carriers, our method is robust and self-consistent. However, we remind that by also varying the incident photo-excitation energy, we were able to develop an application for the optical study of metastabilities in CIGS. Once again, and based on the variation of the excitation wavelength, the potential of a new and innovative application, surfaces. Knowing that the trap states possess an energetic distribution within the band gap of a semiconductor, we imagined that from each of the time-resolved photoluminescence decays corresponding to specific excitation energy, we can extract a specific trapping defects density. And, by finally plotting these densities as a function of excitation energy, we can hope to establish a sort of contactless spectroscopy of the active trapping defects density distribution.

If we carefully examine our system of rate equations in (3.6), we notice that it doesn't take into account the effect of any variations in the excitation energy. So far we have upgraded it so it can take into

account the variation of power and injected current. Our goal is to modify it so it can correctly take into account the effect of excitation energy variations.

From an exploratory point of view, we start by leaving the set of rate equations in its present state, we then apply our developed method to the previous set of excitation energy-dependent TRPL decays of *Section 3.2*. For each TRPL decay a $\Psi_D$ is extracted. It is then plotted, along with the *DCD* parameter, as a function of the excitation energy:

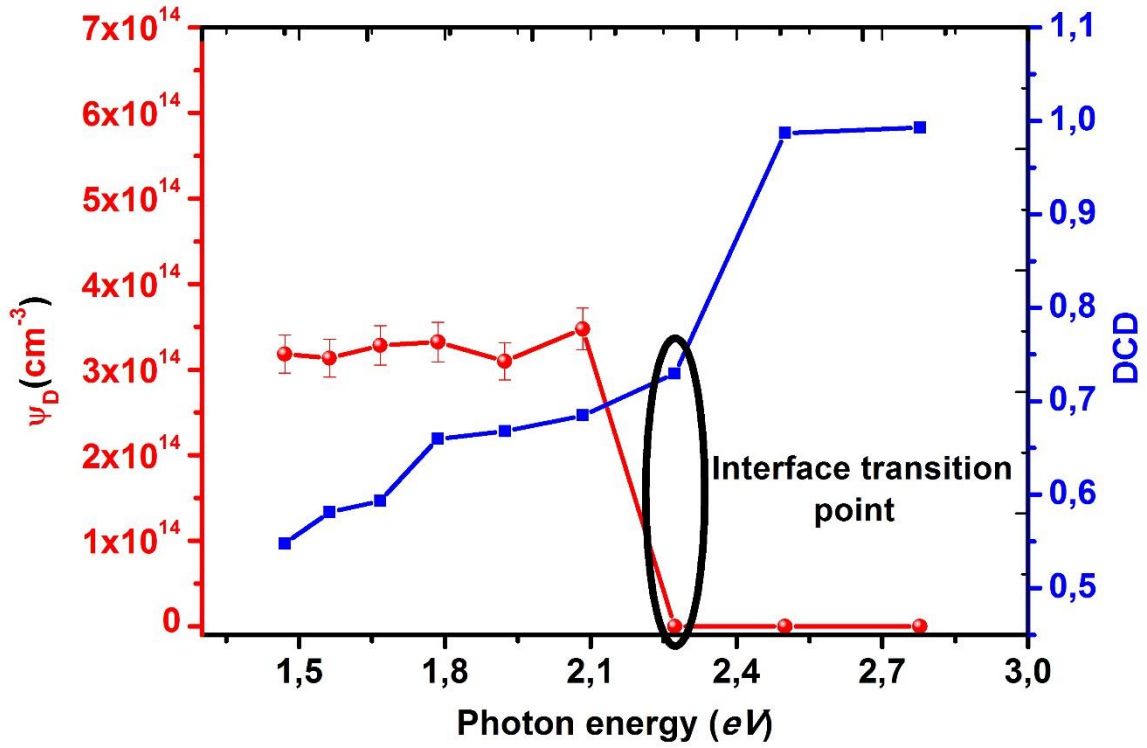



**Figure 3.21: Preliminary evolution of the trapping defects density as a function of the excitation energy**

While examining the evolution of $\Psi_D$ as a function of the excitation energy, we notice a weak fluctuation of the probed active $\Psi_D$ density for excitation energies varying between 1.4 eV and 1.8 eV. This might be a preliminary indicator of a quite stable distribution of traps within the probed energetic depth of the CIGS stack. However, once the energy exceeds 1.8 eV we notice a decrease in the probed active trapping defects density as a function of the excitation energy. Finally, we focus on the excitation energies greater than 2.3 *eV*. For these energies, we previously observed and interpreted the sudden transition of the *DCD* towards unity. We found that it corresponds to complete occupation of the metastabilities acting as interface trapping defects. And for these high energies in particular we can see from Figure 3.21 that our method converges towards $\Psi_D$ values that are strictly equal to zero. Due to the absence of the correction from the excitation energy variation and if we define these $\Psi_D$ values as the probed active trapping defects densities, then, this evolution is expected.

Continuing on an exploratory note, we propose now a modification of (3.6) in order to better mimic the effects of excitation energy variations.

We know that, for the same incident photon flux, the occupation of the traps states distribution varies as a function of the excitation energy as energetically deeper traps are probed. The excitation energy can therefore modulate the occupation of the traps distribution.

So far, this occupation function has been expressed in (3.27) as $f_{occ} = \frac{N_2}{\Psi_D}$.

In this case, the occupation probability is: $P_{occ} = 1 - \frac{N_2}{\Psi_D}$ (3.10)

Let's explore the following solution that may correct the occupation probability from the effect of excitation energy variations: Let's implement into (3.10), a parameter that reflects a quantity that has no dimension like the latter probability, and whose dependence on the excitation energy is well known. To us, it seems that the best candidate is the "*DCD*" parameter.

Let's consider the following particular case: For a constant incident photon flux, and for a DCD equal to unity, we are certain that no event of carrier capture can take place, and that, in this case, the new occupation probability is equal to zero and takes into account both the photo-excitation intensity and the excitation energy effects. Here's how we propose to express this new occupation probability:

$$P_{occ}^{\text{mod}} = \left(1 - \frac{N_2}{\Psi_D}\right)\left(1 - DCD(\lambda)\right) \tag{3.11}$$

This new expression (3.11) represents a trap occupation probability modulated by the effect of the incident excitation energy under constant flux.

Our new system of rate equation is now written as:

$$\begin{cases} \dfrac{dN_1}{dt} = \dfrac{N_3}{\tau_{B2B}} \\ \dfrac{dN_2}{dt} = \left(1 - \dfrac{N_2}{\Psi_D}\right)\left(1 - DCD(\lambda)\right)\left(\dfrac{N_3}{\tau_{Cap}}\right) - \left(\dfrac{N_2}{\tau_{em}}\right) \\ \dfrac{dN_3}{dt} = \dfrac{N_2}{\tau_{em}} - \left(1 - \dfrac{N_2}{\Psi_D}\right)\left(1 - DCD(\lambda)\right)\left(\dfrac{N_3}{\tau_{Cap}}\right) - \left(\dfrac{N_3}{\tau_{B2B}}\right) \end{cases} \tag{3.12}$$

Let us now illustrate the evolution of $\Psi_D$ as a function of the excitation energy, based on the new system of rate equation in (3.12):

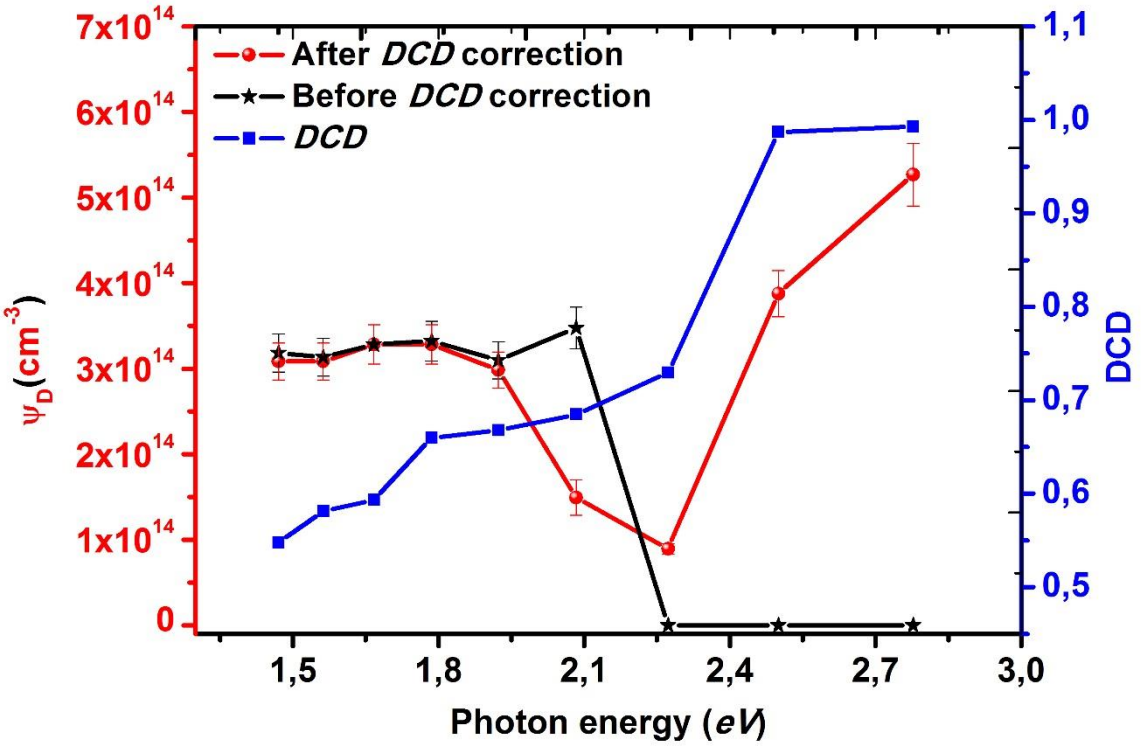



**Figure 3.22: Evolution of the trapping defects density as a function of the excitation energy before and after the correction by the *DCD* parameter**

If we compare Figure 3.21 and Figure 3.22, we can see that for the excitation energies below 1.95 *eV* the correction by the *DCD* yields similar $\Psi_D$ values. The influence of the *DCD* correction seems to start once the excitation energy range becomes high enough to activate the interface metastable defects. We can see that our method stops converging towards zero $\Psi_D$ values. Burt rather values that increase with the excitation energy, similarity to the DCD itself. Keeping in mind that the majority of the metastable defects density is present at the absorber/buffer layer interface, this corrected evolution of $\Psi_D$ may have a physical meaning. It seems as if the correction using the *DCD* transforms the previous definition of $\Psi_D$ in Figure 3.21 where we considered it as the still-accessible density of trapping defects. This new evolution may now mean that the $\Psi_D$ values in Figure 3.22 are the actual material trapping defects density distribution.

This section represented our two first attempts towards a contactless, quantitative spectroscopy of the trapping defects in CIGS solar cells using excitation energy-dependent TRPL decays. The results are encouraging and promising. Further studies will help further understand the observed evolutions and lead to a final and reliable optical spectroscopy of trapping defects.

### 3.4.7 Discussing the choice, the limitations and relevance of the physical model

In this section, we would like to detail our choice of this adapted numerical approach, its relevance when compared to the methods used in the literature, as well as its limitations.

First of all, the recombination terms in our system of rate equations (3.6) reflect a mono-molecular regime. This choice of rate equations is coherent and in accordance with our results in Figures 3.6 and 3.7 where a mono-molecular recombination regime has been identified.

Second of all, we can find in the literature many theoretical studies that elaborate carrier dynamics in CIGS solar cells under pulsed laser excitation and in the presence of trapping defects [163,164]. In particular, the authors of these studies, perform simulation works using a system of rate equations that is similar to ours (equations 3.6). Using their theoretical work, they were able to analytically relate their simulated capture and emission lifetimes to the long characteristic lifetime of the TRPL decay. Therefore, such studies have the advantage of providing a robust, complete understanding of the carrier dynamics in CIGS under the presence of trapping defects. However, a main drawback of these studies is that they are only valid under a quite low injection regime at approximately $10^9$ photons/pulse/cm$^2$. From an experimental point of view, it is very challenging to extract a good TRPL signal quality under such excitation flux. An experimental work on CIGS found in [165] adapted the theoretical findings in [163,164] in an attempt to quantify the trapping defects density behind the TRPL decays, but without respecting the low excitation regime conditions. This resulted in a poor fitting quality of the experimental TRPL decays using the theoretical set of rate equations developed in [163, 164].

In our case, given the adapted photo-excitation fluxes, we are in the presence of a high injection regime. Therefore, and based on the previous discussion, we did not apply the theoretical findings of [163,164] as the injection conditions won't be respected. This led us to the development of the set of rate (equations 3.6). A first limitation of our choice is that we probably won't be able to test our approach on low injection regime TRPL decays. A second limitation is the absence of theoretical, analytical solutions that express the long experimental decay lifetime $\tau_{traps}$ as a function of the different parameters of the set of equation (3.6). However, it is important to be noted that our work logic was device orientated. This means that our priority was first of all, to correctly reconstruct the experimental TRPL decays, and then extract the corresponding trapping defects density. Second of all, our priority was also to test the validity of the extracted densities. This was tested by correlating our findings with the basic photovoltaic performance parameters. This aspect allowed confirming that TRPL can be used as a reliable, quantitative performance indicator.

Finally, to conclude the discussion with a perspective, we strongly believe that on the theoretical side, further studies should be able develop the phenomenological aspect of high-injection TRPL studies in a CIGS material. Doing so will finally bring together all of the theoretical, simulation and experimental aspects of TRPL studies in CIGS under either low or high injection regimes.

# Chapter IV. Quantitative luminescence-based imaging of optoelectronic properties of thin film PV devices

## 4.1 Introduction

Different spatial inhomogeneities are found on CIGS materials and devices. They can consist of bandgap variations owing to composition variations, inhomogeneous series resistances, defect concentrations and electrostatic charges. For example, some photovoltaic properties a CIGS solar cell were found to be particularly inhomogeneous such as the band gap energy[130,133], the external quantum efficiency[134], the quasi-Fermi levels splitting[135] ($\Delta\mu$) and the current-voltage characteristics[136]. Numerous studies investigated and quantified these spatial fluctuations by analyzing the luminescence emission of these solar cells [137-142].

They can be observed from micrometer scale (intrinsic inhomogeneities) to centimeter scale or more (inherent to the deposition process). Such inhomogeneities will reduce the efficiency by, for instance, increasing the global saturation currents and the ideality factor [130, 131].

Non-intuitive strategies can be used to prevent such effects. As an example, it was found that an increased series resistance of the ZnO:i may be beneficial, by reducing the influence of the poorest quality parts of the cell [132]. Moreover, a better understanding of the relations between local and global performances is needed.

The presence of such inhomogeneities is not accounted for using standard macroscopic characterization methods although local optoelectronic properties variations were shown to have an influence on the global photovoltaic performance of the device [131]. For example, a simulation work [64] found that local fluctuations in the maximal obtainable open-circuit voltage of the solar cell most likely arise from inhomogeneous charge transport properties. In particular, the authors of this work showed that by simulating different minority carrier lifetimes, they obtained different spatial profiles of the quasi-Fermi levels splitting.

This chapter will be dedicated to the study of the origins behind the micrometric fluctuations of the optoelectronic properties of CIGS solar devices. In particular, we will add the spatial dimension to the results of the previous chapter where the properties of the CIGS device we locally quantified based on the analysis of the luminescence emission.

We start by performing spatially-resolved and time-resolved photoluminescence measurements using scanning confocal microscopy. This will allow us to quantitatively map all of the previously probed carrier dynamics. In addition, this first step will be concluded by the calculation of a quantitative map of the material trapping defects density using our previously developed approach.

We finally perform a contactless mapping of $\Delta\mu$ using the hyperspectral imager setup. The results of both experiments were quantitatively correlated.

## 4.2 Spatially-resolved, spectrally-resolved and time-resolved luminescence of Cu(In,Ga)$Se_2$ PV devices

### 4.2.1 Quantitative electrical mapping of the variations of PV performance indicators following metastabilities activation

In our local studies in *Chapter III* we have developed an optical alternative for the study of the investigation of metastabilities in CIGS solar cells using time-resolved luminescence. In this first part of Chapter IV dedicated to spatial studies, we aim at investigating the spatial influence of these metastabilities once activated using two different excitation wavelengths: 750 nm and 532 nm respectively.

In this part we use the scanning confocal microscope and will start by mapping and analyzing the variations in the short-circuit current and the open-circuit voltage under different light excitations and the same photo-excitation fluxes. The circular laser excitation spot used here has a 1 micrometer diameter.

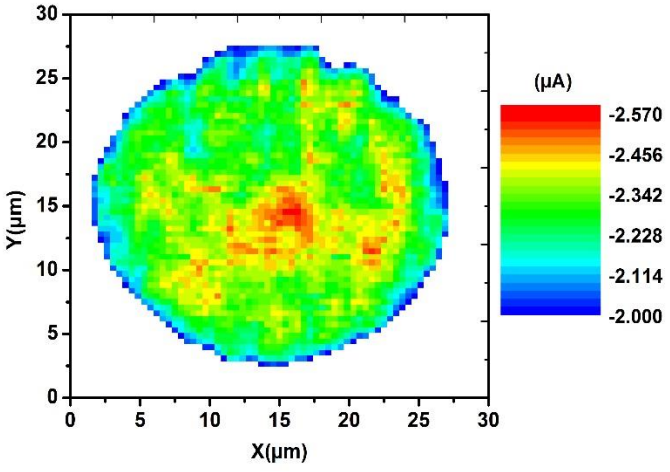



**Figure 4.1.a: Short-circuit current map using a 750 nm excitation wavelength**

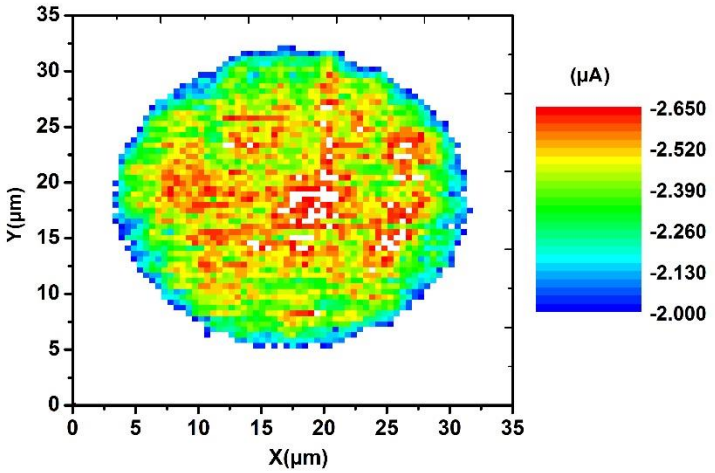



**Figure 4.1.b: Short-circuit current map using a 532 nm excitation wavelength**

We have previously shown that once the photo-excitation energy becomes high enough (>2.4 *eV*) to activate the interface metastabilities, a sudden shift in carrier dynamics is observed. Here, Figures 4.1.a and 4.1.b illustrate a solar cell performance shift following the activations of these metastabilities. In particular, these two figures correspond to LBIC maps, the first obtained at 750 *nm* excitation and the second at 532 *nm* excitation. This means that the first map is obtained for an energy below the 2.4 *eV* threshold whereas the second corresponds to an energy above this metastabilities activation threshold.

In particular, once can notice an enhancement of the solar cell short-circuit current under a 532 nm excitation wavelength. To quantify this enhancement, we perform a statistical analysis of these maps:

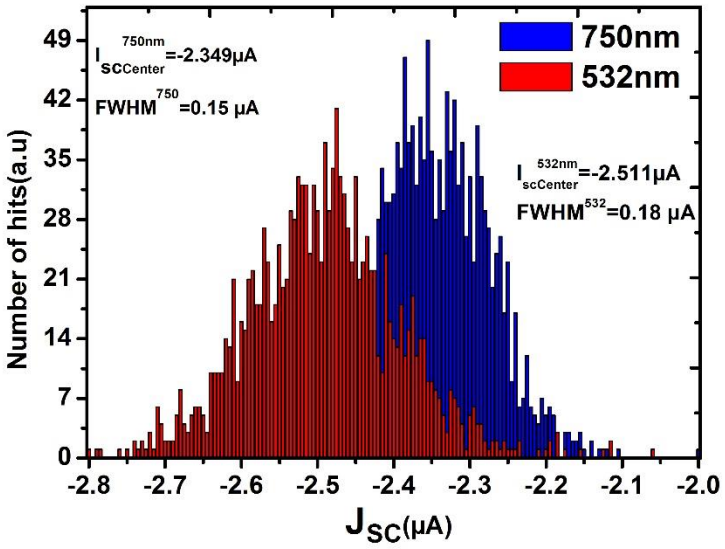



**Figure 4.2: Gaussian distributions of short-circuit current maps obtained under 750 *nm* and 532 *nm* excitations respectively.**

Gaussian distributions of the latter seen in Figure 4.2, reveal a shift in the $J_{sc}$ central values from 2.349 µA to 2.511 µA. This reveals a gain of 0.162 µA in short-circuit current which represents a 7% increase in $J_{sc}$ with respect to its central value at 750 nm. The 532 nm wavelength allowed to optically occupy the accessible density of interface trap states. The trapping activity of the charge carriers is consequently reduced and translated into a gain in current that is quantified here.

We now map the open-circuit voltage under 750 nm and 532 nm excitation wavelengths (Figures 4.3.a and 4.3.b)

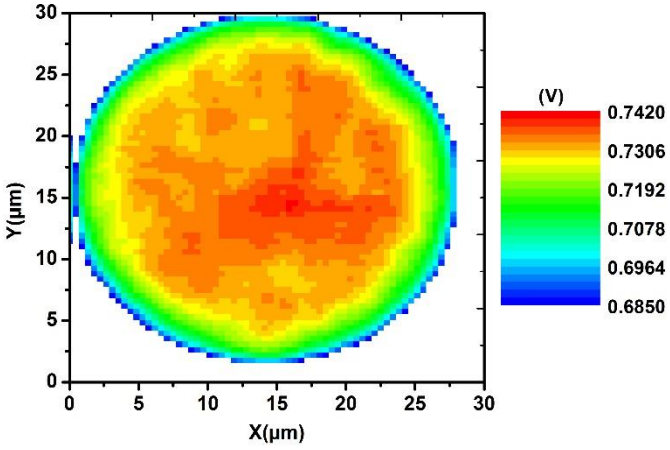



**Figure 4.3.a: Open-circuit voltage map using a 750 nm excitation wavelength**

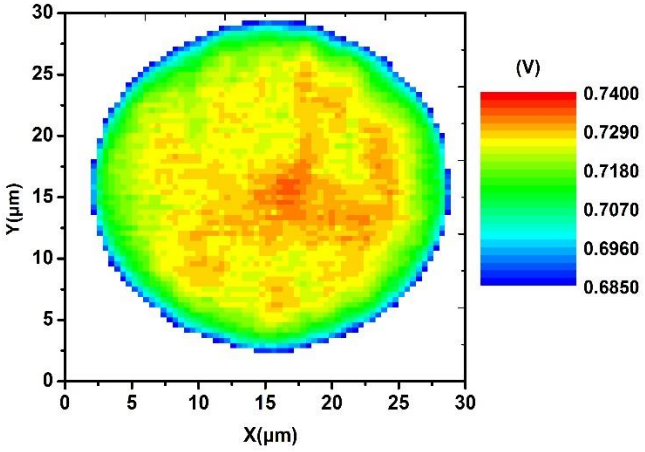



**Figure 4.3.b: Open-circuit voltage map using a 532 nm excitation wavelength**

In comparison with the previous $J_{sc}$ maps and for the same excitation wavelength, one can notice a more homogeneous behavior of the measured voltage. More precisely, a statistical analysis of both maps reveals a Gaussian distribution with a FWHM value of 6 *meV*.

In order to compare such homogeneous behavior in contrast with the $J_{sc}$ case, we start by reminding that measuring a local voltage using local confocal excitation under open-circuit conditions is not equivalent to measuring the actual local $V_{oc}$ of the solar cell. This has been demonstrated by the study found in ref [64].

The relation between $V_{oc}$ and the $J_{sc}$ is well known and expressed as:

$$V_{oc}(x,y) = \frac{kT}{q}\ln\left(\frac{J_{sc}(x,y)}{J_0^{global}} + 1\right) \tag{4.1}$$

where $J_0^{global}$ is the global dark saturation current of the micro CIGS solar cell.

The logarithmic dependence of the $V_{oc}$ on the $J_{sc}$ is one of the reasons behind the more homogeneous behavior of the former when compared with the spatially inhomogeneity of the latter. Second of all, and based on equation (4.1), the open-circuit voltage has a second dependence on the global saturation current $J_0^{global}$.

Based on the four previous maps, we can actually access the values of dark saturation current $J_0^{global}$. This can be done by plotting the short-circuit current maps as a function of the voltage maps, for both 532 nm and 750 nm excitation wavelengths. Then, based on the obtained plots we can use the mathematical relation between these two quantities and extract the corresponding dark saturation currents.

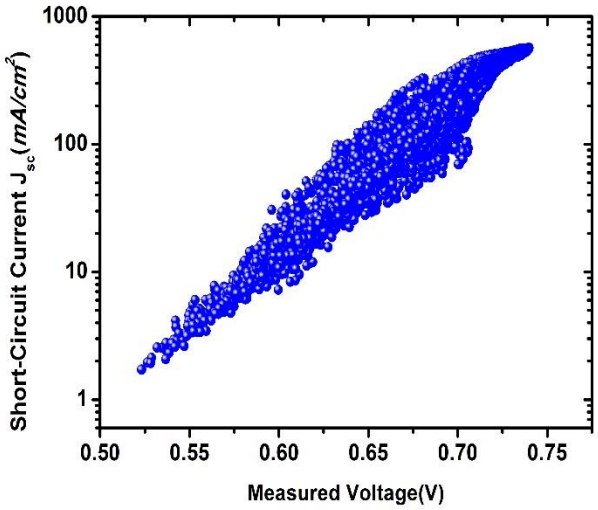



**Figure 4.4.a: Short-circuit current map as a function of measured voltage map for a 750 nm excitation wavelength**

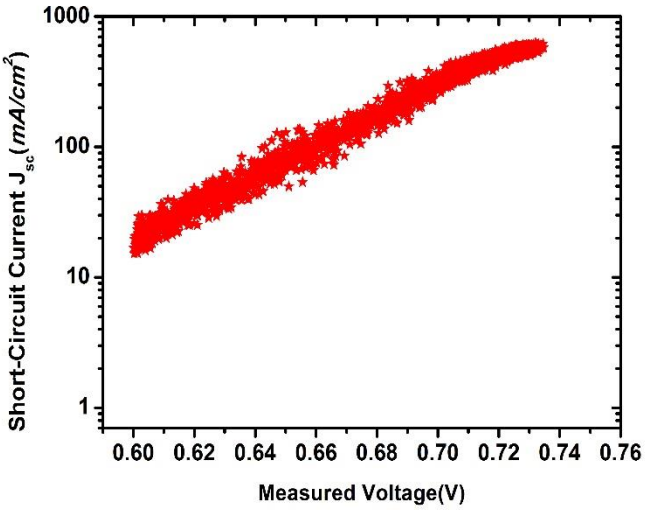



**Figure 4.4.b: Short-circuit current map as a function of measured voltage map for a 532 nm excitation wavelength**

Firstly, and based on equation (4.1), both maps are expected to be linearly related when the logarithm of the short-circuit current map is plotted as a function of the measured voltage map (Figures 4.4.a & 4.4.b).

When examining the two data clouds, we can initially deduce that in the case of the 532 *nm* excitation a narrower data cloud is obtained when compared to the case of the 750 *nm* excitation. From this we deduce that the electrical performance is more spatially inhomogeneous under the 750 nm excitation. This can be explained by the more important spatial presence of the still unsaturated metastabilities in the material under an insufficient excitation energy.

Secondly, another key observation here concerns the linear tendency of the two data clouds. This is an indication that in our case, the $J_{sc}$ is not linked to the voltage by a single exponential component but more likely, double exponential components. Therefore, a more accurate mathematical description in this case is a two-diode model with exponential components corresponding the n=1 & n=2 ideality factors respectively. With such model, the $J_{sc}$ is linked to the open-circuit voltage using:

$$V_{oc}(x,y) = \frac{2kT}{q}\ln\left(\frac{-J_{02}+\sqrt{J_{02}^2+4J_{01}J_{sc}(x,y)}}{2J_{01}}\right) \quad (4.2)$$

$J_{01}$ & $J_{02}$ are the n=1 & n=2 dark saturation currents respectively. We remind that these two types of current were quantified in Chapter III in order to discuss the effect of metastabilities.

Fitting the two data clouds using equation (4.2) allowed us to extract the two saturation currents, for both excitation wavelengths. We find:

For $\lambda = 750nm$, $\begin{cases} J_{01} = (8.2x10^{-11} \pm 2.2x10^{-13} mA/cm^2 \\ J_{02} = (6x10^{-8} \pm 1.2x10^{-10}) mA/cm^2 \end{cases}$

For $\lambda = 532nm$, $\begin{cases} J_{01} = (9x10^{-11} \pm 1.4x10^{-14} mA/cm^2 \\ J_{02} = (1x10^{-9} \pm 1.6x10^{-12}) mA/cm^2 \end{cases}$

One of the evidence of reduced trapping activity of the charge carriers under sufficient excitation energy is the previously quantified gain in short-circuit current. Here, the stable value of bulk-related $J_{01,}$ and the decrease in the defects-related $J_{02}$ dark saturation current form a second evidence of the electrical performance shift under metastabilities activation. The change in performance is quantified in this section in terms of local values of electrical parameters and in terms of change in their spatial behavior and homogeneity. We would like to remind that similar results were obtained in *Section 3.3.2* of the previous chapter while investigating the hysteresis phenomenon for carrier dynamics using excitation energy-dependent TRPL studies. In both the present and previous cases, the $J_{01}$ remains constant, only $J_{02}$ varies significantly. This means that in both studies, we are looking at metastabilities at the SCR/interface of the CIGS absorber/buffer layer.

### 4.2.2 Quantitative optical mapping of trapping defects-induced variations in PV performance indicators

In this part, we quantify the effect of metastabilities on the performance of CIGS solar devices at the micrometric scale using luminescence mapping.

#### 4.2.2.1 Mapping the effect of light-soaking on the quasi-Fermi levels splitting deduced from electroluminescence imaging

In this part we quantify the shift in device performance under light soaking. In particular, we perform hyperspectral imaging of the electroluminescence signal of the micro CIGS solar cell. The first experiment is performed after placing the solar cell in dark conditions where the metastabilities are in relaxed state. We then light-soak the sample during 1 hour using the solar simulator. The second experiment is immediately performed under the light-soaking. For both experiments, we calculate a map of the quasi-Fermi levels splitting $\Delta\mu$. Both maps are then compared and the difference is quantified.

We start by recording a spatially and spectrally resolved electroluminescence maps of our solar device under a 0.83 V applied voltage-bias. The electrical excitation here is equivalent to a 116 Suns and the corresponding injected current is equal to 4.7 *A/cm*$^2$. According to our electrical injection-dependent TRPL experiments in Chapter III, 116 Suns is below the electrical excitation threshold (19.2 *A/cm*$^2$)

after which the accessible density of metastabilities is filled. We can therefore consider the effect of electrical bias application to be weak enough for us to clearly see the effect of optical light soaking.

The maps are then calibrated and expressed in absolute photon flux units as seen in Figures 4.5.a and 4.5.b:

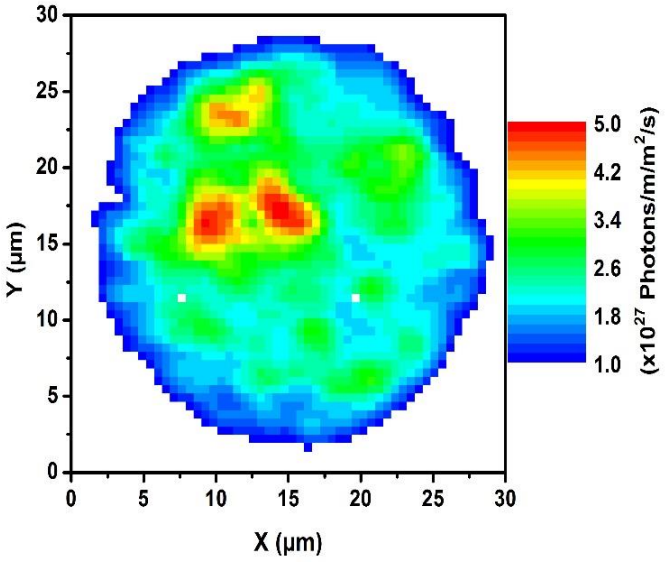



**Figure 4.5.a: Spectrally integrated, absolute electroluminescence image at relaxed solar cell state**

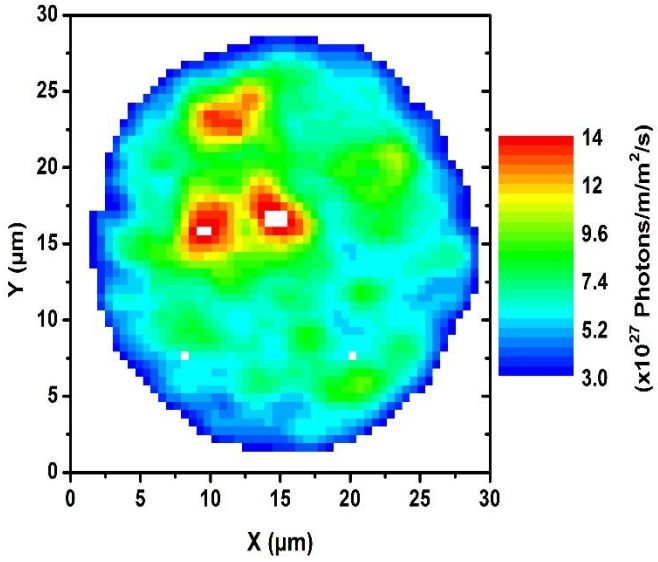



**Figure 4.5.b: Spectrally integrated, absolute electroluminescence image at light-soaked solar cell state**

A visual inspection of the latter EL maps reveals a three-fold enhancement in the solar cell EL intensity. This represents an evidence of the effect of light soaking. In some areas of the micro CIGS solar cell, the luminescence intensity is increased by a maximum of three folds.

The boost in the EL intensity translates into a boost in quasi-Fermi levels splitting of the studied solar cell. In order to quantify the potential $\Delta\mu$ boost we apply the generalized Planck's law (Eq. 1.26 where the absorptivity is replaced by the EQE of the device) to both maps and then calculate the $\Delta\mu$ maps expressed in *eV* as seen in Figures 4.6.a and 4.6.b.

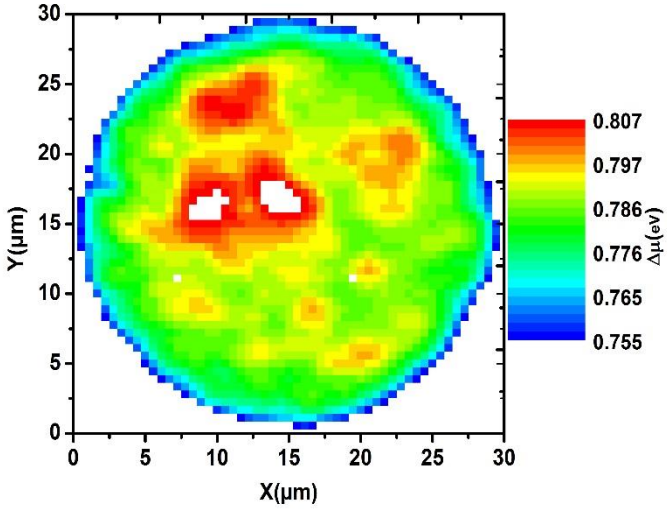



**Figure 4.6.a: Absolute quasi-Fermi levels splitting map at relaxed solar cell state**

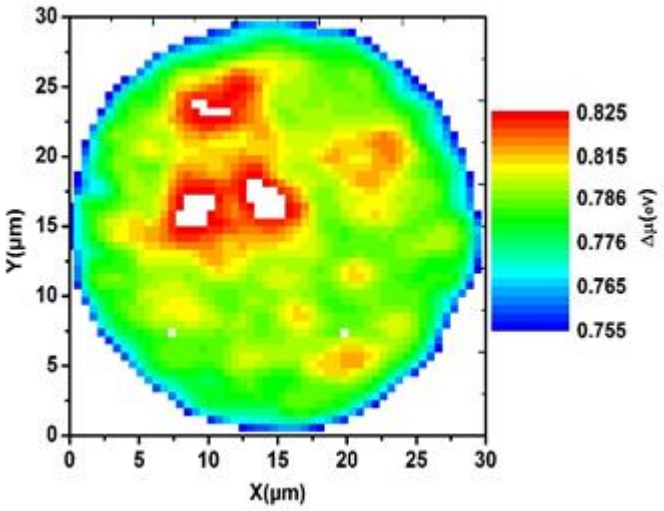



**Figure 4.6.b: Absolute quasi-Fermi levels splitting map at light-soaked solar cell state**

The previously calculated three-fold boost in absolute EL intensity mathematically translates into a 25 *meV* increase in quasi-Fermi levels splitting. However, depending on the spatial distribution of the trapping defects that are at the origin of the metastabilities, the light-soaking enhancement will be spatially inhomogeneous. In particular, the "performance healing effect "will be spatially dependent. By comparing the two Δµ maps we were able to spatially resolve the positive increase in Δµ that we denote as $\Delta(\Delta\mu)$ also expressed in *eV*:

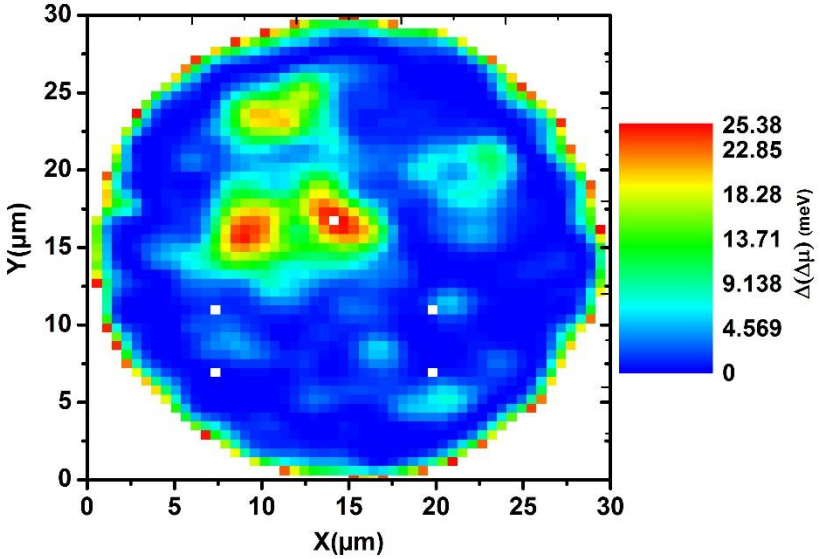



**Figure 4.7: Spatially resolved increase in the quasi-Fermi levels splitting**

Figure 4.7 represents a direct reflection of the spatial distribution of the trapping defects density. The light-induced activation of the metastabilities is clearly spatially inhomogeneous. The areas in the map

where the $\Delta(\Delta\mu)$ is at its maximum represents the area where the highest amount of metastabilities were optically filled by light-soaking. As a result, a map of the absolute trapping defects density would have the same features and morphology as those observed in Figure 4.7.

We can see the Δμ boost varied between 0 and 26 *meV*. We can also deduce that the majority of the micro CIGS solar cell did not exhibit any change in its Δμ. Which could be a good sign. The case we have here contains only localized important densities of metastabilities.

#### 4.2.2.2 Micrometric mapping of charge carrier lifetimes and trapping activity

Now we move from hyperspectral imaging of luminescence to scanning confocal luminescence microscopy. As mentioned earlier, the aim here to reveal the spatial behavior of the minority carrier dynamics and then establish a full micrometric map of the trapping defects density. The micro CIGS solar cell used here is different from the ones used in sections 4.2.1 and 4.2.2.1.

For the spatially-resolved and time-resolved photoluminescence (TRPL) experiments, we used the scanning confocal microscope setup illustrated in Figure 2.8. The selected pulsed excitation wavelength was 700 *nm*. In the present configuration the minimum achievable excitation spot size is 0.8 *μm* The first result is a reconstruction the time-resolved photoluminescence emission of the micro CIGS solar cell as seen in Figure 4.8 below:

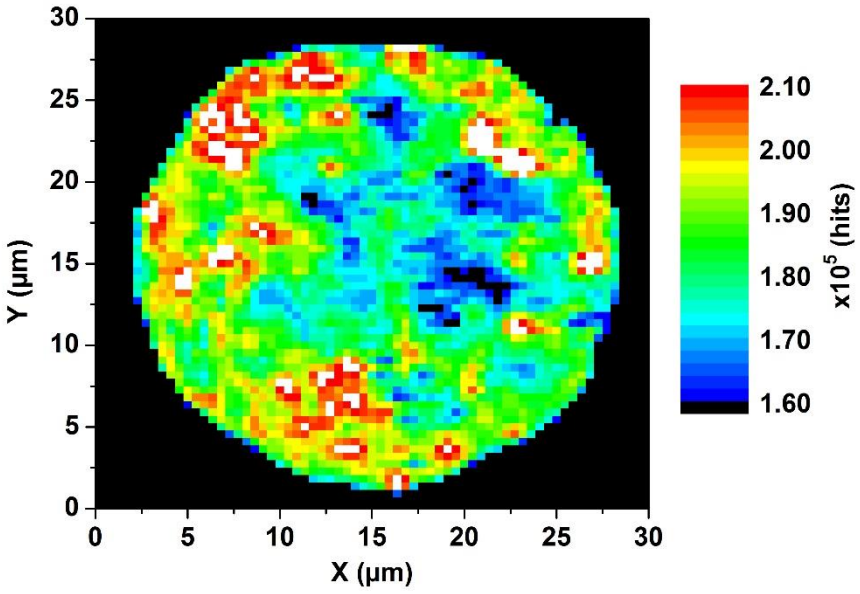


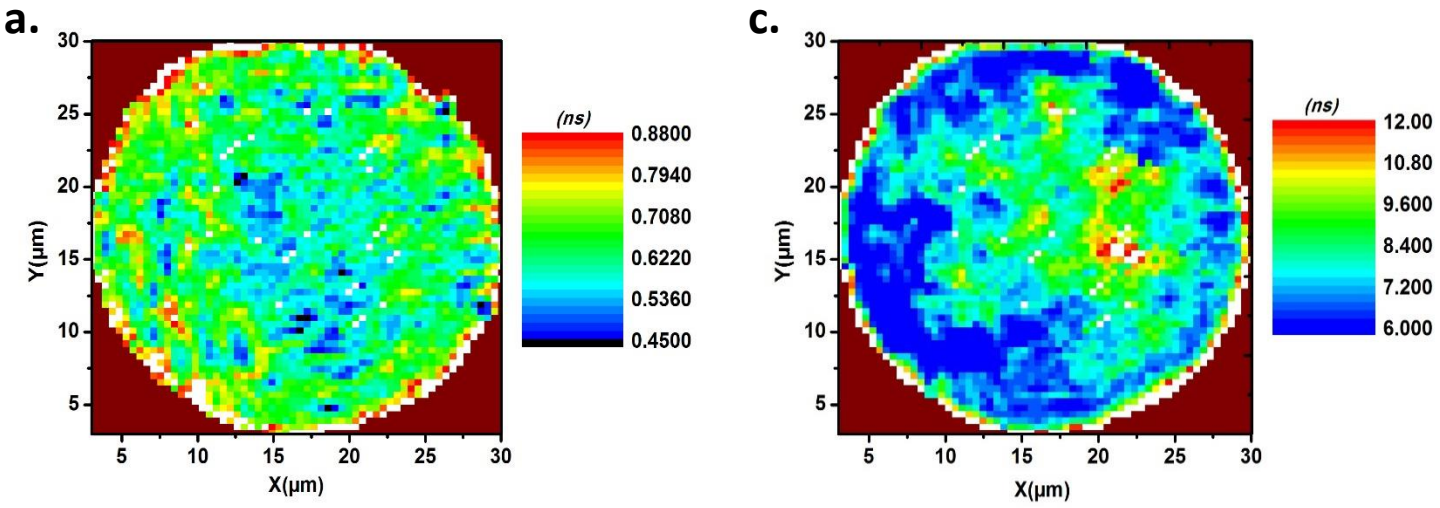

**Figure 4.8: Time-Integrated photoluminescence intensity map**

The latter map is calculated by integrating the spatially-resolved and time-resolved luminescence intensities over time. The calculation of the time-integral of the luminescence intensity $I_{TRPL}^{tot}$ is made using the following expression:

$$I_{TRPL}^{tot} = \int_0^{\infty} I_{TRPL}(t)dt \tag{4.3}$$

After the scanning confocal microscopy (SCM) of the TRPL emission, comes the part where the spatially resolved TRPL decays are analyzed and fitted. We then map the different TRPL decay parameters: The minority recombination lifetime $\tau_{\mathrm{Rec}}$, the minority carrier trapping lifetime $\tau_{Traps}$ and finally the *DCD* parameter based on the extracted occurrence weights $W_{\mathrm{Rec}}^{occ}$ & $W_{Traps}^{occ}$ as previously expressed by equations (3.1) & (3.2).

We start by illustrating the SCM maps related to both minority carrier lifetimes, as well as their corresponding spatial statistical distributions:



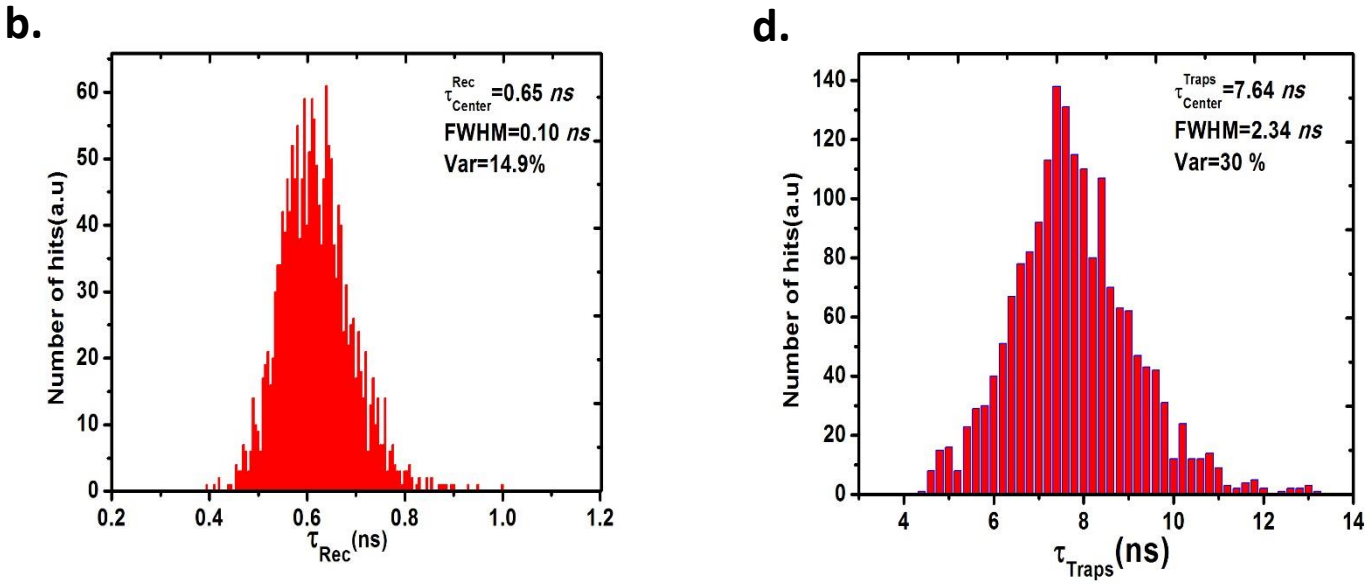



**Figure 4.9: Micrometric map of the minority carrier direct recombination lifetime (a.) and its corresponding statistical distribution (b.). Micrometric map of the minority carrier trapping lifetime via shallow traps (c.) and its corresponding statistical distribution (d.)**

Even though local TRPL measurements are an important tool for the characterization of PV devices, revealing the spatial dimension of these measurements is crucial.

Multiple zones with a maximum and a minimum of the trapping lifetime are observed in Figure 4.9.c. In order to quantify these fluctuations, a histogram plot of the values is illustrated in Figure 4.9.d. Fitting the data with a Gaussian model, we find a central value of $\tau_{Traps}$ that is equal to 7.64 *ns* and a FWHM of 2.34 *ns*. This means that $\tau_{Traps}$ fluctuates spatially in the range of ±30%.

Figure 4.9.a represents the map of the minority carrier lifetime $\tau_{\mathrm{Rec}}$, corresponding to direct recombination events. As expected from [108], no similarity was observed between the spatial fluctuations of $\tau_{\mathrm{Rec}}$ and those of $\tau_{Traps}$. In addition, Figure 4.9.b shows that $\tau_{\mathrm{Rec}}$ fluctuates in the range of ±14.9% with respect to its central value of 0.65 *ns*. Taking into account the systematic fitting error, the fluctuations of $\tau_{Traps}$ are double the fluctuations observed for $\tau_{\mathrm{Rec}}$.

At this stage, the observed spatial fluctuations of $\tau_{Traps}$ & $\tau_{\mathrm{Rec}}$ come again in good agreement with our proposed definitions. In addition, for the sake of device characterization and evaluation of material quality, it is important to justify the compatibility between nature of the observed lifetimes and their spatial behavior.

Moving on to mapping the *DCD* parameter, and based on its previously proposed definition, the *DCD* quantifies the dominance of shallow trap states on the overall minority carrier dynamics. An increasing

value of the *DCD* reflects a decreasing activity and influence of traps on minority carrier dynamics. In particular when the *DCD* tends to get closer to unity, we can hence expect a better carrier transport quality based on a low carrier trapping activity.

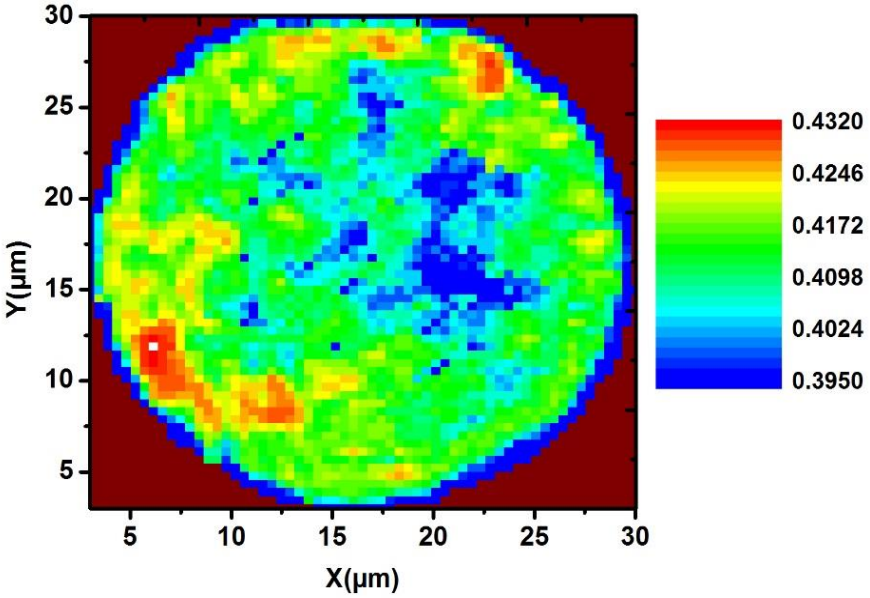



**Figure 4.10: Micrometric mapping of the DCD parameter**

Interestingly, the micrometric DCD map illustrated in Figure 4.10 exhibits a spatial anti-correlation behavior with the $\tau_{Traps}$ map presented in Figure 4.9.c. Figure 4.11 shows that an increase in the carrier trapping lifetime originates from the increasing dominance of traps on the overall carrier dynamics.

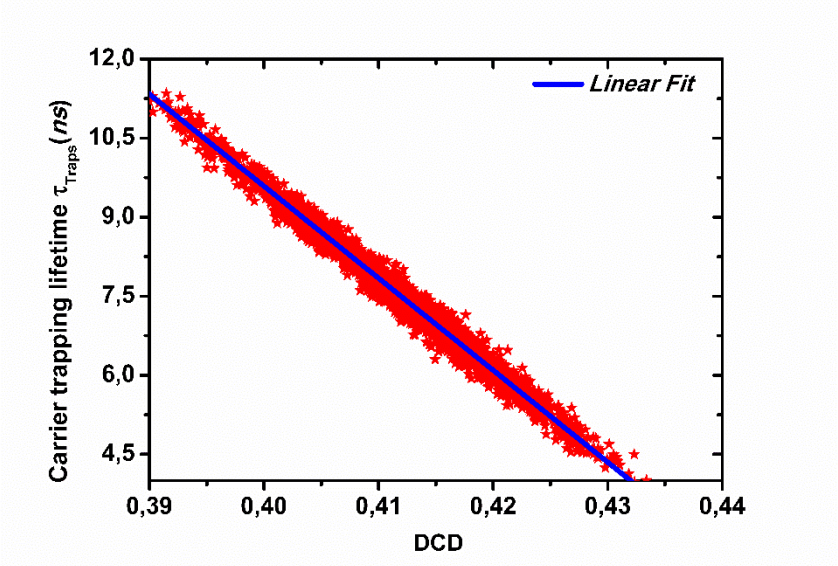



**Figure 4.11: Minority carrier trapping lifetime $\tau_{Traps}$ as a function of the DCD parameter**

It turns out that the minority carrier trapping lifetime $\tau_{Traps}$ decreases linearly from 11 *ns* to 4 *ns* as the *DCD* parameter increases from 0.39 to 0.435. In particular, a spatial area of the solar cell where the *DCD* is minimized corresponds to a maximum of carrier trapping lifetime $\tau_{Traps}$. The regions that revealed a minimum of carrier trapping activity are red colored for the case of the DCD map and blue colored for the case of the $\tau_{Traps}$ map. The remaining regions exhibit moderate or a minimum of carrier trapping activity and thus reflect areas of good interface quality between the CIGS absorber and the CdS layer.

#### 4.2.2.3 Optical micrometric mapping of the absolute trapping defects density

Now that the activity of the solar cell trapping defects has been mapped and analyzed by qualitative means, the authors aim at quantifying and mapping the trapping defects density $\Psi_D$. The applied methodology is the one that we developed and exposed in section 3.3 of the thesis. We applied it to each of the spatially resolved 10201 TRPL decays and the whole process results in a micrometric map of $\Psi_D$ as seen in Figure 4.12.

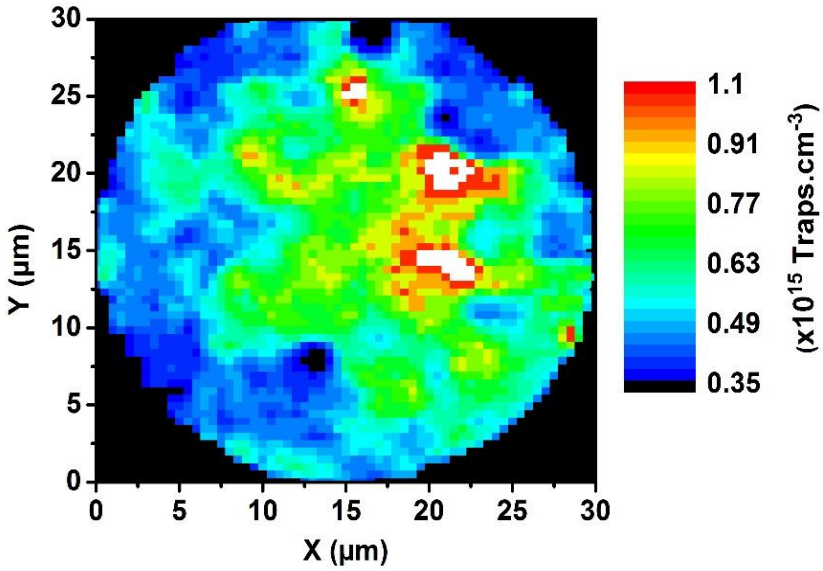



**Figure 4.12: Spatially resolved trapping defects density of the studied CIGS solar cell**

Figure 4.12 exhibited important fluctuations ranging between *3.5x10$^{14}$ traps/cm$^3$* and *1.05x10$^{15}$ traps/cm$^3$*. Even though the calculation process of this key quantity differs from the one used to calculate the previous maps of minority carrier dynamics, an initial observation reveals a correlation between Figures 4.9.c, 4.10 & 4.12. The same regions that reveal maximum values of *DCD* and minimum values of $\tau_{Traps}$, exhibit a spatial minimum of $\Psi_D$. This correlation holds true for all the

remaining regions of the solar cell. In order to investigate the nature of such correlation, the data points of Figures 4.9.c & 4.10 are plotted against those in Figure 4.12, pixel per pixel. The result can be seen in Figures 4.13.a & 4.13.b:

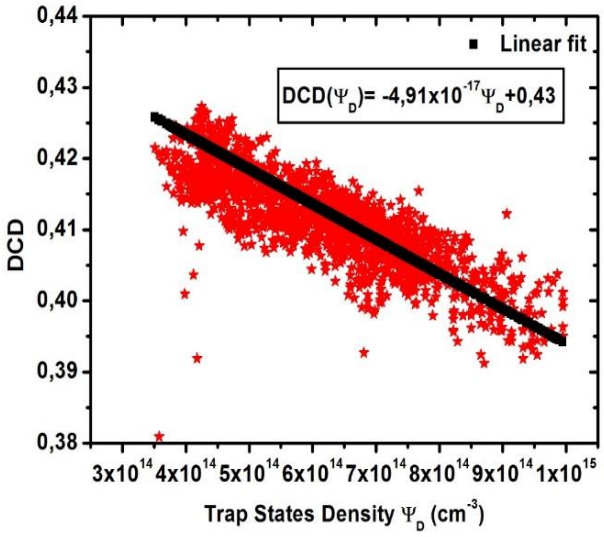



**Figure 4.13.a : Spatial distribution of *DCD* as a function of [the spatial distribution] of the trap states density $\Psi_D$**

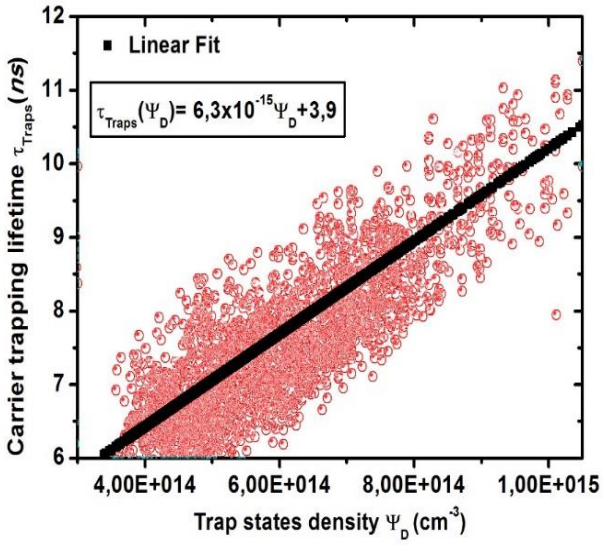



**Figure 4.13.b : Spatial distribution of trapping lifetime $\tau_{Traps}$ as a function of the spatial distribution of the trap states density $\Psi_D$**

From Figures 4.13.a & 4.13.b we deduce that on the one hand, the relationship between the *DCD* parameter and $\Psi_D$ is linear with a negative slope. This negative correlation shows that the CIGS solar cell trap states density ( $\Psi_D$ ) is linearly reflected by its activity (*DCD*). On the other hand, Figure 8.b. comes in good agreement with the physical definitions of $\tau_{Traps}$ and $\Psi_D$. It can be seen that as $\Psi_D$ increases, $\tau_{Traps}$ increases, owing it to their increasing influence on the charge transport mechanism.

Such dependence has been proven at the local scale in one of our recent works [108]. In this present part, this dependence is proven again but this time at the global solar cell scale and its nature is revealed.

### 4.2.2.4 Mapping the micrometric losses in quasi-Fermi levels splitting

Using the HI system, the entire solar cell area is homogeneously illuminated with a photo excitation intensity equivalent to 450 Suns at 532nm. Under these conditions, the solar cell operating points are represented by a short circuit current Jsc=12.73 $A/cm^2$ and an electrically measured open-circuit voltage Voc=0.783 *V*.

We start by calculating the Δμ map expressed in *eV* as seen in Figure 4.14.

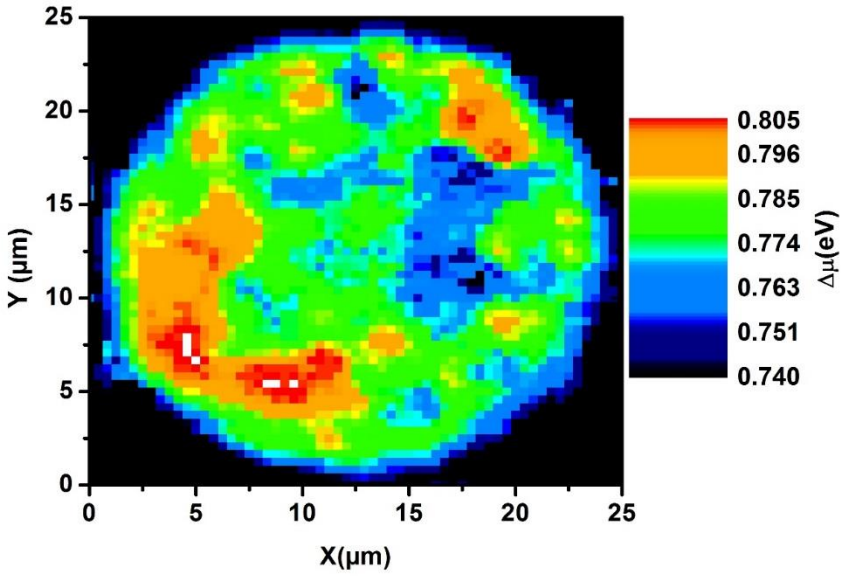



**Figure 4.14: Spatially resolved quasi-Fermi levels splitting Δµ *(eV)* of the studied CIGS solar cell**

The Δµ map seen in Figure 4.14, is the optically determined quasi-Fermi levels splitting and represents the spatial fluctuations of the maximum open-circuit voltage that can be achieved under the previous excitation conditions. A statistical analysis of the Δµ map data revealed a Gaussian distribution with a central value $\overline{\Delta\mu}$ that is equal to 0.789 *eV*. A close match is found between the optically determined central Δµ value and the electrically measured Voc that equals 0.783 *V*. Such spatial fluctuations have been explained by local transport properties difference rather than local voltage differences. In fact, given the small scale of the cell, it could be considered equipotential.

An initial visual assessment of Figure 4.12 and Figure 4.14 reveals spatial anti-correlation between the two maps. Given the different spatial resolutions of the two systems, we applied a resolution interpolation algorithm on both maps so they can be correctly compared and correlated. In order to quantify such correlation, the data points of Figure 4.14 are plotted against those in Figure 4.12, pixel per pixel. The result can be seen in Figure 4.15:

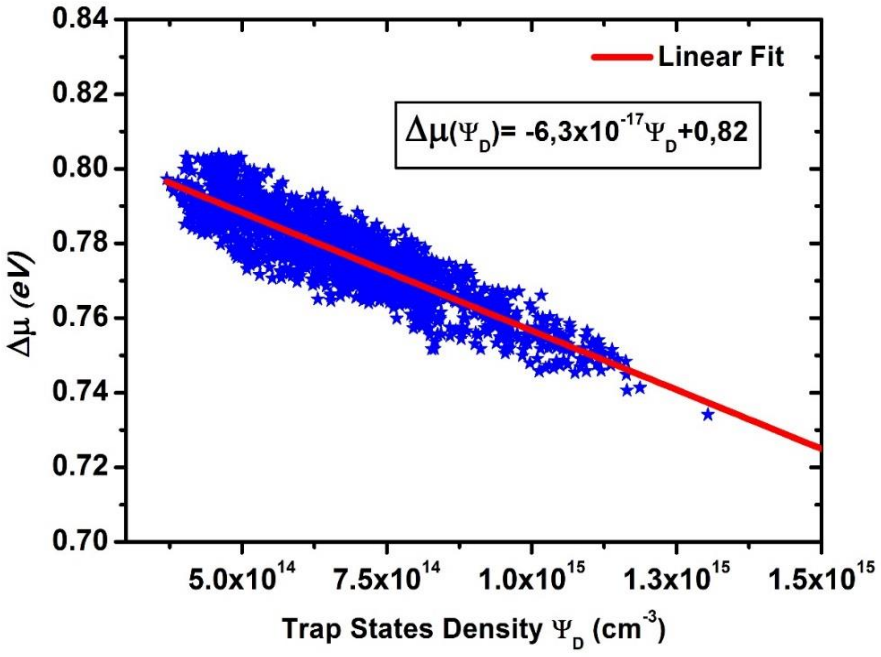



**Figure 4.14: Spatial fluctuations of Δμ as a function of the spatial fluctuations of the trapping defects density**

Figure 4.14 reveals a dependence of the spatial fluctuations of quasi-Fermi levels splitting in a CIGS solar cell on its trapping defects density $\Psi_D$. We can see that an increase in $\Psi_D$ from 3.5x10$^{14}$ *traps/cm*$^3$ to 1.05x10$^{15}$ *traps/cm*$^3$ induces a linear decrease in the Δμ from 0.801 *eV* to 0.76 *eV*. This comes in good agreement with a link between the $V_{oc}$ of a solar cell and its trapping defects density determined from admittance measurements at the global solar cells scale [128].

In addition, Figure 4.14 shows that the spatial fluctuations of Δμ are correlated to those of the trapping defects density $\Psi_D$. Consequently, this result helps to determine one of the origin of the spatial inhomogeneities of the quasi-Fermi levels splitting in thin film solar cells.

From a quantitative point of view, the applied linear fit to the data cloud shows that in case no trapping defects density exists in our material, the latter would exhibit a maximum achievable open-circuit voltage of $V_{oc}^{\max}(\Psi_D = 0) = 0.82$ *V*. In order to test if the trapping defects are solely responsible for the drop in the ideal Δμ value, we set out by calculating the radiative open-circuit voltage of our solar cell $V_{oc}^{rad}$ given by:

$$V_{oc}^{rad} = \frac{kT}{q}\log\left(\frac{J_{sc}}{J_0^{rad}} + 1\right) \tag{4.4}$$

In Eq. (4.3), $J_{sc}$ and $J_0^{rad}$ are the solar cell short-circuit current density and the radiative dark saturation current density, respectively. $J_0^{rad}$ is calculated as follows:

$$\frac{J_0^{rad}}{q} = \int_0^{\infty} EQE(E)\phi_{bb}(E)dE \tag{4.5}$$

Our calculations result in a radiative open-circuit voltage of $V_{oc}^{rad}$ = 0.93 *V*. Which means that among the $V_{oc}^{rad} - \overline{\Delta\mu}$=141 *meV* average total loss in open-circuit voltage, we have $\Delta\mu(\Psi_D = 0) - \overline{\Delta\mu}$ =31 *meV* losses due to interface defects.

Hence, we conclude that the solar cell trapping defects are responsible for about 25 % of the total loss in the open-circuit voltage that can be obtained in the ideal radiative limit.

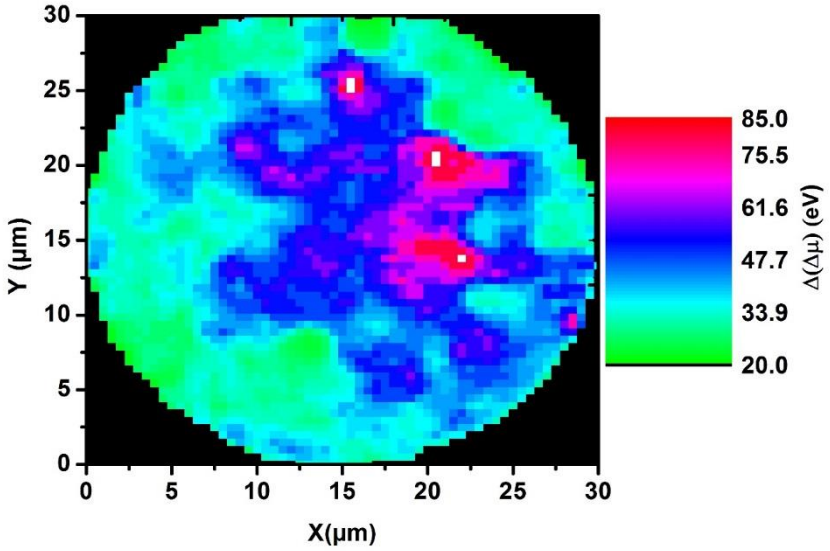



**Figure 4.15: Spatially-resolved absolute losses in open-circuit voltage**

Based on our previous calculations and the linear correlation revealed by Figure. 4.14, we can finally calculate a map showing the different Δμ losses in each particular region of our solar cell, due to the presence of the quantified trapping defects. Based on Figure 4.15, the performance losses vary mainly between 25 *meV* and 85 *meV*.

Based on contactless TRPL measurements we thus evidence at the micrometric scale and in an absolute quantitative way, the different losses in PV performance due to the existence of trapping defects at the interface.

#### 4.2.2.5 Investigating the effect the photo-excitation energy

We have so far demonstrated that through a combination of the spatial, spectral and temporal dependencies of the luminescence in CIGS solar cells, one can optically calculate and map the absolute losses in open-circuit voltage that originate from the material's trapping defects. However, from our local quantitative studies in Chapter III we have clearly demonstrated a high sensitivity of the dynamics

of the luminescence signal to the photo-excitation energy. Given that what we have previously achieved was made using 700 nm and 532 nm excitation wavelengths, we found the necessity to test the excitation energy dependence of the results and the maps of *section 4.2.4.1* and to what extent the latter hold true.

We start by performing excitation-energy dependent, spatially-resolved and time-resolved photoluminescence measurements on the CIGS solar cell. For each excitation energy, we thus deduce a single map of the trapping defects density. We remind that our losses in Δμ in Figure 4.15 were calculated via an extrapolation towards a situation corresponding to $\frac{V_{oc}^{\max}}{q}(\Psi_D = 0)$.

In other words, in order to demonstrate that our developed methodology reveals Δμ losses due to $\psi_D$, we must be able to prove that all of the excitation energies that we use here yield the same extrapolation value $\frac{V_{oc}^{\max}}{q}(\Psi_D = 0)$. From an experimental point of view, it was impossible for us to perform excitation energy-dependent maps of Δμ. Therefore, we looked for an alternative using only the scanning confocal microscope. We know that for a given excitation energy, for each TRPL decay, if we apply equation (4.2) we can calculate the total luminescence intensity. Then, according to the generalized Planck's law, we know that the quasi-Fermi levels splitting is logarithmically related to this total PL intensity.

We finally propose plotting the map of the logarithm of the total PL intensity $I_{tot}$ as a function of the map of $\psi_D$, for each excitation energy. The extrapolated $\ln\left(I_{tot}(\Psi_D = 0)\right)\left|\lambda_i\right.$ value is then calculated.

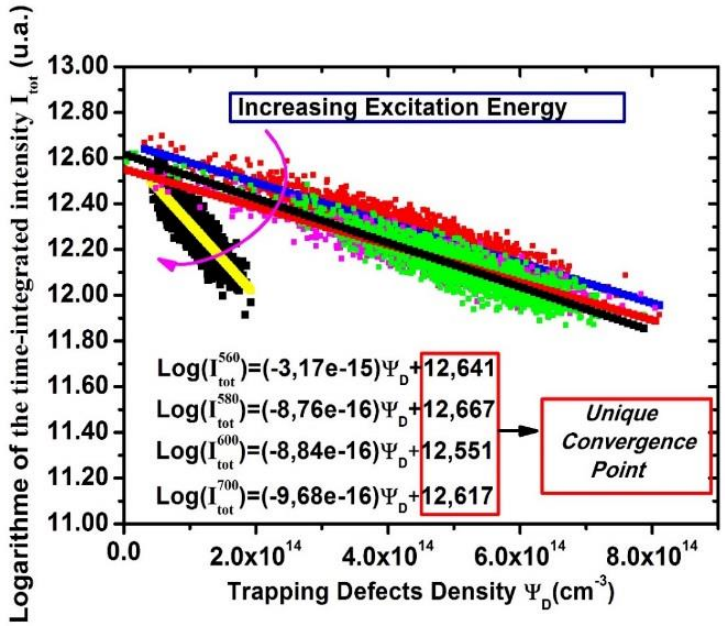



**Figure 4.16: Evolution of the integrated PL intensity as a function of the trapping defects density and as a function of the excitation energy**

We have learned from our previous excitation-energy dependent TRPL studies that once the excitation energy becomes high enough to activate interface trap states, a significant change in the carrier dynamics is observed. In particular, for excitation wavelengths greater than 600 *nm* the behavior of the material charge carriers is quite constant. These previous observations are once again confirmed by Figure 4.16. We can see that for 700 *nm*, 600 *nm* and 580 *nm* excitation wavelengths, the data clouds of $\ln(I_{tot}) = f(\Psi_D)$ are highly similar in both value ranges and slope behavior. However, for the particular case of the 560 *nm* excitation wavelength, we can see that only a 20 *nm* difference in wavelength, causes a substantial change in $\ln(I_{tot}) = f(\Psi_D)$.

In particular, we notice the important shrinkage of the data cloud which means that the probed $\psi_D$ value range became narrower as the excitation energy is high enough to activate the large majority of the material trapping defects.

Finally, the main and most important observation revealed by Figure 4.16 is the fact that regardless of the excitation energy, all data clouds converge towards a unique extrapolation point of $\ln(I_{tot}(\Psi_D = 0)) \cong 12.6 | \forall \lambda_i$.

This key result proves that our previously quantified map of losses in open-circuit voltage due to trapping defects holds true as a function of the excitation energy.

## 4.3 Time-Resolved Fluorescence Lifetime Imaging (TRFLIM) of Solar Cells

In this section we move to the third major step of the project execution phase. We will be presenting a first application of our TRFLIM technique. This will demonstrate the successful operation of our homemade TFRLIM setup and the usefulness of this technique for PV characterization.

### 4.3.1 GaAs solar cell – An experimental study

After the first proof of concept of TRFLIM on a perovskite-based solar cell, we set our TRFLIM setup in wide-field luminescence imaging mode. Here the entire solar PV device is homogeneously illuminated using our *Talisker* source and our previously described excitation systems. The sample that is under study here is a GaAs-based solar cell bought from the *Fraunhofer ISE*. Its structure is given in Figure 4.17. In addition, a two layer anti-reflective coating of 52 *nm* $Ta_2O3$ and 80 nm $MgF_2$ is deposited on the surface. The sample has an area of 0.47 $mm^2$.

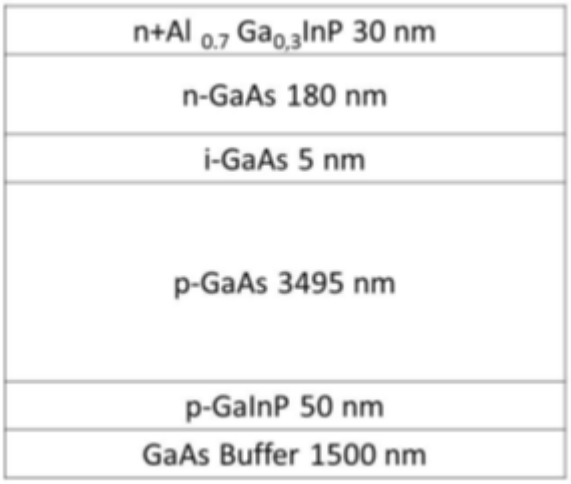



**Figure 4.17: Layers sequence of the GaAs based solar cells under study**

In the present TRFLIM configuration, we start by synchronizing the excitation and the detection. The result is a series of frames representing photoluminescence images of the whole studied sample as a function of time. The results are shown in Figure 4.18:

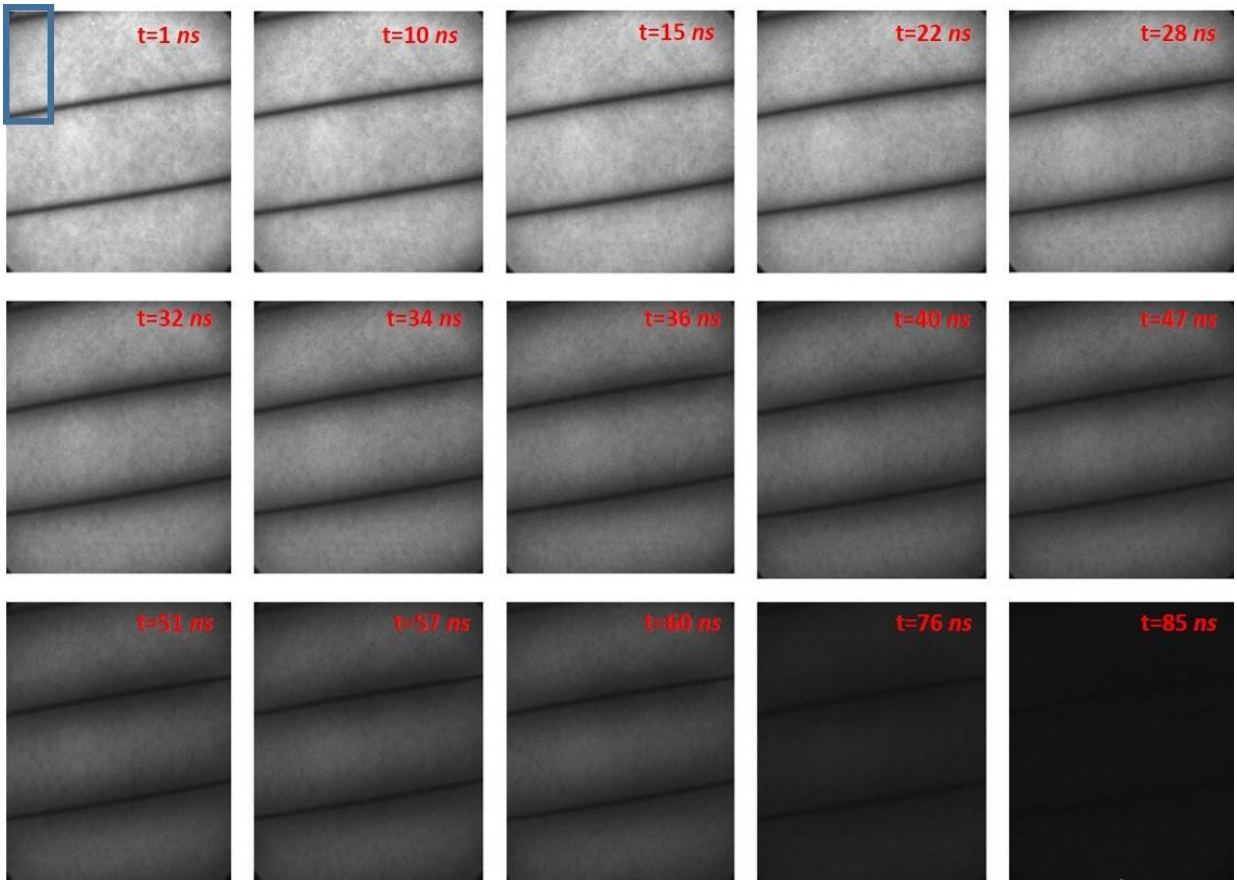



**Figure 4.18: Time-resolved photoluminescence images of the full GaAs-based solar device**

The whole TFRLIM hypercube consisted of 300 photoluminescence images separated by a 12 *ps* time step. The shortest possible time separating two TFRLIM frames is 6.02 *ps*.

In Figure 4.18 we displayed 15 PL images that clearly show what we were hoping to obtain since the beginning of the project: High resolution, time-gated PL images of a complete PV device with picosecond time-resolution. These 15 PL images, show the clear decay of the PL intensity as a function of the time-lapse.

Given that our *em-ICCD* chip is *1024 pixels *1024 pixels* in size, this means that our complete TRFLIM data cube of the GaAs sample, contains *1048576* time-resolved photoluminescence decays. Each decay being the temporal profile of each pixel intensity.

In Figure 4.19 we show an example of a TRPL decay extracted from the TFRLIM cube of our GaAs sample.

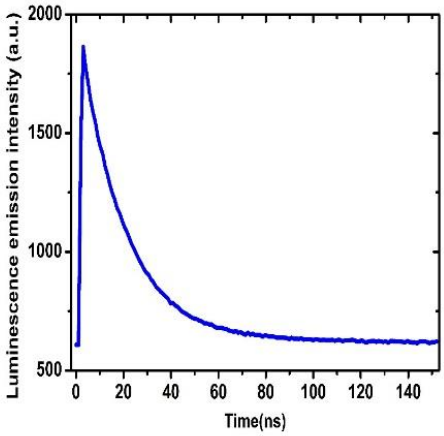



**Figure 4.19: Spatially-averaged Time-resolved photoluminescence decay of the GaAs-based solar device**

In order to go deep in our analysis, we aim at investigating the spatial behavior of the extracted photoluminescence decays within particular regions of the studied solar cell. In particular, we are interested in studying the evolution of the carrier dynamics near the metallic contacts and the solar cell edge. Therefore, we focus in Figure 4.18 on a region (highlighted in the blue rectangle) that includes both the metallic contact and the solar cell edge. For the selected region, we extracted the corresponding time-integrated TRPL intensity map. Given the known physical dimensions of the metallic contact, we were able to extract *pixel/µm* ratio and transform our pixels axes into a physical length expressed in µm. The calibrated map is illustrated in Figure 4.20:

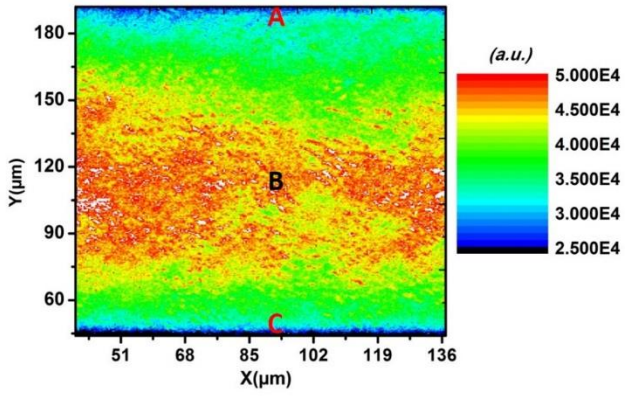



**Figure 4.20: Time-integrated, luminescence intensity map of the GaAs solar cell (central zone B) including the contact (region C) and sample edge regions (region A)**

The region that contains the metallic contact is the black stripe in the upper edge of Figure 4.20 (region A). Whereas the region that contains the edge of the solar is the black stripe located at the bottom of Figure 4.20 (region C). The GaAs solar cell material is located between these two stripes (region B).

Initially, we can detect a certain intensity gradient whereby the integrated luminescence intensity decreases as we move away from the central area, towards the contact and edge areas. Such gradient reflects different carrier recombination and dynamics. In order to quantify this gradient, we illustrate in Figure 4.21 the vertical intensity profiles for different decay times.

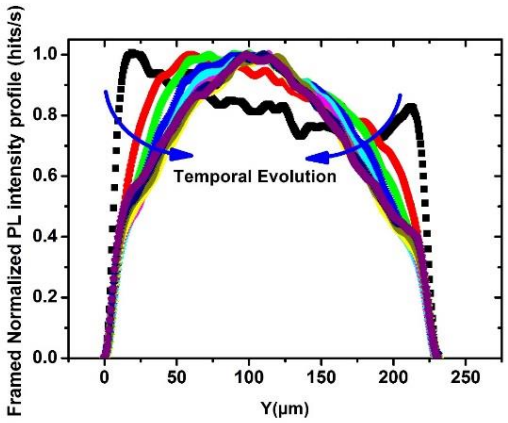



**Figure 4.21: Evolution of the Vertical PL intensity profiles as a function of time extracted from each PL image**

The intensity profile presented in black corresponds to the maximum intensity point of the time-resolved luminescence decay (i.e. sub-image 1 of Figure 4.18). We can see the profile is relatively monotonous compared to the remaining profiles where the central gradient is pronounced. We can see that the profiles become narrower as a function of time. This means that the intensity gradient towards the center becomes more important.

Given that carrier recombination gives rise to observed PL intensity, these profiles actually reflect their spatial distribution. For the very first frame, the intensity profile arises from a rather uniform carrier distribution. At this very instant the photogenerated carrier concentration is at its maximum. The charge carriers are not drawn by contact and edge recombinations.

However, as their concentration decreases as a function of time, the carriers become increasingly influenced by several mechanisms and their migration towards the contact and edge becomes greater. This explains the sharper intensity profile which is the representation of their dynamics towards these two areas where they recombine. Indeed, the steepness of the profiles in the contact and edge regions will depend on the corresponding surface recombination velocities. Different carrier behavior as a function of their spatial position, should lead to different time-resolved luminescence decay dynamics. To illustrate such fact, we extract three different TRPL decays, each corresponding to one of the particular areas that we define here as area *A* for the edge, area *B* for the center and area *C* for the contact (see Figure 4.20).

The three decays are shown in Figure 4.22:

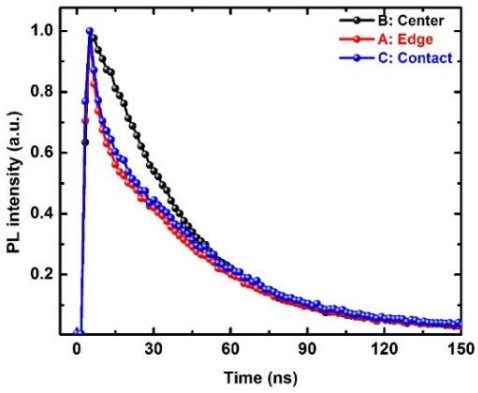



**Figure 4.22: Time-resolved photoluminescence decays of the GaAs solar cell at regions A, B and C of Fig 4.21**

An observation of the TRPL decays informs us that the latter are spatially-dependent. In particular, we can see that the central area of GaAs solar cell yields slower TRPL decay dynamics compared to the faster dynamics at the edge and contact areas.

This comparison however is only valid for the first part of the TRPL decays. For the remaining part, we obtain quite similar TRPL decay dynamics. This is a first hint according to which we can conclude that the first part of the decay is related to edge and contact recombinations. The second longer part being spatially-independent, probably points out towards bulk recombination within the GaAs material.

Still on a qualitative side, we can also notice that the intensity decays faster in the edge region in comparison with the contact area. This difference probably arises from a faster surface recombination velocity at the edge of the GaAs solar cell.

To quantify all of these differences in TRPL dynamics, we start by fitting the three decays using simple exponential–based models. Firstly, the fitting converged using a double exponential decay model for the central, contact and edge area decays. Whereas for the contact and edge regions, double exponential decay model is needed.

Based on these observations, we define $\tau_2$ as the recombination lifetime that mainly characterizes the bulk of the GaAs material, $\tau_1^{edge}$ & $\tau_1^{cont}$ the surface recombination lifetimes of carriers at the edge and the contact of the solar cell, respectively. Finally, for the central region, a $\tau_1^{center}$ lifetime can be observed. Quantitatively, it seems to be longer than $\tau_2^{center}$. At this stage, we speculate that it is a type of a latency lifetime where carriers generated at the central area, decay much slowly before their

concentration becomes small enough to be influenced by the transport towards the edge and the contact. Further investigation is needed in order to confirm its nature.

In our case we obtain:

For zone A: $\begin{cases} \tau_2^{edge} = (41 \pm 0.38)ns \\ \tau_1^{edge} = (3.05 \pm 0.04)ns \end{cases}$

For zone B: $\begin{cases} \tau_1^{center} = (55 \pm 1.23)ns \\ \tau_2^{center} = (32 \pm 0.26)ns \end{cases}$

For zone C: $\begin{cases} \tau_2^{cont} = (39 \pm 0.29)ns \\ \tau_1^{cont} = (6.06 \pm 0.12)ns \end{cases}$

We learn from these fitting results that the studied GaAs material has an effective bulk recombination lifetime of $\tau_2$ that possesses a constant component of around 32 *ns* modulated by a spatial dependence on the edge and contact recombinations.

We also learn that its photogenerated carriers recombine twice as faster at its edge than at its contact area.

### 4.3.2 GaAs solar cell – A numerical study & material properties extraction

In order to deepen our understanding of the underlying physics behind the previous TFRLIM experiment on the GaAs sample, we refer to a numerical study. In particular, our objective is to model the behavior of the carrier dynamics in a GaAs material at both temporal and spatial scales. Then, after a successful mimic of the experimental results, we vary the parameters of the simulated material until a match is obtained between the decays in Figure 4.22 and the simulated ones. This operation will help us extract the electronic properties of our GaAs sample.

Our numerical too consists of *Matlab* toolbox called *pdetool* where *pde* stands for *Partial Differential Equation*. The procedure consists of an initial definition of a medium with fixed dimensions, in which we will map the spatial behavior of the carrier distribution. The numerical tool then allows us to simulate time-resolved, spatial carrier distribution which corresponds to a TRFLIM experiment. With such configuration, the toolbox will handle the partial differential equation:

$$d\frac{\partial u}{\partial t} - \nabla.(c\nabla u) + au = f \tag{4.6}$$

In the scope of our numerical study, we define the following parameters that will be used to solve (4.6):

$$\begin{cases} d = 1 \\ c = D_n \\ a = 1/\tau_n \\ f = G \end{cases}$$

where $D_n$ is the electron diffusion coefficient, $\tau_n$ the characteristic carrier lifetime of the material and the inverse of the recombination rate, and *G* is the a time-dependent photogeneration. *G* is taken here as *G=0* because experimentally, the photogeneration occurs during the pulse width of 15 *ps* and then excess concentration decays as a function of time. Our experimental photogeneration is thus an initial condition for the variable *u* which stands for *n* the excess electron concentration. Hence, *n(t=0)* is the experimental photogeneration of $2.7 \times 10^{14}$ $cm^{-3}$. We rewrite (4.6) as:

$$\frac{\partial n}{\partial t} - D_n \nabla.(\nabla n) + \frac{n}{\tau_n} = 0 \tag{4.7}$$

As we are performing luminescence imaging we define our photogeneration as being homogeneous all over the medium. Numerically, the medium is 137 $\mu m$ in width and 192 $\mu m$ in length, similarly to the studied area in the experimental section. The boundary conditions have to be defined in order to replicate those at the edge and contact regions of the GaAs solar cell. At the boundaries, the excess carrier concentration obeys the following differential equation in which the recombination velocity parameter $S_n$ appears:

$nS_n + D_n \frac{\partial n}{\partial y} = 0$, with the following boundary conditions: (4.8)

$$\begin{cases} S_n(X = 0) = 0 \\ S_n(X = 137) = 0 \\ S_n(Y = 0) = S_n^{cont} \\ S_n(Y = 192) = S_n^{edge} \end{cases}$$

where, $S_n^{cont}$ & $S_n^{edge}$ are the electron contact and edge surface recombination velocities, respectively, expressed in $cm.s^{-1}$.

As mentioned above, our goal is to mimic the spatial and temporal behavior of the excess carriers obtained in the experimental section. For the central regions the bulk characteristic lifetime and the diffusion coefficient were varied until a temporal and spatial match are found. Whereas for the edge and contact regions, $S_n^{cont}$ & $S_n^{edge}$ were varied until the matches are found also.

We start by displaying a first result which is a simulated mimic of Figure 4.20:

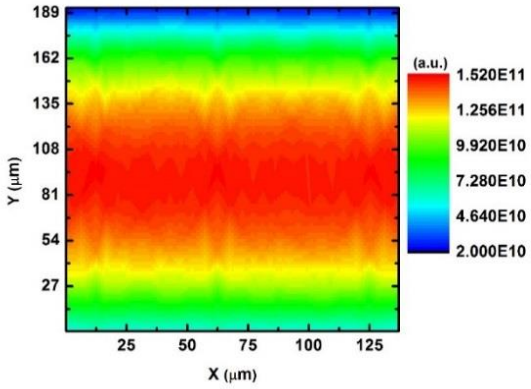



**Figure 4.23: Simulated, time-integrated luminescence intensity map of the GaAs solar cell**

Figure 4.23 reveals a reconstruction of the spatial gradient observed in Figure 4.20. We can see that the luminescence intensity peaks at the central area and decreases as it reaches the simulated edge and contact regions. In addition, we can notice a more important decrease in the edge region compared to the contact region. This arises from the experimental difference we observed and that is numerically mimicked here.

Moving from the spatial to the temporal dependency, we plot again the vertical intensity profiles taken from each simulated TRFLIM image:

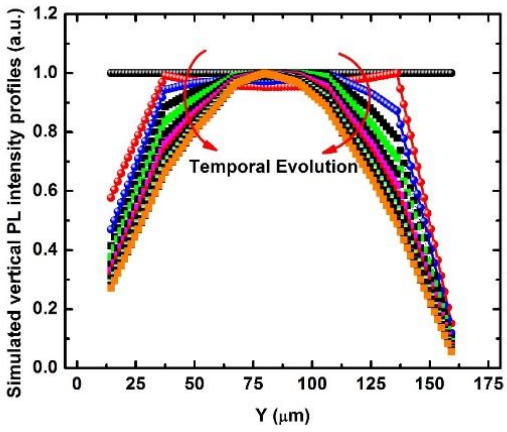



**Figure 4.24: Simulated evolution of the Vertical PL intensity profiles as a function of time**

When compared with Figure 4.21, we again observe that for the very first instant of the simulation, the intensity profile is flat. The latter becomes narrower and slightly asymmetric as a function of time, revealing the simulated intensity gradient towards the central area. This allows to conclude that so far, our simulation match the spatial and temporal behavior of our carrier dynamics extracted from the TRFLIM experiment on GaAs. Therefore, the numerical reconstructions of the experimental spatial and temporal dependencies come as addition confirmation and evidence.

In order to further elaborate on the reconstruction of the temporal dependency of the experimental results, we extracted three simulated TRPL decays taken at the edge, center and contact areas similarly to the case of Figure 4.22.

In Figure 4.25, we plot together the simulated and experimental TRPL decays:

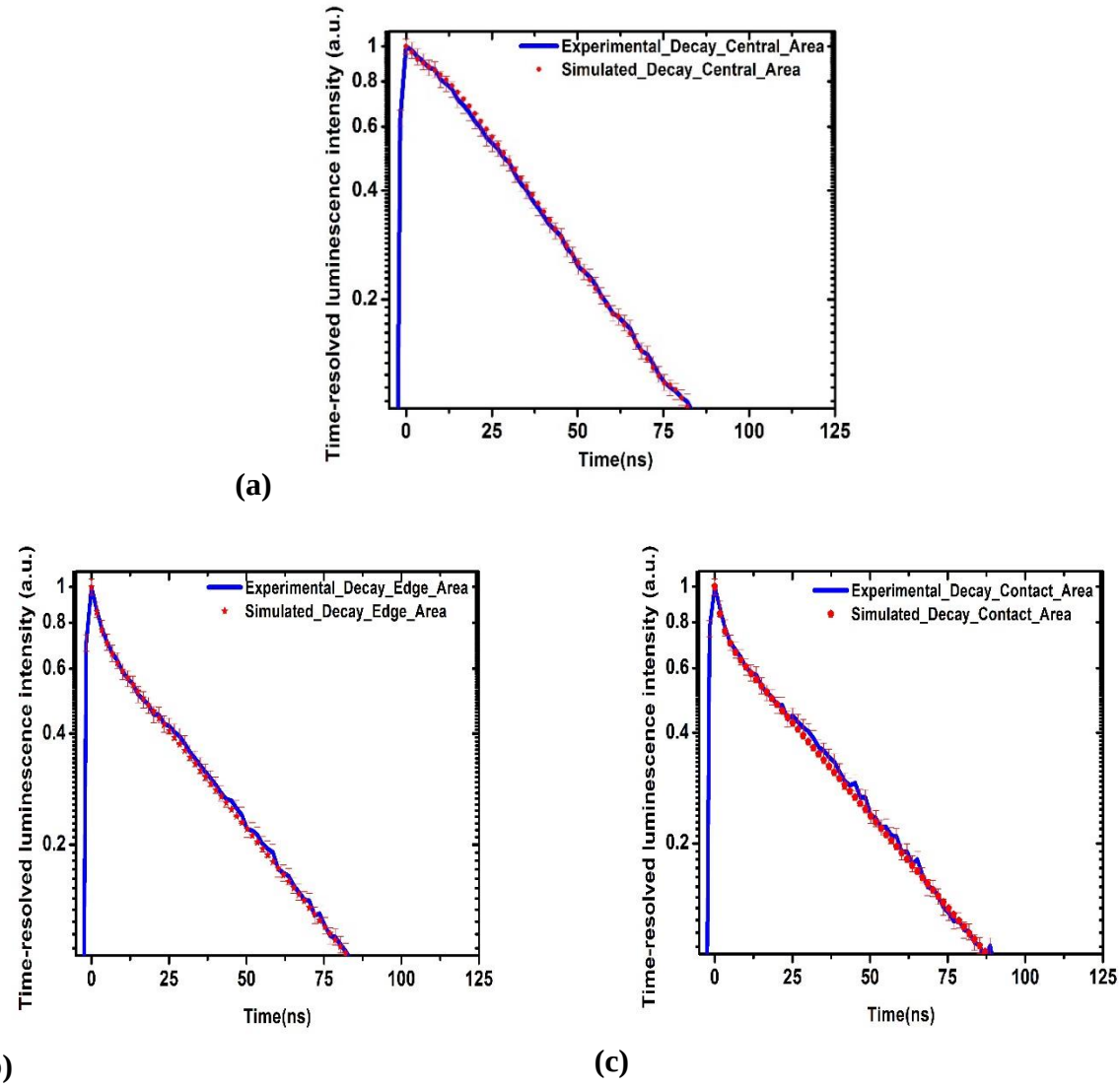



**Figure 4.25: Experimental and simulated TRPL decays for the central (a), edge (b) and contact (c) regions of the GaAs solar cell**

The global reconstruction error for the simulated TRPL decays is in the order of $\pm 5\%$. Figure 4.25 comes as additional evidence regarding the ability of our simulation to take into account the different parts of the experimental TRPL decays and come in good agreement with their variations according to their spatial domain that they belong to.

Our simulation has also a quantities advantage regarding the properties of the GaAs material we are studying here. The latter that made all of the matching with the experimental work possible are:

- The material diffusion coefficient: $D_n = 135 cm^2 s^{-1}$
- The material bulk carrier lifetime: $\tau_n = 50 ns$
- The edge recombination velocity: $S_n^{edge} = 10^5 cm.s^{-1}$
- The contact recombination velocity: $S_n^{cont} = 5.12x10^4 cm.s^{-1}$

The simulation work revealed that indeed, the surface recombination velocity at the edge is double the surface recombination velocity at the contact of the solar cells confirming the initial guess from the experimental data.

This adds as a quantitative agreement between the experimental and simulation TRFLIM studies and helped determine key electronic properties of the GaAs solar cell.

Based on these findings, we are also able to calculate the carrier diffusion length $L_n$ and the carrier mobility $\mu_n$ and the doping density $N_d$ within our GaAs solar cell.

Using $L_n = \sqrt{\tau_n D_n}$, we find $L_n = 25\mu m$.

Using Einstein's relation, given T=300K, $D_n = \frac{kT}{e}\mu_n$, we find $\mu_n = 5224 cm^2 V^{-1} s^{-1}$

Then, based on Hilsum's law [162], the relation between the electron mobility in GaAs and its doping density is given by:

$$\mu_n = \frac{9400}{\sqrt{(1+10^{-17} N_d)}} \tag{4.9}$$

In our case, by considering that the mobility is mainly dependent on the doping density of the material, we estimate that our GaAs material has a doping density of $N_d = 3.3x10^{17} cm^{-3}$.

Finally, in order to test the significance of the values of the extracted material properties, we compared them to those found in the literature [162]. Here are the value ranges that we found:

$$\begin{cases} D_n \leq 200 cm^2 s^{-1} \\ \tau_n = 5x10^{-9} s \rightarrow 2.5x10^{-7} s \\ L_n = 10\mu m \rightarrow 70\mu m \\ S_n = 10^4 cms^{-1} \rightarrow 10^7 cms^{-1} \\ \mu_n \leq 8500 cm^2 V^{-1} s^{-1} \end{cases} \quad [162]$$

All of our extracted values fit well within the previous ranges.

# Conclusion

My PhD work was dedicated to the development of new luminescence-based characterization methods of thin film solar PV devices. We started by revisiting and upgrading the analysis of time-resolved photoluminescence decays on CIGS solar cells. This lead to a physical model that explained the different experimental tendencies of TRPL decays on our samples. Our revisited explanation of the TRPL decays in CIGS distinguishes and quantifies the effect of recombination centers and the effect of shallow traps.

This allowed us to develop a new application that resulted in an all-optical study of the well-known metastabilities in CIGS devices. This first achievement represents a contact-less alternative for the typical electrical studies. In addition, our methodology showed that thanks to its excitation energy-dependence, it is possible to estimate the physical location of these metastabilities. In our case we were able to deduce that the latter are mainly present at the absorber/buffer layer interface.

Our second achievement was inspired from the first one. Our experimental understanding of carrier dynamics and its behavior under the influence of traps led to the development of a system of rate equations. The latter replicates the experimental TRPL observations. Once coupled to a developed optimization algorithm, we managed to reconstruct the obtained TRPL decays with less than 5% relative reconstruction error. Most importantly, our developed TRPL decay reconstruction methodology has a single output, which is an estimation of the PV material trap states density. Applying our work to a set of different CIGS solar cells, revealed a correlation between the open-circuit voltage and SCR-related dark saturation current and the trapping defects density that we quantify. In addition to its quantitative nature, our optical tool is also able to predict a PV performance and quantify the properties of the CIGS absorber/buffer layer interface. However, this quantitative section was concluded by listing some its major limitations and the ambiguities that it can suffer from, especially when it comes to the values of the some of the simulations parameters and their validity. Therefore, we believe that this numerical approach is promising but needs to be upgraded and improved.

The third major step of my PhD was to apply all of the previous findings at the global solar cell scale. In other words, we set off by mapping our previous findings, at the micrometric scale. This had initially involved a micrometric mapping of the carrier dynamics using spatially-resolved and time-resolved photoluminescence measurements. This was followed by optically mapping the material trapping

defects density using our developed method. We examined and analyzed their inhomogeneities and found direct spatial correlation between the way charge carriers behave and the trapping defects density.

Given that we have already discovered a correlation between the global open-circuit voltage and the trapping defects density, we wanted to test if this correlation is valid at the micrometric scale. Therefore, using the hyperspectral imager, we acquired spatially-resolved and spectrally-resolved absolutely calibrated photoluminescence images. Applying the generalized Planck's law led to the calculation of a map of the absolute quasi-Fermi levels splitting that represents the maximum-obtainable open-circuit voltage. The comparison of the latter with the trapping defects map revealed a linear correlation between the two maps. From this, we were able to predict the absolute losses in open-circuit voltage due the presence of traps. This prediction was made for every micrometer of the solar cell. The final result is a complete map of the absolute losses in PV performance. This revealed particular regions where the loss in performance in maximized.

The final major step of my PhD project was dedicated to the design and the development of a new opto-mechanical setup at IRDEP. The latter was built to perform time-resolved fluorescence lifetime imaging (TRFLIM) experiments. I detailed in my manuscript the different building blocks of this project. I then showed the different system characterization steps. We successfully obtained submicron and subnanosecond spatial and temporal resolutions, respectively. After completing the total setup, I have illustrated a proof of concept on a perovskite-based solar cell. This confirmed the successful operation of our TFRLIM system and helped illustrate its working principle. I ended this part of the PhD by showing an application on a GaAs sample. By using this technique and combining with a thorough simulation work, we developed an understanding of the spatial and temporal dependencies carrier dynamics in a GaAs solar cell. In addition, this helped us quantify its key electronic properties such as the diffusion coefficient, the bulk lifetime, doping density and carrier mobility.

I would like to add that I summarized in Appendix A, a collaboration work on the quantification of the spatial inhomogeneites of perovskite-based solar cells by mapping its luminescence. This work done in parallel with my core PhD work, was particularly interesting for me. It gave me a hands-on research experience on perovskite material which is a rising star in the PV field and that is quickly approaching the industrialization phase given the unprecedented rise in its power conversion efficiency. I would like to thank my PhD supervisor Laurent Lombez for offering me such a beautiful opportunity.

Finally, I truly hope that we managed through this PhD, to highlight the importance of the luminescence of solar cells. We showed that by finding the right way to analyze it, one derives and quantifies a large array of key PV parameters and material properties. We successfully merged together the spatial, intensity-dependent temporal and spectral aspects of the luminescence of CIGS solar cells. This merger further widened our knowledge and understanding of the optoelectronic properties of CIGS down to the micrometric scale. We have also managed to introduce a new technique to the field of PV

characterization, which is our homemade TRFLIM setup. In the future, I also hope that this setup will be exploited to further push the boundaries of quantitative, luminescence-based PV characterizations and continue to introduce new innovative applications to this field.

# Bibliography


[1] International Panel on Climate Change, 2007, Fourth Assessment Report.

[2] A.Luque and S.Hegedus, 2003, The Handbook of Photovoltaic Science and Engineering, Wiley.

[3] Green Energy – Solar Energy, Photovoltaic (PV) Cell, 2011.

[4] International Energy Commission, Energy technology Perspectives: Scenarios and Strategies to 2050, 2008.

[5] Japan's Largest Solar Panel Factory Reaches Full Commercial Operations, Announces Solar Frontier. 2011; Available from: http://www.solar-frontier.com/eng/news/2011/C002132.html.

[6] TSMC Solar – best-in-class production of groundbreaking products. Available from: http://www.tsmc-solar.com/technology/production.

[7] CIGS PV firm MiaSolé raises a further $55m from VC investors. 2012; Available from: http://www.semiconductor-today.com/news_items/2012/MAR/MIASOLE_080312.html.

[8] Fan-Tai Kong, Song-Yuan Dai, and Kong-JiaWang, Review of Recent Progress in Dye-Sensitized Solar Cells, 2007.

[9] GmbH, S. (2015). Solar Frontier hits 22.3% on CIGS cell. [online] pv magazine. Available at: http://www.pv-magazine.com/news/details/beitrag/solar-frontier-hits-223-on-cigs cell_100022342/ [Accessed 22 Dec. 2015].

[10] Empa.ch. (2016). Empa - A new world record for solar cell efficiency. [online] Available at: https://www.empa.ch/web/s604/weltrekord [Accessed 10 May 2016].

[11] J. Poortmans and V. Archipov, Thin Film Solar Cells, John Wiley & Sons, New York, NY, USA, 2006.

[12] J.-F. Guillemoles, L. Kronik, D. Cahen, U. Rau, A. Jasenek, and H.-W. Journal of Physical Chemistry B, vol. 104, no. 20, pp. 4849–4862, 2000.

[13] J. H. Scofield, A. Duda, D. Albin, B. L. Ballard, and P. K. Predecki, Thin Solid Films, vol. 260, no. 1, pp. 26–31, 1995.

[14] R. J. Matson, O. Jamjoum, A. D. Buonaquisti et al. vol. 11, no. 3, pp. 301–305, 1984.

[15] E. Moons, T. Engelhard, and D. Cahen, Journal of Electronic Materials, vol. 22, no. 3, pp. 275–280, 1993.

[16] M. Powalla and B. Dimmler, Thin Solid Films, vol. 361, pp. 540–546, 2000.

[17] R.Menner, E. Gross, A. Eicke, et al., in Proceedings of the 13th European Photovoltaic Solar Energy Conference, p. 2067, Nice, France, 1995.

[18] R. A. Hoffman, J. C. Lin, and J. P. Chambers, Thin Solid Films, vol. 206, no. 1-2, pp. 230–235, 1991.

[19] K. Granath, A. Rockett, M. Bodegard, C. Nender, and L. Stolt, in Proceedings of the 13th European Photovoltaic Solar Energy Conference, pp. 1983–1986, Nice, France, 1995.

[20] G. Gordillo, M. Griz´alez, and L. C. Hernandez, Solar Energy Materials and Solar Cells, vol. 51, no. 3-4, pp. 327–337, 1998.

[21] M. A. Mart´ınez and C. Guill´en, Surface and Coatings Technology, vol. 110, no. 1-2, pp. 62–67, 1998.

[22] T. Haalboom, T. Godecke, F. Ernst, M. Ruhle, R. Herberholz, and H. W. Schock, in Proceedings of the 11th International Conference on Ternary and Multinary Compounds, pp. 249–252, Salford, UK, 1998.

[23] J. C. Mikkelsen, Journal of Electronic Materials, vol. 10, no. 3, pp. 541–558, 1981.

[24] H. Jitsukawa, H. Matsushita, and T. Takizawa, Journal of Crystal Growth, vol. 186, no. 4, pp. 587–593, 1998.

[25] U. Rau, M. Schmitt, J. Parisi, W. Riedl, and F. Karg, Applied Physics Letters, vol. 73, no. 2, pp. 223–225, 1998.

[26] V. Nadenau, D. Hariskos, H.-W. Schock et al., Journal of Applied Physics, vol. 85, no. 1, pp. 534–542, 1999.

[27] D. Schmid, M. Ruckh, and H. W. Schock, Solar Energy Materials and Solar Cells, vol. 41-42, pp. 281–294, 1996.

[28] M. A. Contreras, M. J. Romero, B. To et al., Thin Solid Films, vol. 403-404, pp. 204–211, 2002.

[29] U. Rau and M. Schmidt, Thin Solid Films, vol. 387, no. 1-2, pp. 141–146, 2001.

[30] W. E. Devaney, W. S. Chen, J. M. Stewart, and R. A. Mickelsen, IEEE Transactions on Electron Devices, vol. 37, no. 2, pp. 428–433, 1990.

[31] Singh, U. and Patra, S. (2010). International Journal of Photoenergy, 2010, pp.1-19.

[32] J. Nelson, 2003, *The physics of solar cells*, Imperial College Press.

[33] Steven S. Hegedus and William N. Shafarman. Progress in Photovoltaics: Research and Applications, 12(23):155-176, March 2004.

[34] Slooff, L., Veenstra, S., Kroon, J., Moet, D., Sweelssen, J. and Koetse, M. (2007). Appl. Phys. Lett., 90(14), p.143506.

[35] Dennler, G., Forberich, K., Scharber, M., Brabec, C., Tomiš, I., Hingerl, K. and Fromherz, T. (2007). J. Appl. Phys., 102(5), p.054516.

[36] Law, M., Beard, M., Choi, S., Luther, J., Hanna, M. and Nozik, A. (2008). Nano Letters, 8(11), pp.3904-3910.

[37] S.B. Zhang, S-H Wei, and A. Zunger, Phys. Rev. B, Vol 57, No. 16 pp 9642-9668 (1998).

[38] L.L. Kerr et al. NCPV and Solar Program Review Meeting 2003, NREL/CD-520-33586 Page 866.

[39] Peter Würfel, Physics of Solar Cells, 2005 WILEY-VCH

[40] Henry Mathieu, Physique des Semiconducteurs et des Composants Electroniques, Dunod 2004

[41] P. Würfel, J. Phys.C 15, 3967–3985 (1982), http://dx.doi.org/10.1088/0022-3719/15/18/012.

[42] U. Rau, Physical Review B, vol. 76, 2007.

[43] C. Adachi, M. A. Baldo, S. R. Forrest, and M. E. Thompson, Appl. Phys. Lett. 77, 904 (2000)

[44] W. Shockley and H. J. Queisser, J. Appl. Phys. 32, 510 (1961).

[45] Amaury Delamarre, Laurent Lombez, and Jean-François Guillemoles, Applied Physics Letters, 100(13):131108, 2012.

[46] B. Feuerbacher and P. Würfel. Journal of Physics: Condensed Matter, 2:3803-3810, 1990.

[47] K. Schick, E. Daub, S. Finkbeiner, and P. Würfel. Applied Physics A: Materials Science & Processing, 54(2):109-114, 1992.

[48] S. Finkbeiner, E. Daub, and P. Würfel. In Proceedings of the 11th EU-PVSEC conference, Montreux, 1993.

[49] G Smestad and H Ries. Solar Energy Materials and Solar Cells, 25(1-2):51-71, January 1992.

[50] T. Trupke, R. A. Bardos, M. D. Abbott, and J. E. Cotter. Applied Physics Letters, 87(9):093503, 2005.

[51] V. D. Rumyantsev and J. A. Rodriguez. Solar energy materials and solar cells, 31(3):357-370, 1993.

[52] G. H. Bauer, R. Brüggemann, S. Tardon, S. Vignoli, and R. Kniese. Thin Solid Films, 480:410-414, 2005.

[53] Levent Gütay, David Regesch, Jes K. Larsen, Yasuhiro Aida, Valérie Depredurand, and Susanne Siebentritt. Applied Physics Letters, 99(15):151912, 2011.

[54] L. Ferraioli, P. Maddalena, A. Parretta, A. Wang, and J. Zhao. Applied Physics Letters, 85(18):4222, 2004.

[55] A. Bahraman and W. G. Oldham. Solid-State Electronics, 15(8):907-917, 1972.

[56] T Trupke, E Daub, and P Würfel. Solar Energy Materials and Solar Cells, 53(1-2):103-114, May 1998.

[57] A. Le Bris, L. Lombez, S. Laribi, G. Boissier, P. Christol, and J.-F. Guillemoles. Energy & Environmental Science, 5(3):6225, 2012.

[58] Markus Glatthaar, Johannes Giesecke, Martin Kasemann, Jonas Haunschild, Manuel The, Wilhem Warta, and Stefan Rein. Journal of Applied Physics, 105(11):113110, 2009.

[59] J. Müller, K. Bothe, S. Herlufsen, T. Ohrdes, and R. Brendel. IEEE Journal of Photovoltaics, 2(4):473- 478, October 2012.

[60] Takashi Fuyuki, Hayato Kondo, Tsutomu Yamazaki, Yu Takahashi, and Yukiharu Uraoka. Applied Physics Letters, 86(26):262108, 2005.

[61] T. Trupke, R. A. Bardos, M. C. Schubert, and W. Warta. Applied Physics Letters, 89(4):044107, 2006.

[62] Jonas Haunschild, Markus Glatthaar, Matthias Demant, Jan Nievendick, Markus Motzko, Stefan Rein, and Eicke R. Weber. Solar Energy Materials and Solar Cells, 94(12):2007-2012, December 2010.

[63] Ziv Hameiri and Pooja Chaturvedi. Applied Physics Letters, 102(7):073502, 2013.

[64] Delamarre, A., Paire, M., Guillemoles, J. and Lombez, L. (2014). Prog. Photovolt: Res. Appl., 23(10), pp.1305-1312.

[65] W.K. Metzger et al., Conference Paper NREL/CP-520-37028 January 2005.

[66] R.K. Ahrenkiel in Semiconductors and Semimetals Vol. 39 Ch. 2, Elsevier Science, ISBN 9780080864365 (1993).

[67] Spenke, E. (1958). In Electronic Semiconductors, p. 45. McGraw-Hill, New York.

[68] Sze, S. M. (1981). In Physics of Semiconductor Devices. Wiley-lnterscience, New York.

[69] Shockley, W., and Read, W. T. (1952). Phys. Rev. 87, 335.

[70] Hall, R. N. (1952). Phys. Rev. 87, 387.

[71] Sah, C. T., Noyce, R. N., and Shockley, W. (1957). Proc. IRE 45, 1228.

[72] Grove, A. S. (1967). In Physics and Technology of Semiconductor Devices, p. 129. John Wiley and Sons, Inc., New York.

[73] Rose, A. (1978). In Concepts in Photoconductivity and Allied Problems, p. 11. Robert Krieger Publishing Company, Huntington, New York.

[74] Ahrenkiel, R. (1987). J. Appl. Phys., 62(7), p.2937.

[75] Rosenwaks, Y., Thacker, B., Ahrenkiel, R., Nozik, A. and Yavneh, I. (1994). Phys. Rev. B, 50(3), pp.1746-1754.

[76] Ohnesorge, B., Weigand, R., Bacher, G., Forchel, A., Riedl, W. and Karg, F. (1998). Appl. Phys. Lett., 73(9), p.1224.

[77] Repins, I., Metzger, W., Perkins, C., Li, J. and Contreras, M. (2010). IEEE Trans. Electron Devices, 57(11), pp.2957-2963.

[78] Ahrenkiel, R., Keyes, B., Levi, D., Emery, K., Chu, T. and Chu, S. (1994). Appl. Phys. Lett., 64(21), p.2879.

[79] Metzger, W., Albin, D., Levi, D., Sheldon, P., Li, X., Keyes, B. and Ahrenkiel, R. (2003).J. Appl. Phys., 94(5), p.3549.

[80] Kraft, C., Hempel, H., Buschmann, V., Siebert, T., Heisler, C., Wesch, W. and Ronning, C. (2013). J. Appl. Phys., 113(12), p.124510.

[81] Mundt, L., Schubert, M., Schon, J., Michl, B., Niewelt, T., Schindler, F. and Warta, W. (2015). IEEE Journal of Photovoltaics, 5(5), pp.1503-1509.

[82] Haughn, C., Schmieder, K., Zide, J., Barnett, A., Ebert, C., Opila, R. and Doty, M. (2013). Appl. Phys. Lett., 102(18), p.182108.

[83] Metzger, W., Albin, D., Levi, D., Sheldon, P., Li, X., Keyes, B. and Ahrenkiel, R. (2003). J. Appl. Phys., 94(5), p.3549.

[84] Shirakata, S. and Nakada, T. (2009). physica status solidi (c), 6(5), pp.1059-1062.

[85] Shirakata, S., Ohkubo, K., Ishii, Y. and Nakada, T. (2009). Solar Energy Materials and Solar Cells, 93(6-7), pp.988-992.

[86] Metzger, W., Repins, I. and Contreras, M. (2008). Appl. Phys. Lett., 93(2), p.022110.

[87] M. Keyes, P. Dippo, W. K. Metzger, J. Abusham, and R. Noufi, J. Appl. Phys. 94, 5584-2003.

[88] Shirakata and T. Nakada, Thin Solid Films 515, 6151 -2007.

[89] L. Repins, B. J. Stanbery, D. L. Young, S. S. Li, W. K. Metzger, C. Perkins, W. N. Shafarman, M. E. Beck, L. Chen, V. K. Kapur, D. Tarrant, M. D. Gonzalez, D. G. Jensen, T. J. Anderson, X. Wang, L. L. Kerr, B. Keyes, S. Asher, A. Delahoy, and B. Von Roedern, Prog. Photovoltaics 14, 25- 2006.

[90] L. Sheng, B. J. Stanbery, C. H. Huang, C. H. Chang, Y. S. Chang, and T. J. Anderson, in Proceedings of the 25th IEEE Photovoltaic Specialists Conference, Washington D.C., 1997, p. 821.

[91] H. Huang, S. L. Sheng, B. J. Stanbery, C. H. Chang, and T. J. Anderson, in Proceedings of the 26th IEEE Photovoltaic Specialists Conference, Anaheim, California, 1997 p. 407.

[92] Shimakawa, K. Kitani, S. Hayashi, T. Satoh, Y. Hashimoto, Y. Takahashi, and T. Negami, Phys. Status Solidi A 203, 2630 2006.

[93] B. Ohnesorge, R. Weigand, G. Bacher, A. Forchel, W. Riedl, and F. H. Karg, Appl. Phys. Lett. 73, 1224 -1998.

[94] R. Weigand, G. Bacher, B. Ohnersorge, A. Forchel, W. Riedl, and F. H. Karg, in 2nd World Conference and Exhibition on Photovoltaic Solar Energy Conversion, Vienna, Austria, 1998.

[95] V. Probst, W. Stetter, W. Riedl, H. Vogt, M. Wendl, H. Calwer, S. Zweigart, K. D. Ufert, B. Freienstein, H. Cerva, and F. H. Karg, Thin Solid Films 387, 262 -2001.

[96] Maiberg, M., Spindler, C., Jarzembowski, E. and Scheer, R. (2015). Thin Solid Films, 582, pp.379-382.

[97] Kuciauskas, D., Li, J., Contreras, M., Pankow, J., Dippo, P., Young, M., Mansfield, L., Noufi, R. and Levi, D. (2013). J. Appl. Phys., 114(15), p.154505."

[98] Kuciauskas, D., Li, J., Kanevce, A., Guthrey, H., Contreras, M., Pankow, J., Dippo, P. and Ramanathan, K. (2015). J. Appl. Phys., 117(18), p.185102.

[99] Aspnes, D. (1984). Journal of Vacuum Science & Technology A: Vacuum, Surfaces, and Films, 2(3), p.1309.

[100] Choi, S., Chen, R., Persson, C., Kim, T., Hwang, S., Kim, Y. and Mansfield, L. (2012). Appl. Phys. Lett., 101(26), p.261903.

[101] Choi, S., Zhao, H., Persson, C., Perkins, C., Donohue, A., To, B., Norman, A., Li, J. and Repins, I. (2012). J. Appl. Phys., 111(3), p.033506.

[102] Ma, J., Kuciauskas, D., Albin, D., Bhattacharya, R., Reese, M., Barnes, T., Li, J., Gessert, T. and Wei, S. (2013). Phys. Rev. Lett., 111(6).

[103] Kuciauskas, D., Kanevce, A., Burst, J., Duenow, J., Dhere, R., Albin, D., Levi, D. and Ahrenkiel, R. (2013). IEEE Journal of Photovoltaics, 3(4), pp.1319-1324.

[104] Rau, U., Abou-Ras, D. and Kirchartz, T. (2011). *Advanced characterization techniques for thin film solar cells*. Weinheim, Germany: Wiley-VCH.

[105] Sakurai, Takeaki et al. Jpn. J. Appl. Phys. 50.5 (2011).

[106] Paire, M., Lombez, L., Péré-Laperne, N., Collin, S., Pelouard, J., Lincot, D. and Guillemoles, J. (2011). Appl. Phys. Lett., 98(26), p.264102.

[107] Paire, M., Shams, A., Lombez, L., Péré-Laperne, N., Collin, S., Pelouard, J., Guillemoles, J. and Lincot, D. (2011). Energy & Environmental Science, 4(12), p.4972d.

[108] El-Hajje, G., Ory, D., Paire, M., Guillemoles, J. and Lombez, L. (2016). Solar Energy Materials and Solar Cells, 145, pp.462-467.

[109] Uwe Rau, Daniel Abou-Ras and Thomas Kirchartz: Advanced Characterization Techniques for Thin Film Solar Cells (April 18, 2011).

[110] Igalson, M., and H. W. Schock. J. Appl. Phys. 80.10 (1996): 5765.

[111] Rau, U. et al. Appl. Phys. Lett. 73.2 (1998): 223.

[112] Lany, Stephan, and Alex Zunger. Phys. Rev. Lett. 100.1 (2008).

[113] Müller, T. C. M. et al. Appl. Phys. Lett. 103.18 (2013).

[114] M.Igalson and A.Urbaniak, BULLETIN OF THE POLISH ACADEMY OF SCIENCES TECHNICAL SCIENCES Vol. 53, No. 2, 2005.

[115] M.Igalson and P.Zabierwoski, OPTO-ELECTRONICS REVIEW **11**(4), 261–267 (2003)

[116] Tran, T.M.H. et al. Thin Solid Films 535 (2013): 307-310.

[117] Pudov, A., Ph.D thesis - Department of Physics. 2005, Colorado State University.

[118] Eisgruber, I., et al., Solar Energy Materials and Solar Cells, 1998. 53(3): p. 367-377.

[119] Pudov, A., et al., Journal of applied physics, 2005. 97(6): p. 064901-064901-6.

[120] Song, T., thesis- Department of Physics. 2013, Colorado State University.

[121] Igalson, M., and H. W. Schock. J. Appl. Phys. 80.10 (1996): 5765.

[122] Rau, U. et al. Appl. Phys. Lett. 73.2 (1998): 223.

[123] Scheer, R. and Schock, H. (2011). *Chalcogenide photovoltaics*. Weinheim: Wiley-VCH.

[124] Alonso, M., Garriga, M., Durante Rincón, C. and León, M. (2000). J. Appl. Phys., 88(10), p.5796.

[125] Eisenbarth, T., Caballero, R., Nichterwitz, M., Kaufmann, C., Schock, H. and Unold, T. (2011). J. Appl. Phys., 110(9), p.094506.

[126] Serhan, J., Djebbour, Z., Favre, W., Migan-Dubois, A., Darga, A., Mencaraglia, D., Naghavi, N., Renou, G., Guillemoles, J. and Lincot, D. (2011). Thin Solid Films, 519(21), pp.7606-7610.

[127] Heath, J., Cohen, J., Shafarman, W., Liao, D. and Rockett, A. (2002). Appl. Phys. Lett., 80(24), p.4540.

[128] Cao, Q., Gunawan, O., Copel, M., Reuter, K., Chey, S., Deline, V. and Mitzi, D. (2011). (Adv. Energy Mater. 5/2011). Advanced Energy Materials, 1(5), pp.844-844.

[129] Paul, P., Cardwell, D., Jackson, C., Galiano, K., Aryal, K., Pelz, J., Marsillac, S., Ringel, S., Grassman, T. and Arehart, A. (2015). IEEE Journal of Photovoltaics, 5(5), pp.1482-1486.

[130] Susanne Siebentritt. Solar Energy Materials and Solar Cells, 95(6):1471-1476, June 2011.

[131] Jürgen H. Werner, Julian Mattheis, and Uwe Rau. Thin Solid Films, 480-481:399-409, June 2005.

[132] U. Rau, P. O. Grabitz, and J. H. Werner. Applied Physics Letters, 85(24):6010, 2004.

[133] Rau, U. and Werner, J. (2004). Appl. Phys. Lett., 84(19), p.3735.

[134] Lombez, L., Ory, D., Paire, M., Delamarre, A., El Hajje, G. and Guillemoles, J. (2014). Thin Solid Films, 565, pp.32-36.

[135] Bauer, G. and Gütay, L. (2007). Thin Solid Films, 515(15), pp.6127-6131.

[136] Helbig, A., Kirchartz, T., Schaeffler, R., Werner, J. and Rau, U. (2010). Solar Energy Materials and Solar Cells, 94(6), pp.979-984.

[137] Mundt, L., Schubert, M., Schon, J., Michl, B., Niewelt, T., Schindler, F. and Warta, W. (2015). IEEE Journal of Photovoltaics, 5(5), pp.1503-1509.

[138] Eich, D., Herber, U., Groh, U., Stahl, U., Heske, C., Marsi, M., Kiskinova, M., Riedl, W., Fink, R. and Umbach, E. (2000). Thin Solid Films, 361-362, pp.258-262.

[139] Schubert, M., Riepe, S., Bermejo, S. and Warta, W. (2006).J. Appl. Phys., 99(11), p.114908.

[140] Larsen, J., Gütay, L., Aida, Y. and Siebentritt, S. (2011). Thin Solid Films, 519(21), pp.7332-7336.

[141] Bothe, K., Bauer, G. and Unold, T. (2002). Thin Solid Films, 403-404, pp.453-456.

[142] Tennyson, E. M., Garrett, J. L., Frantz, J. A., Myers, J. D., Bekele, R. Y., Sanghera, J. S., Munday, J. N. and Leite, M. S. , Advanced Energy Materials 5.23 (2015)

[143] Y. Sun, N. Hatami,M. Yee et al., Journal of Biomedical Optics, vol. 15, no. 5, Article ID056022, 2010.

[144] X. F. Wang, T. Uchida, D. Coleman et al., Applied Spectroscopy, vol. 45, no. 3, pp. 360–366, 1991.

[145] C. Liu, Y. Zhou, X. W. Wang et al., CN201210184350.9.

[146] M. Y. Berezin and S. Achilefu, Chemical Reviews, vol. 110, no. 5, pp. 2641–2684, 2010.

[147] F. Pinaud, X. Michalet, L. A. Bentolila et al., Biomaterials, vol. 27, no. 9, pp. 1679–1687, 2006.

[148] J. M. Klostranec and W. C. W. Chan, Advanced Materials, vol. 18, no. 15, pp. 1953–1964, 2006.

[149] H. C. Gerritsen, R. Sanders, A. Draaijer, C. Ince, and Y. K. Levine, Journal of Fluorescence, vol. 7, no. 1, pp. 11–15, 1997.

[150] D. Sud and M. Mycek, Journal of Biomedical Optics, vol. 14, no. 2, Article ID020506, 2009.

[151] El-Hajje, G., Momblona, C., Gil-Escrig, L., Ávila, J., Guillemot, T., Guillemoles, J., Sessolo, M., Bolink, H. and Lombez, L. (2016). Energy Environ. Sci., 9(7), pp.2286-2294.

[152] Myriam Paire. PhD thesis - Université Paris VI , 2012.

[153] Amaury Delamarre. PhD thesis - Université Paris VI , 2013.

[154] GH Bauer, K Bothe, T Unold, Photovoltaic Specialists Conference, 2002. Conference Record of the Twenty-Ninth IEEE, pp.700-703, 2002.

[155] S. M. Sze. Physics of Semiconductor Devices. John Wiley and Sons, 1981.

[156] W. Shockley. Bell System Technical Journal, 28(3):435-489, 1949.

[157] Bube, R. (1992). Photoelectronic properties of semiconductors. Cambridge: Cambridge University Press.

[158] Nixon, M., Redding, B., Friesem, A., Cao, H. and Davidson, N. (2013). Optics Letters, 38(19), p.3858.

[159] Peter Würfel. Physics of solar cells: from basic principles to advanced concepts. Wiley-VCH, Weinheim, 2nd edition edition, 2009.

[160] Rau, U. (2012). IEEE Journal of Photovoltaics, 2(2), pp.169-172.

[161] Scheer, R. and Schock, H. (2011). Chalcogenide photovoltaics. Weinheim: Wiley-VCH.

[162] Ioffe.ru. (2016). Electrical properties of Gallium Arsenide (GaAs). [online] Available at: http://www.ioffe.ru/SVA/NSM/Semicond/GaAs/electric.html#Recombination.

[163] Maiberg, M. and Scheer, R. (2014). Journal of Applied Physics, 116(12), p.123711.

[164] Maiberg, M., Hölscher, T., Zahedi-Azad, S. and Scheer, R. (2015). J. Appl. Phys., 118(10), p.105701.

[165] Maiberg, M., Hölscher, T., Zahedi-Azad, S., Fränzel, W. and Scheer, R. (2015). Appl. Phys. Lett., 107(12), p.122104.

# List of peer-reviewed publications & proceedings


1. **El-Hajje, G**., Ory, D., Guillemoles, J. and Lombez, L. (2016). On the origin of the spatial inhomogeneity of photoluminescence in thin-film CIGS solar devices. *Appl. Phys. Lett., 109(2), p.022104.*
2. **El-Hajje, G.,** Momblona, C., Gil-Escrig, L., Ávila, J., Guillemot, T., Guillemoles, J., Sessolo, M., Bolink, H. and Lombez, L. (2016). Quantification of spatial inhomogeneity in perovskite solar cells by hyperspectral luminescence imaging. *Energy Environ. Sci., 9(7), pp.2286-2294.*
3. **G. El-Hajje**, D.Ory et al "Local transport properties investigation by correlating hyperspectral and confocal luminescence images", *Proceedings of SPIE - The International Society for Optical Engineering· March 2016, DOI: 10.1117/12.2208329.*
4. ***G. El-Hajje***, D.Ory et al "Quantitative luminescence-based measurement of trapping defects density in thin film solar cells", Submitted to *Progress in Photovoltaics*.
5. ***G. El-Hajje***, D.Ory et al., "Contactless characterization of metastable defects in Cu(In,Ga)$Se_2$ solar cells using time-resolved photoluminescence", *Solar Energy Materials and Solar Cells* 145 (2016): 462-467.
6. **G. El-Hajje** , D.Ory et al. , "Optoelectronic characterization of polycrystalline solar cells using time-resolved biased luminescence techniques", *Proc. SPIE 9358, Physics, Simulation, and Photonic Engineering of Photovoltaic Devices IV, 93580M (16 March 2015); doi: 10.1117/12.2076942.*
7. Pierre Rale, Amaury Delamarre, ***G. El-Hajje,*** R.Tamaki, et al. , "Quantitative optical measurement of chemical potentials in intermediate band solar cells" , *Journal of Photonics for Energy 5.1 (2015): 053092.*
8. L. Lombez, D. Ory, M. Paire, A. Delamarre, ***G. El-Hajje***, J.F. Guillemoles, *"Micrometric investigation of external quantum efficiency in microcrystalline CuInGa(S,Se)$_2$ solar cells", Thin Solid Films, Volume 565, 28 August 2014, Pages 32-36,* doi:10.1016/j.tsf.2014.06.041.
9. Jean-François Guillemoles, Amaury Delamarre, ***G. El-Hajje***, P. Rale *et al, "Characterization of Photovoltaic Absorbers for High Throughput Processing", MRS proceedings/ Volume 1709/2014,* http://dx.doi.org/10.1557/opl.2014.896.
10. Jean-François Guillemoles, Amaury Delamarre, ***G. El-Hajje***, P. Rale *et al, "Hyperspectral Imaging of Photovoltaic Conversion", MRS proceedings/ Volume 1670/2014,* http://dx.doi.org/10.1557/opl.2014.700.

# Appendix A

## Quantification of spatial inhomogeneity in perovskite solar cells by hyperspectral luminescence imaging

Apart from the global and main *PhD* project, we additionally established a collaboration with a team from the University of Valencia. The collaboration consisted of a characterization of hybrid perovskite solar cells using the hyperspectral imaging of their luminescence. This work was of an exploratory nature and the main motivation was to investigate the spatial inhomogeneites of perovskite-based solar cells that are the current rising start of the PV sector. The collaboration resulted in a paper published in *Energy & Environmental Science* found in ref [151] under the title of *"Quantification of spatial inhomogeneity in perovskite solar cells by hyperspectral luminescence imaging".*

Below, we start by representing the broad context of this study. We then show the Figures of the main results and end with a conclusion.

High efficiency solar cells employing inexpensive hybrid perovskite absorbers have been widely studied as a potential future energy source. Investigation of the PL and EL properties of perovskites is a valuable tool to unveil their properties and limitations. Interestingly, many studies have highlighted a rather inhomogeneous spatial distribution of the luminescence, in contrast to the very high efficiencies reported. Most of those studies used local excitation at very high intensity and, importantly, the luminescence has been observed only qualitatively. In this study, we use hyperspectral luminescence imaging to study planar p–i–n solar cells employing vacuum deposited CH3NH3PbI3 perovskite absorbers. Through this technique, it is possible to quantify the number of photons emitted from every point of the device at every wavelength. We investigated spatial fluctuations from a few microns to the millimeter scale and show that both photo- and electroluminescence are spatially not uniform, leading to a distribution of the quasi-Fermi level splitting which strongly depends on the position in the device. We also map the carrier transport efficiency, finding areas where the photogenerated carrier collection efficiency is lower than 60%. We show that this inefficient charge collection is most likely due to interfacial resistance fluctuations. This work is relevant for perovskite and organic based opto-electronic devices.

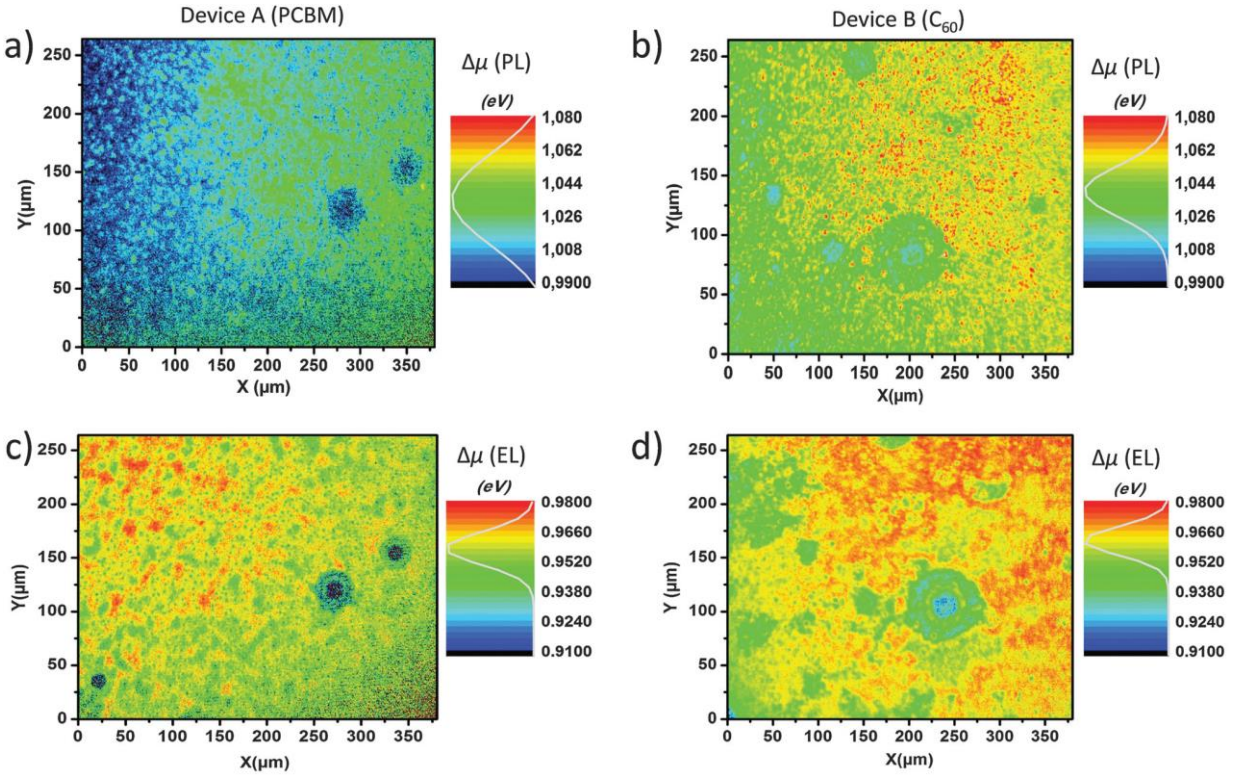



**Figure App.1.1: (a) Absolute mapping of the quasi-Fermi level splitting derived from photoluminescence (a and b, top) and electroluminescence (c and d, bottom), for perovskite solar cells using PCBM (left, device A) or C60 (right, device B) as the ETL.**

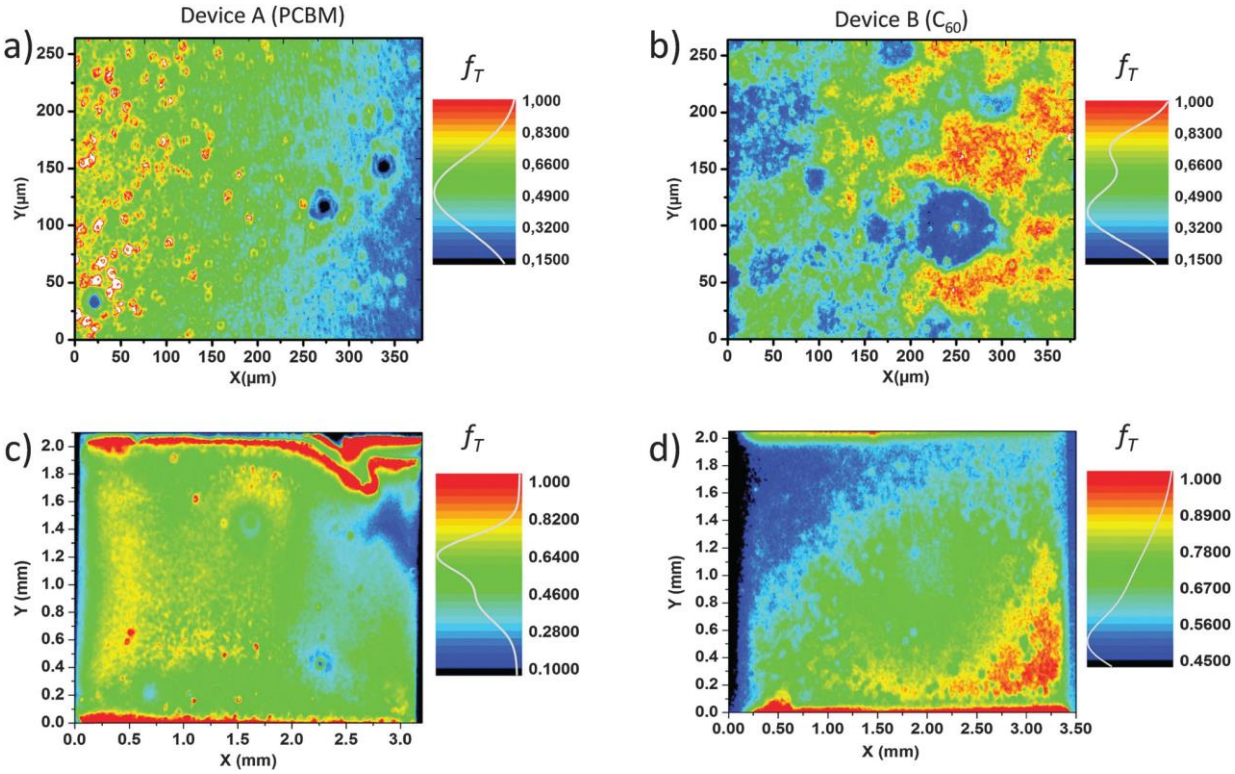



**Figure App.1.2: Mapping of the current transport efficiency $f_T$ obtained from two EL hyperspectral images taken at 1.15 V and 1.16 V applied bias. $f_T$ mapping was performed at the microscale (top) and at the whole device level (bottom) for perovskite solar cells using PCBM (a and c, device A) or C60(b and d, device B) as the ETL.**

In summary, we have investigated efficient p–i–n hybrid perovskite solar cells through luminescence hyperspectral imaging. The small mismatch between the electrically measured $V_{oc}$ and the optically (from both photoluminescence and electroluminescence) deduced quasi-Fermi level splitting is indicative of the high quality of the perovskite absorber. Yet the spatially resolved analysis identified profound inhomogeneities in this novel type of devices. These spatial inhomogeneities appear to be related to problems with carrier extraction, leading to the limited fill factor of the cells. This hypothesis is supported by the dispersion of the spatially resolved carrier transport efficiency function, which identifies areas of the cell with severely hindered charge transport. We ascribe these losses first to local fluctuations of interface series resistance and, with a lower impact, to inefficient lateral transport. The origin of the inhomogeneities observed here is not yet clear, but its understanding would allow us to significantly enhance the performance of these already efficient photovoltaic devices. This work also demonstrated that hyperspectral luminescence imaging is a powerful tool to investigate the lateral variations of novel devices such as hybrid perovskite solar cells.

**Gilbert EL-HAJJE**

# Développement de nouvelles méthodes de caractérisation optoélectroniques des cellules solaires photovoltaïques par imagerie de luminescence


## Résumé

La connaissance approfondie sur la luminescence des dispositifs photovoltaïques (PV) en a fait un outil de caractérisation puissant qui capte l'intérêt de la recherche et des industries du PV. Dans cette thèse, nous nous concentrons sur la luminescence des cellules solaires photovoltaïques à base de $Cu(In,Ga)Se_2$. En particulier, nous explorons et revisitons ses dépendances temporelles, spectrales et spatiales. Cela a abouti dans un premier temps à la mise au point de nouvelles méthodes de caractérisation basée sur la luminescence de cette technologie PV en particulier. Nous montrons d'abord que par l'intermédiaire d'une méthode sans contact toute optique, nous sommes en mesure de détecter et de localiser les métastabilités de cette technologie. En utilisant une approche numérique basée sur des résultats expérimentaux de photoluminescence résolue en temps (TRPL) nous avions réussi à quantifier la densité des défauts de piégeage qui sont derrière ces métastabilités. Une fois quantifiée, nous traduisons cette densité en pertes absolues de performance PV de la cellule solaire.

Ensuite, en explorant la dépendance spatiale de la luminescence des cellules solaires à base de $Cu(In,Ga)Se_2$, nous avions corrélé avec succès, ses aspects temporels et spectrales en se basant sur la microscopie confocale à balayage et l'imagerie hyperspectrale. Cela nous a permis de généraliser nos résultats précédents à l'échelle globale des cellules solaires. Cette partie de la thèse nous a aidés à mieux comprendre une des origines fondamentales derrière l'inhomogénéité spatiale de la luminescence de ce type de dispositifs photovoltaïques.

La dernière partie de la thèse était essentiellement technique et exploratoire. En particulier, nous introduisons une nouvelle technique optique dans le domaine de la caractérisation des dispositifs PV. Cette technique est dédiée à l'imagerie résolue en temps du temps de vie de fluorescence (TRFLIM). Le principe de cette technique consiste essentiellement en acquisition d'images de luminescence du dispositif PV qui sont résolues temporellement. Avec ce nouveau dispositif expérimental, nous sommes maintenant en mesure de résoudre spatialement, et en temps réel la dynamique des porteurs de charge d'une technologie photovoltaïque donnée et accéder à ses propriétés électroniques clés. Une première démonstration a été faite sur une cellule solaire à base de GaAs, et pour laquelle nous avions extrait optiquement, la longueur de diffusion, la mobilité et le temps de vie de ses porteurs. De plus, nous avions pu estimer le coefficient de diffusion du matériau et son taux de dopage.


**Mots-clefs** : Luminescence, photovoltaïque, CIGS, dynamique de porteurs, TRFLIM, caractérisation, Hyperspectral, TRPL

# Summary

The extensive knowledge on the luminescence of photovoltaic (PV) devices has made it a powerful characterization tool that captures the interest of both research and industrial PV communities. In this thesis, we focus on the luminescence of Cu(In,Ga)$Se_2$-based solar PV. In particular, we explore and revisit the luminescence temporal, spectral and spatial dependencies.

This resulted in the development of new luminescence-based characterization methods for this particular PV technology. We show initially that by means of an all-optical, contactless methodology, we are able to detect and localize the metastabilities of this technology. Using a numerical approach based on experimental time-resolved photoluminescence (TRPL) we managed to quantify the trapping defects that are behind these metastabilities. Once quantified, we translated it into absolute losses in the PV performance of the solar cell.

By exploring the spatial dependence of the luminescence of Cu(In,Ga)$Se_2$ solar cells, we successfully correlated its temporal and spectral aspects based on scanning confocal microscopy and hyperspectral imaging. This allowed us to generalize our previous findings at the global solar cell scale. This part of the thesis helped us better understand one of the fundamental origins behind the spatially inhomogeneous luminescence of Cu(In,Ga)$Se_2$ PV devices.

The final part of the thesis was mainly technical and exploratory. In particular, we introduced a new optical technique to the field of PV characterization. It is dedicated to time-resolved fluorescence lifetime imaging (TRFLIM) which basically consists of acquiring time-resolved luminescence images of the PV device. With this new setup we are now able to spatially resolve, in real-time the charge carrier dynamics of a given PV technology and access its key electronic properties. A first application was made on a GaAs-based solar cell, for which we were able to optically extract the mobility, diffusion length and lifetime of its carriers. Finally, we were also able to estimate the diffusion coefficient of the material and its doping density.



**Keywords**: Luminescence, photovoltaic, CIGS, carrier dynamics, TRFLIM, characterization, Hyperspectral, TRPL